Novel Transition Metal Complexes for the Photocatalytic CO_2 Reduction

Zur Erlangung des akademischen Grades einer

DOKTORIN DER NATURWISSENSCHAFTEN

(Dr. rer. nat.)

von der KIT-Fakultät für Chemie und Biowissenschaften

des Karlsruher Instituts für Technologie (KIT)

genehmigte

DISSERTATION

von

M.Sc. Lisa Lou Gracia

aus Venissieux

Dekan: Prof. Dr. Hans-Achim Wagenknecht

Referentin: Dr. Claudia Bizzarri

Korreferent: Prof. Dr. Frank Breher

Tag der mündlichen Prüfung: 15.02.2023

« Je suis de ceux qui pensent que la science est d'une grande beauté. Un scientifique dans son laboratoire est non seulement un technicien : il est aussi un enfant placé devant des phénomènes naturels qui l'impressionnent comme des contes de fées. »

Marie Curie

Neuartige Übergangsmetallkomplexe für die photokatalytische CO_2 Reduktion

HONESTY DECLARATION

This work was carried out from September 2, 2019 through January 9, 2023 at the Karlsruhe Institute of Technology (KIT) under the supervision of Dr. Claudia Bizzarri in the Department of Organic Chemistry, Faculty of Chemistry and Biosciences.

Hereby I, Lisa Lou Gracia, declare that I completed this work independently and without any improper help. All material published by others is cited properly.

KURZZUSAMMENFASSUNG

Künstliche Photosynthese ist ein chemischer Prozess, der darauf abzielt, die natürliche Photosynthese nachzuahmen, indem CO_2 nur unter Verwendung von Sonnenenergie in wertvolle Rohstoffe umgewandelt wird. Es bietet eine Chance, die ökologischen und ökonomischen Probleme zu beantworten, die mit dem gestörten Kohlenstoffkreislauf verbunden sind und der für den Klimawandel verantwortlich ist. Die ersten künstlichen Photosynthesesysteme wurden in den frühen 80er Jahren von LEHN und Mitarbeitern eingeführt und haben seitdem beträchtliche Aufmerksamkeit auf sich gezogen. Um die verschiedenen Schritte der natürlichen Photosynthese nachzuahmen, kombinieren die beschriebenen homogenen Systeme ein lichtsammelndes Molekül (Photosensibilisator, PS), einen metallhaltigen Katalysator, der in der Lage ist, mit CO_2 zu reagieren und es zu reduzieren, sowie Protonen- und Elektronenquellen, um die Umwandlung von CO_2 in C_1-Bausteine zu ermöglichen (Kohlenmonoxid, Formiate, Methanol, Methan). Erst kürzlich wurden unedle Metalle in die Strukturen integriert, um die seltenen und teuren Edelmetalle zu ersetzen, wodurch die Systeme nachhaltiger und kostengünstiger wurden. Ihre unterschiedliche Reaktivität erfordert jedoch ein gründliches Verständnis der beteiligten Mechanismen sowie ein spezifisches Ligandendesign und angepasste Reaktionsbedingungen. In dieser Dissertation wurden neue Komplexe auf Übergangsmetallbasis für die photokatalytische Reduktion von CO_2 hauptsächlich zu CO und H_2 als Nebenprodukt entworfen. Im ersten Projekt wurde ein System mit dem bekannten und leichtverfügbaren Ni(cyclam)Cl_2 als Katalysator in Kombination mit neuen Cu^I-basierten Photosensibilisatoren entworfen. Das System wurde optimiert und produzierte selektiv CO mit einer TON von 8, wenn der bimetallische Cu^I-Komplex PS-**4** als PS mit einer Quanteneffizienz von 2,1% verwendet wurde. Diese Ergebnisse gehören zu den höchsten, die mit Ni(cyclam)Cl_2 als Katalysator berichtet wurden, der zum ersten Mal mit einem unedlen Metall als PS in Verbindung gebracht wurde, was zeigt, dass Edelmetalle ersetzt werden können. In einem zweiten Schritt wurden neue auf unedlen Metallen-basierte einkernige Katalysatoren für die photokatalytische CO_2-Reduktion mit 2,6-Bis(1,2,3-triazol-yl-methyl)pyridin-Ligandenstrukturen entworfen, aus denen ein bestimmter Eisenkomplex hervorstich. Er produzierte CO mit einer TON von 576 und einer Quanteneffizienz von 7,1% in Kombination mit einem Cu^I-Photosensibilisator. Seine Aktivität als Katalysator wurde untersucht und ein katalytischer Mechanismus vorgeschlagen. Die Umwandlung des Phenylliganden in ein Chinolin ermöglichte die Bildung eines zweikernigen Kobaltkomplexes, der bei Verwendung als Katalysator dreimal mehr CO produzierte als sein einkerniges Analogon. Dies erlaubte die Annahme eines kooperativen Effekts zwischen den beiden Metallen. Ein anderer Syntheseansatz führte zur Bildung eines trimetallischen Eisenkomplexes, dessen Eigenschaften untersucht und beschrieben wurden. Weder seine magnetischen Eigenschaften noch seine Verwendung als Katalysator für die CO_2-Reduktion zeigten das Vorhandensein von Kooperativitätseffekten zwischen den Metallen. Schließlich wurde das Design von Multimetall-Photokatalysatoren untersucht, die einen Photosensibilisator und einen Katalysator im selben Molekül kombinieren. Aus den Synthesewegen gingen jedoch nur einkernige Komplexe hervor, die interessante katalytische Aktivitäten zeigten.

ABSTRACT

Artificial photosynthesis is a chemical process which aims at mimicking natural photosynthesis by converting CO_2 into valuable feedstock, only using solar energy. It offers an opportunity to answer the ecological and economic problems associated with the disturbed carbon cycle, responsible for climate change. The first artificial photosynthetic systems were introduced in the early 80s by Lehn and coworkers and since then, have drawn considerable attention. To mimic the different steps of natural photosynthesis, the homogeneous systems described combine a light harvesting molecule (photosensitizer, PS), a metallic catalyst able to react and reduce CO_2, and proton and electron sources to enable the transformation of CO_2 into C_1 building blocks (carbon monoxide, formate, methanol, methane). Only recently, earth-abundant materials were implemented into the structures to replace the rare and expensive metals, rendering the systems more sustainable and less expensive. However, their different reactivity requires a thorough understanding of the mechanisms involved, as well as a specific ligand design and adjusted reaction conditions.

In this thesis, new transition metal-based complexes were designed for the photocatalytic reduction of CO_2 into mainly CO and H2 as a co-product. In the first project, an earth-abundant system with the known Ni(cyclam)Cl_2 as catalyst in combination with new Cu^I-based photosensitizers was designed. The system was optimized and produced CO selectively with a TON of 8 when the bimetallic Cu^I complex 4 was used as PS with a quantum efficiency of 2.1%. Those results are amongst the highest reported with Ni(cyclam)Cl_2 as catalyst, which was associated with earth-abundant PS for the first time, proving the achievability of replacing noble metals.

In a second step, new earth-abundant based mononuclear catalysts for the photocatalytic reduction of CO_2 were designed with 2,6-bis(1,2,3-triazol-yl-methyl)pyridine ligand structures, from which one particular iron complex stood out. It produced CO with a TON of 576 and a quantum efficiency of 7.1% in combination with a Cu^I photosensitizer. Its activity as catalyst was investigated and a catalytic mechanism was proposed.

The transformation of the phenyl ligand into a quinoline allowed the formation of a bimetallic cobalt complex, which produced three times more CO than its mononuclear analogue when employed as catalyst. This allowed to postulate the existence of a cooperative effect between the two metals.

A different synthetic approach led to the formation of a trimetallic iron complex, whose properties were investigated and described. Neither its magnetic properties nor its use as a catalyst for CO_2 reduction showed the presence of cooperativity effects between the metals.

Lastly, the design of multi-metallic photocatalysts, combining a photosensitizer and a catalyst in the same molecule, was explored. However, only mononuclear complexes emerged from the synthetic pathways, showing interesting catalytic activities.

TABLE OF CONTENTS

1 INTRODUCTION

1.1 GENERAL INTRODUCTION

The notion of global warming was introduced for the first time in 1896 by Swedish scientist Svante Arrhenius who predicted a link between the atmospheric carbon dioxide level and change of the surface temperature through the greenhouse effect.[1] This effect, consisting of trapping the sun´s heat or infrared radiations, is necessary to make Earth warm enough to be livable, but causes severe deregulations when increasing uncontrollably. In 1938, for the first time, scientists demonstrated the heat-trapping nature of carbon dioxide and other gases, responsible for the greenhouse effect.[2]

Throughout time, Earth´s climate has changed continuously cyclically from cold to warm periods. These cycles were attributed to different amount of solar energy received due to small variations in Earth´s orbit. Until the mid-1900s and for millennia, the atmospheric carbon dioxide level had an average value of 230 ppm and never exceeded 300 ppm (Figure 1).[3] A clear end of the trend from 1950 to today is visible and measurable with concentrations of CO_2 exceeding 400 ppm. The Earth´s temperature has since risen by about 0.75 °C and it was determined that today, doubling the concentration of CO_2 results in a 3 °C raised in temperature.[4] Noteworthy, the mid-1900s correspond to the industrial revolution and the pervasive use of fossil fuels. The anthropogenic causes of the disturbed carbon cycle and the deregulation of climate change are undeniable. This too rapid increase in temperature leads to biodiversity loss, forest fires, higher sea level, less accessibility to fresh water, mass human migration, and wars.[5-7]

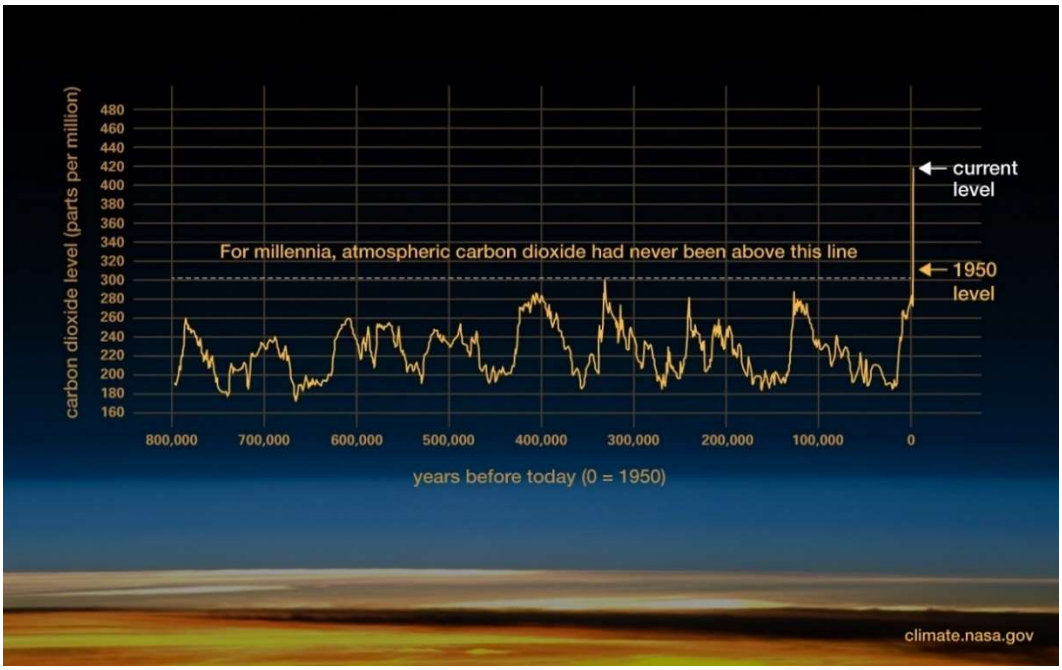

Figure 1. Evolution of atmospheric CO_2 concentration, reproduced with permission (Credit: Luthi, D., et al.. 2008; Etheridge, D.M., et al. 2010; Vostok ice core data/J.R. Petit et al.; NOAA Mauna Loa CO_2 record, Copyright Scripps CO_2 program).

Earth has a natural way of absorbing and use CO_2. Forests absorb a net 7.6 billion metric tons of CO_2 per year but the largest carbon sink is the ocean.[8] CO_2 dissolves in sea water to form carbonic acid, but photosynthesis by phytoplankton is the main carbon consumer, absorbing 10 to 20 billion metric tons of CO_2 per year and releasing the major part of the 21% of oxygen contained in the atmosphere.[9] Photosynthesis is thus the main solution for the earth to absorb CO_2 using forests or phytoplankton. For this process, the used energy source is solar, the most abundant energy on earth and entirely renewable. The energy potential is outstanding with 122 PW (or 3 850 000 EJ per year) received by the Earth[10] and in 2020 solar energy has been the cheapest energy. Photosynthesis seizes 3000 EJ per year to convert it into biomass.[11] Harvesting solar energy constitutes therefore a major challenge for human as well as converting it efficiently into other usable energy like electric or thermic energy.

1.2 CO_2 Reduction

Reducing, or better using, the atmospheric CO_2 to stabilize, climate change has become one of the most important challenges for humans. Governments have come together to set laws and objectives to answer this threat. For example, the Paris agreement was adopted in 2015 by 196 parties with the main objective of keeping the global increase of temperature under 2 °C. On their side, scientists from all over the world also search for and develop new systems to answer this threat.[12] The main ideas are to reuse the CO_2 anthropogenically produced to transform it into valuable material.[13-16] CO_2 can be directly used, for example by the food industry (e.g., carbonated drinks)[17] or as inert gas for fire extinguishers[18] but it can also be chemically transformed. Today several catalytic processes convert CO_2 at industrial scales by using renewable energies.[19] Some consist of hydrogenating CO_2 to biofuels like alcohols and hydrocarbons through metal catalysis[20-23] or converting CO_2 into a monomer for polymers and plastics.[24-25] For example, CO_2 was very recently (2021) inserted into polymers with a bimetallic Ni catalyst.[26]

To efficiently and industrially transform CO_2 into valuable material or fuel, the capture of CO_2 is being extensively studies[27-30] but the chemical conversion of CO_2 is a more significant challenge[31]. Indeed, CO_2 is one of the most thermodynamic stable molecules and kinetically inert (Gibbs free energy $\Delta_f G = -394.38$ kJ mol^{-1}). The C=O double bond with a bonding energy of 750 kJ mol^{-1} is the reason of this high stability, as the activation energies for C-C and C-O are much lower (336 and 327 kJ mol^{-1} respectively). The two reactive sites are the electrophile carbon center and the nucleophile oxygens (Scheme 1).[32]

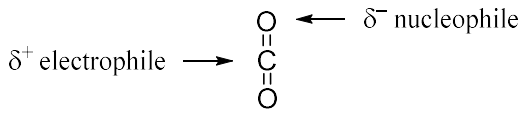

Scheme 1. Active sites of CO_2.

The use of renewable energies to transform sustainably CO_2 is necessary, with the most abundant being the solar energy. By mimicking nature, systems were created to reproduce a simplified version of photosynthesis, using solar energy to electrochemically or photochemically convert CO_2 into C_1 or C_2 building blocks. To electrocatalytically or photo-catalytically reduce CO_2 a lot of energy is then needed. Electrons can be directly transferred to CO_2 but the redox potentials are highly negative (-1.97 V to form CO_2^- in DMF so highly unfavorable.[33] To overcome this barrier, proton-assisted multiple electron transfer strategies through catalysis allowed the production of various products reachable with less negative potentials. (Table 1). Thus, CO, COOH, CH_4, CH_3OH can be formed as C_1 blocks but C_2 products like C_2H_4 or CH_3CH_2OH can also be synthesized using heterogeneous catalysts.[34-36] As all of the different possible reactions leading to different products have similar reduction potentials (including the formation of H_2), those reactions are thus competitive. This will later accentuate the importance of the design of selective systems.

Table 1. Reduction potentials of CO_2[37]

Reduction potentials of CO_2	*E* [V] *vs* SHE at pH 7
$CO_2 + e^- \rightarrow CO_2^-$	−1.9
$CO_2 + 2H^+ + 2e^- \rightarrow HCOOH$	−0.61
$CO_2 + 2H^+ + 2e^- \rightarrow CO + H_2O$	−0.52
$2CO_2 + 12H^+ + 12e^- \rightarrow C_2H_4 + 4H_2O$	−0.34
$CO_2 + 4H^+ + 4e^- \rightarrow HCHO + H_2O$	−0.51
$CO_2 + 6H^+ + 6e^- \rightarrow CH_3OH + H_2O$	−0.38
$CO_2 + 8H^+ + 8e^- \rightarrow CH_4 + 2H_2O$	−0.24
$2H^+ + 2e^- \rightarrow H_2$	−0.42

1.3 PHOTOCATALYTIC REDUCTION OF CO_2

As discussed above, one way to convert CO_2 using renewable energy is mimicking nature´s way of transforming CO_2 into energy (sugars): photosynthesis. Photosynthesis consists of producing carbohydrates and O_2 from water and CO_2 following the equation:

$$6CO_2 + 12H_2O \rightarrow 2C_3H_6O_3 + 6O_2$$

through the energy of the solar light. Although the total efficiency considering the solar energy stored, is not very high (maximum efficiency of 26% but in reality 1%), it involves extremely sophisticated and efficient processes that scientists have studied for many years.[38]

Artificial photosynthesis and electrocatalysis are two different strategies generally proposed that convert CO_2 into fuel or valuable molecules using renewable energies. While electrocatalysis (Scheme 2, bottom right) involves an anode and a cathode creating a sufficient potential to reduce CO_2 using electrocatalysts, artificial photosynthesis (Scheme 2, bottom left) uses the visible range of solar radiation as an energy source. It involves the direct absorption of solar energy by light-harvesting molecules called photosensitizers (PS) and charge transfers in a homogeneous media[39-40]. Moreover, the electrocatalysis of CO_2 driven by electrical energy involves adsorption of CO_2 on the electrocatalyst, electron transfer and desorption of the product formed. The electrical energy sent, electrolyte and electrocatalysts are the main components influencing the CO_2 reduction.[41-44]

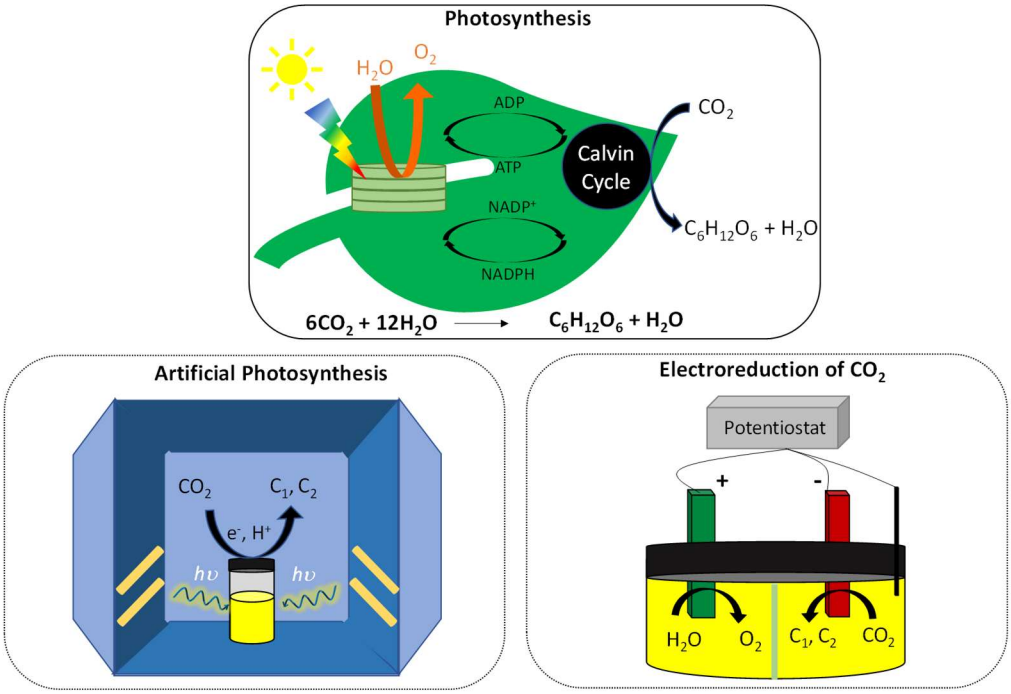

Scheme 2. Top: Natural photosynthesis system, Bottom left: Artificial photosynthesis system, Bottom right: Electrocatalysis system. Scheme adapted from literature.[37]

Nevertheless, the approach of artificial photosynthesis allows a straightforward setup, the possibility of high turnover numbers and low costs. Moreover, homogenous systems rather than heterogeneous allow a higher control of the molecular design and, thus, of the product selectivity. However, efforts must be made to counter the drawbacks of homogeneous systems, such as their difficult separation and recovery. In fact, in industry, heterogeneous systems and catalysts are more commonly employed due to their easier separation with the product after reaction and high efficiency.[45]

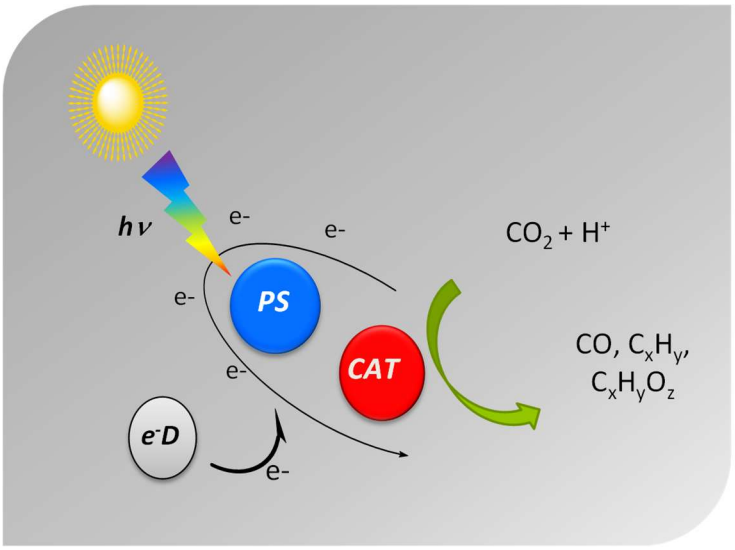

Scheme 3. Artificial photosynthesis system.

In homogeneous artificial photosynthesis (Scheme 3), three main components are necessary to mimic natural photosynthesis. To replace the complex photochemical processes involving chlorophyll, a photosensitizer (PS) is used, that can be metallic or organic.[46-50] It must be able to absorb a photon from the visible range of the sunlight, populate its excited state long enough to undergo an electron transfer process, triggering a cascade of redox reactions. Another important property for a molecule to be a photosensitizer is its stability under irradiation, thus, it must be photostable. During photocatalysis, irradiation at a specific wavelength allows the PS to promote an electron from its ground state to an excited state PS*. From this excited state, the electron can either go back to the ground state emitting photons (fluorescence or phosphorescence) or, if the excited state has a long enough lifetime (τ >100ns), the PS* can trigger outer-sphere electron transfers such as a reduction (reductive quenching) or an oxidation (oxidative quenching) (Scheme 4). Indeed, excited states are better electron donors and acceptors than their ground-state precursors[51], because the electron excited is at a higher energy level which makes it a better reductant and the hole created is lower in energy that the previous ground state LUMO, which makes it a better oxidant. To favor the reduction of the excited state PS*(in the case of the reductive quenching) before undergoing back electron transfer, an excess of electron donor is generally employed, enhancing the quantum yield.[52-53]

To mimic the dark cycle responsible for the reduction of CO_2 in the photosynthesis, a metallic catalyst (CAT) is needed to stand at the end of the chain of electron transfers to be reduced and reduce back CO_2 using two electrons. (Scheme 4) The catalyst needs to have appropriate redox potentials to accept the electrons generated during the photo-driven process and to transfer them to CO_2. Its use is necessary to lower the activation energy of the reaction an make the reduction of the kinetically inert CO_2 possible.[53]

To replace the source of electrons and protons, mainly played by water in natural photosynthesis, organic molecules and solvents/co-solvents are employed. Several electron donors are commonly used, such as

ascorbic acid, dimethylphenylbenzimidazoline (BIH), triethanolamine (TEOA), triethylamine (TEA), benzyl-dihydronicotinamide (BNAH), and so on.[53-55]

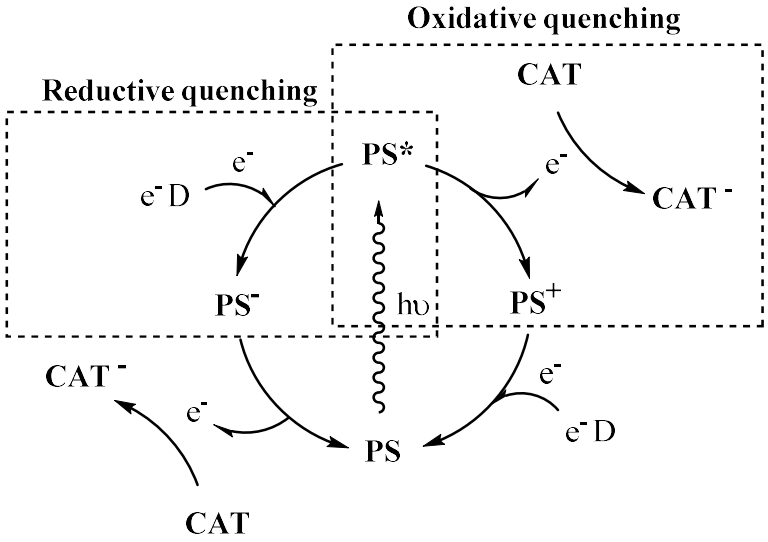

Scheme 4. Reductive and oxidative quenching of PS*.

With its outstanding redox potential of -0.204 V *vs* Fc^+/Fc in acetonitrile[56], BIH is an excellent reductant. Indeed, after a first reduction to $BIH^{+\cdot}$, its fast deprotonation by a base generates the very strong reductant BI. which makes it a two-electron donor. (Scheme 5) Its excellent electron-donating properties are well known[55] (scheme of BIH) and makes it one of the most employed electron donor. Nevertheless, its use in excess and sacrificial nature constitutes a major drawback of the process.

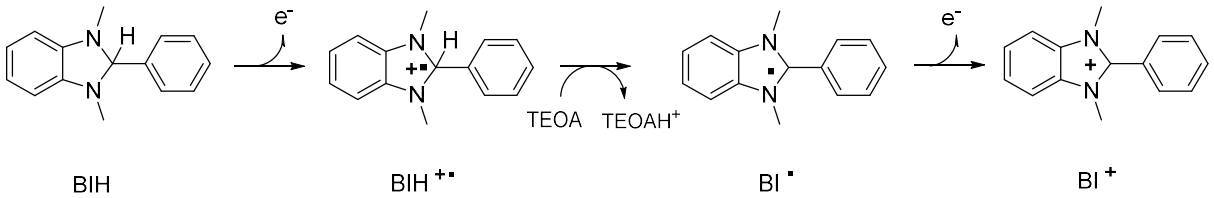

Scheme 5. Oxidation mechanism of BIH.

TEOA with its three OH groups is a common proton donor and also acts as a base to ensure the deprotonation of BIH (Scheme 5). Other amines such as TEA are also commonly used but TEOA triggers more interests as it has other advantages, not only it acts as a base and proton donor, it also act as a trap for CO_2, increasing its solubility in the solvent.[57-58] Moreover, it was also proved in specific cases to directly participate in the catalytic cycle by first reacting with CAT enabling a fast CO_2 insertion in the M-TEOA bond.[59-60] Finally, a solvent is needed to ensure the solubility and contact between all the different molecules. Aqueous systems are target systems because water can also act as both the electron- and the proton donor. Other solvents such as acetonitrile or DMF are commonly used, due to the higher solubility of organic molecules and CO_2 in them.

1.3.1 Evaluation of the System Performance

Photocatalytic systems can be evaluated using different values. The efficiency and durability of the catalyst is calculated using the turnover number (TON) and rate of catalysis with the turnover frequency (TOF) (Equation 1 and 2). These values refer to the maximum number of product molecules formed by each catalyst molecules (per second for the TOF value). The efficiency of the photocatalytic system is assessed by the quantum yield (Equation 3), that refers to the number of product molecules formed compared with the number of photons absorbed by the system (by the photosensitizer). Many factors can have a high impact on the systems like the light intensity, the concentration of CO_2, the standard redox potential values of PS and CAT, the nature and concentration of the components and many more.[61]

$$TON = \frac{N(product)}{N(catalyst)} \tag{1}$$

$$TOF = \frac{TON}{t\ (s)} \tag{2}$$

$$\Phi(\%) = \frac{CO\ molecules\ \times 2}{incident\ photons\ \times fap} \times 100 \tag{3}$$

In Equation 3, fap is the fraction of the absorbed photons of the photocatalytic system at the excitation wavelength (fap = $1–10^{-Abs}$). The efficiency values (TON, TOF, Φ) and a detailed description of the systems employed are crucial to not only evaluate the performance of the system, but also and more importantly to ensure reproducibility and comparison with other systems. Indeed, reproducibility and comparison are tremendous challenges.[62] Even with all the necessary values reported, it is important to note that those values are necessary but not sufficient to evaluate a system (see section 4 - Reproducibility).

1.3.2 Artificial Photosynthetic Systems

Photoreduction of CO_2 *via* visible light emerged in the 1980s with pioneer studies from LEHN *et al.* where Ru- or Re(bpy)(CO)X acted as the PS in combination with $Co(bpy)_3^{2+}$ as the catalyst The system produced at first CO and H_2 with a TON_{CO} of 9, then 45 with Re and later 326 in 1990 with Ru(bpy)Cl complexes and Ru(bpy) as PS in DMF/TEOA.[63-65]. Another molecular system extensively studied and early found (1984-1986) is the electrocatalytic reduction of CO_2 with nickel macrocycle catalysts, converting CO_2 into CO and H_2 but reported in the literature only with rare and expensive metal-based PS.[66-67] While scientists first employed Co and Ni to construct their catalysts, they soon employed mostly rare and expensive metals (Ir, Re, Ru). Indeed, 4th and 5th row transition metals show astonishing

properties with rich redox properties, forming very stable complexes and, for some, even manifest luminescent properties allowing their use as photocatalysts (catalyst and photosensitizer in one single molecule).[6, 68-71]

The necessity of reducing CO_2 is critical but also the systems employed to do so must be, to the greatest extent possible, ecofriendly to stay coherent with our goal. To do this, several directions can be followed, for example the use of earth-abundant and cheap materials or the use of water as electron and proton donor. Following this logic, new eco friendlier systems have been created since 2010. The use of earth-abundant based catalysts and PS (Fe, Ni, Co, Mn, Cu) were proposed with interesting results.[72-73] Additionally, systems using water as electron and proton donor instead of sacrificial electron donors were reported, reducing the chemical waste of the reaction. Nevertheless, the efficiency and/or selectivity of the systems are relatively low and few systems are presented with complete studies or understanding of the mechanism of the reaction.[45]

1.3.3 Homogeneous earth-abundant CAT for CO_2 Reduction and Selectivity

In artificial photosynthetic systems, together with the photosensitizer, the catalyst is one of the key elements to reach an efficient system and this work focuses on CAT. As previously mentioned, homogeneous catalysts have numerous advantages compared with heterogenous ones. They are generally designed in the first steps of the research and when optimized, heterogenized for industrialization. One of the most interesting advantages is the easy molecular design by selecting a metal and ligand structure creating a specific and controlled geometry of the complex. Other advantages are the numerous and well-known techniques to understand the mechanism (e.g., spectroscopy, cyclic voltammetry, theoretical calculations).[57] Every homogeneous catalyst reported for CO_2 reduction is metal based so far. The reasons for this are the highly stable nature of CO_2 and the very rich redox chemistry offered by transition metals (TM), helping during the numerous electronic transfers necessary for CO_2 reduction. Transition metals can carry multiple charges to generate reactive high-valent intermediates for CO_2 reduction and lower the kinetic barrier for CO_2 reduction.

Fourth and fifth row transition metal-based catalysts active for CO_2 reduction can allow multi-electron transfers (up to 3 or 4) while the third-row metals undergo only one or two electron transfers.[57] 4d metals also form less labile complexes with less isomerization possible, making them stable. It is only since 2010 that earth-abundant catalysts were brought back to light due to their eco-friendlier nature.[74-76] Because of their higher abundance, nature could utilize third raw transition metal for very complex transformations but with highly sophisticated systems (enzymatic reactions) and ligand structures. To compete with the more efficient fourth row metals, an efficient and innovative ligand system with optimized conditions must be developed.

The activity (measured by means of TON or TOF) and the selectivity (towards CO_2 and for products) are two of the most important aspects of an efficient catalyst. Other important aspects are the stability of the complex (also under irradiation for photocatalysis), non-competition in visible-light absorption

with PS, and suitable redox properties (reduction/oxidation thermodynamically feasible). It is easy to understand why the catalyst should have the highest activity or efficiency, but the notion of selectivity is more complex. Indeed, the catalyst has to be selective towards CO_2 versus hydride formation (from water or other proton donors) but also selective towards one product. The catalysts selectivity is therefore essential to avoid H_2 formation and to form a pure product.[42, 77] Commonly, CO_2 binds in three different ways with the catalyst: (Figure 2)[78-79]

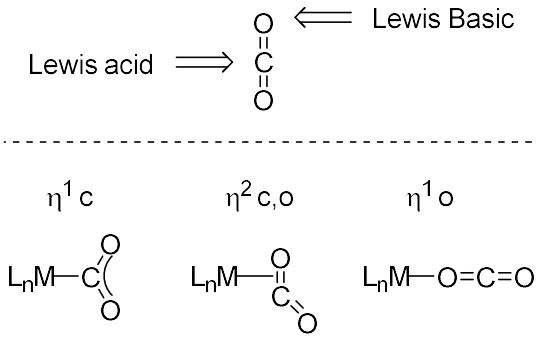

Figure 2. Coordination mode of CO_2 on metals, Scheme adapted from literature [80]

Once a catalyst binds with CO_2 and is able to reduce it, several C_1 products can be formed such as CO, methane, formate or methanol, (Scheme 6) although CO and formate are the most produced and studied products. Only few systems producing methanol or methane were published and the mechanisms involved are still not well understood and studied.[13, 15, 19, 32, 81-82] As for them, C_2 products (ethanol) are reported with heterogenous systems.[33] Because a multitude of factors can influence the activity and the selectivity of CAT, the mechanisms and reactivity are, in general, not well understood. Nevertheless, tremendous work in the last 20 years allowed to propose some explanations for specific systems and postulate general guidelines for product selectivity. The general pathways to form the common products (H_2, CO, COO^-) are shown in Scheme 7.

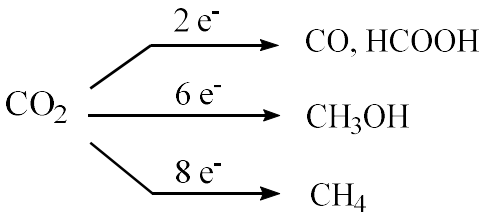

Scheme 6. Common product obtained from CO_2 reduction.

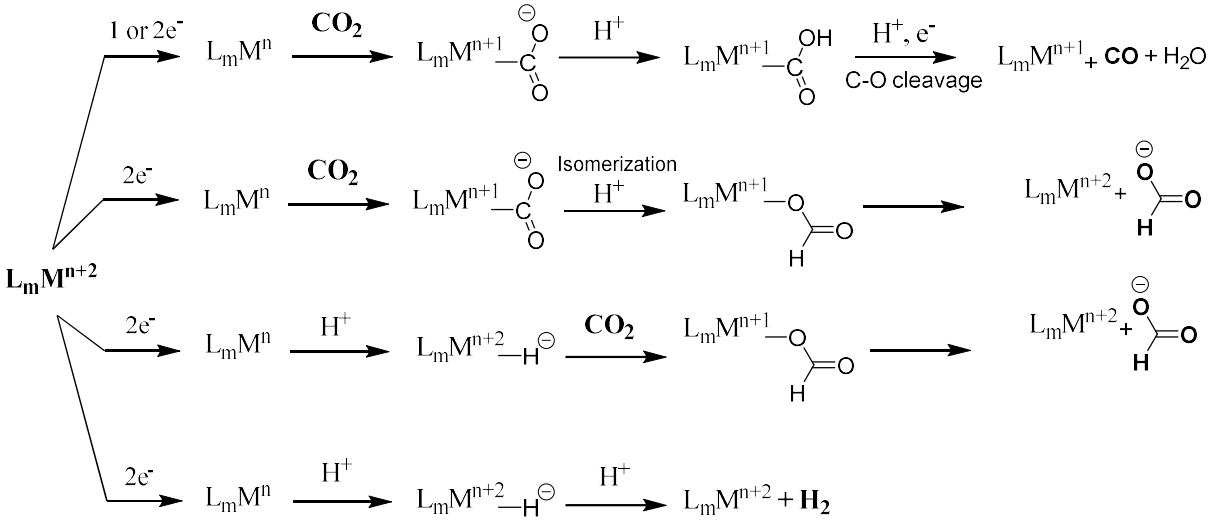

Scheme 7. General pathways for CO, COO^- and H_2 formation, Scheme adapted from literature.[83-84]

H_2 is in some cases a target product ($2H^+ + 2e^- \rightarrow H_2$), that was found to commonly come from hydrides.[45] The negatively charged hydride can attract a positively charged proton from the system and form molecular hydrogen, system that was extensively studied.[85-86] In our case, the target transformation of CO_2 asks for a preferential selectivity towards this molecule or the prevention of hydride formation. It also relies on using the available protons for the hydrogenation of CO_2 rather than for H_2 formation. Catalysts for the production of H_2 are commonly designed with an already present hydride as a ligand but hydrides can also be formed during the reaction.[86] In our photocatalytic system, the catalyst will be reduced by electrons and can potentially attract a positively charged proton found in the system or from its own structure (intramolecular). The affinity of the designed catalyst must then be higher towards CO_2 than towards hydrogens and several factors can be tuned to reach this selectivity. For example, a too acidic pH of the solution can push toward the formation of metallic hydrides and H_2.[86] A too acidic intramolecular and accessible proton can also lead to hydride formation.[87] The redox properties of the designed catalyst ML_n is also an important factor for selectivity. Indeed, the more basic the metallic center is (that means it is electron rich), the more it can attract positively charged protons. This can be due to high electron donation from the ligands (σ donors and bad π acceptors) like some phosphines for examples, to the metal.[86] Nevertheless, H_2 should not be considered as a waste because not only it is itself a reducing reagent for many reactions, but it also forms synthetic gas (syngas) when produced with CO in the right proportion. Syngas is a very useful reagent for fuel production for example (methanol, formylation, Fisher-Tropsch, and so on).[22]

Concerning the selectivity towards the different possible products, the characteristics leading to CO or formate are the most known. Commonly, to form CO, a reduced form of the molecular catalyst interacts with CO_2 through the carbon in η_1-CO_2 (Figure 2, Scheme 7). The catalyst is then further reduced and electron density is given to the CO_2 adduct, which triggers its oxygen protonation. After two-electron reduction and protonation, water is formed as a by-product.[73] The cleavage of the C-O(H) bond to free this molecule of water is generally the rate limited step of the catalytic cycle.[57] After the loss of water,

the intermediate state M-CO releases CO to go back to the first step. The crucial steps determining the selectivity towards CO are thus the η_1-CO_2 adsorption involving the reactivity and accessibility of the active center, and suitable redox properties that favor oxygen CO_2 protonation, possible when the CO_2-adduct is stable enough. The pH and electron density control are crucial to favor the C-O cleavage step.[88]

To produce formate, two different pathways are generally described : through insertion of CO_2 into a metal-hydride (Scheme 7), or through direct bonding to a vacancy of the metal center (ηC or ηO) (Figure 2 and Scheme 7).[80, 89-90] The insertion of CO_2 into a metal-hydride bond is well described in the literature and first requires hydride formation with electrostatic attraction between the polarized CO_2 and M-H bonds. The hydride acts as the nucleophile and CO_2 as the electrophile. The second pathway involves direct binding between CO_2 and the metallic active center, either through the oxygen or the carbon. When CO_2 is adsorbed through the oxygen, the protonation of the carbon of CO_2 is favored and leads to formate production. When CO_2 is adsorbed through the carbon, formate can still be formed if the carbon of CO_2 becomes basic enough (electronic properties of the catalyst). Its protonation can thus occur.[44] Formate can also be produced even if CO_2 binds through the carbon when the CO_2^- transition state formed is not stabilized enough leading to isomerization from ηC to ηO and triggering easy C protonation (Scheme 8).[91]

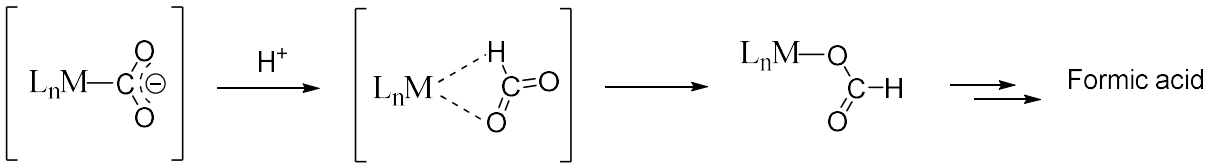

Scheme 8. Pathway showing the isomerization of CO_2 leading to COO^- as product.

The design of a system (conditions and catalysts) can thus be optimized to reach the desired selectivity. However, given the multitude of factors to take into account and their possible superposition, it is complex to balance the characteristics and properties. Often the system and catalysts are tested and their activity and selectivity are then studied. In this report, some characteristics inducing a specific selectivity were collected and listed. Conditions of the reaction, ligand design, metal identity and additives playing a role to stabilize species are described.

1.3.4 Selectivity

1.3.4.1 Reaction Conditions

Reaction conditions are one of the factors influencing the activity and the selectivity. Pressure, temperature, solvent system and pH can drive the reaction towards different pathways and products. In 2020, research showed a system selectively converting CO_2 into either formate, formaldehyde or methanol with a cobalt complex depending on reaction conditions.[92] This system did not use visible light mediated reactions but driving forces like pressure and temperature. In this publication they reported a cobalt catalytic system enabling adaptive and selective CO_2 transformation with molecular

control over the product. Formate was preferably formed at low temperature and high pressure, formaldehyde was formed a medium temperature and low pressure in neat condition (without solvent) and methanol was formed selectively at high temperature and low pressure. Nevertheless, artificial photosynthesis requires to work under normal conditions (atmospheric pressure and room temperature at 22 °C.) and most of the photocatalytic systems focus on normal conditions. Since the beginning, the solvent also proved to have an influence on the activity and the selectivity in particular due to the difference of polarity.[65]

In artificial photosynthetic systems, the pH of the solution and nature of the acid employed have been found to be paramount. Electron transfers are necessary to reduce CO_2 but so are proton transfers. This suggests that proton donors (Brønsted acid) must be present.[93] Depending on their nature and/or concentration, protons allow the conversion of CO_2 and are either part of the desired product (formate, methanol, methane) or in the co product formed (for example water co-produced with CO). Concerning the acids used, phenol, trifluoroethanol (TFE) (or trifluoroacetic acid (TFA)), acetic acid, HCl or simply water, have been commonly employed and their role in the mechanism was sometimes successfully determined. In general, the use of a strong acid appears to drive the reaction towards CO formation. Indeed, if the acid is strong enough, the protonation step leading to water is easier. Nevertheless, if the pH is too acidic it can also promote the formation of hydrides after reduction of CAT, leading to either H_2 or formate.[33]

Moreover, intramolecular proton donors acting as proton shuttle were also proposed. OH groups (Figure 3), Phenol, COOH or pendant amines were attached to the ligand structure, which allowed a faster rate of reaction and a higher selectivity towards CO when the proton is directly available in the sphere of the metal center.[94-97] However, intramolecular proton shuttles can also lead to formate production by protonation of the carbon. This can happen if the C-O cleavage step is prevented by lack of π-back donation from to metal to CO_2, due to the presence of electron withdrawing groups on the ligands for example. The protonation step can then target the carbon of CO_2 forming formate as product.[84] Not only acids can be good proton donor but also other organic molecules like TEOA through the OH groups. TEOA has been widely employed as proton donor and even show other interesting roles (capture of CO_2, useful for the electron donor process involving BIH and so on).[59]

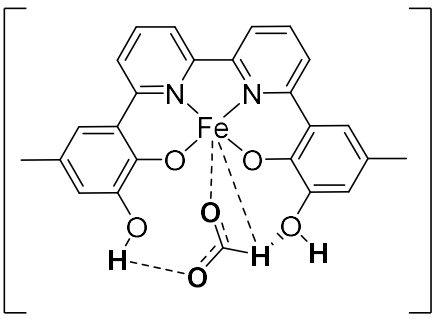

Figure 3. Example of proton shuttle and H-bond stabilization provided by intramolecular phenol.[98]

1.3.4.2 Choice of Metal and Oxidation State

The type of metal and its oxidation state are other aspects to consider. Although Co, Ni, Fe, Mn, Cu and Zn all proved to be active for CO_2 activation[72, 99-101], depending on the ligand system or on the conditions, the mechanisms that are involved lead to different activities and selectivities.[102] Two different metals with the same ligand and solvent system can produce different products. Computational studies made in 2015 by ROBERT *et al* presented two Fe- and Co-based complexes with a pentadentate N_5-donor ligand (dmpbop=2,13-dimethyl-3,6,9,12,18-pentaazabicyclo[12.3.1]-octadeca-1,2,12,14,16-pentaene) as catalysts for CO_2 reduction. The cobalt complex forms CO selectively and the iron forms rather formate. This was explained by the different oxidation state of the active species involved in the mechanism (Scheme 9). The cobalt complex oxidized (+II) becomes after one reduction +I and binds with CO_2. On the other hand, the iron complex intervenes with an Fe^{III} which becomes +II after one reduction to bind CO_2. The CO_2-metal transition state is then electron richer in the cobalt case than the Fe which means less π-back donation from Fe to CO_2 and therefore a less easy C-O bond cleavage. This rate-limiting step triggers isomerization of the CO_2 adduct ηC to ηO and formate is formed.[89, 103]

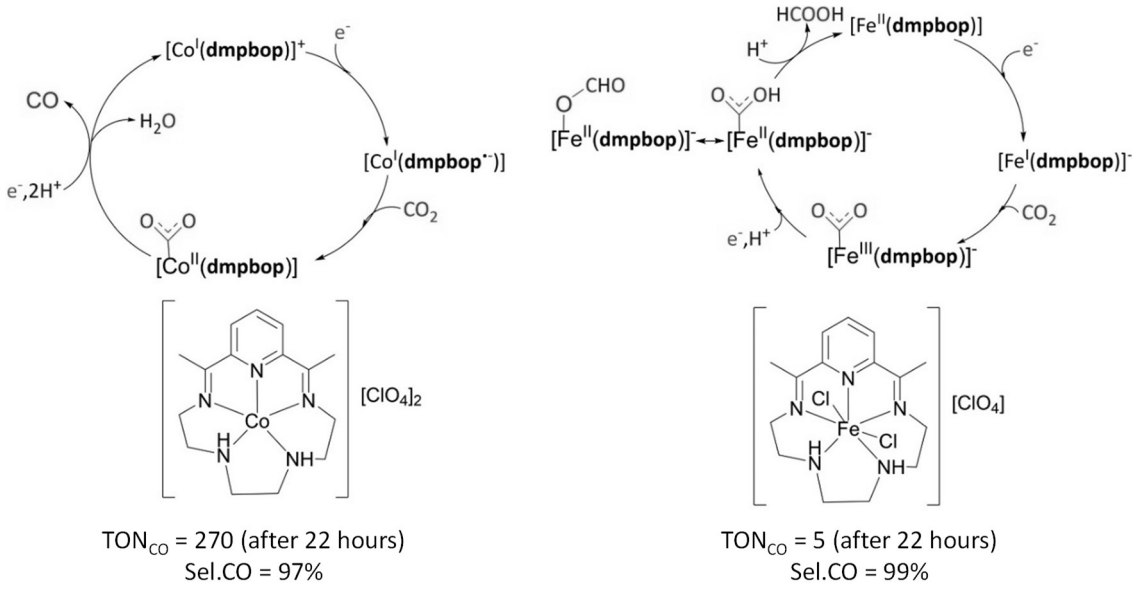

Scheme 9. Example of two catalysts for CO_2 reduction with same ligand structure, different metal and different product selectivity.[89]

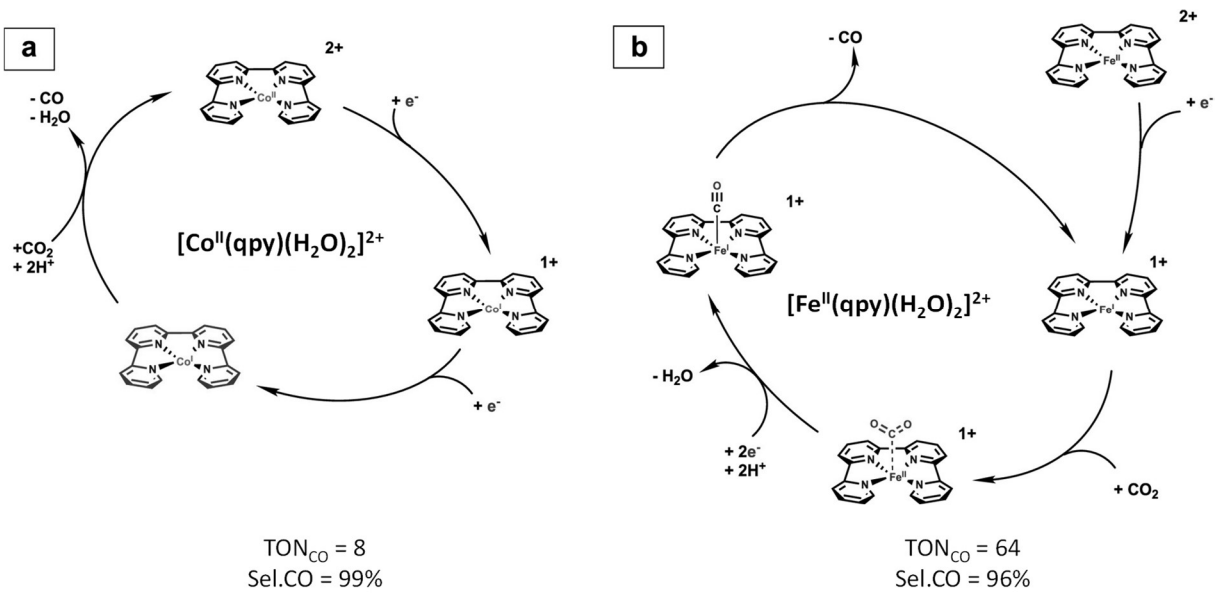

Scheme 10. Example of two catalysts for CO_2 reduction with the same ligand structure, both forming CO with different mechanisms involved.

Two different metals with the same ligand can also lead to the same product but through different pathways and thus different kinetics and activity. An example is the system reported by ROBERT *et al.*,where an iron catalyst with a quaterpyridine backbone goes through a ECE mechanism (reduction, reaction with CO_2, second reduction, with E standing for electron transfer and C for chemical reaction) while the cobalt complex undergo a EEC mechanism (two consecutive reductions, reaction with CO_2) (Scheme 10).[104-105] This is due to the stronger π-back donation from Fe to CO_2 than from Co to CO_2. In the Fe complex, less electron density is shared with the quaterpyridine ligand and thus more available to be transferred to CO_2. On the contrary, in the Co complex, the d electrons of the cobalt are more strongly shared with the ligand structure and less available for CO_2.

The choice of metal is therefore important because it involves its electron differently with the ligands and allow different reactivities towards CO_2. Another example is the well-known Re(bpy)CO catalyst that forms CO but its manganese analogue Mn(bpy)CO forms formate. Re has more electrons to give to π-back donation to CO_2, forming CO, while Mn doesn't have enough. Functionalizing the ligand with electron donor groups such as OMe make the Mn catalyst active to form CO.[106]

Furthermore, some metals tend to form one product preferentially such as Fe that usually produces CO and H_2, but for each metal, counterexamples exist. Fe^{II} forms preferentially CO but Fe^{III} can produce formate through direct binding and even through hydride formation.[107]

Ni, Co, Mn were reported to produce CO, formate and H_2 in varied ratios depending on the system.[72, 108] Both Zn and Cu were scarcely employed in mononuclear systems and produced mainly CO and H_2.[109-111]

1.3.4.3 Ligand Structure

The majority of ligands found in the literature for CO_2 reduction are divided into three main classes of ligands: macrocycles (cyclam, porphyrins), pyridine-based (quaterpyridines, bipyridine, phenanthroline) and cryptate ligands (Figure 4).[83] Nevertheless, more unique and peculiar structures were also scarcely reported.[112-115] The main advantage about these structures is the high stability they provide when complexing a metal to form robust and stable catalysts. The ligands also ensure the solubility of the complex in the solvent system employed for the reaction. To shift the selectivity in aqueous solutions, the ligand scaffolds are often functionalized with SO_3H or ionic groups.[116-117]

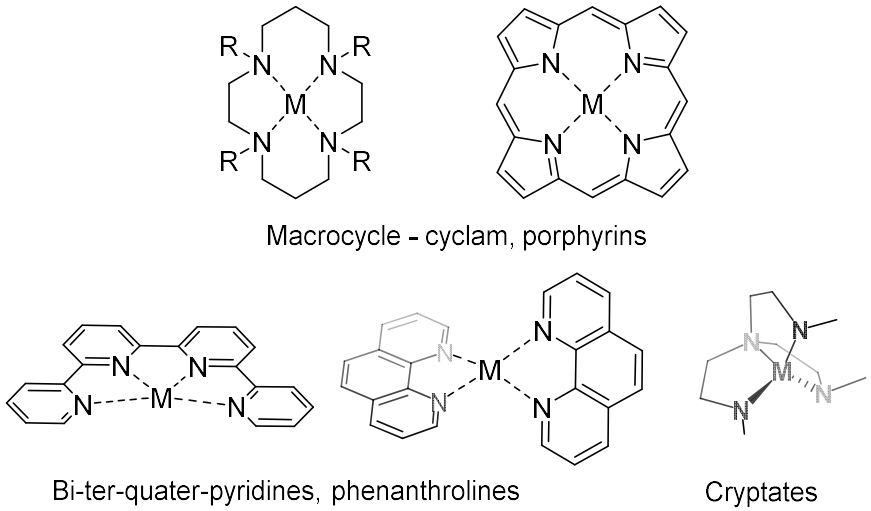

Figure 4. Common classes of ligands employed for CO_2 reduction catalysts.

Macrocycle 1,4,8,11-tetraazacyclotetradecane (cyclam)-based complexes were the first reported for CO_2 reduction by SAUVAGE *et al.* (1984 and 1986)[66-67] and are still today among the most efficient ones. They form rather CO as product thanks to a facile protonation of the oxygen of CO_2 by the adjacent NH groups. Porphyrins are also widely employed but have been reported to not be very stable during the catalysis. They produce mainly CO but also formic acid when the porphyrins are functionalized with electron withdrawing groups.[118] Bipyridine-based catalysts were first introduced in 1981 by LEHN *et al.* with rhenium as metal and then with manganese.[63-64, 119] This class of ligand is also known to degrade forming polymers or dimers which can be prevented by using bulky substituents and controlling the pH.[120]

The structure of ligands can drastically increase the efficiency and activity by their electronic structure, geometry and steric hindrance. They allow a very easy and controlled design of the complex to give its targeted properties allowing the use of third row transition metals as catalyst possible by tuning the electronic properties but also their geometry, to give the exact space for an easy access of CO_2 to the metal center.[121]

Concerning their electronic properties, the ligands are generally used as electron reservoir to store the electrons received from the photo-induced process, necessary to reduce CO_2. When they possess a very

high electron density (σ donor and bad π acceptors), they can donate it to metal that can π-back donate it to the bound CO_2. If this π-back donation to CO_2 is strong enough, the carbon of CO_2 will become very basic and nucleophilic, which will then likely be attacked by a proton to form formate.[122] When the π-back donation is strong but not enough to make the carbon basic, the electrons will be given to the antibonding orbital of CO_2 weakening the C-O bond and facilitating its cleavage to generate CO and water. On the other hand, when the metal is too electron-poor (because of electron-withdrawing groups on ligands for example), the cleavage of the C-O bond will be slower which can allow isomerization of the ηC bound CO_2 to the ηO, leading to an easier protonation of C and production of formate.[57] In most of the cases, it was reported that redox active ligands with extended π-conjugated ligands with low lying π* orbitals allow a lower electronic density around the metal, reducing the reactivity towards protons, which avoid H_2 formation.

To control the electron density of the ligand, and thus control the product selectivity, the ligand can be tuned by adding electron withdrawing or donating groups. This results in a specific electron density around the metal which will lead to product selectivity. Moreover, outer-sphere mechanisms start to be extensively employed by functionalizing the ligand scaffold with for example pendant amines, phenol or carboxylic acids to act as protons shuttle, H-bond giver and stabilizer of intermediates.[98] Depending on the pK_a of the proton and its position, the protonation of the carbon or of the oxygen is facilitated and the reaction rate is increased. For example, pendant amine attached to porphyrins allow very fast protonation of the carbon, (because the electron-withdrawing group prevents π-back donation and isomerization of CO_2).[95] Not only intramolecular proton donor groups on the ligand make the protonation step easier, but they also can help stabilize the intermediates formed through H-bonds, leading to a better activity.[98]

The geometry of the ligand also demands care. First of all, they should create a stable complex with the metal to avoid degradation and pollution (by CO for example).[123] Furthermore, after a first reduction and if a coordination site is not available, they should to be able to undergo ligand dissociation or distortion to create a vacant coordination site for CO_2 to bind. That is why pocket shaped ligands are widely used as they embed the metal and create a super stable complex with already available coordination space for CO_2. Some ligands are even employed to create a space during the catalytic cycle: carbenes are good electron donors and helps to push another ligand out to free a space for CO_2.[124]

1.3.4.4 Additives – Lewis Acids

Nature uses Lewis acids (LA) in several processes to help in the complicated reactions involved. For example it uses Mg^{2+} to make the carbon fixation possible in the photosynthesis process operating with RuBisCO.[125] Inspired by nature, scientists also started to use Lewis acids such as Mg or Ca to accelerate the catalytic process by stabilization of intermediates through ion-pairing between the negatively

charged oxygen of CO_2 and the LA (Scheme 11). This electrophilic assistance helps the C-O cleavage and leads to CO selectivity. Their usefulness was proved by simply being added to the solvent mixture[126] but were later also integrated to ligand structures thanks to pendant pyridines (Figure 5). This way, the Lewis acid atom is precisely situated next to the reduced CO_2 adduct and stabilizes it very efficiently.[114]

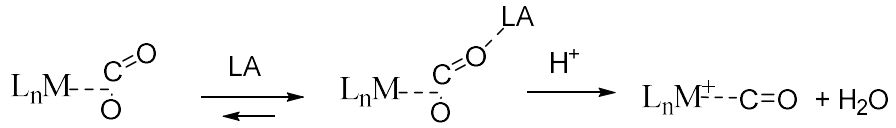

Scheme 11. Lewis acid stabilization**.**

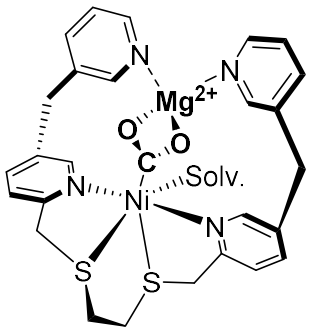

Figure 5. Example of stabilization of CO_2 by intramolecular Mg^{2+}.[114]

1.3.4.5 Six-and eight-electrons Reduced Products (methanol/methane)

Highly reduced products are also accessible through homogenous artificial photosynthesis and although scarcely described, they trigger more and more attention. Methanol is a very interesting molecule to produce as it is a "hydrogen carrier" but also a feedstock employed in large quantity for the production of formaldehyde, olefins and many others.[13, 127]. Several processes exist today which convert CO_2 into methanol thanks to transition metals. Mechanistic studies were proposed[128] but very few were described using artificial photosynthesis and even less (none) with complete earth-abundant systems.

Methanol requires six electrons to be produced from CO_2 and the few electro- or photocatalytic systems reported show that it is most of the time a further reduction product of formate.[129]

The eight-electrons reduction of CO_2 to methane by homogeneous catalysts was also rarely described in the literature. Fe porphyrins were reported to photocatalytically produce methane from CO_2 with iridium-based photosensitizers. A TON of 80 was reached but the selectively was really low (17%).[82] Similarly with methanol generally coming from the further reduction of formate, methane is commonly formed from the reduction of CO, either previously formed or as feedstock.[81] To enhance the selectivity towards methanol and methane, the availability of protons is important (low pH or intramolecular protons) but also the stabilization of the intermediates responsible for those products formation. The intermediate associated with the formation of methane is M-CO that needs to be stable enough to trigger further reduction and protonation. Examples with intramolecular charged ammonium groups attached

on iron complexes were shown to stabilize this intermediate which, after a two-electrons reduction, triggered a higher activity and selectivity towards methane.[82] Intermediates responsible for methanol production are considered M-CO_2H- adducts but the mechanism and stabilization strategies were not yet proposed.

Heterogeneous catalysts appear to be better systems for producing highly reduced products.[83, 130] Indeed, heterogeneous surfaces allow easier multi-electronic transfers thanks to a high electronic density compared with the discrete electrons transfers allowed with homogeneous molecular catalysts. Another possibility is the use of homogeneous multi-metallic complexes allowing to keep the advantages of homogenous processes while enhancing the electronic properties and characteristics of the catalyst.[131]

1.4 Multi-Metallic Complexes

Multi-metallic complexes have been fascinating researchers for many years. When combined either covalently or ionically in the same structure, metals can cooperate and engender unexpected properties. A cooperative effect is a phenomenon which relates the ability of two or more entities (elements, molecules) to act dependently on each other. Cooperativity between metals can enhance or shut down desired properties in a very controlled way, with a minimum of atoms employed. The common property required to identify cooperativity between metals is that the global effect/property observed by the system combining those metals must be greater or lower than the sum of their corresponding individual effect. (Scheme 12)

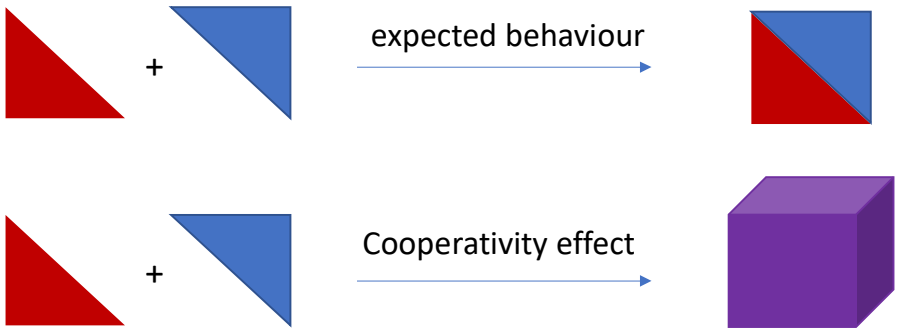

Scheme 12. Cooperativity effect.

Regarding artificial photosynthesis, multi-metallic systems were created in order to combine the catalyst and the photosensitizer in the same molecule. The new species called photocatalyst (PC) is thought to allow faster electron transfer between the PS and the catalyst part thanks to the intramolecular nature of the transfer, avoiding recombination. Supramolecules are also more stable and robust during the photocatalytic process which makes them interesting to design.[70, 132-135] To design a photocatalyst, PS and CAT can be bound covalently, ionically or electrostatically through H bond or π stacking (Scheme 13).[6]

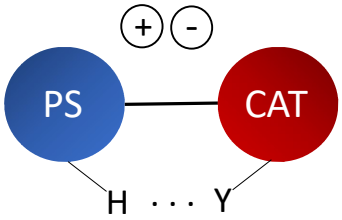

Scheme 13. Bonds types to bind PS and CAT.

Nevertheless, some examples of monometallic molecules were also shown to act as photocatalysts but were based on rare and expensive metals such as iridium, rhenium or ruthenium[136].[71, 137] Bimetallic or multi-metallic complexes are thus of high interest, to combine systems (photocatalysts) and to aim for cooperative effects, which could increase the desired properties (electron transfer, light absorption, emission, lifetime etc.).

Concerning bimetallic homogenous catalysts for CO_2 reduction, the synergistic effects observed are commonly due to the differentiation of the role of each metal during the catalytic cycle (Scheme 14).[103]

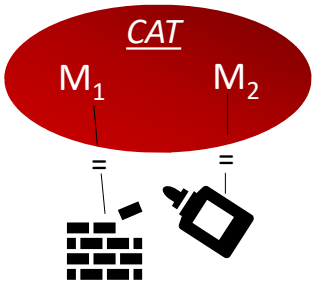

Scheme 14. Bimetallic catalyst with cooperativity effect.

In nature, one can observe this effect with numerous catalytic reactions using metalloenzymes like the NiFe CO dehydrogenase (CODHase), allowing anaerobic bacteria to convert CO and water into CO_2. Fe and Ni are bound through sulfur bridges and both metals have distinct roles: Ni^{2+} is the active center coordinating with CO and Fe acts as LA and OH vessel. To form the C-O bond, the OH group carried by Fe must be in an equatorial position with the Ni center. This synergistic system allows a controlled and efficient reaction (TOF_{CO2} 31000 s^{-1}).[138]

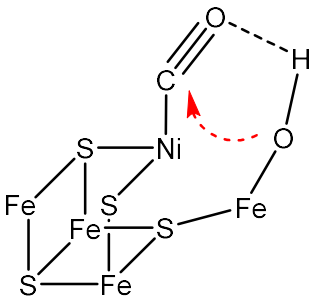

Scheme 15. CODHase and its bimetallic active center.

Trying to mimic nature, several systems were described using bimetallic complexes that greatly enhanced the efficiency and selectivity.[139] The main reason is the facilitation of intermediate steps, for example, the cleavage of the C-O bond responsible for CO selectivity can be facilitated when a second Lewis acidic metal attracts and binds the leaving oxygen.[140] The first metal acts as the active and coordination site while the second metal can either act as a stabilizer or as proton, electron or group shuttle (OH group transferred in the NiFe CO-dehydrogenase) (Scheme 15).

The same metal can be used, but heterobimetallic structures allow better differentiation of the roles leading to a higher activity. For example Zn-Co cryptate showed a better activity than Co-Co cryptate thanks to the higher LA nature of Zn compared to Co.[141]

2 OBJECTIVES OF THE THESIS

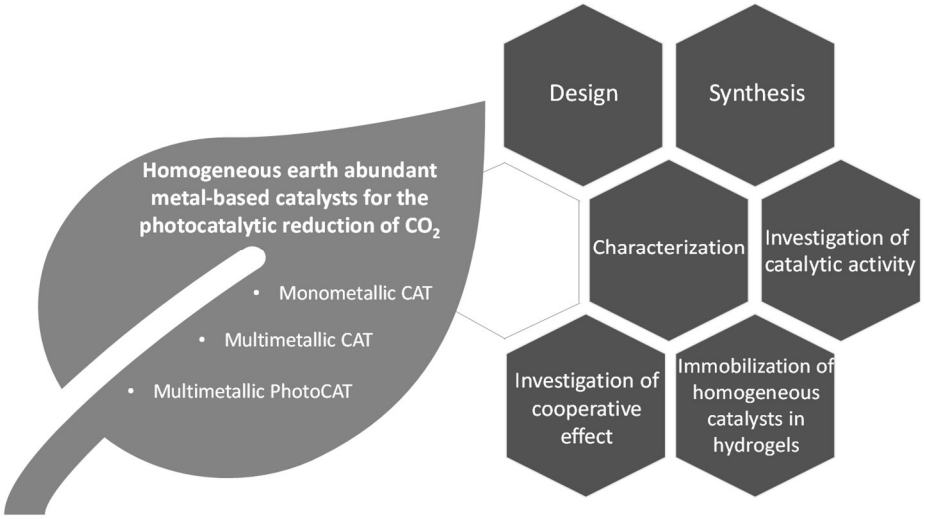

The excess of CO_2 in the atmosphere is one of the main reasons of the disturbance of the carbon cycle and climate change. It has become essential to reduce its emission by turning to renewable energy sources and limiting the use of fossil fuels. In addition, another approach to balance back the carbon cycle is the reuse and transformation of CO_2 into valuable chemicals which is already the focus of scientist's attention. Combining solar energy, the most available and powerful energy source, with earth-abundant-based catalysis is one possible way to convert CO_2 into green fuels such as syngas, methanol or methane. Artificial photosynthetic processes already showed great potential and encouraged us to pursue further in this domain.

This thesis aims at contributing to the development of more sustainable systems converting CO_2 into valuable chemicals focusing on homogeneous earth-abundant-based complexes for the photocatalytic reduction of CO_2 (Scheme 16). A higher focus will be given to the design of transition metal-based catalysts.

Mono- and multi-metallic complexes will be designed, characterized and tested for the photoreduction of CO_2. Striving for higher efficiency, cooperativity effects between the multi-metallic species formed compared with their monometallic analogues will be investigated. The new systems proposed will be optimized and their efficiency and selectivity will be evaluated.

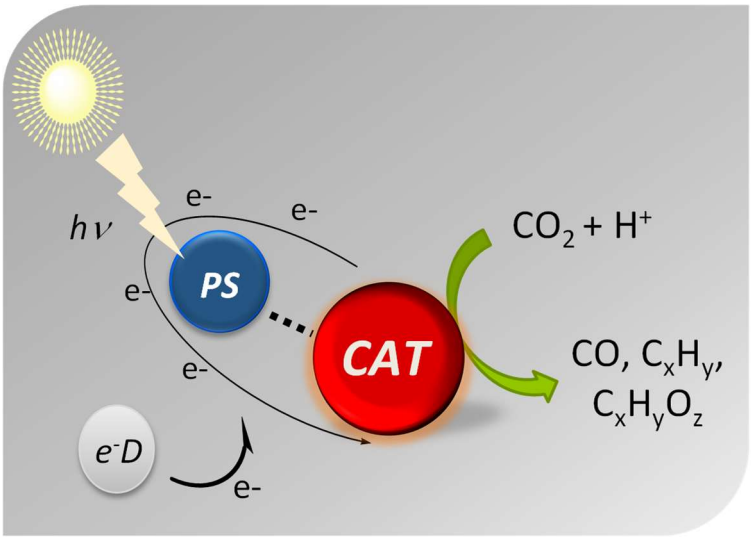

Scheme 16. Focus on earth-abundant catalysts for CO_2 reduction.

More in detail, heteroleptic, homoleptic, mononuclear and multinuclear complexes will be synthesized using different ligand structures and metallic precursors (Scheme 17).

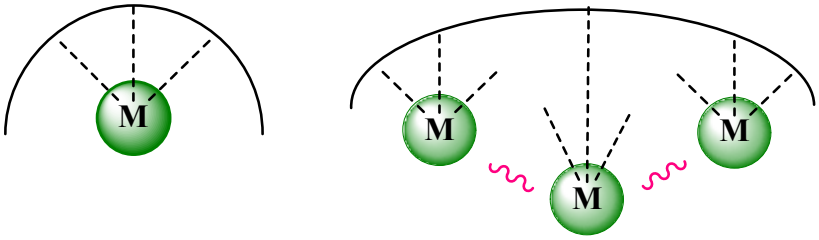

Scheme 17. Focus on monometallic and multi-metallic complexes to investigate cooperativity effect.

Collaborations within the collaborative research center 3MET, will be developed in particular for characterization (X-ray, mass, magnetic properties) and for mechanistic investigation (theoretical calculations) with Prof. Powell, Prof. Ruben, Prof. Fink, Dr. Fuhr, PD. Weis. An international collaboration with the university of Bologna UNIBO with Prof. Sambri will be discussed to further develop the new homogeneous systems created by their immobilization into hydrogels.

During this project, care and efforts will be provided to design and synthesize ecofriendly complexes using earth-abundant metals, in particular with Fe, Ni, Cu. Cobalt complexes were also studied due to their known activity for CO_2 reduction. Although cobalt is not officially considered to be a conflict mineral, its extraction involves strong human rights abuses in particular in Democratic Republic of Congo.

In line with this project, which intends to mimic photosynthesis, the processes that will be employed for the photocatalytic tests will be conducted at room temperature and atmospheric pressure with visible light as renewable source of energy. The molecular catalysts will be as much as possible designed to be air-stable, easily synthesized and cheap.

3 RESULTS AND DISCUSSION

3.1 EARTH-ABUNDANT PHOTOCATALYTIC SYSTEMS INTRODUCING NEW CU^I AS PS AND OPTIMIZATION WITH NI(CYCLAM)CL_2

Preface

Parts of the following chapter were published in 2020 in Chemistry European Journal (WILEY-VCH).

Lisa-Lou Gracia, Luisa Luci, Cecilia Bruschi, Prof. Dr. Letizia Sambri, Dr. Patrick Weis, Dr. Olaf Fuhr, Dr. Claudia Bizzarri, New Photosensitizers Based on Heteroleptic Cu^I Complexes and CO_2 Photocatalytic Reduction with $[Ni^{II}(cyclam)]Cl_2$. Chem. Eur. J. 2020, 26, 9929 – 9937 DOI: 10.1002/chem.202001279

The synthesis of the Cu^I complexes was supported by the Erasmus master student Luisa Luci and the Stern-Volmer analysis by the Ph.D. student Cecilia Bruschi. The photocatalytic experiments and manuscript were prepared by the first author and Dr. Claudia Bizzarri. This work was supported by the DFG-funded Collaborative Research center (SFB) TRR 88/3MET "Cooperative effect in Homo- and Heterometallic complexes".

3.1.1 Introduction

Ni(cyclam)Cl_2 (CAT-**1**) was one of the first catalysts employed to reduce CO_2 electrochemically[66, 142] and later on photochemically[143]. Its mechanism and activity have been therefore extensively studied and are now well understood.[144] It produces selectively CO electrochemically, but it is known to also produce H_2 photochemically. It usually binds in η1-**C** with CO_2 after a first reduction from Ni^{2+} to Ni^+. A protonation follows to form a $[Ni\text{-}CO_2H]^{2+}$ (Scheme 18) intermediate state that undergoes a simultaneous reduction and protonation that releases water to produce the $[Ni\text{-}CO]^{2+}$ intermediate state. The last step consists of the de-coordination of CO, forming back the active species $[Ni]^{2+}$. This last step can also lead to the deactivation of the catalyst when CO stays coordinated to the metal center because of a too high affinity Ni-CO. With TEOA as an additive, the neutral cyclam ligand is less likely to be protonated by TEOA because of charge repulsion and the formate route through a hydride is less probable. TEOA can, on the other hand, protonate the negatively charged carboxylate species generated after the binding of CO_2 on Ni.[144]

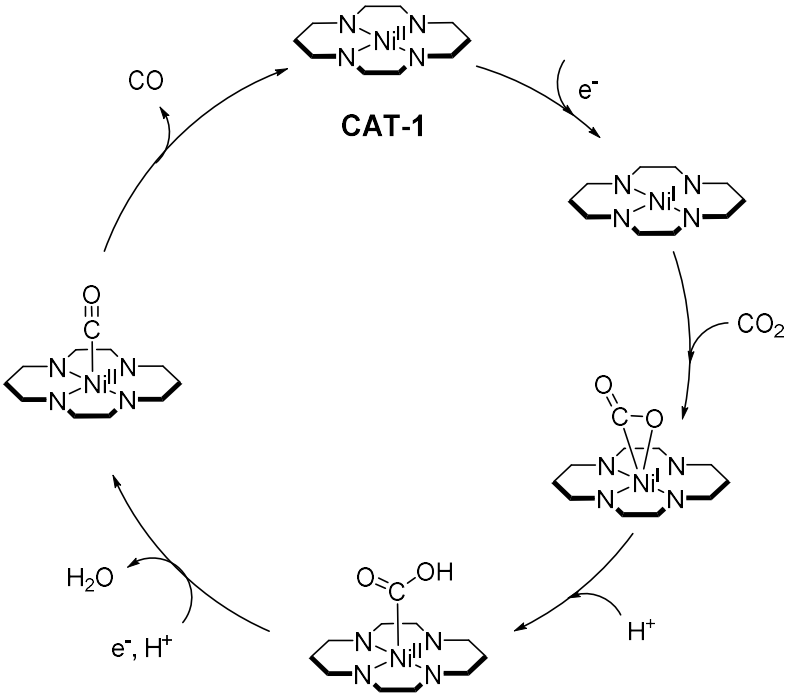

Scheme 18. General catalytic mechanism for CO_2 reduction with Ni(cyclam)Cl_2, scheme adapted from literature.[123, 144-145]

This well-known catalyst was only employed with rare and expensive metallic PS (Ruthenium based, Figure 6) and was never used in a complete earth-abundant system until now.

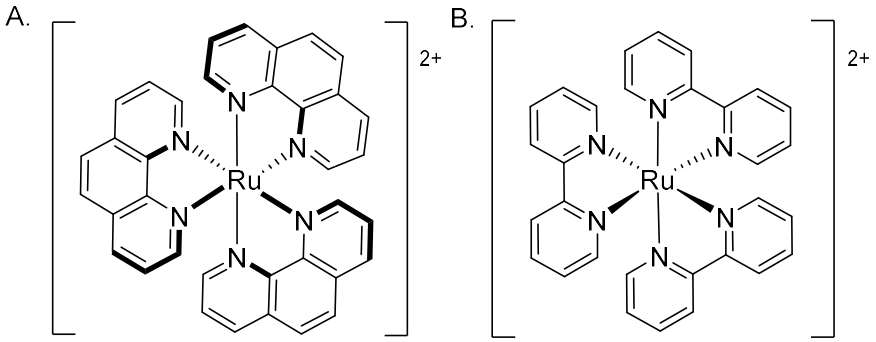

Figure 6. Photosensitizers used with Ni(cyclam)$^{2+}$ A. Ru(phen)$_3^{2+}$, B. Ru(bpy)$_3^{2+}$.

Table 2. Reported systems for CO_2 reduction using Ni(cyclam)Cl_2 as catalyst.[56]

PS	e⁻D	Solvent	TON(CO)	additional info[a]	Time	Reference
$[Ru(bpy)_3]^{2+}$	ascorbate	H_2O	n.r.	50 μL CO	4 h	[146]
$[Ru(bpy)_3]^{2+}$	ascorbate	H_2O	n.r.	Φ = 0.06%	4 h	[147]
$[Ru(phen)_3]^{2+}$ (b) (c)	ascorbate	H_2O	n.r.	0.32 μL CO	4 h	[143]
$[Ru(bpy)_3]^{2+}$ (c)	ascorbate	H_2O	n.r.	23.6 μL CO	n.r.	[148]
$[Ru(bpy)_3]^{2+}$	ascorbate	H_2O	8.2 (d)		1 h	[149]
$[Ru(bpy)_3]^{2+}$	ascorbate	H_2O/supercritical CO_2	2.1		4 h	[150]
$[Ru(bpy)_3]^{2+}$	ascorbate	CH_3CN/H_2O	5.2		60 h	[151]
$[Ru(bpy)_3]^{2+}$	ascorbate	H_2O	38(e)		5 h	[152]
ZnSe quantum dots	2-(dimethylamino) ethanethiol	DMF(f)/H_2O	283(g)		20 h	[153]
PS-**2**	BIH	CH_3CN/TEOA	4.3	Φ = 1.0%	4 h	This work
PS-**3**	BIH	CH_3CN/TEOA	4..9	Φ = 1.2%	4 h	This work
PS-**4**	BIH	CH_3CN/TEOA	8.1	Φ = 2.1%	4 h	This work
PS-**5**	BIH	CH_3CN/TEOA	4.6	Φ = 1.1%	4 h	This work

[a] additional information regarding the amount of produced CO when TON values are missing; (b) phen = phenanthroline; (c) $[Ni(cyclam)]^{2+}$ covalently attached to PS, (d) with bimacrocyclic catalyst $[Ni(cyclam)]_2^{4+}$; (e) $[Ni(cyclam)]^{2+}$ is incorporated in Cu-azurin; (f) DMF = *N,N*-dimethylformamide; (g) with heterogeneous photosensitizer.

In our group, new monometallic and bimetallic Cu-based PS (PS-**2**, PS-**3**, PS-**4** and PS-**5**) were designed and characterized showing interesting properties (Figure 7 and Figure 8). The four complexes undergo metal to ligand charge transfer (MLCT) when irradiated with visible light which for the four of them reaches the visible range (maximum at around 400 nm). Their excited state show long enough lifetimes in MeCN (τ = 100 ns) and they all demonstrated photostability. In order to determine their ability to photosensitize the photocatalytic reduction of CO_2, a system was designed using the known Ni(cyclam)Cl_2 (**1**) as CAT, BIH as electron donor and a mixture MeCN/TEOA as solvent mixture and proton-donor source. Stern Volmer analysis allowed to determine the feasibility of the electronic transfer with this system. The results of Stern-Volmer analysis confirmed the favored thermodynamics for a reductive quenching from BIH to PS*, resulting in apparent quenching rate constants close to the diffusion limit (k(PS-**2**)=2.0×10^9 $s^{-1}\,m^{-1}$; k(PS-**3**)=2.8×10^9 $s^{-1}\,m^{-1}$; k(PS-**4**)=4.3×10^9 $s^{-1}\,m^{-1}$; k(PS-**5**)=1.91×10^9 $s^{-1}\,m^{-1}$).

In this chapter, the photocatalytic reduction of CO_2 with CAT-**1** as catalyst will be described and optimized with the new earth-abundant-based Cu-complexes as PS-**2**, PS-**3**, PS-**4** and PS-**5**. The cooperative effect will be investigated comparing the catalytic results when using the monometallic complex PS-**2** or bimetallic PS-**3**, PS-**4**, PS-**5**. The optimization of the system will also be reported.

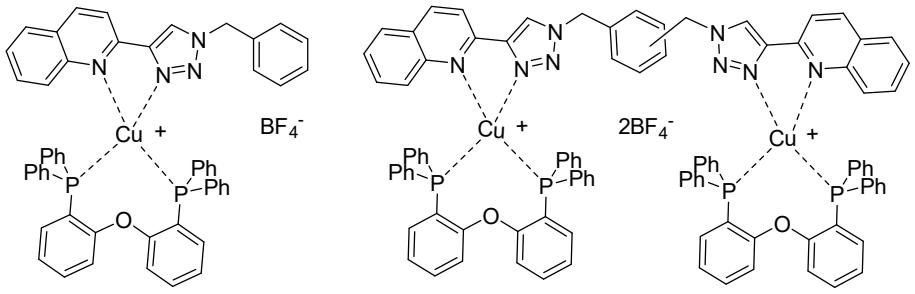

PS-2

PS-3: o-xylene
PS-4: m-xylene
PS-5: p-xylene

Figure 7. Structures of the Cu^{I} complexes employed as PS.

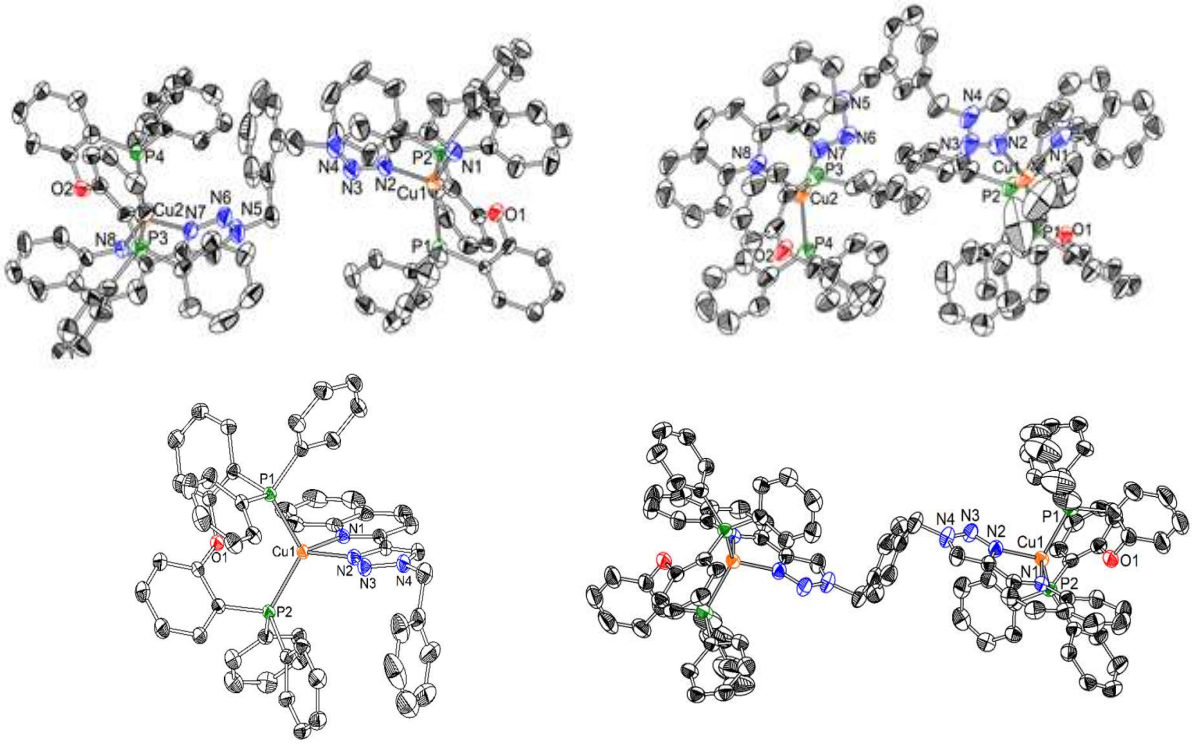

Figure 8. X-ray of the Cu^{I} complexes top left: **PS-3** top right: **PS-4**, bottom left: **PS-2**, bottom right: **PS-5**. Ellipsoids are shown at 50% probability and hydrogen atoms have been omitted for clarity. See **6.4** for individual values of the various bond distances and angles.

3.1.2 Synthesis of the Cu-based PS (2, 3, 4 and 5) and Ni(cyclam)Cl_2 (CAT-1)

Synthesis. The four Cu complexes were prepared previously in our group. For the monometallic complex (PS-**2**), 2-ethynylquinoline was first synthesized *via* SONOGASHIRA coupling in good yield, followed by deprotection. Phenylazide was then reacted with the previously formed 2-ethynylquinoline in 1:1 ratio *via* Cu alkyne-azide cycloaddition[154] (CuAAC) reaching the desired ligand. Furthermore, $Cu(MeCN)_4BF_4$ was then reacted with DPEPhos in 1:1 ratio and added to the ligand. For the bimetallic complexes, the corresponding ortho-, meta-, para- bis(bromomethyl)pyridine compounds were reacted in 1:2 ratio with NaN_3 *via* Cu alkyne-azide cycloaddition (CuAAC). $Cu(MeCN)_4BF_4$ was then reacted with DPEPhos and combined with the ligands to obtain the bimetallic complexes in good yields. The cooperative effect between the metals can be investigated comparing the bimetallic Cu complexes and the monometallic complex. Ni(cyclam)Cl_2 (CAT-**1**) was synthesized according to the known procedure[66] from the precursor $NiCl_2$ and 1,4,8,11-tetraazacyclotetradecane (cyclam) and a suitable crystal for X-ray measurement was obtained (Figure 9).

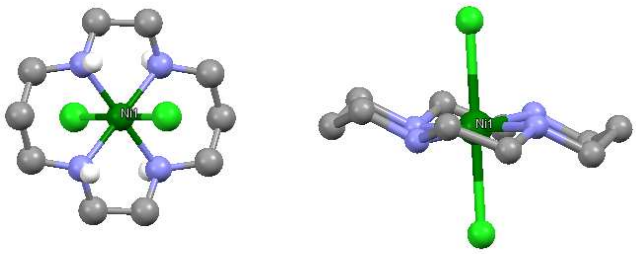

Figure 9. X-ray of Ni(cyclam)Cl_2 (CAT-**1**). Ellipsoids are shown at 50% probability and hydrogen atoms have been omitted for clarity. See **6.4** for individual values of the various bond distances and angles.

3.1.3 Photophysics and Electrochemistry

The absorption spectra of the four new Cu complexes show that the MLCT reaches the visible range with a maximum at around 380 nm and a tail reaching 420 nm (Figure 10). The lifetimes of the excited states were also previously recorded and are long enough to allow electron transfer (0.1 μs) in acetonitrile. Also, Stern-Volmer analyses confirmed the reductive quenching from BIH to the excited state of the Cu complexes due to the higher rate quenching constant and due to the much higher concentration of BIH in solution compared with CAT-**1**. Moreover, electrochemical characterization in acetonitrile showed the feasibility of the electron transfer between the electron donor BIH and the Cu complexes. For the four complexes, the difference between the oxidation potential of BIH and the reductive potential of the excited state of the PS was negative, proving the feasibility of the transfer. Another required property is the photostability of the complexes in the used solvent. The four complexes were irradiated in acetonitrile and their UV-vis spectra show no change after 5 hours proving their photostability.

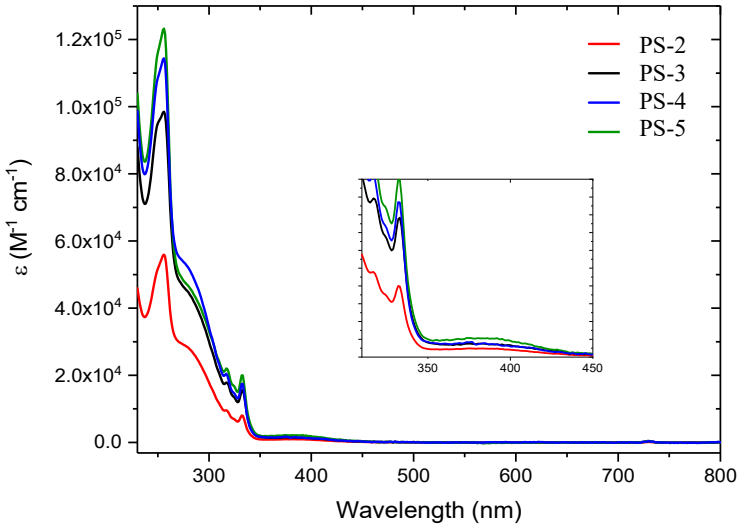

Figure 10. Absorbance spectra of the four Cu^{I} complexes in MeCN.

Table 3. Photophysical data in MeCN.[a]

Sample	λ_{abs} /nm	λ_{em} /nm	PLQY[b]	t [c] / μs
PS-**2**	398	640	<0.001	0.107
PS-**3**	388	646	<0.001	0.109
PS-**4**	388	650	<0.001	0.125
PS-**5**	387	643	<0.001	0.128

[a] in Ar-saturated ACN; [b] Photoluminescence quantum yields were measured with the relative method using $Ru(bpy)_3Cl_2$ in aerated water solution as standard (PLQy = 0.028). [c] Lifetimes were measured with TCSPC using Nanoled for excitation (λ_{exc}= 366 nm).

The four Cu complexes show similar behaviors in MeCN (Table 3). To allow electronic transfer in the excited state, the lifetime should be in the range of 1 μs which is the case in DCM but less in MeCN where the values are at the edge of the range.

The redox properties analyzed by cyclic voltammetry (Table 4) show that the four complexes have similar redox properties. The interesting redox potentials are the ones of the excited states PS*, which are needed determine the thermodynamic feasibility of the electron transfers with the other components. The cyclic voltammogram of $Ni(cyclam)Cl_2$ was recorded in MeCN (Figure 11) and showed its first reduction at -1.87 V *vs* Fc^{+}/Fc. The use in excess of BIH as electron donor likely induces a reductive quenching system, where the electron donor quenches the excited state of the PS and the reduced PS reduces the catalyst. The equations **4** to **11** show that both electron transfers from BIH to PS* and from PS^{-} to CAT are thermodynamically feasible for all Cu complexes presented because the driving force of the electron transfer (ΔG) is negative.

Table 4. Redox properties of the new Cu^{I} photosensitiser in MeCN (0.1 M $TBAPF_6$).[56][a]

Sample(MeCN)	E_{ox} /V *vs* Fc	E_{red} /V *vs* Fc	E_{ox}*/V [b]	E_{red}*/V [b]
BIH	-0.204	-	-	-
PS-**2**	0.95; 1.2	-2.09	-1.75	0.61
PS-**3**	0.90; 1.4	-1.8; -2.5	-1.81	0.85
PS-**4**	1.00; 1.4	-1.95	-1.31	0.75
PS-**5**	0.99; 1.9	-2.6	-1.71	0.06
Ni(cyclam)Cl_2[c]	-	-1.87; -1.97; -2.33	-	-

[a] estimated by cyclic voltammetry, at a scan rate of 100mV/s, reported versus Fc^+/Fc. [b] Redox potentials of the excited states, calculated from the formulas E_{ox}*= E_{ox} – E_{00}; E_{red}*=E_{red} + E_{00}, where E_{00} (≈ 2.7 eV) is the energy of the transition from the lowest excited state in thermal equilibrium to the zero vibrational level of the ground state. It was quantitatively estimated according to equations reported in references [155] and [137]. [c] recorded in MeCN at a scan rate of 100mV/s, reported *vs* Fc^+/Fc.

Quenching of PS* with BIH:

BIH / PS-**2** - EoxBIH – Ered PS* = -0.204 – 0.61 = -0.814 V <0 (4)

BIH / PS-**3** – EoxBIH – Ered PS* = -0.204 – 0.85 = -1.054 V <0 (5)

BIH / PS-**4** - EoxBIH – Ered PS* = -0.204 – 0.75 = -0.954 V <0 (6)

BIH / PS-**5** – EoxBIH – Ered PS* = -0.204 – 0.06 = -0.264 V <0 (7)

Reduction of CAT

PS-**2** / Ni^{II}(cyclam) – Eox/redPS- – Ered/oxCAT = -2.09 + 1.87 = -0.22 V <0 (8)

PS-**3** / Ni^{II}(cyclam) – Eox/redPS- – Ered/oxCAT = -1.8 + 1.87 = +0.07 V >0 (9)

PS-**4** / Ni^{II}(cyclam) – Eox/redPS- – Ered/oxCAT = -1.95 + 1.87 = -0.08 V <0 (10)

PS-**5** / Ni^{II}(cyclam) – Eox/redPS- – Ered/oxCAT = -2.6 + 1.87 = -0.73 V <0 (11)

From the equation (7), one can observe that the quenching of the excited state of PS-**5** is less negative so less thermodynamically feasible than the other complexes. This could predict a less good activity for this complex as PS. Moreover, equation (9) shows the electron transfer from the reduced compound PS-**3** to the catalyst is the least favorable with a driving force close to 0. This could also predict that this compound can perform less as PS in the present system.

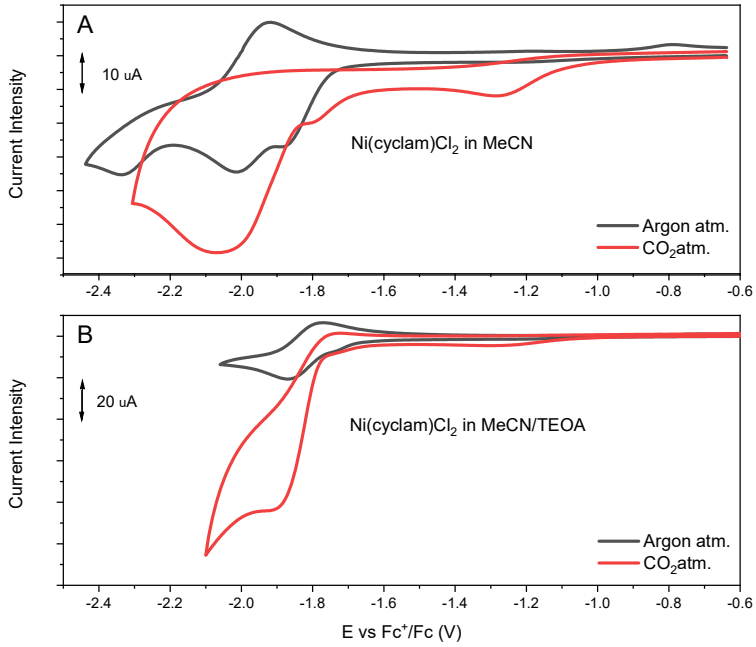

Figure 11. Cyclic-voltammogram recorded of Ni(cyclam)Cl_2 under argon (black curve) and CO_2 atmosphere (red curve) A. in MeCN and B. in MeCN/TEOA (5:1 v/v), for both at a scan rate of 100mV/s, and reported versus ferrocene/ferrocenium couple.

3.1.4 Photocatalytic Reduction of CO_2

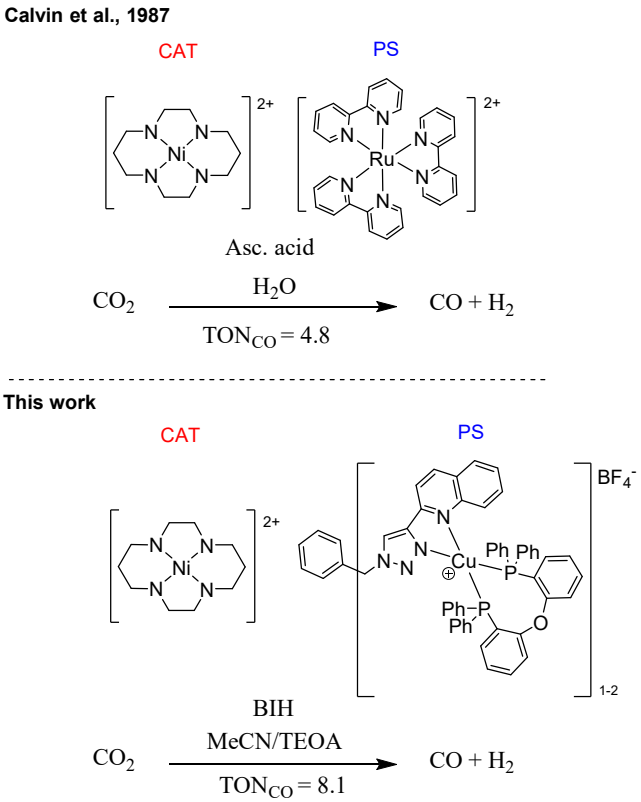

Scheme 19. Overview of a previous system using Ni(cyclam)Cl_2 with rare PS[146] and this work

General set up and conditions. The photocatalytic reduction of CO_2 was performed with Ni^{II}(cyclam) (**1**) as CAT in varied concentrations in combination with the four new Cu complexes (1.0 mM for PS-**2** and 0.5 mM for the bimetallic complexes PS-**3**, PS-**4**, PS-**5**). In this system, the electron donor employed was an excess of BIH and the solvent of the reaction was a mixture of ACN/TEOA (5:1, v/v). Light was applied to the system as the source of energy in a photoreactor, irradiating the reaction vessel at 420 nm. (Scheme 20). The gas formed was analyzed by gas chromatography (GC) with a thermal conductivity detector (TCD) or with a barrier discharge ionization detector (BID). CO and H_2 were the only products observed with this system.

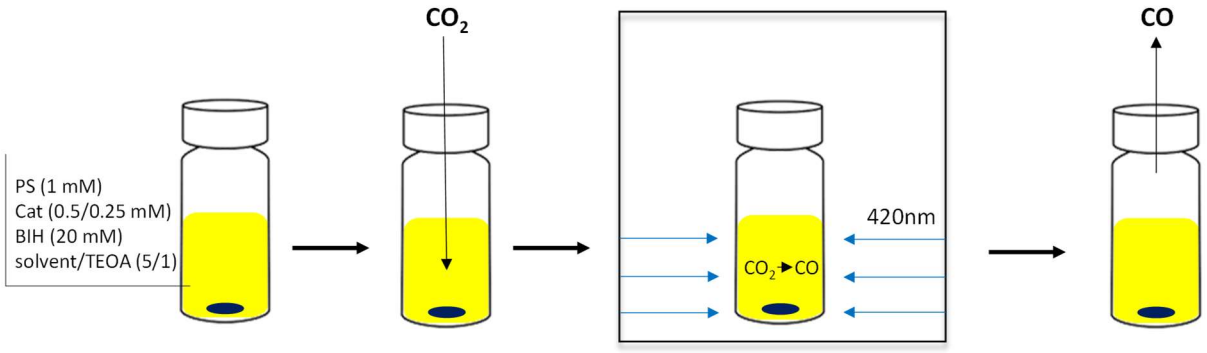

Scheme 20. Set-up of the photocatalytic reduction of CO_2.

Results and Optimization in Position 3 (see Figure 13). The first results of the photocatalytic tests with the four new Cu complexes listed in Table 5, show that they are all active as PS in this system, which produced CO as the product. Molecular hydrogen was not detected with our TCD detector-based GC.

In the position 3, the samples containing the four PS produced CO with TONs of 4.3, 4.9, 8.1 and 4.6 in 4 hours with no hydrogen detected (Table 5, Entries 1, 2, 3 and 4). PS-**4** as PS is the most performant producing 3.24 µmol of CO, approximately twice more product than with PS-**2**, 100% increased expected due to the second Cu moiety involved. The selectivity over H_2 was assigned to >99% as no H_2 was detected.

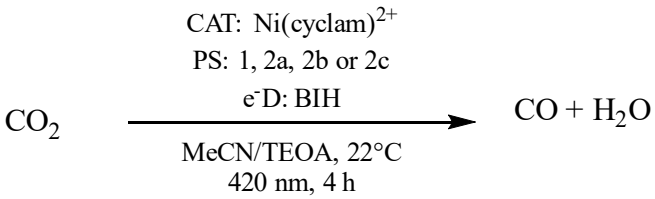

Table 5. Results and optimization in position 3[a]

Entry	PS	[CAT] mM	[BIH] mM	Time / h	CO /µmol	TON^{CAT}	Detector GC
1	PS-**2**	0.1	20	4	1.73	4.3	TCD
2	PS-**3**	0.1	20	4	1.94	4.9	TCD
3	PS-**4**	0.1	20	4	3.24	8.1	TCD
4	PS-**5**	0.1	20	4	1.83	4.6	TCD
5	PS-**2**	0.1	10	4	1.02	2.6	TCD
6	PS-**3**	0.1	10	4	1.40	3.5	TCD
7	PS-**4**	0.1	10	4	2.00	5.0	TCD
8	PS-**5**	0.1	10	4	0.70	1.8	TCD
9[b]	PS-**2**	0.1	10	4	1.13[b]	2.8[b]	TCD
10	PS-**4**	0	10	4	n.d.	n.d.	TCD
11[c]	PS-**4**	0.1	10	4	n.d.[c]	n.d. [c]	TCD
12	PS-**4**	0.1	0	4	n.d.	n.d.	TCD
13[d]	PS-**4**	0.1	10	4	n.d.[d]	n.d.[d]	TCD
14	**none**	0.1	10	4	n.d.	n.d.	TCD
15[e]	PS-**1**	0.1	10	4			TCD
16	**$Cu(MeCN)_4$**	0. 1	10	4	n.d.	n.d.	TCD
17	PS-**2**	0. 1	20	10	2.9	7.3	TCD
18	PS-**3**	0. 1	20	10	2.6	6.5	TCD
19	PS-**4**	0.01	20	4	n.d.	n.d.	BID

[a] From headspace analysis, reactions were repeated twice. [b] ACN/TEOA (4:1, *v/v*); [c] With trimethylamine instead of TEOA. [d] Without CO_2 in Ar atmosphere; [e] in dark (n.d.=not detected).

To optimize the system, different concentrations of electron donor BIH were investigated showing a decrease of yield when using less BIH (Table 5, Entries 5, 6, 7 and 8). The electron donor has to be in excess to promote the reductive quenching and avoid the recombination (PS* to PS). A slight increase in yield was observed when using more TEOA in the system with a ratio 4:1 (v/v) MeCN/TEOA (Table 5, Entry 9) and changing the nature of the amine by using TEA showed no production of CO (Table 5, Entry 11). The role of TEOA is thus not only to give protons but is also involved in other mechanisms. TEOA was recently proved to form zwitterion with CO_2 increasing its solubility in organic solvent. In some specific systems it was even proved to directly affect the catalytic cycle by reacting with the catalyst and promote CO_2 adsorption on the metallic center by insertion in the M-TEOA bond.[59]

Decreasing the amount of CAT-**1** from 0.1 mM to 0.01 mM did not produce any product (Table 5, Entry 19), meaning that the concentration of CAT has to be high enough to observe product formation.

Control tests were performed proving the necessity of all the components to photo-catalytically reduce CO_2 into CO. The absence of CAT, PS, BIH, TEOA, CO_2 or light in the system showed no product formation (Table 5, Entries 10, 12, 13, 14 and 15).

The quantum yield for the photocatalytic systems with the four different PS were calculated to 1.0% (PS-**2**), 1.2% (PS-**3**); 2.1% (PS-**4**), 1.1% (PS-**5**). Those values, dependent on the photosensitizers and the amount of product formed, are not very high but are good, if we compare with those reported in the literature.

Kinetic studies were performed for both PS-**2** and PS-**3** and are shown in Figure 12. For both PS, a plateau was reached after 4 h for PS-**3** and 6 h for PS-**2** and the behaviors are very similar to each other.

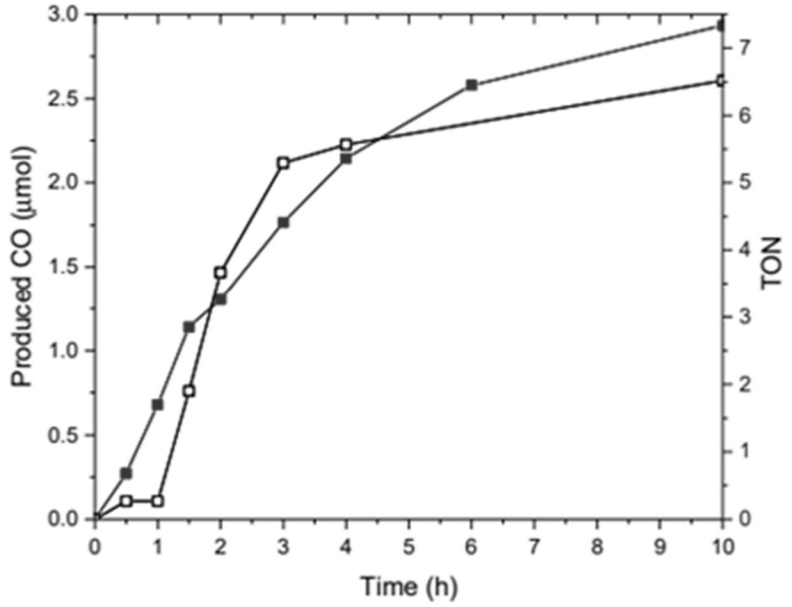

Figure 12. Kinetic results with **PS-2** (red curve) and **PS-3** (black curve).

The cease of the reaction can be attributed to several factors. $Ni(cyclam)^{2+}$ is known to undergo degradation by CO pollution ,and form Ni(CO) species.[144] However, its detection is complicated due to the meagre amount in the solution compared with the many other concentrated compounds. Additional studies were performed by adding either PS, CAT, or BIH after 4-6 hours to see if the catalysis could be repristinated, but unfortunately, a drastic decrease of CO detected revealed the inefficiency of this method, attributed to leakage formation. The degradation of the Cu-based PS is also known to cause the termination of the reaction. The photostability of the four Cu complexes was proved by ^{1}H NMR and UV-vis when dissolved in MeCN after irradiation for 4 h. However, in photocatalytic conditions, a decrease in MLCT absorption was already observed after 30 minutes. Thanks to mass experiments (HR ESI), the formation of DPEPhos-TEOA adduct could be observed (mass of 750 DA) in the photocatalytic reaction. Moreover, CV and UV-vis measurements showed that in the presence of not only TEOA but also BIH and CO_2, the PS starts the degradation process. This led us to postulate the formation of zwitterion carbonate species TEOA-CO_2 reacting with the reduced PS. Nevertheless,

control tests with the precursors $Cu(MeCN)_4BF_4^-$ and DPEPhos showed no production of CO (Table 5, Entry 16) attesting the necessity of the new Cu complexes to sensitize the reaction and reduce CO_2. The degradation of PS was demonstrated to be one of the reasons for the termination of the reaction.

Results and Optimization with different Positions The system was extremely sensitive to different factors. The purity of components and solvent was identified as an important factor[156] which led to the thorough purification of the components (by several recrystallizations) and the solvents (by three to five consecutive distillations over drying agent under inert conditions). However, other factors were found to have a more significant impact on the results, like the position of the sample in the photoreactor which means the intensity of light received by the system. In addition to the previously used position 3, three new positions (1, 2 and 4) shown in Figure 13 and 14 were tested.

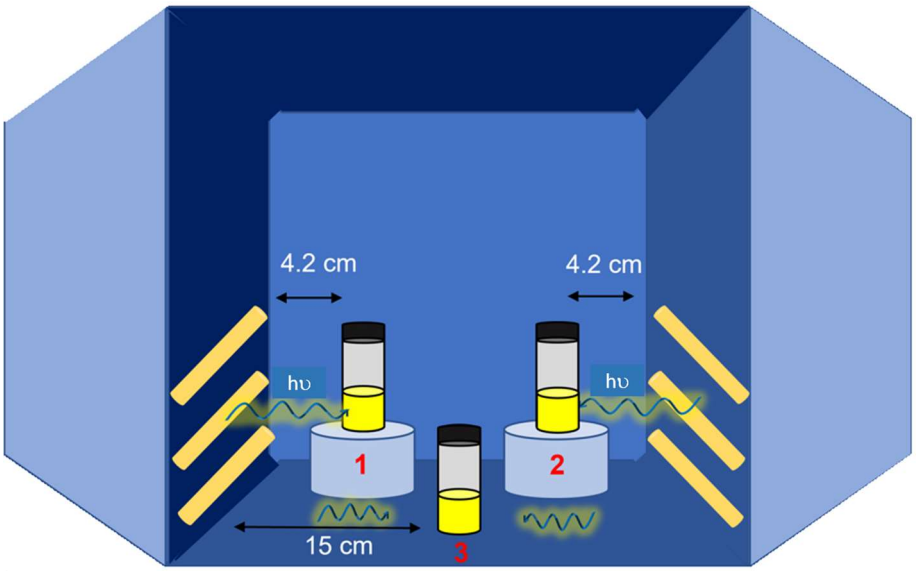

Figure 13. Positions 1, 2 and 3 in the photoreactor.

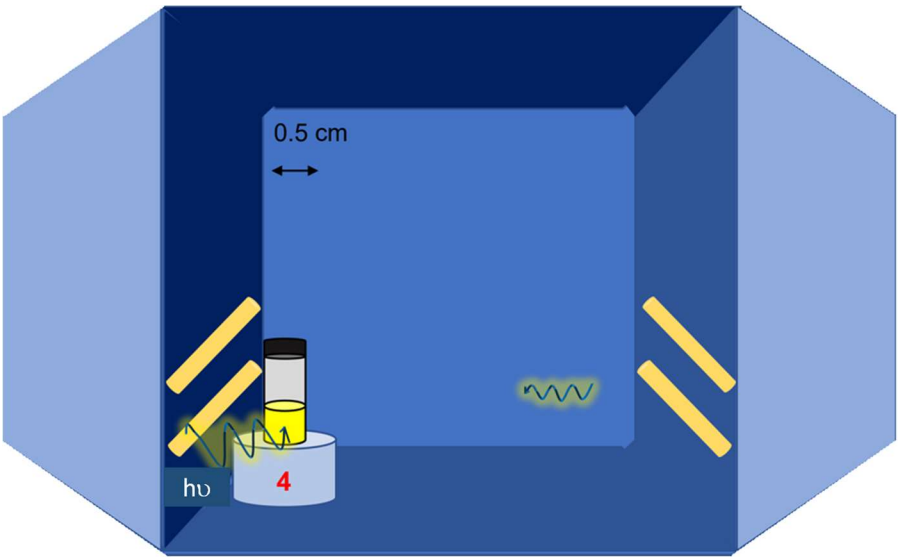

Figure 14. Position 4 in the photoreactor.

The four different positions were compared with the same reagent concentrations and the same conditions (MeCN/TEOA 5:1 v/v as solvent system, Table 6) with PS-**4**. As expected, the closer the sample is to the light source (Table 6, Entries 1, 2, 3 *vs* 4), the higher the production of CO. Positions 1 and 2 gave the same result with a TON_{CO} of 8.6 (Table 6, Entries 1 and 2), which indicate a proper reproducibility regarding the distance from the light used. Moreover, the position 3 gave very similar results than the position 1 and 2 with a TON_{CO} of 8.1 while in position 4, a better TON_{CO} of 12 was obtained. This shows that the impact of the distance and of the light intensity received by the solution high when the sample is close to the light source, but less important when further away from it, with less but more homogeneous light intensity received.

Table 6. Results in the different positions 1, 2, 3 and 4.[a]

Entry	Position	Time / h	TON^{CAT}
1	**1**	4	8.6
2	**2**	4	8.6
3	**3**	4	8.1
4	**4**	4	12

[a] From headspace analysis, reactions were repeated twice, with [CAT] = 0.1 mM, [PS-**4**] = 0.5 mM and [BIH] = 20 mM, 4 hours of irradiation at 420 nm.

However, if the TON increases by narrowing the sample to the light source, the quantum yield of the photocatalytic reaction will also slightly vary.

For easier reproducibility and maximizing the yield, the reaction was further optimized in position 4. Unfortunately, the previously used TCD detector ceased working and a different GC was used with the more sensitive BID detectors. BID detectors allow more sensitive detections and revealed the presence of molecular hydrogen co-produced.[157-158] With PS-**4** as PS, lower quantities of catalyst (CAT-**1**), different ratios PS/CAT and additives were investigated in this new position and are listed in the Table 7 with a selectivity for CO over H_2.

Table 7. Results and optimization in position 4.[a]

Entry	PS	[CAT] (**1**)	Additives	TON^{CAT}	Sel_{CO}
1	[PS-**4**] = 0.5 mM	0.1 mM	-	12	82%
2	[PS-**4**] = 1.0 mM	0.1 mM		12.5	73%
3	[PS-**4**] = 1.0 mM	0.01 mM		97	50%
4	[PS-**4**] = 0.5 mM	0.1 mM	[TFE] = 100 mL	8.5	76%
5	[PS-**4**] = 0.5 mM	0.1 mM	[H_2O] = 100 mL	10.2	81%

[a] From headspace analysis, with [BIH] = 20 mM and 4 hours of irradiation at 420 nm.

In position 4, CO was formed in the standard conditions ([PS-**4**] = 0.5 mM and [Ni(cyclam)Cl_2 (CAT-**1**)] = 0.1 mM) with a TON of 12 and a high selectivity over H_2 of 82% (Table 7, Entry 1). Surprisingly, increasing the ratio PS-**4**/CAT-**1** with 0.1 mM CAT and 1.0 mM PS instead of 0.5 mM did not lead to a change and more precipitate in the mixture was observed after the reaction, which could reveal more degradation of the components (Table 7, Entry 2). Increasing this ratio even more by reducing the concentration of CAT to 0.01 mM and keeping PS-**4** at 1.0 mM led to a drastic increase of the yield with a TON_{CO} of 97 (Table 7, Entry 3). However, the selectivity decreased to 50% with this low catalytic loading. The use of a strong acid or water was demonstrated to increase the CO selectivity in some systems[159] by facilitating the oxygen protonation step. However, the addition of water or TFE as additives (electron and proton donor properties) led to similar and lower catalytic activities and the selectivity over H_2 stayed quite high but did not improve (Table 7, Entries 4 and 5). Ni(cyclam)Cl_2 is known for its excellent product selectivity over H_2 while our results show a non-significant production of molecular hydrogen, detected with the BID detectors. Although Ni(cyclam)Cl_2 was already scarcely reported to co-produce H_2, we expect this hydrogen production to come from other processes that still have to be investigated.[157]

Discussion. Comparing our results with the literature, previous systems using Ni(cyclam)Cl_2 showed either high TON_{CO} (up to 38) with a low selectivity (<10%) or a low activity with a high CO selectivity (TON_{CO} = 2, CO selectivity 94%) both with $[Ru^{II}(bpy)_3]^{2+}$ as PS.[152, 160] In an aqueous solution, this catalyst was reported to produce CO with a TON_{CO} of 3.6 and a Sel.CO 54% over H_2 with $[Ru^{II}(bpy)_3]^{2+}$ as PS.[161] An immobilized $Ni(cyclam)^{2+}$ produced TON_{CO} 4.8 after 7 h with the same Ru-based PS but produced more H_2 than CO.[162]

Concerning our results, in position 3, the maximum TON_{CO} obtained reached 8.1 with a satisfying quantum yield of 2.1% with PS-**4** as PS with 0.1 Mm of CAT-**1**. This result is in line with the results from the literature. However, the use of Cu-based PS instead of Ru makes this new system more pertinent and entirely earth-abundant based. In position 4, with a higher light intensity received, the TON reached 12 and even 97 when decreasing the catalytic loading. Those results are the highest observed from the literature with Ni(cyclam)Cl_2 in an earth-abundant system, which shows that, even though this catalyst was extensively studied, new and interesting results emerge from the design of new PS and there is always an optimization possibility.

Drawbacks. The selectivities obtained are on average around 70% which gives room for improvement. Numerous studies tackled this problem mainly by functionalization of the ligand structure (see Introduction – Selectivity **1.3.4**) and working on the conditions. Moreover, more detailed degradation studies should be carried out to understand all the factors influencing the cessation of the reaction.

Investigation of the cooperativity effects. The comparison of the photophysical properties (lifetime, photoluminescence quantum yield (PLQY)) for the four new PS does not show any evidence of a cooperativity effect between the two metals in the bimetallic structures.

Moreover, no cooperativity effect regarding the photocatalytic results obtained was observed. The use of PS-**4** as PS shows the expected twice higher results than PS-**2** as PS, which is explained by the second Cu moiety adding its property to the first one. However, for both PS-**3** and PS-**5**, one could have expected, also in this case, twice more activity compared with PS-**2** but the results show that the activity is the same. This indicated that both those Cu complexes are active as PS but less efficient than other expensive Ru-based complexes. The absence of cooperativity between the metals can be explained by the methylene groups bridging the benzene-bridge and the quinoline-triazole moieties, chelating Cu nuclei, breaking the conjugation and the electronic communication.

3.2 NEW EARTH-ABUNDANT CATALYSTS FOR CO_2 REDUCTION

3.2.1 Monometallic Complexes

Preface

Part of the following chapter were published in 2022 in ChemCatChem (WILEY-VCH)

Lisa-Lou Gracia, Elham Barani, Jonas Braun, Anthony B. Carter, Dr. Olaf Fuhr, Prof. Annie K. Powell, Prof. Dr. Karin Fink, Dr. Claudia Bizzarri, *ChemCatChem* **2022**, *14*, e202201163, DOI: 10.1002/cctc.202201163.

The synthesis, characterization, photocatalytic tests, Evans tests and Stern-Volmer analysis were conducted by the first author. The bond-valence analysis was handled by Jonas Braun, the Nano-ESI measurements by P.D. Patrick Weis, with the help of Dr. Neumaier. The computational studies were investigated by Dr. Elham Barani. The manuscript was prepared by the first author and Dr. Claudia Bizzarri.

The revision and correction of Jonas Braun and Prof. Powell are gratefully acknowledged and this work was funded by the DFG-funded Collaborative Research Center (SFB) TRR 88/3MET "Cooperative effects in Homo- and heterometallic complexes".

Introduction. In the last 10 years, the design of new and efficient earth-abundant-based catalysts has attracted the attention of scientists. As mentioned previously, a few classes of ligands are commonly described, chelating or surrounding the metal, forming stable complexes. The design of a ligand for complexation and CO_2 reduction is a real challenge to reach a catalyst which is easily reducible in the first steps but also electron-rich for the next steps of the mechanism. Concerning the ligand system, most of the reported catalysts are heteroleptic but homoleptic complexes also were proved to be efficient.[50, 163] Homoleptic complexes usually have the disadvantage of not containing a readily available coordination site, which forces the chelating ligands to first undergo distortion to create a coordination site, either by de-coordinating one part or only by geometrical distortion. However, in some cases, homoleptic complexes proved to be more efficient than their heteroleptic analogue. For example, CHAO *et al*. reported homoleptic Fe^{II} complexes more efficient for CO production than the heteroleptic analogues.[50] However, the oxidation state of the metal also changed (III heteroleptic *vs* II homoleptic) which also likely influenced the catalytic cycle and thus the activity due to different electronic properties. The terpyridine-based complexes described by CHAO and coworkers show that the electron-richer amino-functionalized terpyridine Fe complex has a more negative reduction potential than the unfunctionalized complex. Interestingly, the amino-functionalized complex showed higher CO_2 activity, meaning that even if this functionalized complex is harder to reduce, its richer electronic density triggers a more efficient global catalysis. Another known homoleptic catalyst is $Fe(dmp)_2(NCS)_2$ which showed

interesting catalytic activity, where the dimethylphenanthroline (dmp) ligands act as electron sink upon reduction, making the desired electronic transfers easier.[164] "X" type ligands such as halogens are often present in the structure and are usually employed to create a coordination site for CO_2 after reduction and de-coordination (for example Cl or Br in the case of $Mn(bpy)(CO)_3X$ and $Mn(bpy)(CO)_3X$ complexes).[60] However, other anionic ligands such as NCS groups are employed in metal complexes and assumed to stay coordinated during the catalytic cycle with possible non-innocent effect.[164] NCS is a bidentate ligand that can either coordinate through the nitrogen or through the sulfur atom and is until now only mostly employed as a NCS ligand when complexed for CO_2 reduction catalysts. The NCS group is a weak-field ligand that produces small splitting between the d orbitals and forms rather high spin complexes.[165] Sulfur-containing ligands were investigated in several reports due to the soft donor properties of the sulfur atom and due to its presence in the known biological FeNi CO-dehydrogenase (CODH), responsible for CO/CO_2 reduction.[38, 166]

2,6-Bis(1,2,3-triazol-yl-methyl)pyridine-based ligands. To design efficient earth-abundant based catalysts, work on the ligand system can be addressed. 2,6-bis(1,2,3-triazol-yl-methyl)pyridine as a ligand (L-**6**) (Figure 15) was first introduced in 2011 by ZHU *et al.* forming homoleptic complexes with Fe and Ni.[167] Indeed, the electron-rich 1,2,3-triazole can coordinate either through N_2 or N_3. DFT calculation predicted that the coordination in position N_3 is more stable due to the higher electron density in this position compared with N_2. However, the pendant pyridine on the position N_1 of the triazole making the moiety chelating, contributes to possible binding of the metal to N_2, (Figure 15).[168]

In this work, the ligands were first formed using Cu alkyne-azide cycloaddition (CuAAC) in good yields (>70%) and were used to synthesize homoleptic and heteroleptic Fe, Co, Ni, Mn, Cu and Zn complexes, that were characterized and employed as a catalyst for CO_2 photoreduction.

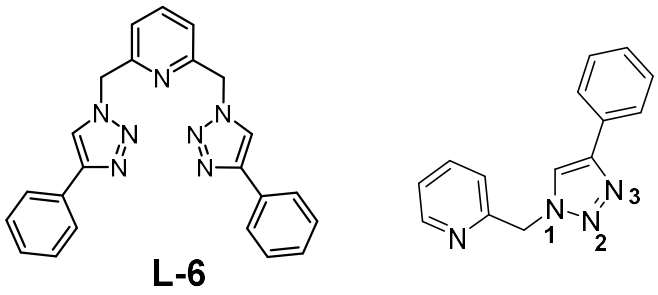

Figure 15. Structure of the ligand 2,6-bis(1,2,3-triazol-yl-methyl)pyridine L-**6** and sites of coordination of 1, 2, 3-triazoles.

3.2.1.1 Synthesis of the Ligands

The HUISGEN Azide Alkyne method is the most common method to produce 1,2,3- and 1,2,4-triazoles,[169] and copper catalyzed variation called Copper-catalyzed Azide-Alkyne Cycloaddition was employed to reach selectively 1,2,3-triazoles.[170] Phenylacetylene as terminal alkyne and sodium azide were needed to obtain the ligands. The source of copper is commonly copper sulfate that was reduced *in situ* to its reactive Cu^{I} form, able to coordinate the reagents.[171-172] Functionalized phenylacetylenes were also employed to obtain functionalization group in the final structure using 4-bromophenylacetylene, 4-ethynylaniline and 4-dimethylaminophenyl acetylene. The respective bromo- and amino-functionalized ligands L-**7**, L-**8**, L-**9** and L-**10** (Figure 16) were obtained with lower yields while L-**9** obtained was further reacted with MeI to obtain the di-cationic trimethylammonium functionalized ligand (L-**10**) with a yield of 36%. All the ligands prepared were purified by chromatography column with DCM/MeOH solvent mixtures.

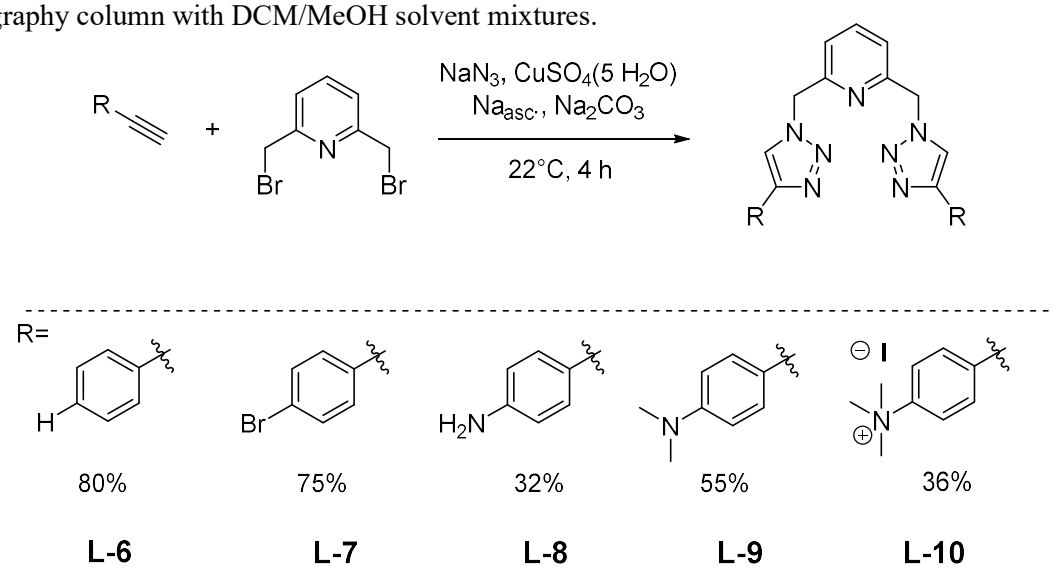

Figure 16. Synthesis of the ligand **L-6** and its functionalized analogues.

3.2.1.2 Synthesis of the Complexes

To form the metallic complexes, two different reactions were performed, leading to homoleptic and heteroleptic complexes (Scheme 21). The L-**6**-based homoleptic complexes of nickel, copper and iron have been known since 2011, while the cobalt and zinc analogues were synthesized first in this work. The precursors utilized are their hydrated perchlorate metal salts, which are simply dissolved together with the ligand in methanol with a one-to-two equivalent ratio. The homoleptic complexes CAT-**17**, CAT-**18**, CAT-**19**, CAT-**20** and CAT-**21** were obtained in excellent yield (85 to 95%). The new heteroleptic complexes CAT-**11**, CAT-**12**, CAT-**13**, CAT-**14**, CAT-**15** and CAT-**16** were synthesized employing the relative $M(NCS)_2py_4$ precursors which were previously synthesized according to a literature procedure by reacting their perchlorate salts with NH_4SCN and pyridine in water.[173] The heteroleptic complexes were synthesized using one equivalent of ligand L-**6** and one equivalent of

$M(NCS)_2py_4$ in methanol, reaching satisfying but lower yields. To purify the homoleptic and heteroleptic complexes, recrystallization was needed. All the synthesized complexes are air-stable, except the heteroleptic iron complex CAT-**11**, which was synthesized and stored in a glovebox. The functionalized ligands L-**8** and L-**10** were also complexed to form hetero- and homoleptic complexes CAT-**22**, CAT-**23** and CAT-**24** in the same way (Figure 17) forming very insoluble powders in aqueous and organic solvents, however, the Br-functionalized ligand L-**7** did not show any reaction with any of the metallic precursors employed. The X-ray structures and crystallographic data of CAT-**11**, CAT **12**, CAT **17**, CAT **18**, CAT-**19**, CAT **20** and of the precursor $M(NCS)_2py_4$ for M=Co, Ni, are presented in the section **6.4**.

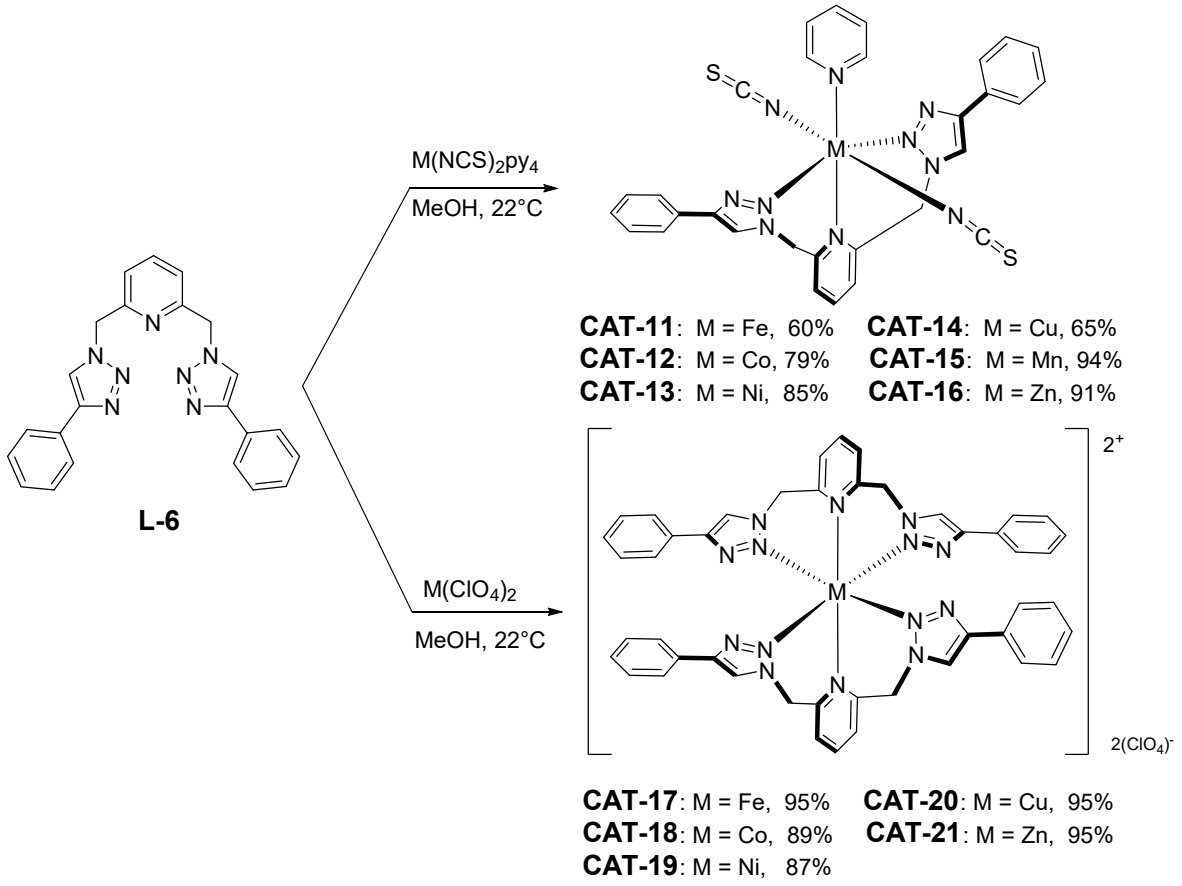

Scheme 21. Synthesis of the new heteroleptic and homoleptic complexes.

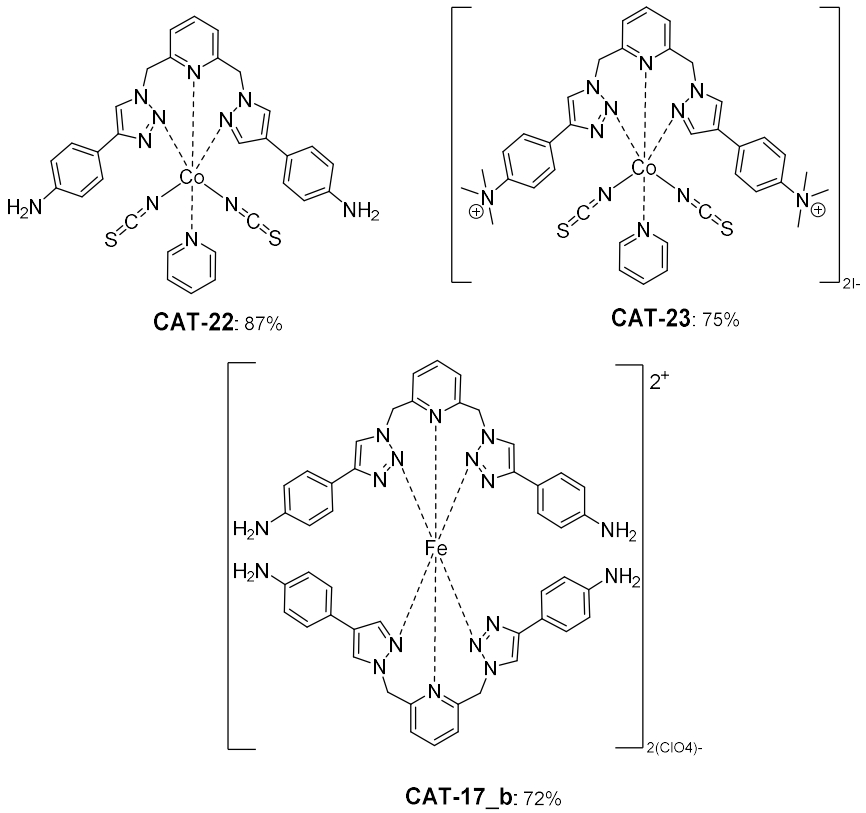

Figure 17. Functionalized ligands complexed with different metals.

3.2.1.3 Characterization

3.2.1.3.1 Electrochemical Characterization

Cyclic voltammetry and differential pulse voltammetry were both employed to characterize (see Supplementary data **5.1**) the electrochemical behaviors of the functionalized ligands and of the complexes formed.

In MeCN/TEOA, the heteroleptic complexes show reduction potentials with a varied potential range (Table 8), influenced by the metal. The iron and cobalt complexes CAT-**11** and CAT-**12** show two reduction processes at -1.01 and -1.76 V *vs* Fc^+/Fc and at -1.23 V *vs* Fc^+/Fc and -2.42 V *vs* Fc^+/Fc respectively, while the Mn, Zn, Ni, and Cu complexes CAT-**15**, CAT-**16**, CAT-**13** and CAT-**14** only show one reduction at -2.05 V, -1.95 V, -1.76 V and -1.37 V *vs* Fc^+/Fc. They all seem to react with CO_2 when present in the atmosphere at different potentials (Table 8).

The reduction potentials observed decrease from CAT-**11**, CAT-**12**, CAT-**14**, CAT-**13** to CAT-**16** (Fe – Co – Cu – Ni – Zn), indicating a potential relation to their position in the periodic table and number of electrons on their d layer, except the higher potential of CAT-**14** (Cu) compared with CAT-**13** (Ni). The less electrons in their d orbitals, the easier is their reduction. The exception of CAT-**15** (Mn) complex do not fit with this remark, being the hardest to reduce. Interestingly, their activity towards CO_2 does not follow the same tendency. The CO_2 catalytic current onset is the more positive, following the order

CAT-**13** (Ni) > CAT-**14** (Cu) > CAT-**11** (Fe) > CAT-**12** (Co) > CAT-**16** (Zn) > CAT-**15** (Mn). They all show CO_2 activation but CAT-**13**, CAT-**14**, CAT-**11** and CAT-**12** show an easier activation in respect to CAT-**16** and CAT-**15**. As expected from the lowest reduction potential obtained, the CO_2 catalytic current onset with CAT-**15** was also the most negatively shifted. In the case of CAT-**13**, the DPV could not prove any activation of CO_2, but it is clearly visible in the CV (Figure 22), which shows the importance of combining both techniques. Except for the iron complex CAT-**11**, that reacts with CO_2 after the second reduction (probably Fe(0) state)[174], all the complexes seem to activate CO_2 in their first reduced state. The CVs and DPVs of the heteroleptic complexes are shown in Figures 18, 19, 20, 21 and 22.

Table 8. Redox properties of the heteroleptic complexes obtained from the DPVs (0.1 M $TBAPF_6$) [a]

Entry	CAT	Red V *vs* Fc^+/Fc	CO_2 catalytic current onset	Solvent
1	CAT-**11**	-1.01; -1.76	- 1.67	MeCN/TEOA
2	CAT-**12**	-1.23; -2.42	- 1.78	MeCN/TEOA
3	CAT-**12**	-1.42	-1.45	DMA/TEOA
4	CAT-**15**	-2.05	-1.91	MeCN/TEOA
6	CAT-**16**	-1.95	-1.85	MeCN/TEOA
7	CAT-**13**	-1.76[b]	-1.40[b]	MeCN/TEOA
8	CAT-**14**	-1.37	-1.54	MeCN/TEOA

[a] estimated by cyclic voltammetry, at a scan rate of 100mV/s, and reported versus ferrocene/ferrocenium couple. [b] potentials obtained from the cyclic voltammogram of CAT-**13**.

Table 9. Redox properties of the homoleptic complexes obtained from the DPVs (0.1 M $TBAPF_6$) [a]

Entry	CAT	Red V *vs* Fc^+/Fc	CO_2 catalytic current onset	Solvent
1	CAT-**17**	-0.91; -1.63	- 1.9	MeCN/TEOA
2	CAT-**18**	-1.81	-1.82	MeCN/TEOA
3	CAT-**18**	-1.46	-1.25	DMA/TEOA
4	CAT-**21**	-1.90	-1.80	MeCN/TEOA
6	CAT-**19**	-1.73	-1.87	MeCN/TEOA
7	CAT-**20**	-1.17; -1.70 [b]	-1.52	MeCN/TEOA
8	$Co(NCS)_2py_4$	-1.16; -1.50	-	DMA/TEOA
9	$Co(NCS)_2py_4$	-1.63; -1.85	-	DMA

[a] estimated by cyclic voltammetry, at a scan rate of 100mV/s, and reported versus ferrocene/ferrocenium couple. [b] potentials obtained from the cyclic voltammogram of CAT-**20**.

The homoleptic complexes show similar behaviors in MeCN/TEOA with respect to their heteroleptic counterparts (Table 9), with easier reduction when they possess less filled d orbitals. Analyses of complex CAT-**18** (Co) were not conclusive due to its very low solubility in this solvent mixture. All complexes show CO_2 activation, in the first reduction state for CAT-**19** (Ni), CAT-**21** (Zn), CAT-**18** (Co) and in the second reduction state for CAT-**17** (Fe) and CAT-**20** (Cu). Surprisingly, the easier CO_2 activation appears to be with CAT-**20**, followed by CAT-**21** and CAT-**18**. In average, the homoleptic complexes show an activation of CO_2 at more negatively shifted potentials than that of the heteroleptic complexes, which could be explained by the need to first form a vacant site for CO_2 adsorption, which is more difficult for these complexes. The CVs and DPVs of the homoleptic complexes are shown in Figures 18, 19, 23 and 24.

In MeCN/TEOA, the cobalt complexes showed poor solubility and were then characterized in DMA/TEOA, where their solubility were complete. In this solvent system, the reduction potential of CAT-**12** decreased strongly from -0.72 to -1.45 V *vs* $Me_{10}Fc^+$/ $Me_{10}Fc$ (Figure 25) while the reduction potential of **18** remained very similar in this solvent compared with the one measured in MeCN (Figure 26). Moreover, in DMA CAT-**12** reacts with CO_2 at a slightly lower potential, from -1.25 V to –1.50 V *vs* $Me_{10}Fc^+$/ $Me_{10}Fc$ (Figure 25) which could predict a lower activity in DMA, however, CAT-**18** reacts with CO_2 at a higher potential, -1.35 V compared with -1.50 V *vs* $Me_{10}Fc^+$/ $Me_{10}Fc$ in MeCN (Figure 25).

The influence of TEOA in the solvent system was also investigated with the precursor $Co(NCS)_2pyr_4$ which shows more negative reduction processes in presence of TEOA than in the pure solvents. (Figure 27) However, the solvent system solvent/TEOA was anyway employed to resemble the most the real photocatalytic system. The decrease of potential with TEOA varied from 0.5 V for the Co precursor $Co(NCS)_2pyr_4$. With TEOA, the oxidation of the species are no longer visible because the very fast oxidation of TEOA at around 0.7 V *vs* Fc^+/Fc and *vs* $Me_{10}Fc^+$/ $Me_{10}Fc$ in both solvents.

Water was proved in several researches to increase the yield for CO_2 reduction and also influence the selectivity toward a product.[50] Therefore the influence of water was investigated for the heteroleptic CAT-**11** complex. The DPV of CAT-**11** with and without water shows that the activation of CO_2 potential of the catalytic current onset) slightly shifted from -1.67 V to -1.59 V *vs* Fc^+/Fc (Figure 28) which could imply a better activity with addition of water in the system.

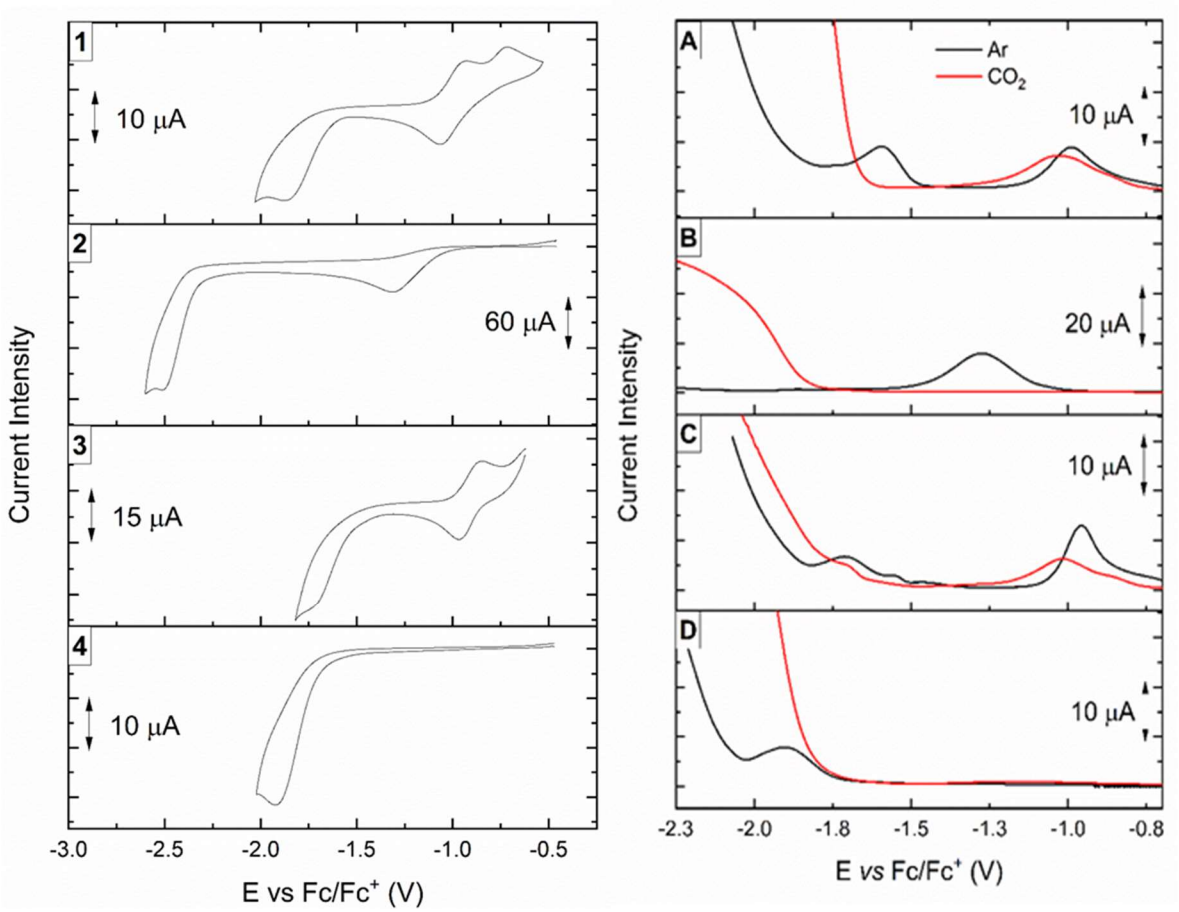

Figure 18. (Left) CVs of **CAT-11** (A), **CAT-12** (B), **CAT-17** (C), **CAT-18** (D) in MeCN/TEOA, 0.1 M $TBAPF_6$, at 100 mV/s, reported *vs* Fc^+/Fc.

Figure 19. (Right) DPVs of **CAT-11** (A), **CAT-12** (B), **17** (C), **CAT-18** (D) in MeCN/TEOA with CO_2 activation (red curves), 0.1 M $TBAPF_6$, at 100 mV/s, reported *vs* Fc^+/Fc.

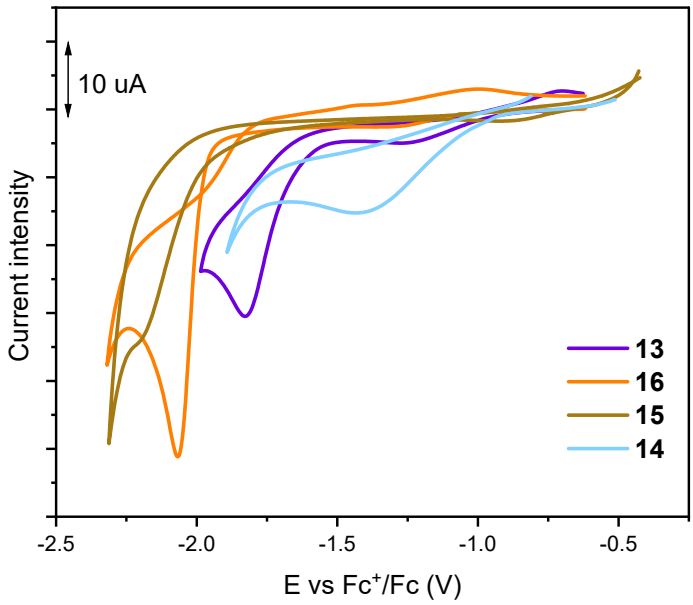

Figure 20. CVs of the heteroleptic complexes **CAT-13**, **CAT-14**, **CAT-15** and **CAT-16**, in MeCN/TEOA, 0.1 M $TBAPF_6$, at 100 mV/s, reported *vs* Fc^+/Fc.

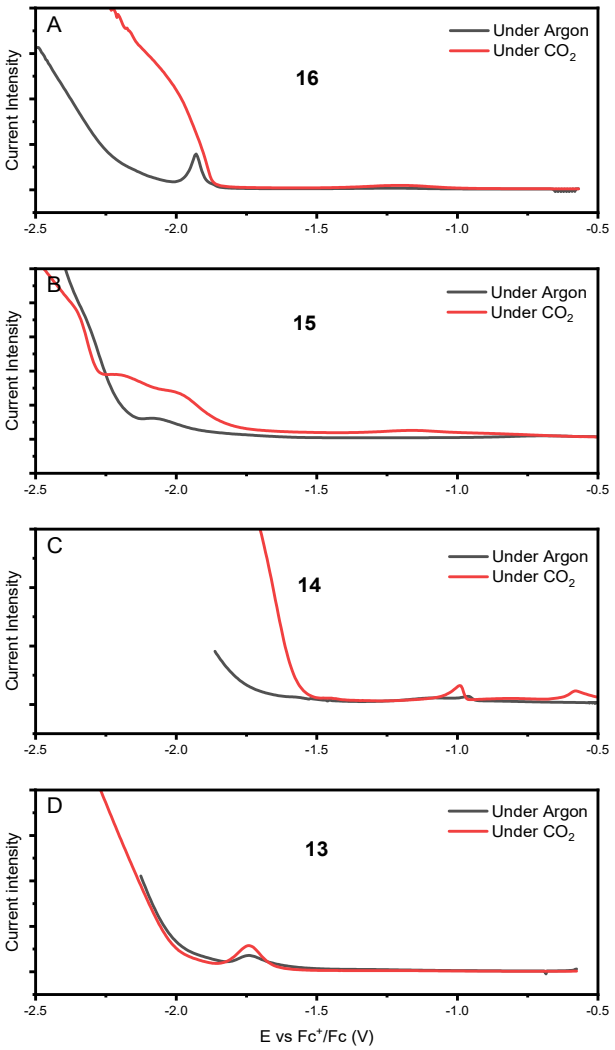

Figure 21. DPVs of the heteroleptic complexes **CAT-13**, **CAT-14**, **CAT-15** and **CAT-16**, in MeCN/TEOA, 0.1 M $TBAPF_6$, at 100 mV/s, reported *vs* Fc^+/Fc and activation of CO_2 (red curves).

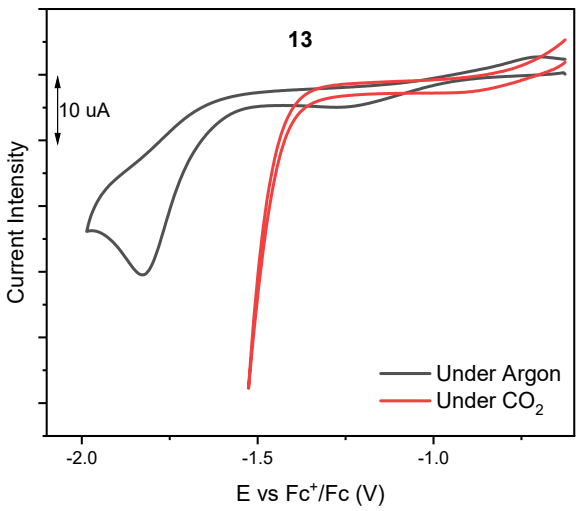

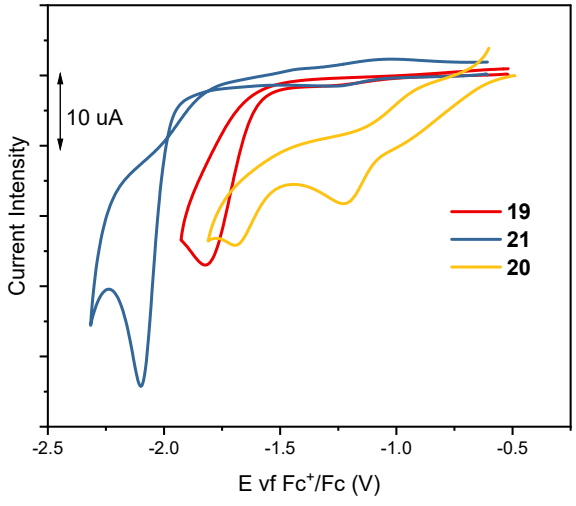

Figure 22. (Left) CV of **CAT-13** in MeCN/TEOA, 0.1 M $TBAPF_6$, at 100 mV/s, reported *vs* Fc^+/Fc, and activation of CO_2 (red curve).

Figure 23. (Right) CVs of the homoleptic **CAT-29**, **CAT-20** and **CAT-21** in MeCN/TEOA, 0.1 M $TBAPF_6$, at 100 mV/s, reported *vs* Fc^+/Fc.

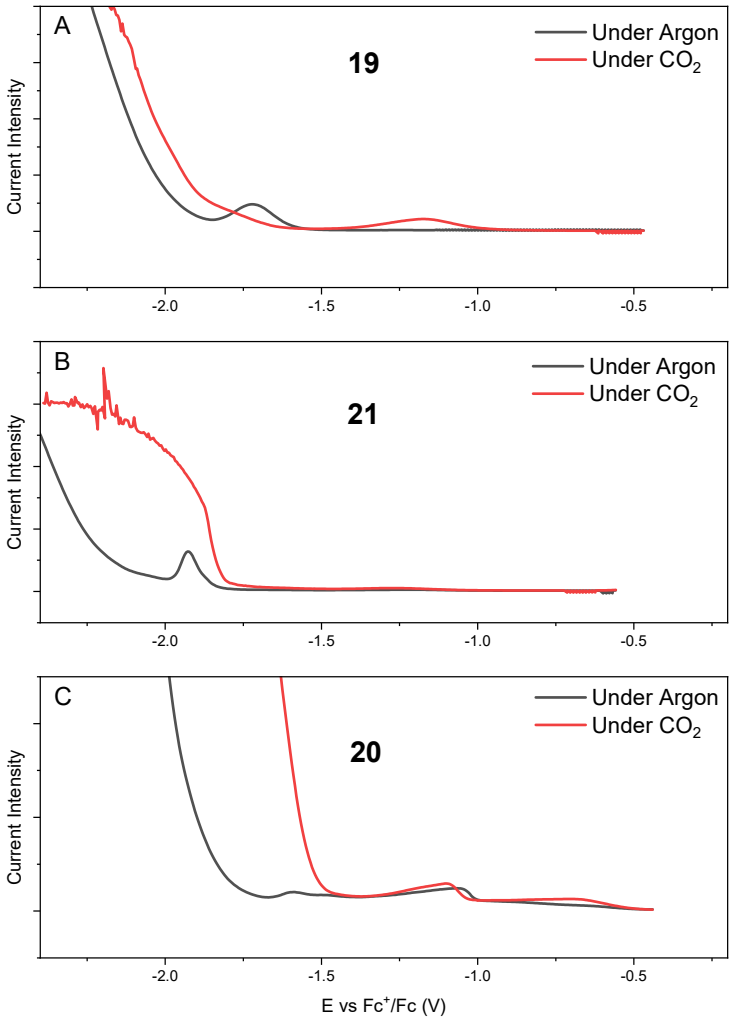

Figure 24. DPVs of the homoleptic **CAT-19**, **CAT-20** and **CAT-21** in MeCN/TEOA with CO_2 activation (red curves), 0.1 M $TBAPF_6$, at 100 mV/s, reported *vs* Fc^+/Fc.

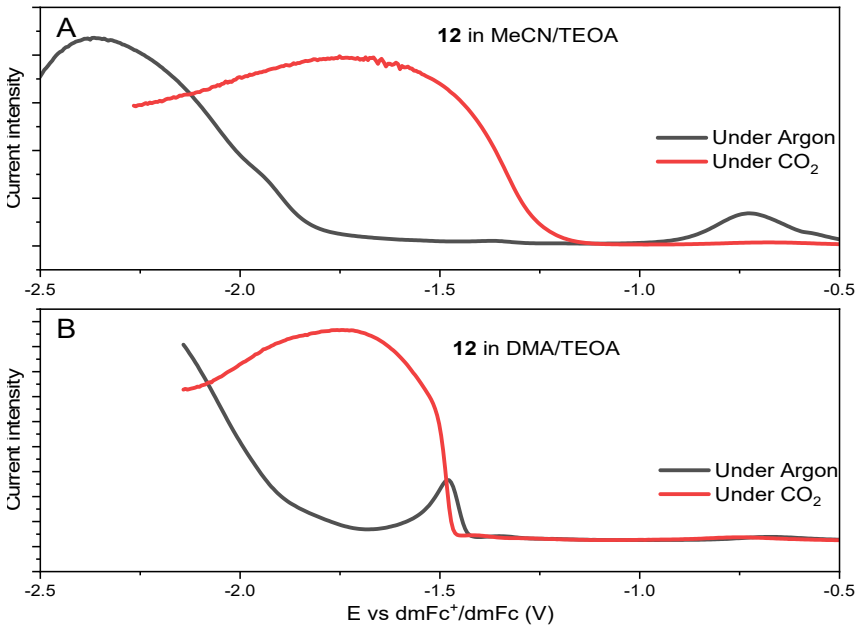

Figure 25. DPVs of **CAT-12** in MeCN/TEOA (Top) and in DMA/TEOA (Bottom) with CO_2 activation (red curves), 0.1 M $TBAPF_6$, at 100 mV/s, reported *vs* Fc^+/Fc.

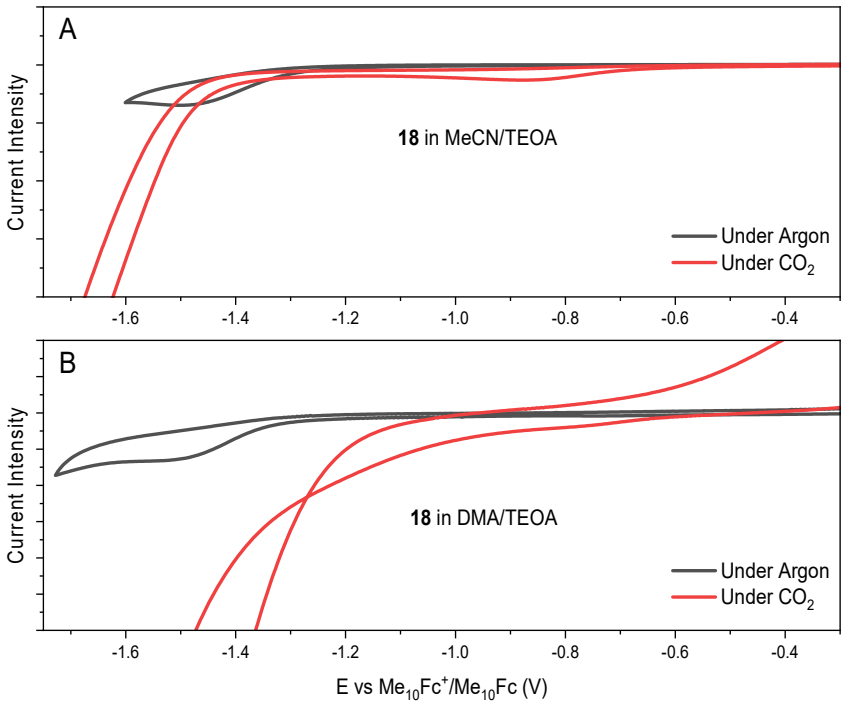

Figure 26. DPVs of **CAT-18** in MeCN/TEOA (Top) and in DMA/TEOA (Bottom) with CO_2 activation (red curves), 0.1 M $TBAPF_6$, at 100 mV/s, reported *vs* Fc^+/Fc.

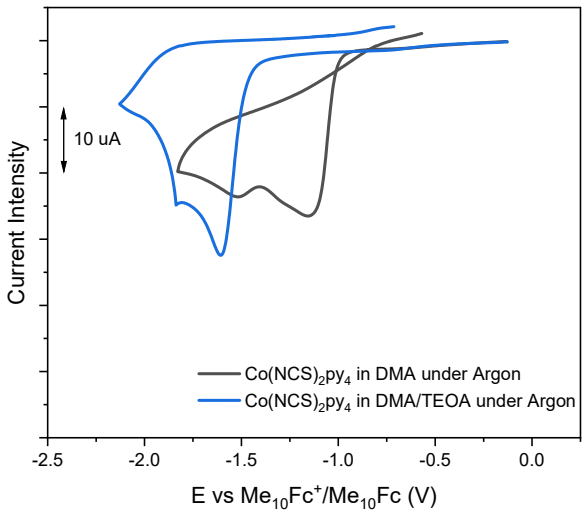

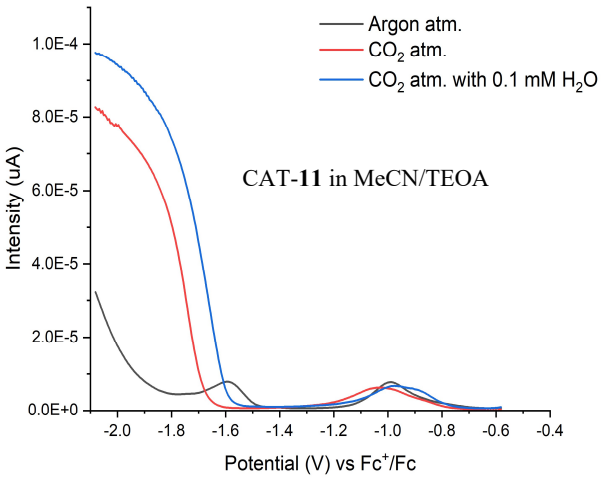

Figure 27. (Left) CVs of $Co(NCS)_2py_4$ in DMA (black) and in MeCN/TEOA (clue), 0.1 M $TBAPF_6$, at 100 mV/s, reported *vs* $Me_{10}Fc^+/Me_{10}Fc$.

Figure 28. (Right) DPVs of **CAT-11** in MeCN/TEOA under argon (black), under CO_2 atm. (red) and under CO_2 atm. with addition of 0.1 mM of H_2O (blue), 0.1 M $TBAPF_6$, at 100 mV/s, reported *vs* Fc^+/Fc.

Functionalization. The functionalization of the ligand with NH_2 and $N(Me)_3^+$ groups L-**8** and L-**10** allowed the study of the influence of electron donor and acceptor groups on the ligand. Amino groups were proven to enhance the catalytic performance in several research by making the complex richer in electrons and enhancing back donation from the metal to the CO_2 adduct which facilitated the cleavage of the bond C-O.[95] However, primary amines were also found to form carbamates with CO_2 and NH_3^+-groups upon protonation, changing their electronic donating properties to withdrawing.[95] Porphyrins functionalized with ammonium groups were proven to enhance the catalytic activity and the selectivity by formic ionic bonds with CO_2 and stabilizing intermediates.[175]

The two functionalized ligands L-**8** and L-**10** were characterized by CV (Figure 29) and compared with the non-functionalized ligand L-**6**. Unexpectedly, the electron donor amino groups on L-**8** do not appear to change the electronic properties as its reduction potential is very similar to the unfunctionalized ligand (-2.73 V *vs* Fc^+/Fc for L-**6** and -2.71 V *vs* Fc^+/Fc for L-**8**). The cationic L-**10** shows a different behavior with three visible reductions at -2.71 V *vs* Fc^+/Fc, -2.49 V *vs* Fc^+/Fc and -2.6 V *vs* Fc^+/Fc with the two ammonium groups that can be reduced.

The DPVs of the heteroleptic Co complex CAT-**12** compared with the cationic CAT-**23** show that both complexes have a reduction process at around -1.5 V *vs* $Me_{10}Fc^+/Me_{10}Fc$ (Figure 30), however the catalytic current onset under CO_2 atmosphere is negatively shifted from -1.43 V for CAT-**12** to -1.64 V for CAT-**23** (both *vs* $Me_{10}Fc^+/Me_{10}Fc$). One could have expected from the trimethylammonium groups that the reduction would be easier than without functionalization, however, the opposite is shown. This negative shift means that the reaction between the reduced complex and CO_2 is harder and needs more energy, leading to a possible lower catalytic activity with the new ligand.

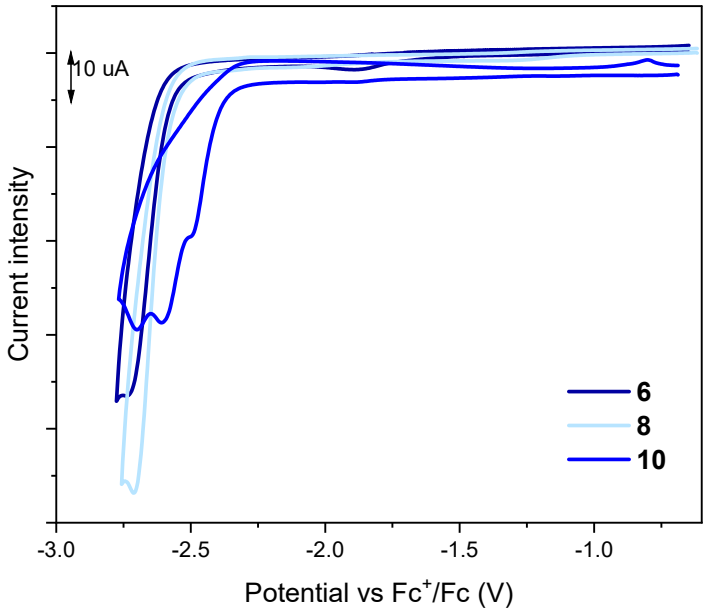

Figure 29. CVs of L-**6**, L-**8** and L-**10** in MeCN, 0.1 M $TBAPF_6$, at 100 mV/s, reported *vs* Fc^+/Fc.

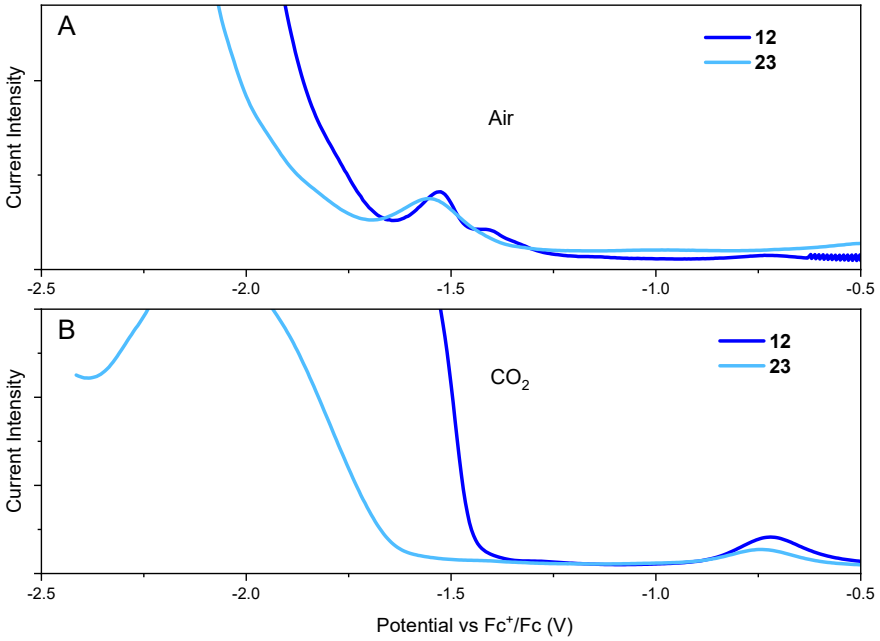

Figure 30. CVs in DMA/TEOA of **CAT-12** and **CAT-23** under argon (Top) and under CO_2 atm. (Bottom) 0.1 M $TBAPF_6$, at 100 mV/s, reported vs Fc+/Fc.

3.2.1.3.2 UV-vis Characterization

All the complexes present bright colors in their solid state, except for the Zn complexes CAT-**16** and CAT-**21**, which is white (Figure 33). In MeCN, they show absorption in the ultraviolet range of the electromagnetic spectrum (Figure 31 and 32). In particular, they show ligand-centered (LC) transitions at high energies with an absorptivity coefficient higher than 11500 $M^{-1}cm^{-1}$. These ligand-centered transitions are broad absorption bands centered at 200 and 250 nm and are associated to n-π* and to π–π* transitions. Metal-centered d-d transition are not observed in the visible range, maybe because they molar extinction coefficient is very low with respect to the LC transitions. The heteroleptic complex CAT-**12** shows a band at 350 nm assigned to the Co-NSC bond.[176] Surprisingly, the similar transition for the other metals is not visible when complexed.

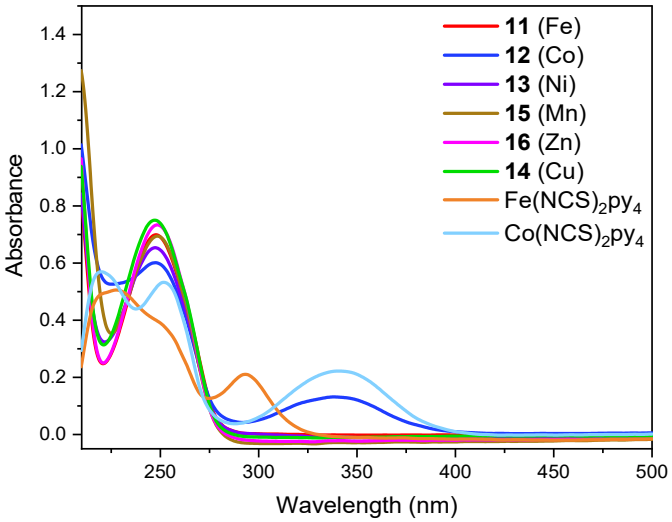

Figure 31. UV-vis absorption of the heteroleptic complexes with concentrations of 10^{-3} mM in MeCN at 22°C.

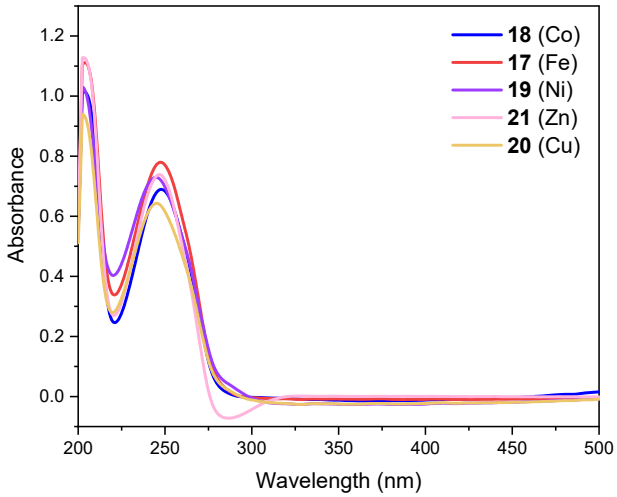

Figure 32. UV-vis absorption of the homoleptic complexes with concentrations of 10^{-3} mM in MeCN at 22°C.

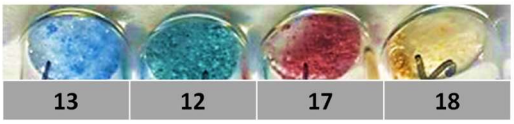

Figure 33. Pictures of some of the new complexes formed in this work, showing their different colors.

3.2.1.3.3 Magnetic Characterization with Evans tests and BVS

Evans tests were employed to determine the spin of the complexes and basic magnetic properties (see Supplementary data **5.3** for the method and calculations). The results shown in Tables 10 and 11 predict that all the complexes investigated with Evans method are paramagnetic in a high spin state (HS) (CAT-**11**, CAT-**12**, CAT-**14**, CAT-**15**, and CAT-**18**) except CAT-**17** which is diamagnetic in a low spin state (LS).

Table 10. Results from the Evans tests conducted in MeOD and MeCN-d_3 at 293 K [a]

CAT	**Δf (Hz)**	**F_{spec} (Hz)**	**C of CAT (moles/L)**	**MW (g/mol)**	**χ_m (cm^3/mol)**	**μ_{eff} calc (Bohr magnetons)**	**μ_{eff} theory (Bohr magnetons)**
11	140	$400x10^6$	0.01	644.5	$6.95x10^{-3}$	4.44	4.9 for n=4
12	132	$400x10^6$	0.015	647.6	$5.24\ x10^{-3}$	3.52	3.8 for n=3
17	16	$400x10^6$	0.024	1041.6	$3.97\ x10^{-3}$	0.96	0 for n=0
18	60	$400x10^6$	0.007	1044.7	$5.10\ x10^{-3}$	3.47	3.8 for n=3
15[b]	180[a]	$400x10^6$			$1.11\ x10^{-2}$	5.2	5.9 for n=5
14	12	$400x10^6$			$9.33\ x10^{-4}$	1.49	1.7 for n=1

[a] See Supplementary data for set up **5.3**, explanations and calculations [b] in acetone d_6.

Table 11. Analysis of the Evans tests and configurations of the complexes

CAT	Oxidation state	Magnetic property	Configuration
11	II	paramagnetic	HS
12	II	paramagnetic	HS
17	II	diamagnetic	LS
18	II	paramagnetic	HS
15	II	paramagnetic	HS (s0 d5)
14	II	paramagnetic	HS (s0 d9)

Bond valence sum (BVS) analysis was also performed to determine and confirm the spin and oxidation state of the four complexes CAT-**11**, CAT-**17**, CAT-**12** and CAT-**18**. This empirical analysis uses the bond lengths around a metal ion to determine the oxidation state of the metal center in coordination compounds. BVS analysis confirmed that the four complexes are oxidized (II) and high spin (HS) expect for CAT-**17** which is in a low spin (LS) state.

$$Bond\ Valence\ Sum = \sum \exp\left((R_0 + R) \cdot B\right)$$

With R = bond length between two atoms (here metal ion to ligand atom). R_0 and R are parameters that can be found in the text file that can be obtained on the website of the International Union of Crystallography (IUCr).[177]

Table 12. Results of the bond valence analysis

CAT	11	17	12	18
BVS analysis	1.952 - Fe^{II} High Spin	1.924 – Fe^{II} Low spin	1.974 - Co^{II} High spin	2.034 - Co^{II} High spin

3.2.1.4 Photocatalytic Tests with the New CATs.

The activity of the new catalysts in the photo-driven reduction of carbon dioxide was evaluated in combination with $[Cu^{I}(dmp)(DPEPhos)]$ (BF_4) (PS-**24**) (Figure 34) as photosensitizer[178] and BIH as electron donor. The photocatalytic experiments were carried out by dissolving all the components in a

4.0 mL mixed solution of MeCN or DMA with triethanolamine (TEOA) in a 5:1 v/v ratio, under irradiation at 420 nm for 4 hours. For a first screening, the concentration of CAT, PS and BIH were fixed at 0.1 mM, 1.0 mM and 20 mM respectively. Analyses of the gaseous contents of the reaction vessel were performed by gas-chromatography, with a chromatograph equipped with two Dielectric-Barrier Discharge Ionization Detector (BID). The produced amount of CO and H_2 for all complexes are shown in Figures 35 and 36 and reported in Table 13 and 14.

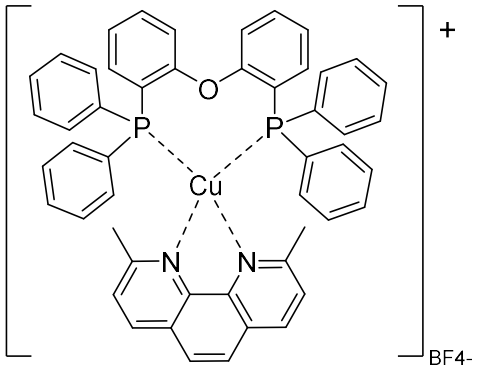

PS-24

Figure 34. [Cu^{I}(dmp)(DPEPhos)] (BF_4) (PS-**24**).[178]

H_2 and CO were quantitatively investigated as product using reference gas and calibration curves, while methanol and formic acid were qualitatively investigated using evaporation of reference solutions also analysed by GC-BID.

Heteroleptic complexes were found to be more efficient than their homoleptic analogues. The presence of the anionic ligand NCS influences the redox potentials (as seen previously), but the easier accessibility to the metal center can also explain this tendency. Indeed, both the heteroleptic and homoleptic complexes need to undergo de-coordination of one ligand moiety to create a vacant site for CO_2. In the case of the heteroleptic, however, the loss of the weakly coordinated pyridine is more feasible than the de-coordination of a chelating arm of the ligand L-**6** through twisting of L-**6**. (see below theoretical calculation part) Moreover, some metals show better activities than others. Thanks to the electrochemical characterization we could see that the activation of CO_2 – or first step of the catalytic cycle – was easier following CAT-**13** (Ni) > CAT-**14** (Cu) > CAT-**11** (Fe) > CAT-**12** (Co) > CAT-**16** (Zn) > CAT-**15** (Mn) but from the photocatalytic tests in MeCN, involving every step of the catalytic cycle, a different behavior is observed. CAT-**11** produces CO with a TON of 107 and selectivity of 71% over H_2 (Table 13, Entry 1) while CAT-**12** produces more H_2 than CO (TON_{CO} 1.1) (Table 13, Entry 3). Interestingly, CAT-**16**, CAT-**13** and CAT-**15** produce almost selectively H_2 with TONs H_2 of 79, 5.7 and 6.8 (Table 14, Entries 5, 6 and 3). Using CAT-**14** no product could be detected (Table 14, Entry 2).

Table 13. Photocatalytic results with the Fe and Co, in MeCN/TEOA and DMA/TEOA 5:1 v/v [a]

Entry	[CAT]	CO /µmol	H_2 /µmol	TON_{CO}	TON_{H2}	Sel.CO	Solvent /TEOA
1	**11**	37.8	15.1	107	43	71%	MeCN
2	**11**	traces		0	6.9	-	DMA
3	**12**	0.4	2.6	1.1	7.4	13%	MeCN
4	**12**	49.9	19.3	139	58	71%	DMA
5	**17**	2.8	0.7	7.8	2	79%	MeCN
6	**17**	2.8	1.1	7.7	3.3	70%	DMA
7	**18**	0.2	1.7	0.7	4.9	12%	MeCN
8	**18**	22.6	8.7	63	26	71%	DMA

[a] with [CAT] = 0.1 mM, [BIH] = 20 mM and [PS-**24**] = 1.0 mM, after 4 hours of irradiation at 420 nm.

The homoleptic complexes present a better stability and are easier to synthesize but show less good performance as catalysts. In MeCN/TEOA, CAT-**17** showed the best results with TON_{CO} of 7.8 and selectivity of 79% over H_2 (Table 13, Entry 5). CAT-**18**, CAT-**19** and CAT-**21** produced more H_2 than CO with TON_{H2} of 4.9, 1.5 and 3.8 respectively (Table 13, Entry 7 and Table 14, Entries 7 and 4). No product was observed using **20** as catalyst (Table 14, Entry 1). An overview of the results in MeCN/TEOA for the heteroleptic and homoleptic catalysts is shown in Figure 35.

Table 14. Photocatalytic results with the Cu, Mn, Zn and Ni based complexes in MeCN/TEOA 5:1 v/v [a]

Entry	CAT	CO /µmol	H_2 /µmol	TON_{CO}	TON_{H2}	Sel.CO
1	**20**	0	0	0	0	-
2	**14**	0	0	0	0	-
3	**15**	0.07	2.41	0.2	6.8	2.8%
4	**21**	0	1.33	0.1	3.8	2.5%
5	**16**	0.1	27,1	0.5	79	0
6	**13**	0-	2.00	-	5.7	-
7	**19**	0-	0.51	-	1.5	-

[a] with [CAT] = 0.1 mM, [BIH] = 20 mM and [PS-**24**] = 1.0 mM, after 4 hours of irradiation at 420 nm.

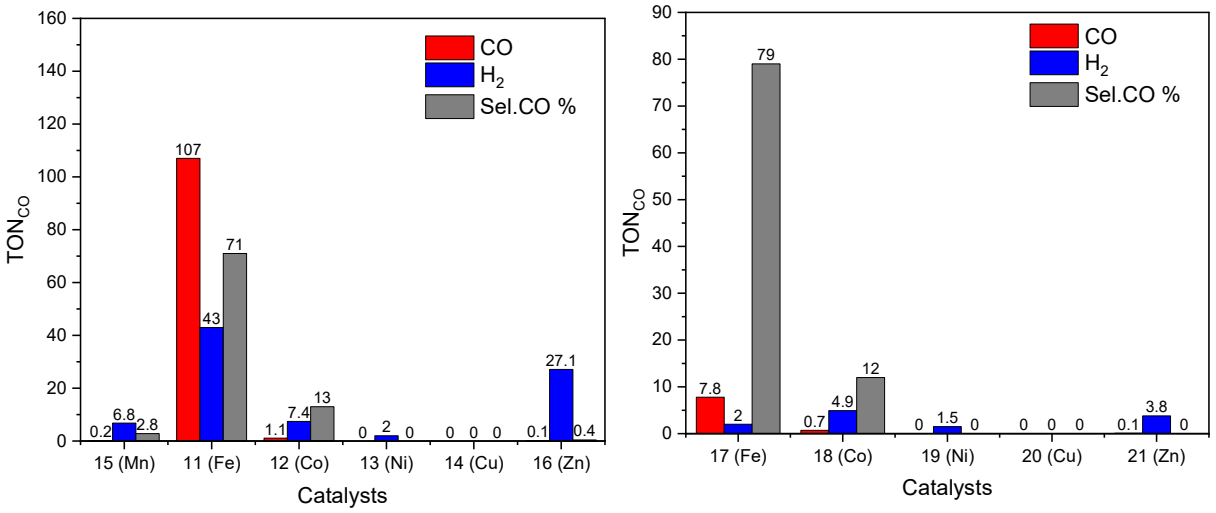

Figure 35. Production and selectivity of CO and H_2 Left: by the heteroleptic catalysts, Right: by the homoleptic catalysts, both in MeCN/TEOA. Amounts of products CO (red -left column) and H_2 (blue – central column) after 4 h of irradiation at 420 nm with 0.1 mM of catalysts with PS-**24** (1.0 mM). The CO selectivity over H_2 in percent is shown in grey (right column).

The thermodynamic feasibility of the electronic transfer from PS^- to CAT obtained by CV and DPV in MeCN/TEOA *vs* Fc^+/Fc show that the four complexes can be reduced by PS^- (equations 12 to 15) which means that the inefficiency of the cobalt complexes CAT-**12** and CAT-**18** in MeCN is due to other factors.

Ered/ox PS- - Ered/ox CAT-**11** = -2.08 + 1.76 = -0.33 V *vs* Fc^+/Fc (reaction feasible) (12)

Eox/red PS- - Ered/ox CAT-**12** = -2.08 + 1.23 = -0.86 V *vs* Fc^+/Fc (reaction feasible) (13)

Eox/red PS- - Ered/ox CAT-**17** = -2.08 + 1.63 = -0.45 V *vs* Fc^+/Fc (reaction feasible) (14)

Eox/red PS- - Ered/ox CAT-**18** = -2.08 + 1.81 = -0.22 V *vs* Fc^+/Fc (reaction feasible) (15)

EoxBI. – EredPS* =-2.06 + 2.08 = 0.02 V vs Fc+/Fc (16)

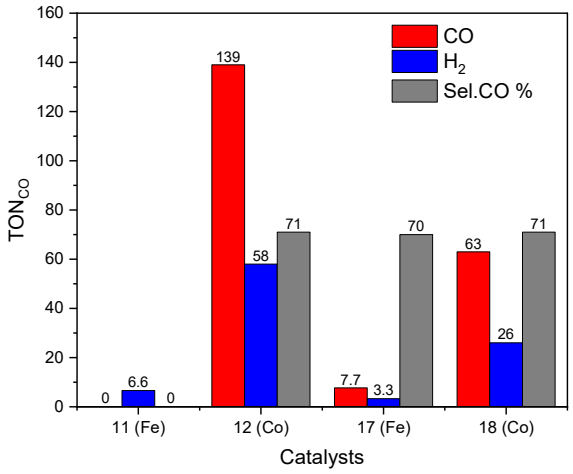

Figure 36. Production and selectivity of CO and H_2 the iron and cobalt-based catalysts DMA/TEOA. Amounts of products CO (red -left column) and H_2 (blue – central column) after 4 h of irradiation at 420 nm with 0.1 mM of catalysts with PS-**24** (1.0 mM). The CO selectivity over H_2 in percent is shown in grey (right column).

In DMA/TEOA, the activity of the cobalt complexes CAT-**12** and CAT-**18** was drastically increased with production of CO as main product and TON_{CO} of 139 (sel.CO 71%) and TON_{CO} of 63 (sel.CO 71%) (Table 13, Entries 4 and 8). This higher activity was attributed to the better solubility of both complexes in this solvent. On the contrary, the activity of both iron complexes CAT-**11** and CAT-**17** dropped to 0 for CAT-**11** and TON_{CO} 7.8 for CAT-**17** (Table 13, Entries 2 and 6), although both soluble in this solvent. The choice of solvent is crucial for the activity of those complexes. The activities of the iron and cobalt complexes in DMA/TEOA are shown in Figure 36.

Although thermodynamic feasibility predictions and electrochemical characterization under CO_2 atm. showed a possible reaction of CO_2, photocatalytic tests with Cu, Mn and Zn-based catalysts did not form CO (Table 13). Several explanations can be proposed, such as their poor solubility in the solvent used, their deactivation when complexed with CO_2 as an adduct, their inability to undergo the complete catalytic cycle by too high activation barrier to reach certain transition states or their pollution by CO in the last step. They also can produce other products than CO but neither formic acid, methanol or methane were detected.

Photocatalytic tests with the functionalized complexes CAT-**17_b**, CAT-**22** and CAT-**23** were performed, showing production of CO and H_2 ($TON_{CO}^{\mathbf{22}}$ = 3.1, $TON_{CO}^{\mathbf{23}}$ = 3.2 and traces of CO for CAT-**17_b**), however those tests were performed with a non-purified solvent system and still need to be performed under optimized conditions.

3.2.1.5 Optimization with CAT-11

The complex CAT-**11** was selected for further optimization because, together with CAT-**12**, presents the best catalytic activity. Iron is one of the cheapest metals and of the most abundant in the earth's crust (Fe: 56,300 ppm)[179] and is therefore the most stimulating metal to design efficient catalysts with, as its cost-effectiveness makes its use for larger-scale application feasible.[174] As stated before, the heteroleptic CAT-**11** complex is however not air-stable and changes its color from yellow to red under air. Also its precursor $Fe(NCS)_2py_4$ shows this trend and turns red when exposed to air. The Figure 37 shows the oxidized CAT-**11** after air exposure in MeCN and a large new band is observed at 490 nm, responsible of the red color. This new band is characteristic from the species Fe^{III}-NCS.[180-181]

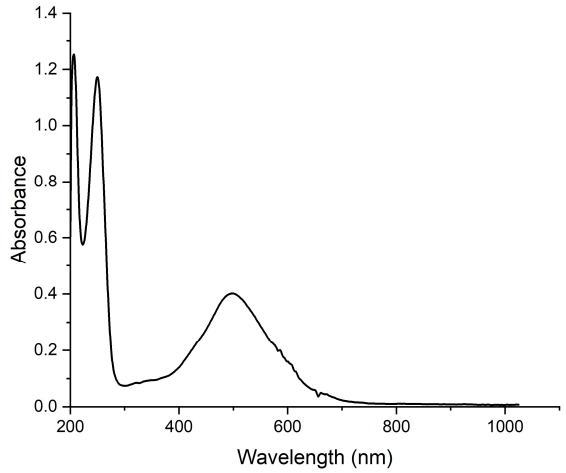

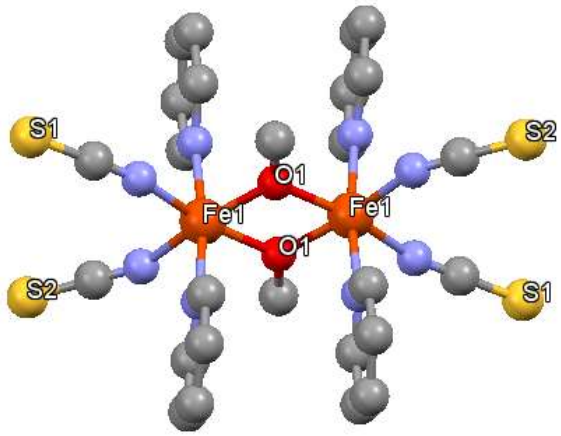

Figure 37. (Left) UV-vis of CAT-**11** in MeCN after air exposure.

Figure 38. (Right) X-ray structure of the precursor $Fe(NCS)_2py_4$ after air exposure. (Crystallography data in section **6.4**)

A single crystal suitable for X-ray from the red Fe precursor $Fe(NCS)_2py_4$ in methanol under air exposure could be obtained (Figure 38), showing a bimetallic Fe complex where both Fe atoms are bridged by two methanol molecules. This molecule has not been reported in the literature yet but similar ones were formed with bipyridines and bridging methanol.[182] Further analysis are needed to explore the properties and activity of such molecules.

To avoid this degradation, the precursor was thus stored under argon and used in its solution containing pyridine in ethanol in a ratio 1/9 and prepared freshly before use.

Optimization. To start with, the influence of the concentration of the components on the system as well as their ratios were investigated. Keeping the same ratio (CAT/PS/e^-D: 1/10/200) and decreasing their concentration by a factor of three ([CAT-**11**] = 0.033mM; [PS-**24**]= 0.33mM; [BIH]= 6.6 mM) led to a higher TON_{CO} of 238 and TON_{H2} of 137 (Table 15, Entry 3). When the ratio PS – e^-D/CAT was increased by using more PS and e^-D, the production of CO increased even more TON_{CO} of 314 and a TON_{H2} of 151 (Table 15, Entry 4). Finally, the best result with a TON_{CO} of 576 and selectivity of 67% was obtained when decreasing the concentration of CAT to 0.01 mM and by doing so increasing also the ratio PS-e^-D/CAT (Table 15, Entry 5). The concentration and ratio change did not influence the selectivity towards CO, which stayed stable at an average of 70%. The evolution of CO and H_2 at different concentrations of CAT-**11** is shown in Figure 39 and reveals the optimum concentration of 0.01 mM. When the concentration of e^-D was increased to 100 mM, a net decrease in efficiency was observed (Table 15, Entry 6) which was already observed in similar systems.[183] Also, the concentration of BIH was kept voluntarily low (20 mM) to avoid waste of product. Indeed not only its production needs the purchase of its expensive and not stable starting material (*N,N'*-Dimethyl-1,2-benzenediamine), but its large-scale use (20 mg per test) and sacrificial nature during the process make it a wasteful product employed.

Table 15. Photocatalytic results with CAT-**11** as CAT and PS **24** in MeCN/TEOA (5:1, v/v).[a]

Entry	Time	CO /μmol	H_2 /μmol	TON_{CO}	TON_{H2}	Sel.CO
1	4h	37.8	15.1	107	43	71%
2	20h	38.7	18.9	109	54	67%
3[b]	4h	84.1	48.1	238	137	63%
4[c]	4h	111	53.0	314	151	67%
5[d]	4h	203	101	576	287	67%
6[e]	4h	28.2	11.6	80	33	71%
7[f]	4h	2.61	2.24	7.4	6.4	54%
8	1h	1.1	0.6	3.2	1.6	67%
9	2h	28.2	11.9	80	34	70%
10	3h	35.4	15.1	100	43	69%
11[g]	4h	n. d.	0.3	0	1	-
12[h]	4h	n. d.	n. d.	0	0	-
13[i]	4h	n. d.	n. d.	0	0	-
14[j]	4h	n. d.	n. d.	0	0	-
15[k]	4h	32.8	17.5	93	50	65%
16[l]	4h	158	122	450	348	56%

[a] The experiments were performed with 20 mM BIH, 0.1 mM of CAT when not otherwise specified and 1.0 mM PS-**24** under CO_2 atmosphere at 22 °C and the products were measured by GC after 4 h irradiation at 420 nm. The products formed were analyzed from the headspace by GC twice. [b] [CAT]=0.033 mM, [PS]=0.33 mM, [BIH]=6.66 mM. [c] with [CAT]=0.033 mM, [PS]=1.0 mM, [BIH]=20 mM. [d] [CAT]=0.01 mM, [PS]=1.0 mM, [BIH]=20 mM. [e] [BIH]=100 mM, [f] with 300 uL of H_2O [g] no CAT. [h] no PS. [i] in the dark. [j] no CO_2. [k] In the presence of 1000 equiv. of molecular Hg. [l] With a solar simulator as source of energy, [CAT]=0.01 mM, [PS]=1.0 mM, [BIH]=20 mM, (n. d.=not detected).

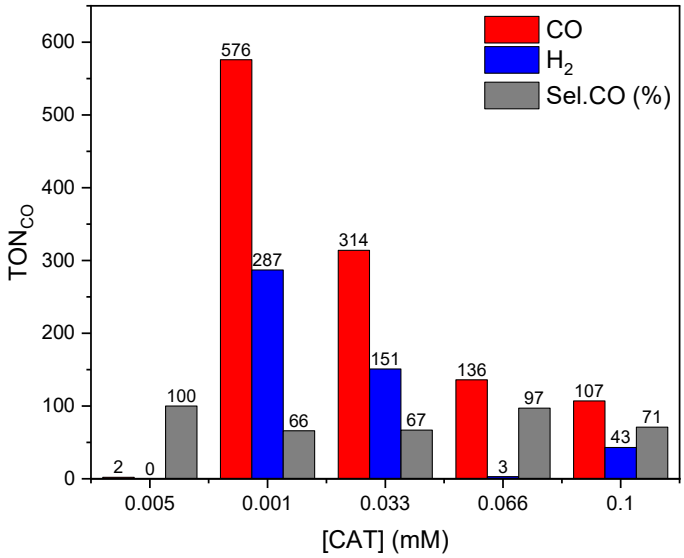

Figure 39. Production and selectivity of CO and H_2 with **CAT-11** in MeCN/TEOA. Amounts of products CO (red -left column) and H_2 (blue – central column) after 4 h of irradiation at 420 nm, with PS 24 (1.0 mM). The CO selectivity over H_2 in percent is shown in grey (right column).

The optimization studies conducted led to find the best performance of CAT-**11** with 0.01 mM, 1.0 mM of PS-**24**, 20 mM of BIH, forming 203 µmol of CO, leading to a TON_{CO} of 576. A value of 101 µmol of molecular hydrogen H_2 were co-produced (TON_{H2} 287), giving a CO selectivity of 67% after 4 h (Table 15, Entry 5). Although the electrochemical analysis showed that water could have a positive influence on the catalysis, addition of 300 µL of water in a standard photocatalytic test (MeCN/TEOA) led to a lower performance (TON_{CO} 7.4 and TON_{H2} 6.4, Table 15, Entry 7). Moreover, the selectivity also dropped to 53% which could be explained by the abundance of protons in the system and other acid additives such as TFE also did not show any interesting properties.

In order to investigate the feasibility of the photocatalytic CO_2 reduction with our system under sunlight, a test was conducted using a solar simulator as energy source. The photocatalytic sample was charged with 0.01 mM of CAT-**11**, 1.0 mM of PS in MeCN/TEOA and irradiated for 4 hours and produced CO and H_2 with TON_{CO} = 450 and TON_{H2} = 348. (Table 15, Entry 16) Unexpectedly, the selectivity decreased to 56% which was then attributed to the higher power of this light source, degrading faster the PS and its active MLCT.[184] To better assess the efficiency of this new system, the quantum efficiency of the photocatalytic system was calculated using chemical actinometry (see Supplementary data **5.6**) by measuring the number of photons received by the sample. With the white light of the solar simulator, CAT-**11** as CAT and after 4 hours of irradiation, the quantum yield was calculated at 4.5% while 7.1% was obtained with the photoreactor.

Kinetics and additional studies with CAT-11. To further investigate the catalytic activity of the system using CAT-**11**, the gas formed by the reaction was recorded every hour for 4 hours and after 20 hours to display a kinetic profile (Figure 40). The production of CO and H_2 is visible after 1 hour of irradiation and reaches its maximum value between 3 and 4 hours before stabilization. The induction period could

be explained by the necessary loss of py ligand to create the vacant coordination site for CO_2 adsorption. After 4 hours no new formation of CO from 4 to 20 hours is visible with the plateau observed while H_2 is still slowly produced. Nevertheless, the selectivity for CO over H_2 after 20 hours of irradiation is not drastically different 71% to 67% (Table 15, Entry 2).

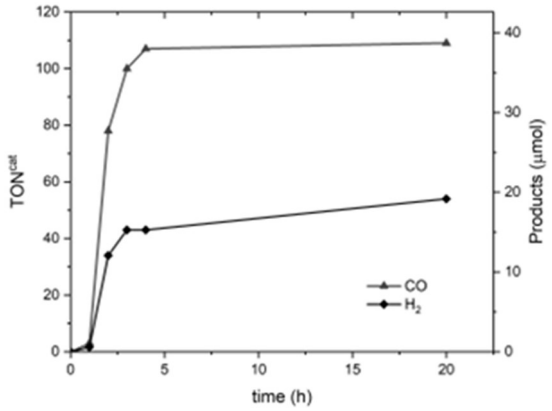

Figure 40. Evolution of the production of CO (red) and H_2 (black) with the time, using 0.1 mM of CAT-**11**, 1.0 mM of PS **24** and 20 mM of BIH in MeCN/TEOA (5 : 1, v/v) at 420 nm (22 °C).[72]

Furthermore, the cease of the reaction was explored to understand the limitations of the system. Due to the solvent mixture used (TEOA), the very low concentration of CAT, and the abundance of high concentrated components in the system, the regeneration and analysis of CAT after reaction could not be performed. Nevertheless, the UV-vis of CAT-**11** in MeCN was recorded after 4 hours of irradiation and proved its photostability. (Figure 41)

The evolution and degradation of the photosensitizer employed PS-**24** is more easily perceptible and was already studied in similar systems.[185] The UV-vis absorption spectra of the photocatalytic solution before irradiation and after 4 h at 420 nm (Figure 42, left) exposes the decrease of the metal-to-ligand charge-transfer (MLCT) band from the PS after irradiation, suggesting the degradation of the heteroleptic Cu^I photosensitizer.

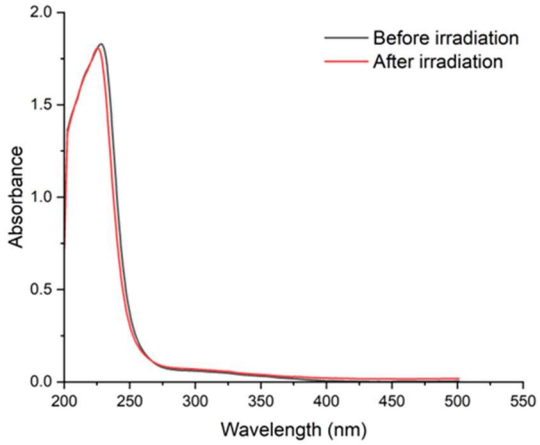

Figure 41. UV-vis absorption of CAT-**11** in MeCN before and after (red) irradiation with a solar simulator for 4 hours.[72]

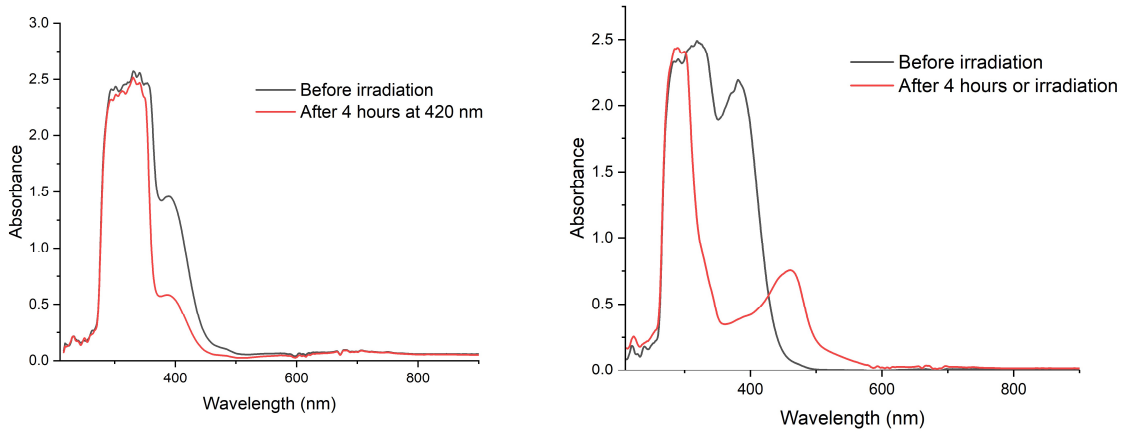

Figure 42. Left: UV-vis of a photocatalytic test containing CAT-**11** (0.1 mM), 24 (1.0 mM) and BIH (20 mM) in MeCN/TEOA (5:1, v/v) before and after irradiation at 420 nm for 4 hours. Right: PS-**24** (1.0 mM) in MeCN/TEOA after irradiation with a solar simulator for 4 hours.[72]

This degradation is also visible when irradiating PS in MeCN/TEOA where a new band is observed at 480nm (Figure 42, right) characteristic from the homoleptic Cu^{I} complex $[Cu(dmp)_2]$. To confirm this hypothesis, ^{1}H NMR samples were recorded before and after irradiation which show the consumption of the active heteroleptic Cu^{I} complex into the not active homoleptic complex (Figure 43). The degradation of PS is thus one of the explanations of the cease of the reaction due to the rarefaction of the MLCT available for excitation through light.

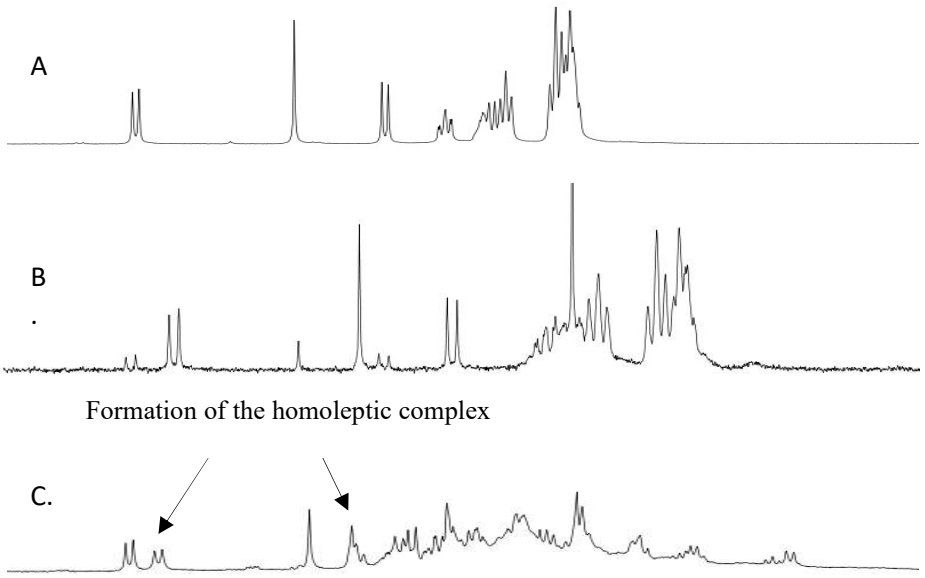

Figure 43. ^{1}H NMR spectra of (A) heteroleptic $[Cu^{I}(dmp)DPEPhos](BF_4)$ (PS-**24**) (1.0 mM) in MeCN before irradiation (B) homoleptic $[Cu^{I}(dmp)_2](BF_4)$ (1.0 mM) in MeCN (with traces of heteroleptic complex) (C) $[Cu^{I}(dmp)DPEPhos](BF_4)$ (PS-**24**) 1.0 mM in MeCN/TEOA after 4 hours of irradiation with a solar simulator. [72]

Control Tests. Striving for integrity, control experiments were carried out to prove the necessity of each component of the photocatalytic system, their homogeneous behavior and the provenance of the carbonated product formed. First, changing the atmosphere from CO_2 to argon did not produce any product. Likewise, in the dark or without PS, no product was formed (Table 15, Entries 12, 13, 14). Interestingly, the control test conducted without CAT produced no CO but traces of H_2 after 4 h (0.4 mmol, $TON_{H2} = 1$; Table 15, Entry 11), which suggest that PS might participate in the formation of H_2. To investigate the homogeneity of the catalysis, control experiments were performed combining two techniques: dynamic light scattering (DLS) experiments of the photocatalytic solutions and mercury test (Figure 44). The DLS spectra recorded display the presence of small amounts of 100 nm nanoparticles before and after irradiation which indicate that they are not formed during the photoreaction but most likely dust particles. Other nanoparticles are observed with an average size of 1 nm after irradiation but with an insignificant intensity. Furthermore, a standard catalytic test was prepared with addition of 1000 equivalents of molecular Hg, which is a common test employed to distinguish between homogenous molecular catalysis and nanoparticles (or clusters) catalysis. It relies on the assumption that molecular mercury will poison or trap nanoparticles or clusters without impacting the molecular metal complexes.[186] The result obtained was not influenced by the presence of Hg (Table 15, Entry 15) which, in combination with the DLS analysis suggest the homogeneity of the catalytic solution.

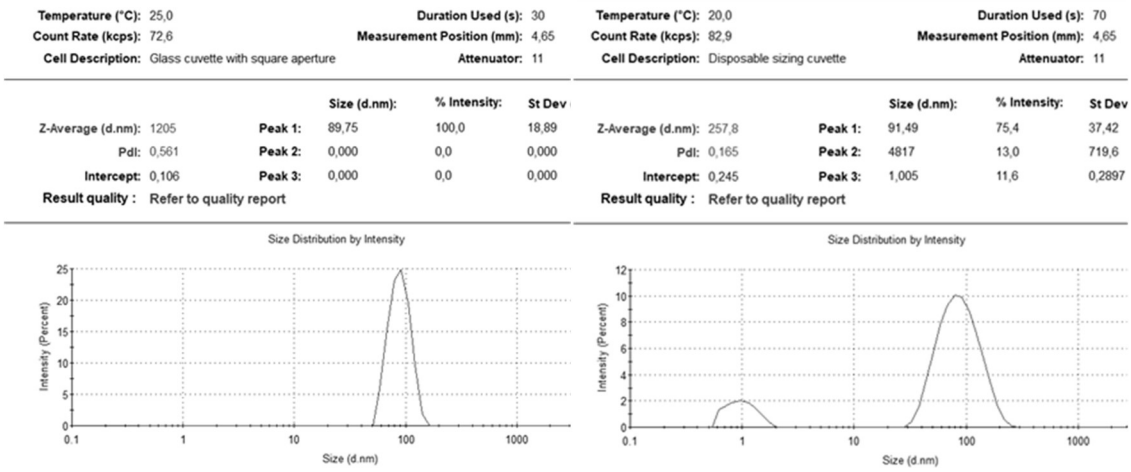

Figure 44. DLS measurement of a photocatalytic test containing CAT-**11** (0.1 mM) as catalyst, 1.0 mM of PS (**24**), 20 mM of BIH in MeCN/TEOA (5:1, v/v) Left: before irradiation and kept in the dark Right: after 4 hours of irradiation at 420 nm.[72]

To verify that the carbon produced (CO) originated from the reduction of CO_2, the isotope ^{13}C was employed to generate $^{13}CO_2$ and observe by ^{13}C NMR the presence of ^{13}CO formed (Figure 45). $^{13}CO_2$ was formed by addition of conc. HCl on $NaH^{13}CO_3$. Three standard photocatalytic tests were performed in J. Young NMR tubes and analysed by ^{13}C NMR. The two first ones were put under $^{13}CO_2$ atmosphere with CAT-**11** as CAT in the first one (Figure 45 (A)) and no CAT in the second one (Figure 45 (B)). The third one was put under $^{12}CO_2$ atmosphere and with CAT-**11** as CAT (Figure 45 (C). After irradiation, the ^{13}C NMR spectrum of the first sample (Figure 45 (A)) shows a signal for the ^{13}C carbon of the dissolved CO at 184 ppm[187] when CAT-**11** is present, while no signal is observed without CAT

or with $^{12}CO_2$ atmosphere. This indicates that the CO formed is indeed coming from CO_2 through photocatalysis with CAT-**11**.

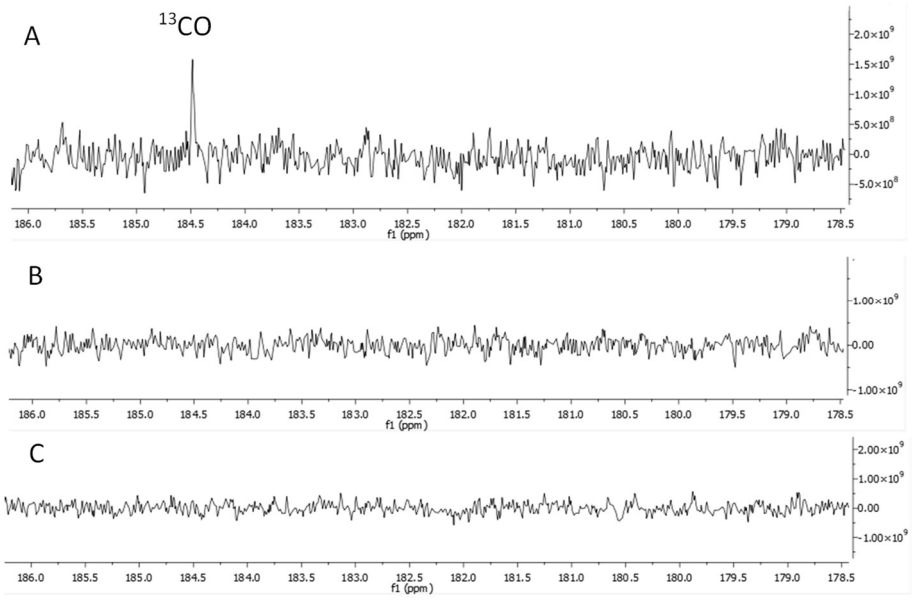

Figure 45. ^{13}C NMR spectra of photocatalytic test with 5.0 mM of PS-**24**, 30 mM of BIH in MeCN/TEOA (5:1, v/v) after 4 hours of irradiation at 420 nm. (A) under $^{13}CO_2$ atmosphere with CAT-**11** as CAT (0.5 mM), (B) under $^{13}CO_2$ atmosphere with no CAT and (C) under $^{12}CO_2$ atmosphere with CAT-**11** as CAT (0.5 mM).[72]

Evaluation of the System and Comparison. The catalytic performance of the new CAT-**11** as catalyst is very interesting and promising for the design of new efficient Fe-based catalysts. The known mononuclear $Fe(dmp)_2(NCS)_2$ [164, 188] employed by ISHITANI and coworkers in combination with a dinuclear Cu^I complex as a photosensitizer in MeCN/TEOA produced CO with a TON of 95 and a selectivity over H_2 of 70.5%.[164] The efficiency was improved with longer irradiation times indicating the higher stability and efficiency of dinuclear Cu complexes as PS, reaching a quantum yield of 6.7%. However, when they employed $Fe(dmp)_2(NCS)_2$ with the same mononuclear $Cu^I(dmp)(DPEPhos)$ than our system, the photocatalysis was less efficient with a TON_{CO} of 69.5, a CO selectivity of 53% and a quantum yield of 1.1%.[164] Our system produced 8 times more CO with a similar selectivity and a higher quantum yield after 4 hours, which is amongst the most efficient homogeneous system based on earth-abundant materials.[72, 164] Very recently, new Fe-based monometallic catalysts were reported to be more efficient in noble metal-free environment such as the $Fe(Ntpy)_2$ from CHAO and coworkers. This CAT produced CO with a TON of 6320 with an excellent selectivity of >99% in combination with an organic PS in DMF/H_2O and a catalyst charge of 0.1 mM, reaching a quantum yield of 9.5%.[50]

Mechanistic Information. To get insights into the mechanism, catalytic tests and Stern-Volmer analysis were conducted. Collaborations with Prof. Weis and Dr. Neumaier allowed the use of Nano ESI measurements to observe the catalyst in the media, and collaborations with Prof. Fink and Dr. Barani worked on theoretical calculation to propose a catalytic mechanism.

Stern Volmer tests (SV) were performed to determine the quenching process in our system with CAT-**11** as CAT. This intermolecular deactivation technique allows determining if the excited state of the PS employed is quenched by the electron donor (BIH) (reductive quenching) or by the catalyst (oxidative quenching) (See Supplementary data **5.4**). It means it can determine if the presence of the electron donor or of CAT accelerates the decay of PS*.

The quenching constants were determined for CAT-**11** and the linear responses of the SV experiments are displayed in Figure 46 and 47. For CAT-**11**, both a reductive quenching by BIH and an oxidative quenching by CAT-**11** are thermodynamically feasible with quenching constants k_{BIH} =0.10×106 s^{-1} m^{-1} and k_{CAT}=0.2×106 s^{-1} m^{-1}. These constants are lower than most in the literature using Cu^{I}(dmp)(DPEPhos) (PS-**24**) and BIH as electron donor, which can be explained by their measure in pure solvent rather than in the solvent system employed (MeCN/TEOA) in our case. The quenching constant is higher in the case of the oxidative quenching, however the use of BIH in excess rather suggests that the reductive quenching by BIH is favored ([BIH] = 20 mM >>> [CAT] = 0.1 mM). To summarize, photoinduced electron transfer from BIH to PS* occurs, and the reduced form of PS reduces the catalyst.

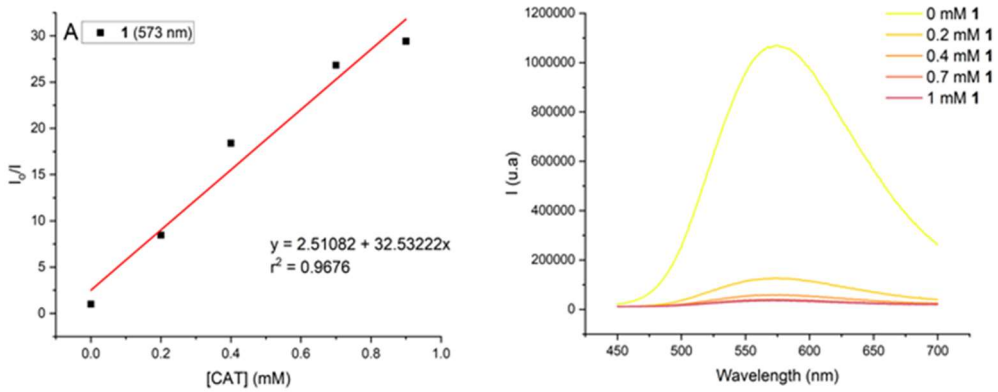

Figure 46. Right: Stern-Volmer quenching analysis. [PS-**24**] = 0.05 mM and a maximum Emission at 573 nm. Left: linear fit recorded with increasing concentration of CAT-**11**.[72]

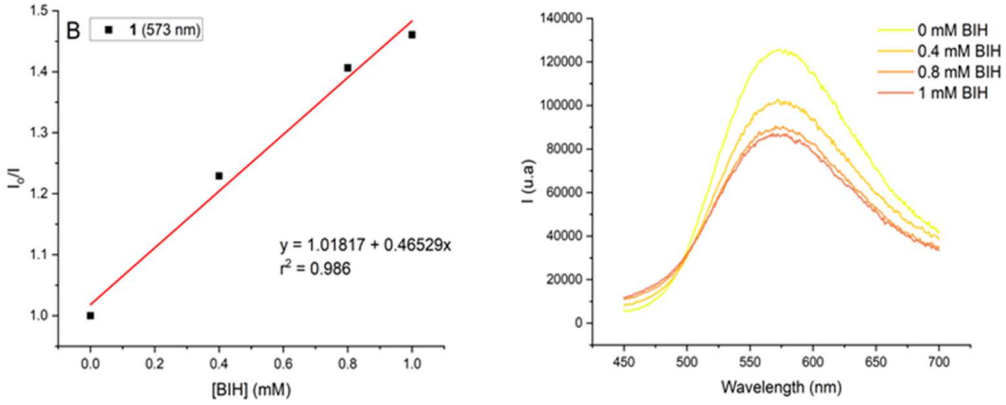

Figure 47. Right: Stern-Volmer quenching analysis. [PS-**24**] = 0.05 mM and a maximum Emission at 573 nm. Left: linear fit recorded with increasing concentration of BIH.[72]

Photocatalytic tests were performed to prove the role of the electron and proton donors employed using [CAT-**11**] = 0.01 mM, [PS-**24**] = 1.0 mM, [BIH] = 20 mM, MeCN/TEOA 5:1 v/v, 4 hours of irradiation at 420 nm. (Table 16). As expected, no product was detected in the case where both BIH and TEOA were omitted (Table 16, Entry 3). On the other hand, the test using no BIH showed production of CO (TON_{CO} = 6.8) without forming any H_2 (Table 16, Entry 1). This means that TEOA can act not only as a proton donor but also as an electron donor. The selectivity was remarkably improved (>99%) as no H_2 production was detected but the TON was very low (ca. 7) meaning that the combination with BIH is still necessary. The test using no TEOA also produced CO (TON_{CO} = 44) without any H_2 detected. This proves that BIH can act as electron and proton donor as some CO was produced without TEOA. Also in this case, no H_2 was produced so the selectivity was also improved (97%). The role of electron donor attributed to BIH and proton donor attributed to TEOA was thus confirmed even if they both also show secondary roles of proton and electron donors.

Table 16. Results of the photocatalytic tests for the electron and proton donors [a]

Entry	Test	CO /µmol	H_2 /µmol	TON_{CO}^{CAT}	TON_{H2}^{CAT}	Sel.CO
1	No BIH	0.27	0	6.8	0	>99%
2	No TEOA	1.73	0	44	0	97%
3	No BIH No TEOA	0	0	0	0	

[a] The experiments were performed in MeCN/TEOA (5:1, v/v) with 20 mM BIH and 1.0 mM PS-**24** and 0.01 mM CAT-**11** under CO_2 atmosphere at 22°C and the products were measured by GC after 4h irradiation at 420 nm. The products formed were analyzed from the headspace by GC.

Nano-ESI measurements. Furthermore, to gain more detail in the catalytic cycle, Nano ESI measurements were conducted to determine the active species entering the catalytic cycle. The catalyst usually undergoes transformation such as ligand loss, reduction or oxidation to generate the active

species on which the catalysis happens. Nano ESI of a sample containing CAT-**11** dissolved in MeCN shows a mass of 507.080 for the fragment [CAT-**11** – NCS – pyridine] and a mass of 585.094 for the fragment [CAT-**11** – NCS]. It indicates that the pyridine stays coordinated to the metal and not being replaced by the MeCN when dissolved (Figure 48). When two equivalents of TEOA were added to a dissolved one equivalent of CAT-**11** in MeCN, a mass of 655.633 for [CAT-**11** – Py + TEOA] was observed, implying that the pyridine can be replaced by TEOA. The role of TEOA has already been demonstrated to be versatile as it can replace ligands in certain systems and even play a role in the catalysis by trapping CO_2 and making the insertion of CO_2 easier in the metal – O(TEOA) bond. The role of TEOA in our system is still to be fully understood and characterized.

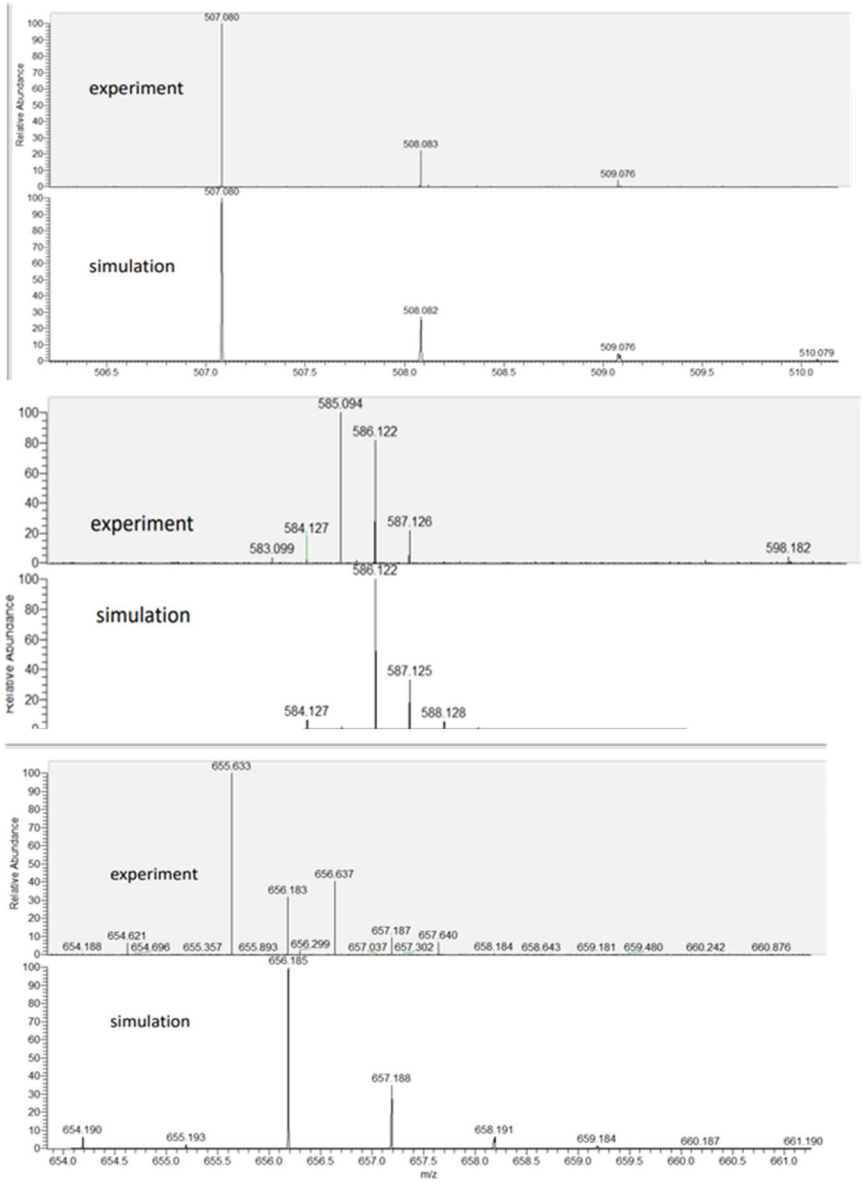

Figure 48. Nano-ESI-MS of Top: CAT-**11** in MeCN, fragment Fe(**6**)$(NCS)_1$; Center: CAT-**11** in MeCN, fragment Fe(**6**)$(NCS)_1$py; Bottom: CAT-**11** in MeCN with 2.00 equivalents of TEOA, fragment Fe(**6**)(NCS)(TEOA).[72]

Theoretical calculations were conducted concerning the new Fe heteroletpic CAT-**11** and its homoleptic analogue CAT-**17** for comparison. The calculations of the CO_2 binding energies were conducted with the program package Turbomole[189] with density functional theory (DFT) using the B3LYP functional[190] and a def2-TZVP basis set.[191-192] For the determination of reaction mechanisms, r^2SCAN-3c method was used,[193] including D4-dispersion [194] with geometrical Counterpoise Correction (gCP). [195] A modified version of the def2-TZVP basis set was employed. [196] The r^2SCAN calculations were conducted with ORCA 5.0.2.[197-198]

First of all, the first possible steps including the reduction of the CAT and loss of a ligand to create a vacant site for CO_2 were investigated. Mulliken spin population represented in Figure 49 show that the electron density is first localised around the metal when neutral and in its most stable quintet state. When the complex is reduced with one electron to reach its most stable sextet state, the electronic density is localised in the ligand L-**6** part around the pyridine and with a second electron added, which is the most stable in a triplet state, the electronic density is stored in the ligand quasi homogeneously. The same tendency was observed for the homoleptic CAT-**17** complex.

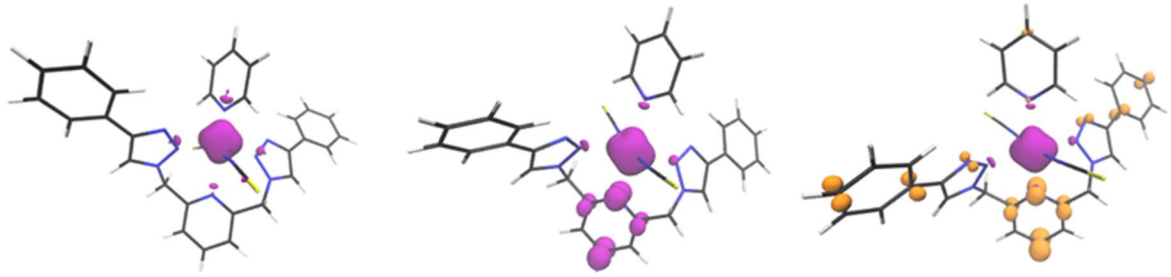

Figure 49. Spin density of Complex CAT-**11** (left) $[Fe(L\text{-}\mathbf{6})(NCS)_2py]^0$, quintet state and (center) $[Fe(L\text{-}\mathbf{6})(NCS)_2py]^{1-}$, sextet state, (right) $[Fe(L\text{-}\mathbf{6})(NCS)_2py]^{2-}$, triplet state. Basis set: def2-TZVP, functional: B3LYP; isovalue: ± 0.01.[72]

The loss of ligand upon reduction or creation of vacant site for CO_2 adsorption was then investigated. For the complex CAT-**11**, both the pyridine and one NCS ligand can be expected to be lost, while a de-coordination of one triazole moiety triggering a twist of one of the ligand was expected for CAT-**17**. The crystal structure of CAT-**11** already suggested that the pyridine would be detached from CAT-**11** because the bond Fe-NCS is stronger (2.09 Å) than the bond Fe-py (2-20 Å). This was then confirmed by the binding energies (Table 17) which are much stronger for the bond Fe-NCS (596.46 kJ/mol *vs* 52.56 for the pyridine), even when this one is reduced (154.73 kJ/mol *vs* 51.87 kJ/mol for the pyridine).

Table 17. Binding energy of different ligands on complex CAT-**11** (kJ/mol). Basis set: def2-TZVP, functional: B3LYP.[72]

Charge of complex 11	Binding energy (kj/mol)	
	Py	**NCS**
0	52.56	596.46
1-	51.87	154.73
2-	50.20	-67.00

The thermodynamics of ligand dissociation and CO_2 adsorption for both complexes allowed to determine that for CAT-**11**, the pyridine de coordinates Fe after one or two reductions and the adsorption of CO_2 is possible only after two reductions (charge of Fe(0), charge of the complex (-2)) (Figure 50 left). However, for the homoleptic CAT-**17**, the opening of the ligand, requiring 17 kJ/mol, is the most stable after one or two reduction and very unlikely feasible before reduction. The adsorption of CO_2 is feasible only after two reduction (charge (0)). (Figure 50 right) Those results are in line with the literature as CO_2 is known to be adsorbed only on reduced metals for similar types of complexes. [79, 199]

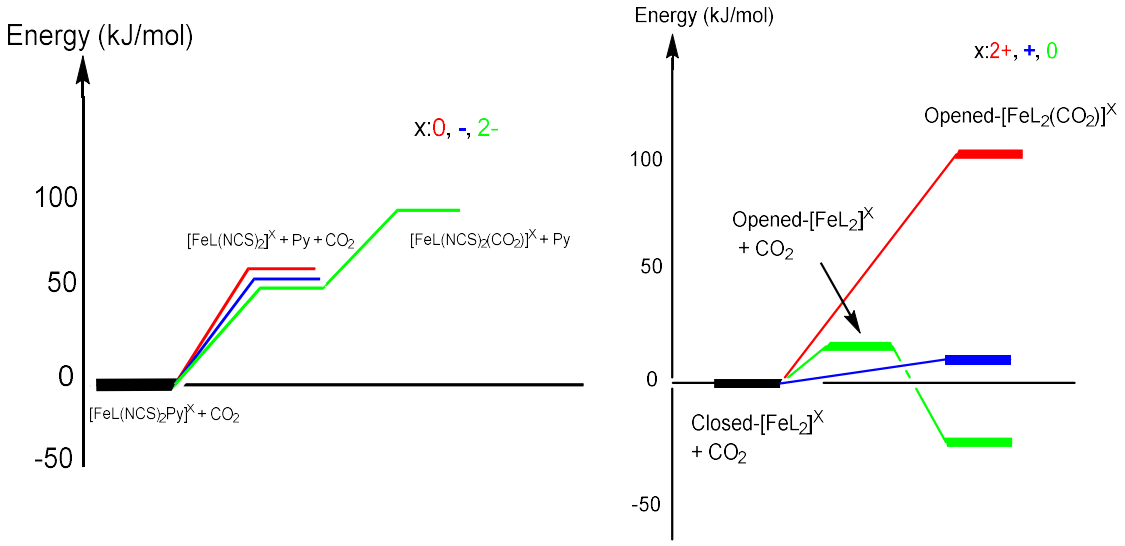

Figure 50. The relative energies of different oxidation states for (left) complex **11**, (right) complex **17**. Basis set: def2-TZVP; functional: B3LYP. In the figure, L = **6**.[72]

The adsorption of CO_2 on both Fe centers was thus further investigated knowing that CO_2 can be adsorbed in different ways on the metal. The four most common adsorptions were tested: linear-O-"end-on" (η_1 O), "side-on" (η_2 C,O), C-bound "Y-on" (η_1 C) and bent-O-"end-on" (η_1 O bent) were tested (Scheme 4).[200-201] It was found that the C-bound (η_1 C) "Y-on" configuration is the most stable in a singlet state for complex CAT-**11** while CO_2 binds preferably "side-on" (η_2 C, O) in a triplet state to the metal in complex CAT-**17** (Table 18).

Table 18. Relative energy (kJ/mol) of different patterns for adsorption of CO_2 in different spin multiplicities, S: Singlet and T: Triplet for complex **11** and **17**.[72]

Complex	Patterns	Spin multiplicity	Relative energy (kJ/mol)
CAT-**11**	**η^1_C**	**S**	**0.00**
		T	0.48
	η^1_O	S	32.99
		T	26.73
	$\eta^2_{C,O}$	S	0.19
		T	0.96
CAT-**17**	η^1_C	S	19.29
		T	16.41
	η^1_O	S	91.66
		T	94.56
	$\eta^2_{C,O}$	S	15.44
		T	**0.00**

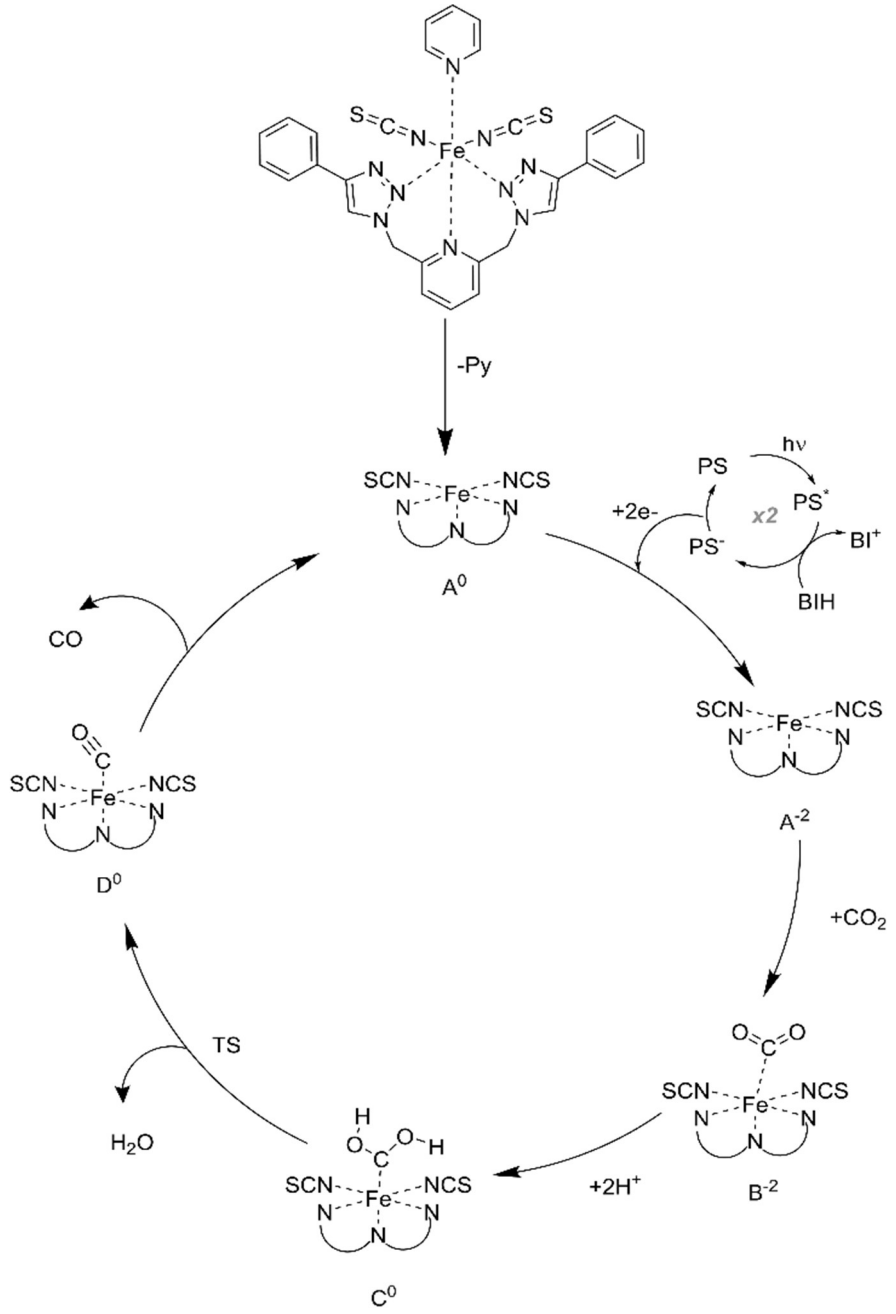

Scheme 22. Proposed catalytic cycle with CAT-**11** as catalyst for CO_2 reduction.[72]

Finally, the catalytic mechanism shown in Scheme 22 was proposed with CAT-**11** as catalyst and the reaction profiles obtained for CAT-**11** in different multiplicities in Figure 51.

To enter the catalytic cycle, the pyridine has to de-coordinate Fe leading to, which is then photo-inductively reduced by two PS forming A_2. Only then, is the adsorption of CO_2 feasible and most preferably in "Y-on" conformation, forming B_2, which can be doubly protonated to form C_0.[202] The protonation step, which weakens the C-O bond, leads to its breaking and the release of H_20 to form D_0. This step is rate limiting with a barrier of 160 kJ/mol to overcome in the singlet state. Lastly, the

desorption of CO to reach back A_0 requires 137 kJ/mol which makes the reaction exothermic (-40 kJ/mol). This step can also cause the cease of the reaction by polluting the catalyst if the affinity of the metal for CO is too strong.[203] The energy profile for CAT-**11** shows that the singlet state pathway is the most favorable.

The catalytic cycle for CAT-**17** reveals a similar mechanism with an easier ligand-to-CO_2 exchange than with CAT-**11**. However, the more sterically hindered structure of CAT-**17** leads to a harder adsorption of CO_2 on the metal but an easier release of CO 120 kJ/mol than with CAT-**11** (Table 19).

Table 19. Desorption energies in kJ/mol for CO from CAT-**11** and CAT-**17**.[72]

	CAT-**11** (0, 1) [kJ/mol]	CAT-**17** (0, 1) [kJ/mol]
Gibbs free energy	137.74	120.79

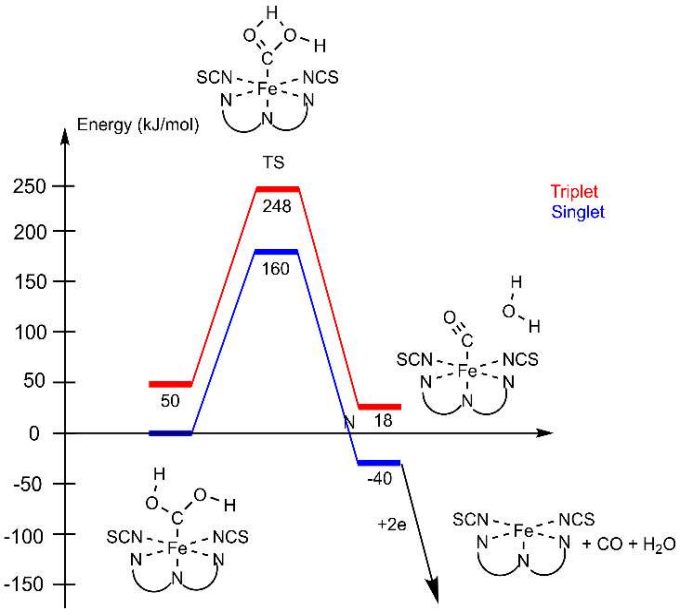

Figure 51. Energy diagram for CAT-**11** in different multiplicities.[72]

New calculations are ongoing to study the possibility of TEOA to participate in the catalytic cycle.

3.2.2 Bimetallic Complexes

Introduction. Earth-abundant-based bimetallic catalysts were already reported with high activities and very high selectivity with for example the bimetallic $Co_2(DPA)Cl_2$ (DPA dipicolylamine) producing CO with a TON of 2600 and CO selectivity of 97%.[204] However, this system does not involve a cooperative effect and both Co centers react independently from each other. Cooperativity effects were observed in several systems, for example in 2022, AUKAULOO *et al.* reported a bimetallic iron and zinc complex with a urea unit bridging the two Fe moieties and acting as a multi-point hydrogen-bonding. Not only the H-bonds stabilize the complex and the CO_2 intermediates, but the bimetallic complex formed four times more CO than its monometallic analogue probably due to a push-pull (role differentiation of the metallic centers) between the two metals.[205] Another very interesting bimetallic system showing cooperativity effect was reported in 2018 by LU *et al.* combining Co and Zn in a cryptate structure forming CO with a TON of 65000, 45-fold higher than its corresponding mononuclear Co moiety.[141]

Concerning this work, once it was demonstrated that the monometallic complexes (CAT-**11** to CAT-**21**) showed activity towards reduction of CO_2, bi- and tri-metallic complexes were designed involving a synthetic strategy with the same coordination scaffold L-**6**, extended to the quinoline and pyridine L-**26** and L-**25** (Scheme 23, 24). In this way, three different places seem available for metal complexation (Figure 52). The aim of having multi-metallic complexes is to investigate cooperativity effects in their catalysis, by comparing them with their mononuclear analogues. The metals Fe, Ni and Co were investigated.

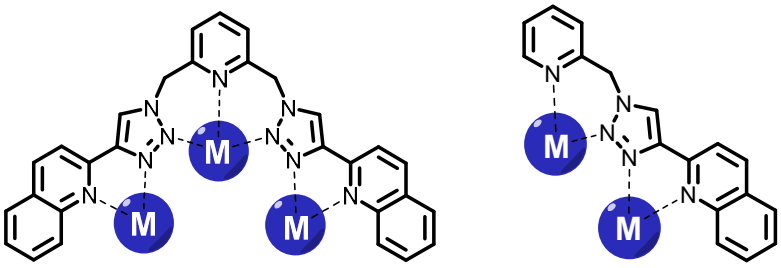

Figure 52. General structures of the target complexes.

3.2.2.1 Plan of Synthesis

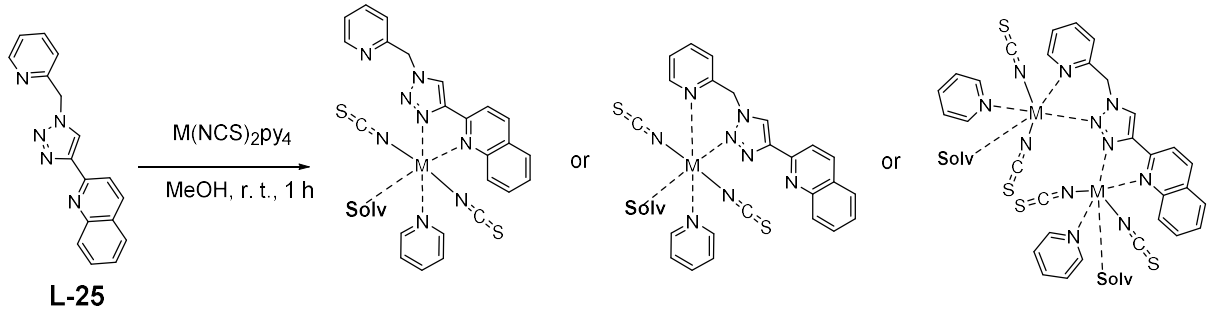

Scheme 23. Plan of synthesis to build mono- and bimetallic complexes.

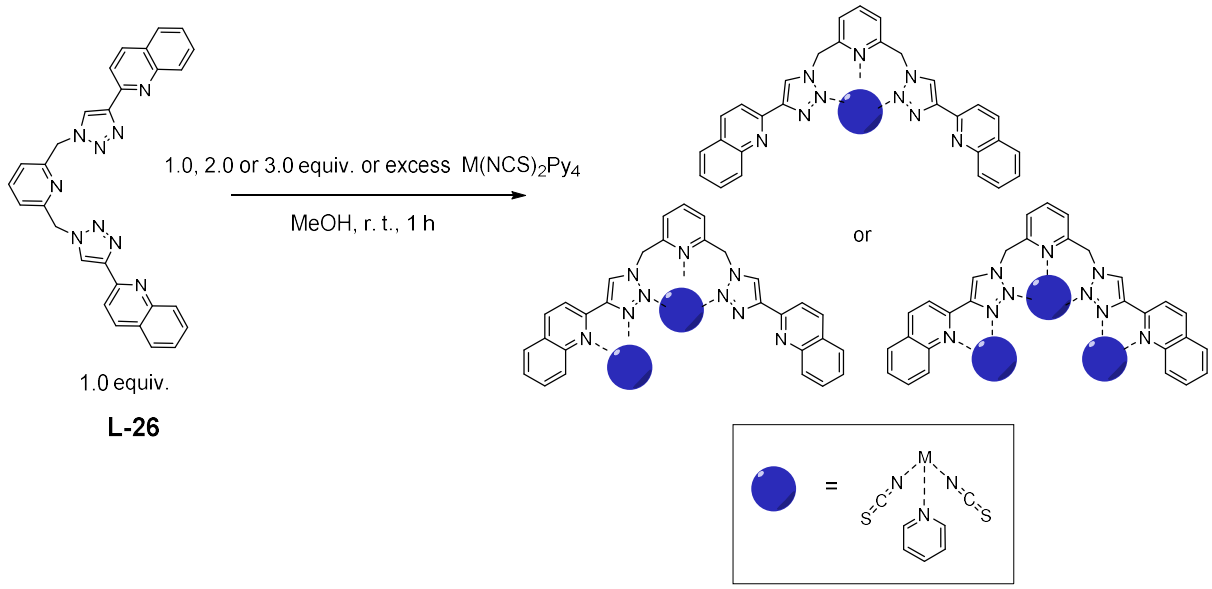

Scheme 24. Plan of synthesis to build mono- and bi- and trimetallic complexes.

Scheme 23 and 24 show the elaborated plan to synthesize new multi-metallic complexes and compare their activity with their mononuclear analogues to investigate cooperativity effects.

3.2.2.2 Synthesis

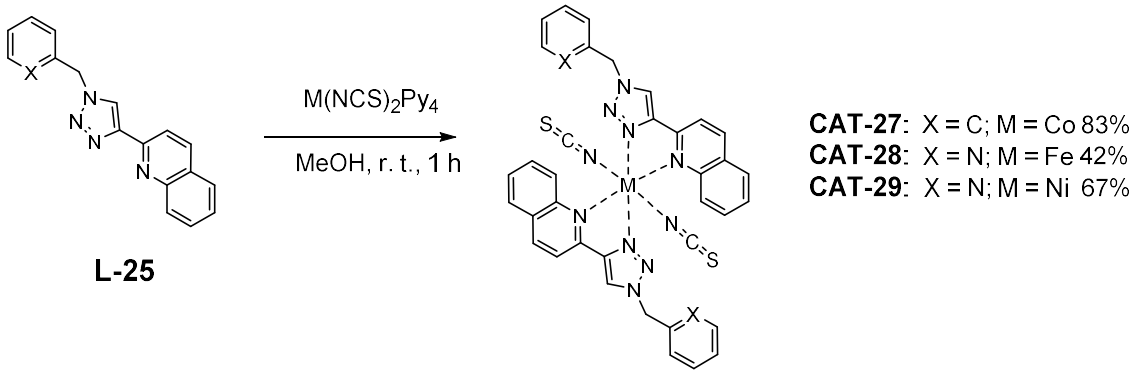

Scheme 25. Result of the planned synthesis with L-**25** forming new different mononuclear complexes.

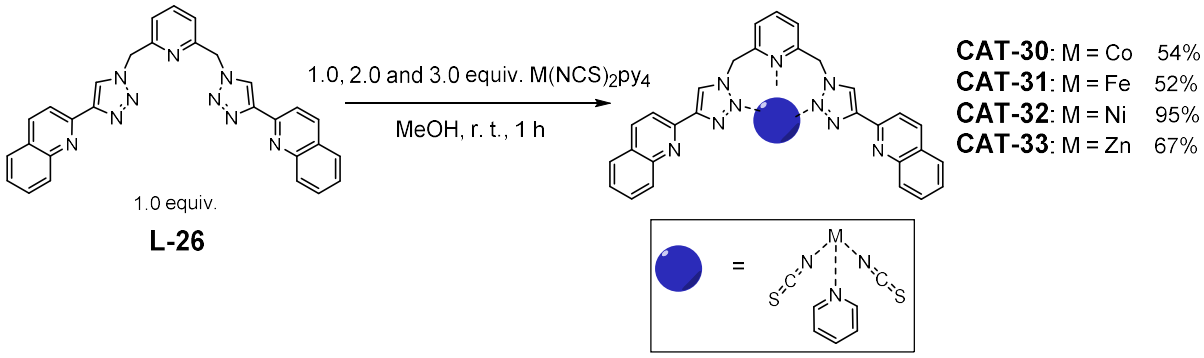

Scheme 26. Result of the planned synthesis with L-**26** only forming mononuclear complexes in the conditions employed.

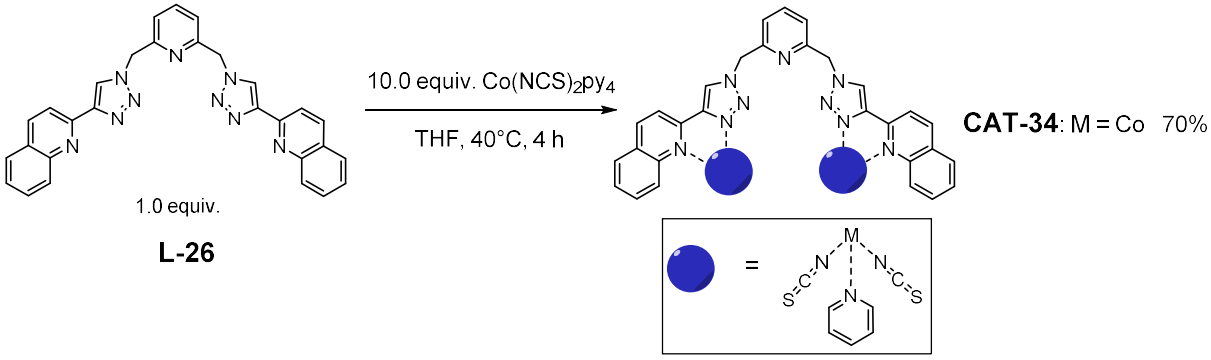

Scheme 27. Result of the planned synthesis with L-**26** only forming a bimetallic complex with the cobalt precursor.

When the ligand L-**25** was dissolved in MeOH to a solution of $Co(NCS)_2py_4$ was added, the monometallic homoleptic complexes CAT-**27**, CAT-**28** and CAT-**29** were obtained in good yields for Co and Ni (83% and 67% respectively) (Scheme 25), however the Fe CAT-**28** which is due to the more difficult purification using recrystallization. For the three of them, ESI mass measurement allowed to see the fragment $[M - NCS]^+$. A crystal suitable for X-ray for the cobalt CAT-**27** was also obtained (Figure 53) and shows the octahedral structure of the complex where the two NCS groups and no pyridine are coordinated to the metal. However, only CAT-**27** could be thoroughly purified and fully characterized, as it was the only one (among the complexes CAT-**28**- CAT-**29**) with a suitable solubility and stability in MeCN, under air atmosphere. The purification of the Fe and Ni complexes CAT-**28** and

CAT-**29** was challenging as the complete removal of the precursor could not be achieved (both precursor and products had the same solubilities and no crystals were formed under recrystallization).

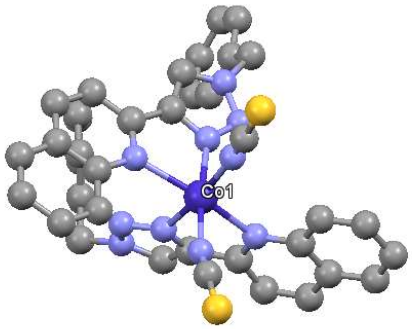

Figure 53. X-ray structure of CAT-**27**. Ellipsoid are shown at 50% probability and hydrogen atoms have been omitted for clarity. See **6.4** for individual values of the various bond distances and angles.

When dissolving the ligand L-**26** ligand in methanol in a 1:1 equivalent system with the metallic precursors (Scheme 26), one metal core was inserted still coordinated to both NCS and the pyridine. However, the very low solubility of the monometallic L-**26**-based complexes formed prevented the introduction of other metals in the structure, as it precipitated off the reaction mixture. Indeed, adding one, two or three equivalents of the metallic precursor to the ligand L-**26** led to the formation of the monometallic species for each of the metals employed, red powder for Fe CAT-**31**, light green for Ni, pink for Co and white for Zn, not soluble in MeCN or MeOH but soluble in DMF and DMA, which allowed them to be more easily purified by washing off the precursor with MeOH. The three complexes could be identified only by ESI mass where the fragment $[M - NCS - py]^+$ was observed and by elemental analysis (EA). Their solubility properties made their recrystallization into measurable crystals impractical.

Interestingly, with the cobalt precursor, changing the solvent to THF and slightly increasing the temperature to 40 °C led to the better solubility of the species and the formation of the bimetallic complex, where both metals are inserted in the quinoline–triazole part (Scheme 27). A purple powder was obtained after four hours of reaction and after washing the excess of precursor with acetone (comparison between the bimetallic and monometallic Co-based CAT-**30** and CAT-**34** in Figure 54).

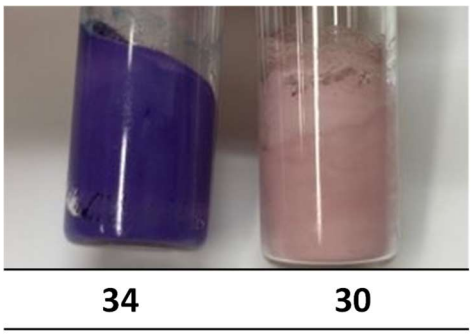

Figure 54. Pictures of the colored new cobalt complexes CAT-**34** and CAT-**30** in their solid state.

3.2.2.3 Characterization

3.2.2.3.1 X-ray Structure

The product CAT-**34** was analyzed by ESI mass where the fragment $[M\text{-}NCS\text{-}py]^+$ was observed and a crystal structure could also be obtained (Figure 55). In the crystal structure, it can be seen that the two arms of the pyridine [triazole + quinoline] twisted to form a pincer shape where both [triazole + quinoline] parts seem to pack with π-bond. The two planes formed by both [triazole + quinoline] (orange and light blue in the Figure 56) are quasi-parallel and distanced by 3.52 Å, in the range 3.3 – 3.8 Å described in the literature.[206] The powder obtained is soluble in DMF, DMA and warm THF.

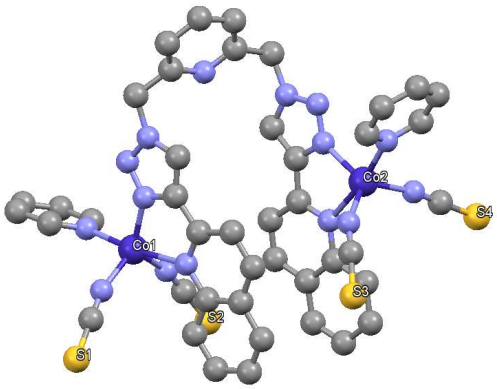

Figure 55. X-ray structure of the bimetallic complex CAT-**34**. Ellipsoid are shown at 50% probability and hydrogen atoms have been omitted for clarity. See **6.4** for individual values of the various bond distances and angles.

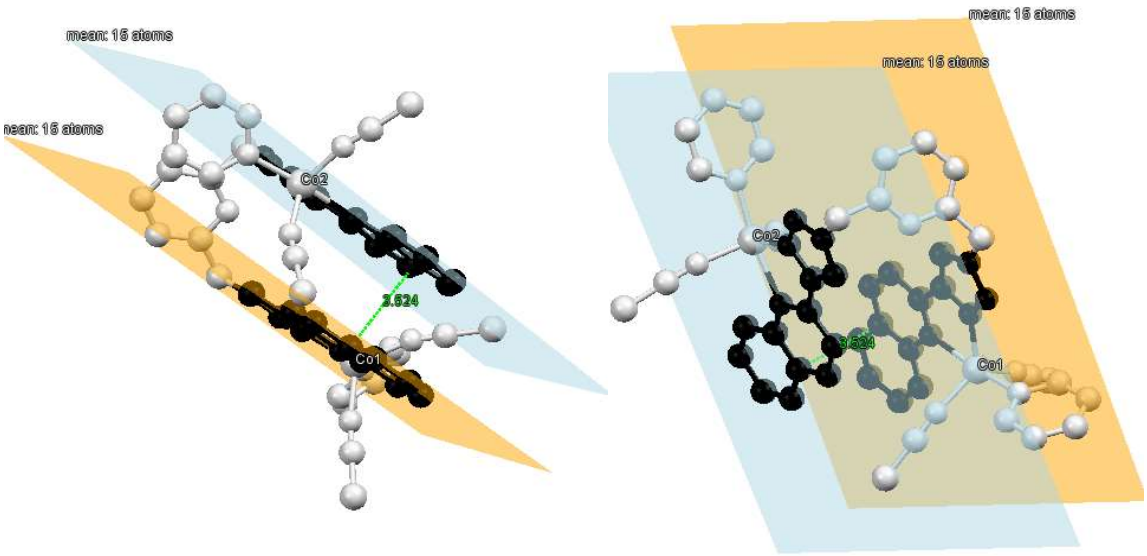

Figure 56. X-ray structure of CAT-**34** and evidence of π-bond using planes and distances. Ellipsoid are shown at 50% probability and hydrogen atoms have been omitted for clarity. See **6.4** for individual values of the various bond distances and angles.

3.2.2.3.2 Electrochemical Characterization

The new CAT-**27**, CAT-**30**, CAT-**31**, CAT-**32**, CAT-**33** and CAT-**34** complexes formed were characterized by cyclic voltammetry and differential pulse voltammetry to determine their redox potentials and ability to react with CO_2.

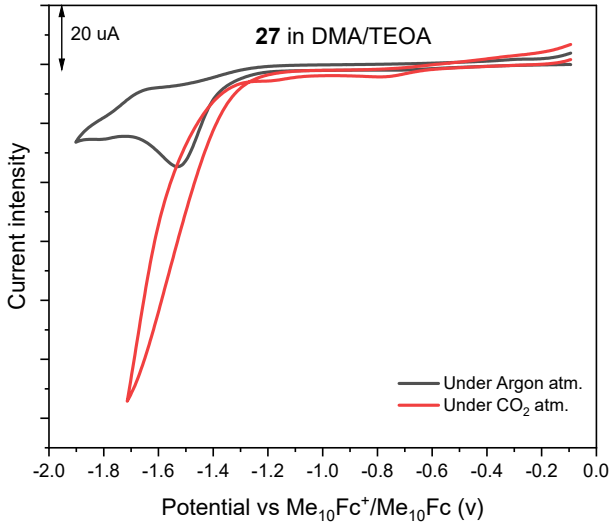

Figure 57. Cyclic voltammogram of CAT-**27** in DMA/TEOA, reported *vs* $Me_{10}Fc^{+}/Me_{10}Fc$, activation of CO_2 (red curve), , 0.1 M $TBAPF_6$, at 100 mV/s.

The new homoleptic Co CAT-**27** complex undergoes one visible non reversible reduction in DMA/TEOA at -1.53 V *vs* $Me_{10}Fc^{+}/Me_{10}Fc$ and a catalytic current at -1.32 V *vs* $Me_{10}Fc^{+}/Me_{10}Fc$ under CO_2 atm (Figure 57), showing that a reduced species reacts with CO_2. When comparing with CAT-**12**, the reduction potentials and the catalytic currents under CO_2 atm are very similar, suggesting a similar reactivity as a catalyst. However, the structure of the homoleptic complex CAT-**27** has a more stable configuration compared with the heteroleptic CAT-**12** complex. For the latter one, the pyridine is easily removable and, due to its low concentration, is unlikely to re-coordinate the metal after de-coordination, while the homoleptic CAT-**27** needs to either lose one NCS ligand by oxidation or, as in the homoleptic complexes case (CAT-**17** to CAT- **21**), undergo ligand distortion for CO_2 insertion, less favorable. The stability of CAT-**27** might be an issue in going through the whole catalytic cycle.

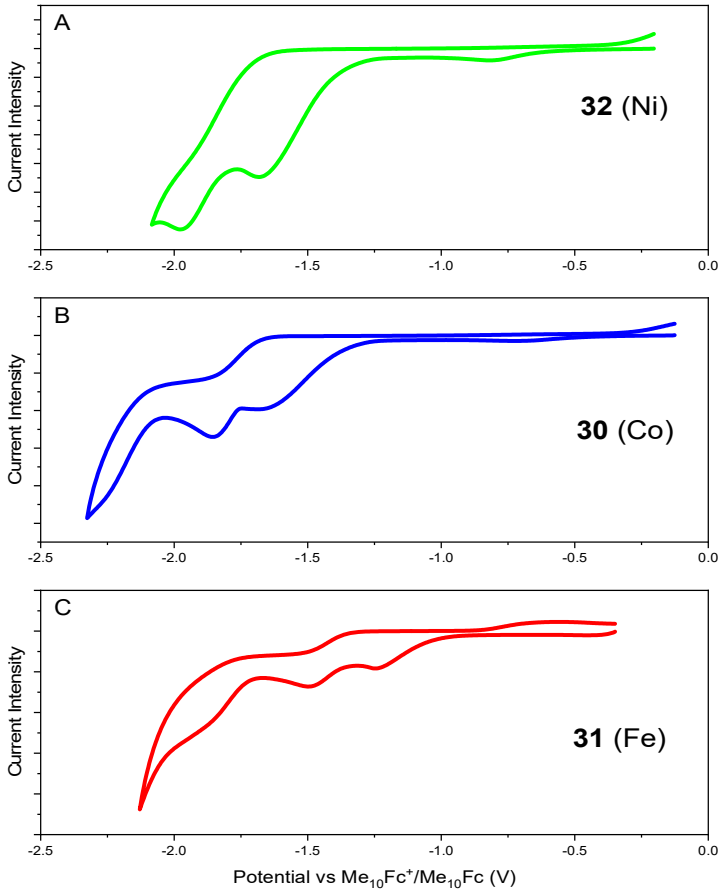

Figure 58. Cyclic voltammograms of CAT-**30**, CAT-**31** and CAT-**32** in DMA/TEOA, reported *vs* $Me_{10}Fc^{+}/Me_{10}Fc$, activation of CO_2 (red curve), , 0.1 M $TBAPF_6$, at 100 mV/s.

The cyclic voltammograms of CAT-**30** and CAT-**31** (Figure 58, B and C) show three visible reductions in DMA/TEOA at -2.26, -1.85, -1.65 V *vs* $Me_{10}Fc^{+}$/ $Me_{10}Fc$ while only two are visible for CAT-**32** -1.97 and -1.67 V *vs* $Me_{10}Fc^{+}$/ $Me_{10}Fc$ (Figure 58, A). The ligand L-**26** shows a very intense reduction at -2.10 V *vs* $Me_{10}Fc^{+}$/ $Me_{10}Fc$ (see Supplementary data **5.2**). The Fe complex CAT-**31** shows more positive reductions processes than the Co and Ni which makes it the easiest to reduce. The reduction processes of **32** are very similar to the two first reductions of **30**. In the DPVs shown in Figure 59, three reduction processes are observed for CAT-**31** (C) while only two are for CAT-**30** (B), CAT-**32** (A) and CAT-**33** (D). Both CAT-**30** and CAT-**32** have very similar reductions very close to each other at around -1.5 V and -1.7 V *vs* $Me_{10}Fc^{+}$/ $Me_{10}Fc$ while CAT-**31** shows the two consecutive reductions earlier at -1.44 V and -1.18 V, with a third lower reduction at -1.86 V *vs* $Me_{10}Fc^{+}$/ $Me_{10}Fc$. The DPV was also obtained for the complex with zinc CAT-**33** which showed similar behavior than the cobalt complex with two very close reductions at -1.63 V and -1.78 V $Me_{10}Fc^{+}$/ $Me_{10}Fc$. The small peak observed at -0.67 V *vs* $Me_{10}Fc^{+}$/ $Me_{10}Fc$ is attributed to the presence of oxygen. Under CO_2 atm, they all show CO_2 activation with visible catalytic currents at -1.43 V for CAT-**32** (Ni), -1.25 V for CAT-**30** (Co), -1.42 V for CAT-**31** (Fe) and -0.75 V *vs* $Me_{10}Fc^{+}$/ $Me_{10}Fc$ for **33** (Zn). For both Co and Ni complexes, the reaction with CO_2 is observed at the first reduction, while the Fe complex needs to be doubly reduced to react with CO_2. Moreover, one new reduction wave is visible for Ni and Fe under

CO_2 atmosphere at around -0.75 V *vs* $Me_{10}Fc^+/Me_{10}Fc$ which can be either attributed to the formation of new species or the presence of molecular oxygen. Interestingly, for the zinc CAT-**33** complex a very high catalytic current at the first reduction under CO_2 atmosphere was observed.

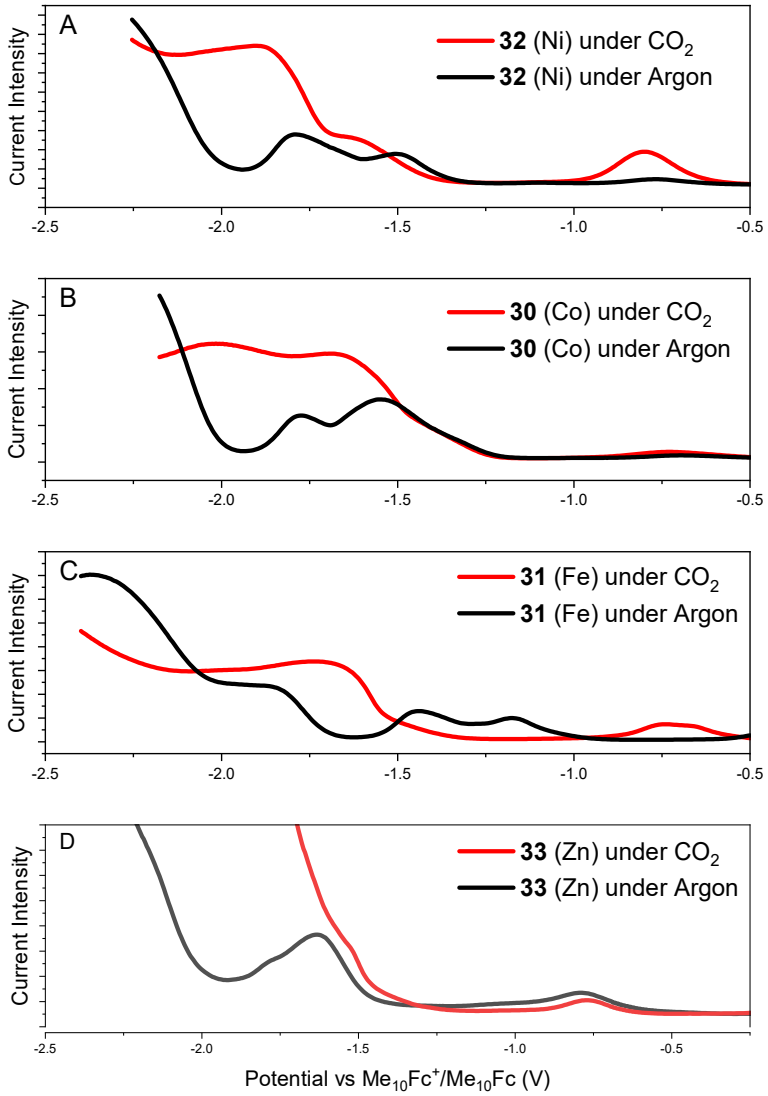

Figure 59. DPVs of CAT-**30**, CAT-**31**, CAT-**32** and CAT-**33** in DMA/TEOA, reported *vs* $Me_{10}Fc^+/Me_{10}Fc$, activation of CO_2 (red curve), , 0.1 M $TBAPF_6$.

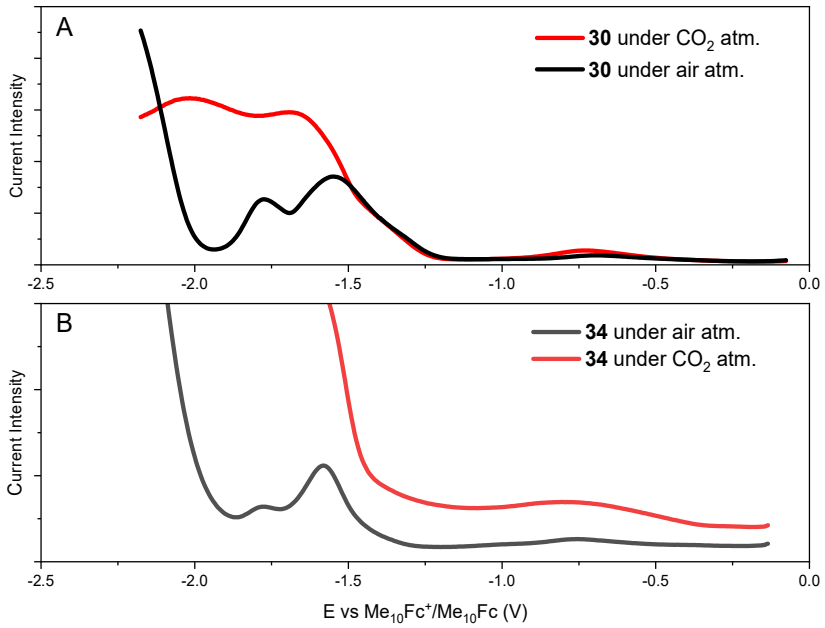

Figure 60. DPVs of the bimetallic Co CAT-**34** complex (B) and comparison with the monometallic analogue CAT-**30** in DMA/TEOA, reported *vs* $Me_{10}Fc^{+}/Me_{10}Fc$, activation of CO_2 (red curve), , 0.1 M $TBAPF_6$.

The DPV in DMA/TEOA of the bimetallic CAT-**34** in Figure 60 (B) shows very similar reductions compared with the monometallic CAT-**30** at -1.58 and -1.77 V *vs* $Me_{10}Fc^{+}/Me_{10}Fc$ (Figure 60, A). Under CO_2 atmosphere, the catalytic current is also observed at a very similar potential and after the first reduction, however, the ratio catalytic current/reduction current seems to be higher for CAT-**34** than for CAT-**30**, which could predict a better activity.

3.2.2.3.3 Photophysical Characterization

The absorption spectra of the new complexes in a mixture DMA/MeCN (1/50) show mainly high energy absorption band, likely due to ligand-based transitions, between 200 and 280 nm. All the presented complexes also show two smaller bands at 320 nm and 330 nm, also present in the ligand L-**26**. For all the Co complexes, a very small band is observed at 360 nm characteristic of the Co-NCS bond, not visible for the other M-NCS. (Figure 61 and 62)

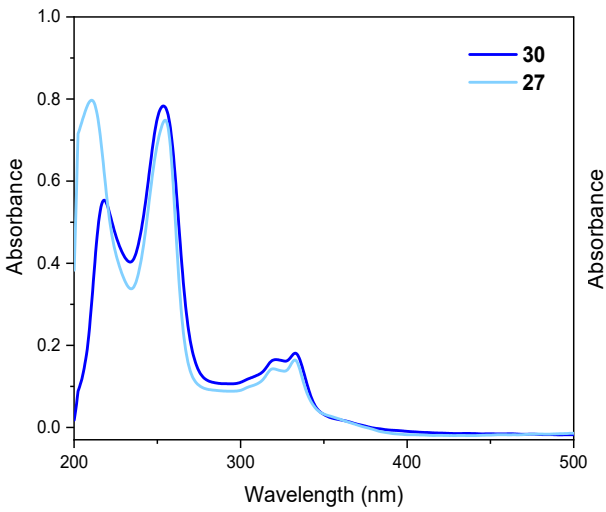

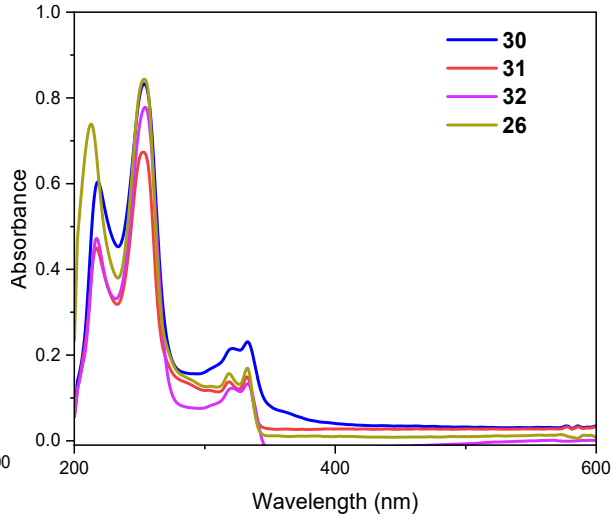

Figure 61. (Left) UV-vis absorption of CAT-**30**, CAT-**27** at 10^{-4} mM in DMA/MeCN.

Figure 62. (Right) UV-vis absorption of CAT-**30**, CAT-**31**, CAT-**32**, L-**26** at 10^{-4} mM in DMA/MeCN.

To investigate cooperativity effects using the monometallic CAT-**30** complex and the bimetallic CAT-**34** complex, the absorption spectra were recorded in MeCN (Figure 63). Both spectra are very similar with a slightly higher contribution of the Co-NCS for the bimetallic which was expected due to the second Co-NCS moiety. Moreover, in DMF, the ligand-based transitions result in a very high absorption band but a concentrated solution (>10 mM) allowed a small but a broad band at 610 nm to emerge, responsible for the blue color observed (Figure 64). No evident cooperative effect was thus observed by the UV-vis technique.

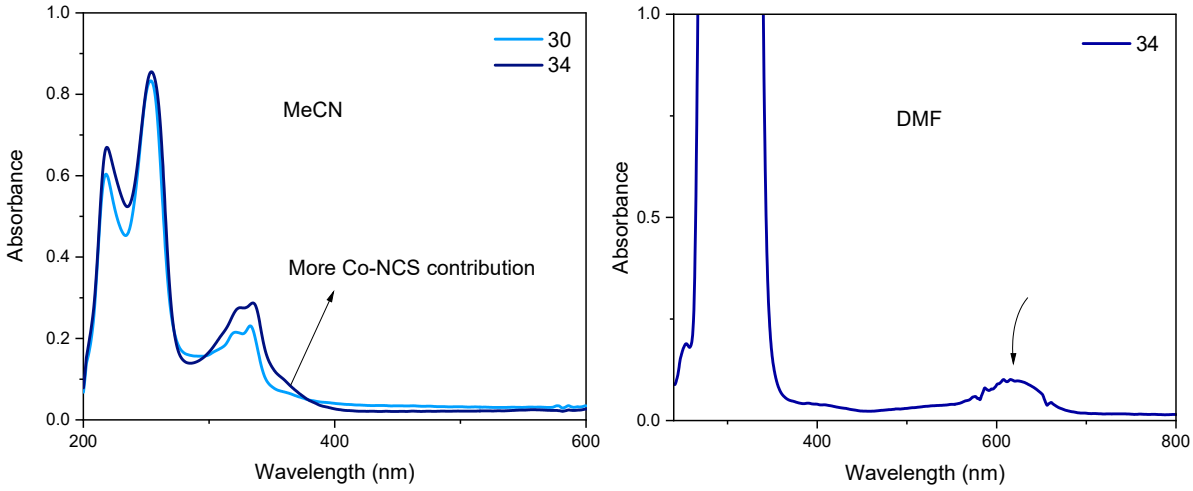

Figure 63. (Left) UV-vis absorption of CAT-**30**, CAT- **34** at 10^{-4} mM in DMA/MeCN

Figure 64. (Right) UV-vis absorption of CAT-**34** conc. in DMF.

3.2.2.3.4 Evans Tests

An Evans test was conducted with 3.0 mg of the bimetallic CAT-**34** in 0.5 mL THF-d_8 ([CAT-**34**] = 0.00598 mol/L) giving a chemical shift of the THF signal of 204 Hz (0.51 ppm) (see Supplementary data **5.3**). The calculated μ_{eff} was found at 7.01 Bohr magneton, which correlates with a total number of unpaired electrons of six, coherent with the presence of two Co^{II} metal-centers with three unpaired electrons each.

3.2.2.4 Photocatalytic Tests

All the L-**26**-based complexes were tested as catalyst for CO_2 reduction in DMA/TEOA except the iron complex CAT-**31** that was tested in MeCN/TEOA due to the previous results obtained showing higher activity for Fe-based complexes in this solvent (Table 20). Interestingly, using 0.1 mM of CAT, CAT-**31** gave the best results in MeCN with TON_{CO} 30 and Sel.CO of 60% (Table 20, Entry 2) while in DMA/TEOA, CAT-**30** did not show the expected similar activity as its analogue CAT-**12** (Table 20, Entry 1). Indeed CAT-**30** formed CO with a TON of 28 but almost three times more H_2 (TON_{H2} = 84). Similarly to the other Ni complexes presented herein, the Ni complex (CAT-**32**) did not show any CO production but only H_2 (TON_{H2} 24; Table 20, Entry 3). The Zn analogue CAT-**33** produced little CO (TON_{CO} 15) but a very high amount of H_2 (TON = 411; Table 20, Entry 4). This zinc complex could be further developed for H_2 production as its selectivity and activity are very high.

A possible explanation for the poor activity and selectivity compared with their L-**6**-based analogues is that the L-**26**-based complexes can coordinate another ligand molecule **26** leading to a more stable complex CAT-**35** ([L-**26**-Co$(NCS)_2$-L-**26**], see Experimental **6.2**). Indeed, the complex CAT-**30** dissolved in MeCN also shows a mass at 1108 *m/z* for the rearranged fragment [L-**26**-Co(NCS)-L-**26**]. This complex might allow a less favorable CO_2 insertion.

Moreover, the homoleptic CAT-**27** complex showed less good results in DMA/TEOA with formation of CO (TON 14.1) and twice more H_2 (TON_{H2} 35), which can also be explained by the stability of the complex disfavoring the CO_2 insertion.[168] (Table 20, Entry 6)

Table 20. Photocatalytic results with the new L-**26**-based CAT and PS-**24** in solvent/TEOA 5:1 v/v [a]

Entry	CAT	Time	CO /µmol	H_2 /µmol	TON_{CO}	TON_{H2}	Sel.CO	solvent
1	**30**	4h	4.4	17.7	11	43	20%	DMA
2	**31**	4h	12.1	6.2	30.1	15	66%	ACN
3	**32**	4h	0	9.7	0	24	-	DMA
4	**33**	4h	6.2	165	15.5	411	3%	DMA
5	**34**	4h	15.6	48.5	39	121	24%	DMA
6	**27**	4h	5.64	14	14,1	35	28%	DMA

[a] The experiments were performed with 20 mM BIH and 1.0 mM PS-**24** under CO_2 atmosphere at 22 °C and the products were measured by GC after 4 h irradiation at 420 nm. The products formed were analyzed from the headspace by GC.

In the crystal structure of the bimetallic cobalt CAT-**34** complex, the two metals are pointing towards different directions, thus, cooperation by synergistic roles might be prevented. Nevertheless, one could expect that the π-stacking of the quinoline-triazoles moiety allows faster or stronger electronic transfers between the two cobalt cores during reduction from PS. Moreover, the position of the two pyridines, sites of CO_2 insertion after de-coordination, are nicely accessible because they are facing the exterior with less steric hindrance. The bimetallic CAT-**34** complex shows indeed a three times better activity for CO production than the monometallic CAT-**30** with a TON of 39 after 4 hours. The production of molecular hydrogen also triples using the bimetallic complex with a better selectivity for H_2 than for CO (Sel.H_2 of 75%). Cooperativity between the two Co might be an explanation for the three-fold better activity and further analysis together with theoretical calculation would be needed to confirm this hypothesis and to understand the mechanism involved.

Interestingly, the complex CAT-**33** (Zn) shows very promising results for H_2 production with a TON of 411 and a very good H_2 selectivity of 96%. It can thus be considered as a hydrogen evolution catalyst (HEC) and should be further characterize to optimize it and understand its mechanism. Moreover, very few zinc complexes were reported to be active catalysts for CO_2 reduction[207], among them an example producing CO with outer-sphere CO_2 absorption on a phosphine-based ligand structure.[110]

3.3 TRINUCLEAR FE COMPLEX AND ITS MAGNETIC PROPERTIES

Introduction. Trinuclear molecular catalysts were scarcely reported for CO_2 reduction and are often Ru- or Re-based PS associated with a metallic catalyst forming photocatalyst (PC).[70] Commonly, the molecular catalysts reported for CO_2 reduction are mononuclear, binuclear or multinuclear (>3 metallic centers).[208] In this work, when a different synthesis strategy was employed to form the mononuclear heteroleptic compound **6**-based (section 3.2.1.2) using a different Fe precursor $Fe(NCS)_2$, an unexpected trimetallic complex (CAT-**36**) was observed. The species was only detected with Fe as metal and its structure was determined by X-ray thanks to measurable crystals obtained. The trimetallic CAT-**36** complex was synthesized in a glovebox and rapidly turned red under an air atmosphere.

3.3.1 Synthesis

The precursor $Fe(NCS)_2$ was synthesized according to the literature.[209] In a glovebox, $Fe(SO_4)$ (1.00 equiv.) was dissolved in 3.0 mL of dry-degassed MeOH, and $Ba(NCS)_2$ (1.00 equiv.) was then added to the solution. The light yellow mixture was stirred at 22°C for 30 minutes and the precipitate $Ba(SO_4)$ was filtered off (equation 17). The 3 mL mixture was then filtered and used without any further purification or evaporation. Considering a 100% conversion and yield (lit), the adequate volume of $Fe(NCS)_2$ solution was added to a vial. To this vial, a solution of L-**6** to reach a one-to-one equivalent system was dissolved in MeOH and added dropwise and the mixture and stirred at room temperature for 1 hour (Scheme 28). The solution was then evaporated under a Schlenk line and the powder was recrystallized by slow diffusion of Et_2O in MeCN in which it was highly soluble. The suitable for X-ray light yellow crystals were collected with a yield of 42%. The product CAT-**36** obtained was kept and stored in the glovebox as powder because when it was put in contact with air, it turned red in matter of seconds, in a solid form or dissolved in MeCN. However, dissolved in methanol or in TEOA, the product kept its light yellow color under air atmosphere.

$$Fe(SO_4), H_2O + Ba(NCS)_2 \xrightarrow[\text{argon, r.t. 30 min.}]{\text{MeOH}} Ba(SO_4) + Fe(NCS)_2 \qquad (17)$$

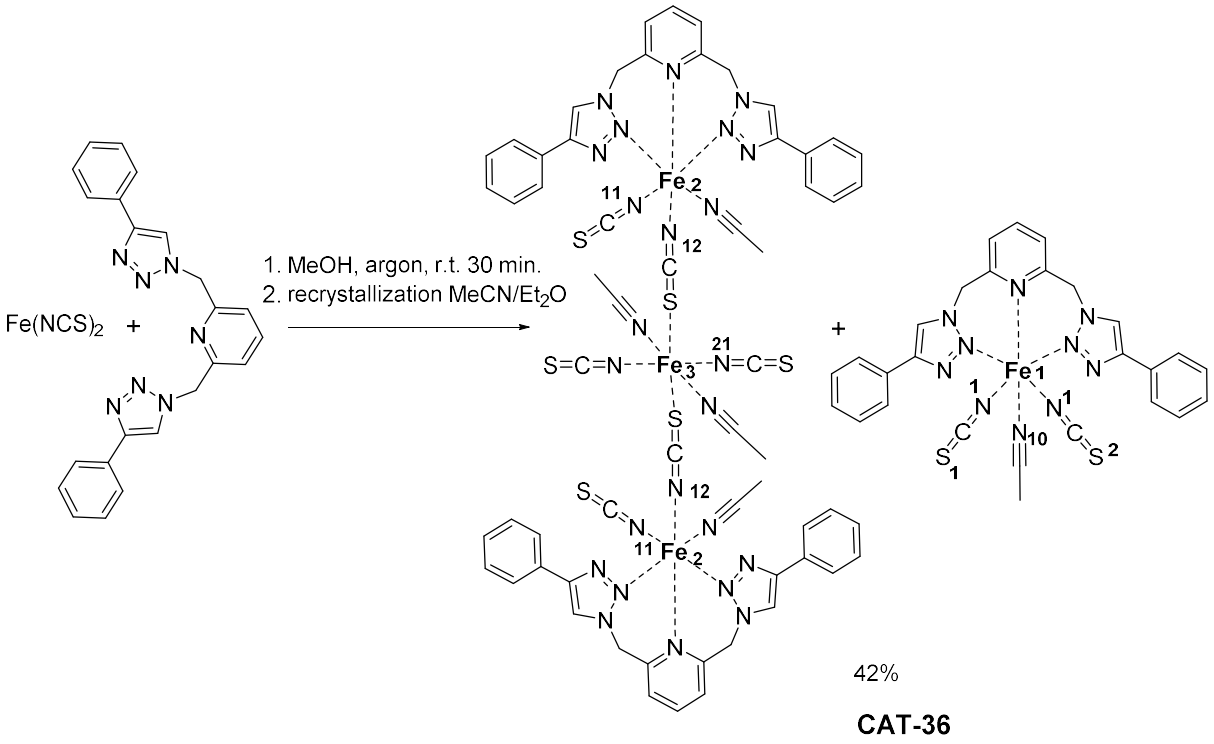

Scheme 28. Synthesis of the trinuclear iron-based complex co-crystallizing with the mononuclear analogue species

3.3.2 Characterization

3.3.2.1 X-ray structure

X-ray measurement allowed to determine the structure of the product obtained, a co-crystallized trinuclear Fe complex with a monometallic complex named CAT-**36** (Figure 65). Four different reaction conditions using different equivalents of precursors ($Fe(NCS)_2$/L-**6**: 1/1, 2/1, 3/1 and 1/3) gave the exact same X-ray structures with co-crystallization of the two species (trimetallic + monometallic) in MeCN. In the mononuclear complex, the sixth coordination of the octahedral is taken by the recrystallization solvent MeCN, which also coordinates the trimetallic structure. The three Fe nuclei are linked through bridging NCS groups and the two external Fe coordinates one ligand L-**6** while the central Fe is a molecule of starting material $Fe(NCS)_2$ with two MeCN and coordinating two NCS bridging groups. The three iron atoms Fe(2), Fe(2) and Fe(3) are distances by exactly 6.069 Å from each other and Fe(1) from the monometallic complex is 7.643 Å away from the exterior Fe(2) of the trimetallic complex and 8.353 Å away from the internal Fe(3) of the trimetallic complex (Figure 66). Concerning the bonds Fe-NCS (Figure 67), the external Fe(2)-N(11)CS of the trimetallic complex bonds measure 2.077 Å while the internal Fe(3)-N(21)SC bonds are shorter and measure 2.065 Å. The bridging NCS have Fe(2)-N(12)CS bonds slightly weaker and measure 2.079 Å. The MeCN ligand bonding Fe_2 through the nitrogen are 2.189 Å long for both external Fe while they are stronger with 2.162 Å for the internal Fe(3). Compared with the monometallic, the bond Fe(1)-NCC is much weaker with 2.213 Å while the

bonds Fe(1)-(N(1)CS)(1) and Fe-(N(2)CS)(2) are 2.075 Å and 2.092 Å. The bonds with the bridging sulfur Fe(3)-S(4) are much longer with 2.625 Å.

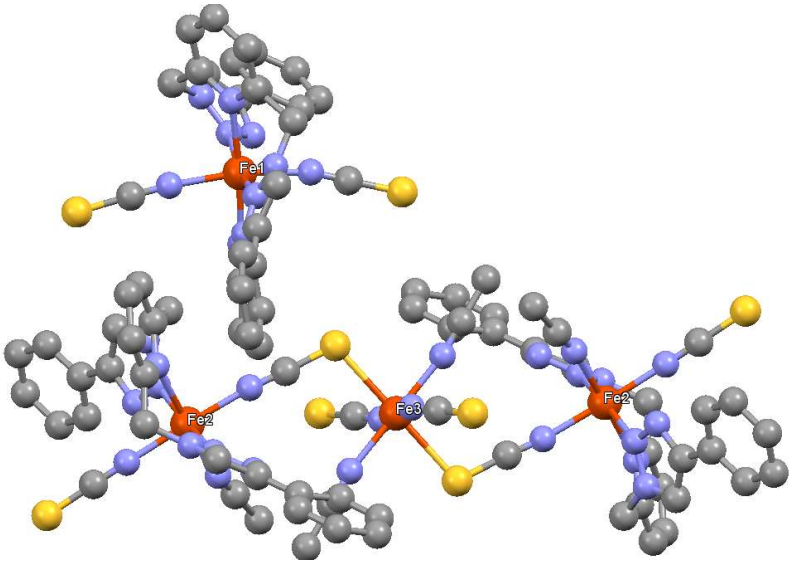

Figure 65. X-ray structure of CAT**-36**, a trinuclear Fe complex co-crystallizing with a mononuclear Fe species. Ellipsoids are shown at 50% probability and hydrogen atoms have been omitted for clarity. See **6.4** for individual values of the various bond distances and angles.

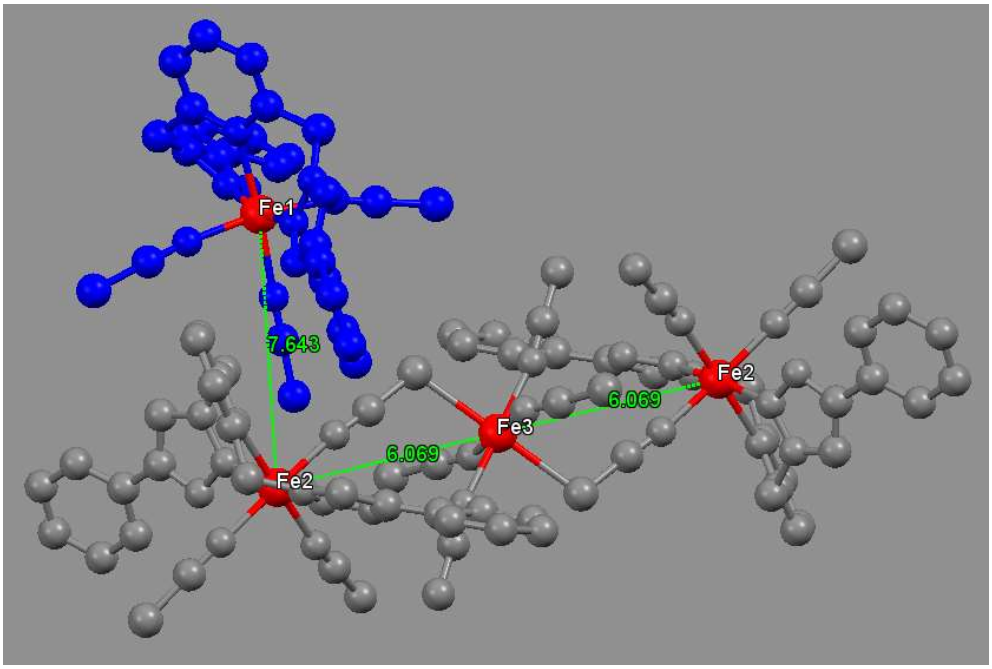

Figure 66. X-ray structure of CAT-**36**, distances between the Fe atoms. Ellipsoids are shown at 50% probability and hydrogen atoms have been omitted for clarity. See **6.4** for individual values of the various bond distances and angles.

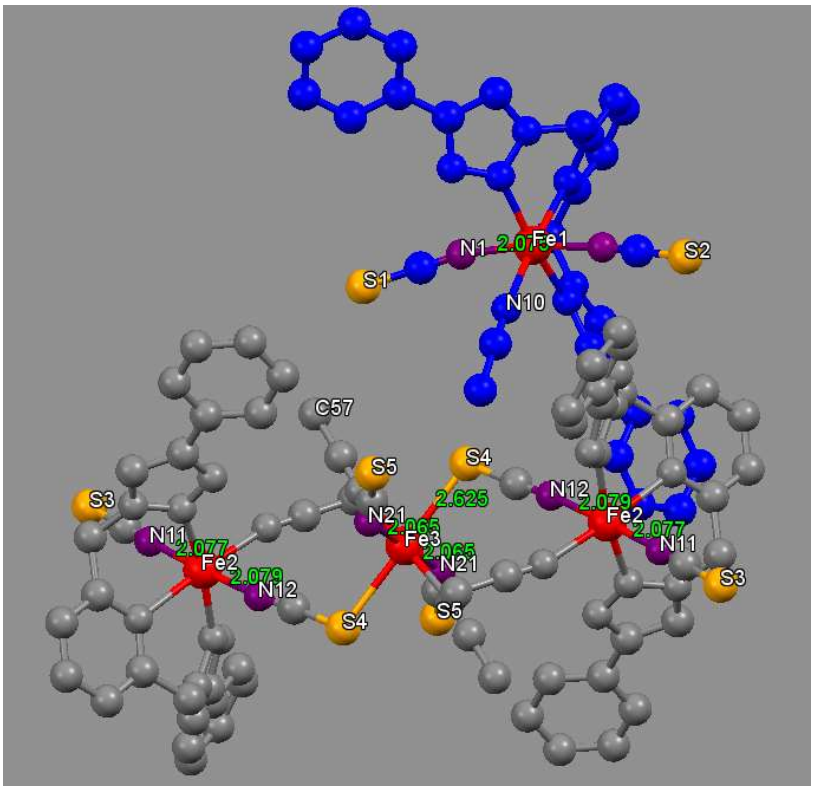

Figure 67. X-ray structure of CAT-**36**, Fe-N and Fe-S distances. Ellipsoids are shown at 50% probability and hydrogen atoms have been omitted for clarity. See **6.4** for individual values of the various bond distances and angles.

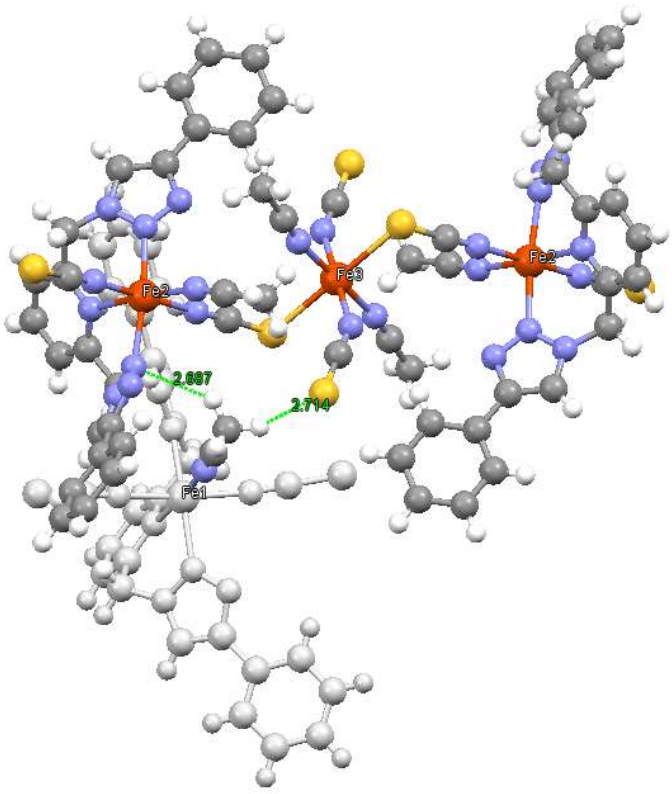

Figure 68. X-ray structure of CAT-**36**, H-bond evidence between the mononuclear species (white) and the trinuclear complex. Ellipsoids are shown at 50% probability and hydrogen atoms have been omitted for clarity. See **6.4** for individual values of the various bond distances and angles.

Hydrogen bonds are visible between the monometallic and trimetallic complexes (Figure 68), the protons from the MeCN of the monometallic form H-bonds with the nitrogen of the triazole of the external Fe of the trimetallic complex and the other proton form an H-bond with the not bridging **S**CN of the internal Fe of the trimetallic complex (bond length of 2.687 Å and 2.714 Å).[210] The monometallic and trimetallic complexes are also linked through π-stacking between the benzene of L-**6** of the monometallic and the pyridine of L-**6** of the external Fe of the trimetallic complex, with both their centroid spaced from 3.730 Å (Figure 69).[206]

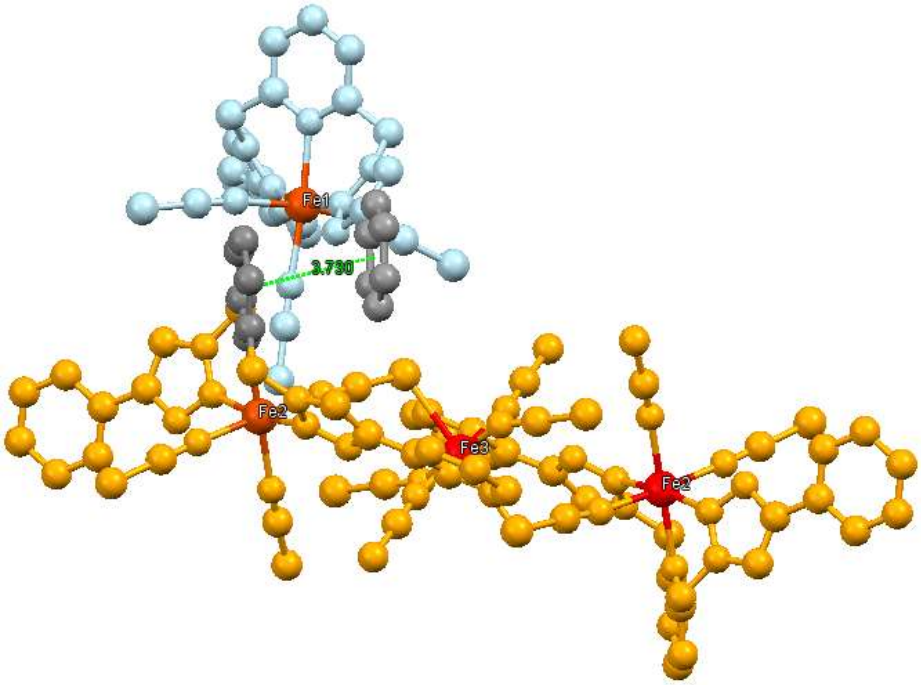

Figure 69. X-ray structure of CAT-**36**, π-stacking evidence between the mononuclear species (light blue) and the trinuclear complex (orange). Ellipsoids are shown at 50% probability and hydrogen atoms have been omitted for clarity. See **6.4** for individual values of the various bond distances and angles.

The same synthesis with $Ni(NCS)_2$ was also conducted in the exact same way as with Fe and only a monometallic species (CAT-**37**) (Figure 70), without multi-metallic species, was obtained. A suitable crystal for X-ray was obtained with Ni, and even after recrystallization in $MeCN/Et_2O$, a molecule of methanol from the solvent of the reaction in the sixth coordination was observed. Methanol seems to act as an "L" type ligand without inducing oxidation of the Ni center as the proton on the oxygen is visible and the bond length Ni-N are all in average 2.1 Å which predicts a Ni^{II} HS.[211] Moreover, the bond length Ni-OMe in the case of Ni^{III}-OMe generally measure 1.88 Å[212] while for CAT-**37** the bond is much weaker with 2.84 Å. Contrary to its iron analogue, this Ni complex was stable under air.

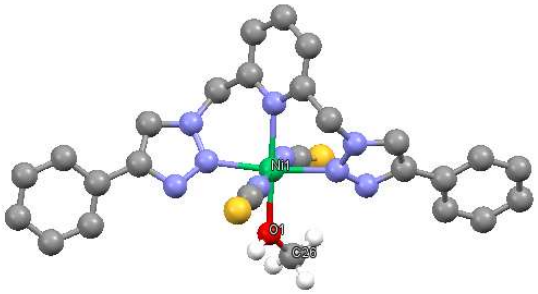

CAT-**37**

Figure 70, X-ray structure of CAT-**37**. Ellipsoids are shown at 50% probability and hydrogen atoms have been omitted for clarity. See **6.4** for individual values of the various bond distances and angles.

3.3.2.2 Magnetic Properties

To investigate any cooperativity effects, variable-temperature magnetic susceptibility (χ or "Chi") studies can be conducted to determine if the sample is para- or diamagnetic and undergoes magnetic coupling, spin cross over and other properties. ChiT plots show the magnetic susceptibility in function of the temperature and were recorded in the groups of Prof. Ruben and Prof Fink. The variable-temperature magnetic susceptibility studies were carried out on crystalline samples in the temperature range 2 to 300 K and in an applied field of 1000 Oe, for the trimetallic co-crystallized with the monometallic complex (CAT-**36**), the monometallic analogue CAT-**11**, and for a doped CAT-**11** with CAT-**16** (Zn) (10% Fe). This measurement was also conducted on the Ni complex CAT-**37**.

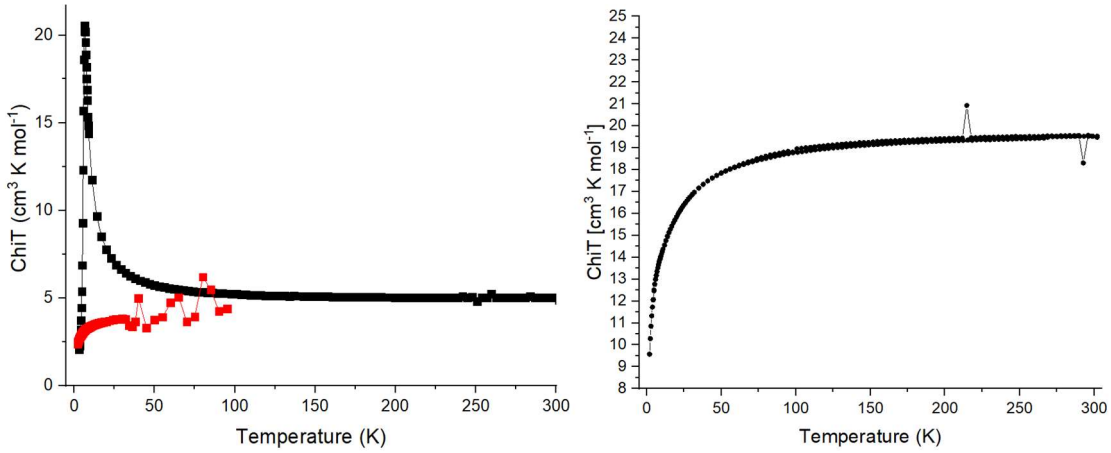

Figure 71. Left: ChiT plot of the monometallic CAT-**11** (black curve) and CAT-**11** dopped with Zn (CAT-**16**) (red curve) Right: ChiT plot of the co-products CAT-**36** with trinuclear and mononuclear species.

The monometallic CAT-**11** complex shows unexpected behaviors with a high increase of magnetic susceptibility upon cooling below 50K with a maximum at 12K (black curve, Figure 71, left) followed by an abrupt descrease at lower T (5-2K), which could be attributed to ferromagnetic properties. To understand if the alignment of the electrons is coming from intramolecular Fe due to the unkown presence of multi-metallic entities or due to the coupling between Fe ions of neighbouring molecules, another sample of CAT-**11** doped with CAT-**16** (Zn) (10% Fe) was recrystallized and also analyzed

(red curve, Figure 71, left). The behavior is completely different with a stable magnetic susceptibility in function of the temperature, as expected by the diamagnetic nature of Zn and which indicates that the ferromagnetic behavior would be due to a small dipolar coupling between the Fe ions of neighbouring molecules.[213] However, this behavior is surprising, seeing that the distance between two Fe ions of two molecules is quite long to expect to couple in the X-ray structure (8.651 Å) and further investigations are necessary for correct understanding. Surprisingly, the ChiT of the trimetallic-monometallic CAT-**36** crystals shows a different behavior with no ferromagnetic properties. Upon cooling, the χT values decrease slowly between 300 and 50 K and very quickly between 50 and 2 K, reaching a minimum value of 10 $cm^3K\ mol^{-1}$ at 2 K, indicating the presence of a weak antiferromagnetic exchange interaction between the Fe^{II} ions. The χT values for both CAT-**11** and CAT-**36** are too high compared to the simulated ones and would need to be repeated for further calculations. This can be due to low purity of the sample or small error measuring the exact mass of the sample. In our case, it the measured mass was recorded with imprecision due to the quality of the scale and the difficulty of measuring inside the glovebox. Moreover, the crystalline samples were all measured after several recrystallizations.

With this environment, spin cross-over from HS to LS on lowering the temperature could have been expected[214] but was not observed in the trimetallic species CAT-**36**, which prevents easy detection of cooperative effects between the Fe atoms.

A ChiT graph could also be obtained for the CAT-**37** (Ni), which shows the expected paramagnetic nature of Ni^{II} without any further coupling between the neighbouring molecules. (Figure 71)

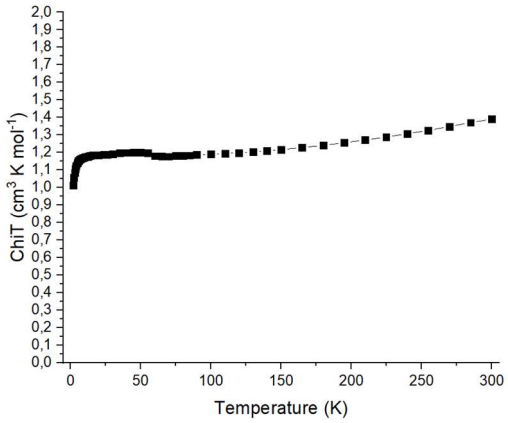

Figure 72. ChiT plot of the monometallic CAT**-37**

BVS analysis was conducted by Dr. Christoph Anson in the group of Prof. Powell on the trimetallic complex of the species CAT-**36** and the three Fe came out as: (for HS Fe^{II})

Fe(1) 1.964
Fe(2) 1.983
Fe(3) 1.929

With R(ij) for HS-Fe^{II}-N = 1.753, and for Fe^{II}-S = 2.125, both with B = 0.37, from the literature.[215]

3.3.3 Photocatalytic tests

The new species CAT-**36** was employed as CAT (0.1 mM) for CO_2 reduction with the known PS-**24** in MeCN/TEOA. It produced CO with a TON of 77.1 and a low selectivity of 57% after four hours (Table 21, Entry 1). No cooperativity effect in terms of catalytic results was observed compared with the monometallic CAT-**11** species as lower product formation and lower selectivity were observed. Indeed, this complex is thought to be trinuclear only in solid state and to decompose when dissolved in MeCN into mononuclear species mixed with Fe(NCS)(MeCN) fragments, lowering the catalytic activity and selectivity. Nano-ESI measurement of the trimetallic compound dissolved in MeCN showed different species in solution with a predominant fragment of 900 g/mol for $[(L\text{-}\mathbf{6})_2Fe(NCS)]^+$ with no characteristic mass observed from the trimetallic complex (Figure 73).

Table 21. Photocatalytic results with **36** as CAT and **24** as PS in MeCN/TEOA 5:1 v/v [a]

Entry	[CAT]b	CO /µmol	H_2 /µmol	TON_{CO}	TON_{H2}	Sel.CO
1	**36**	30.8	23.6	77.1	59	57%

[a] The experiment was performed with 20 mM BIH and 1.0 mM PS-**24** under CO_2 atmosphere at 22 °C and the products were measured by GC after 4 h irradiation at 420 nm. The products formed were analyzed from the headspace by GC.

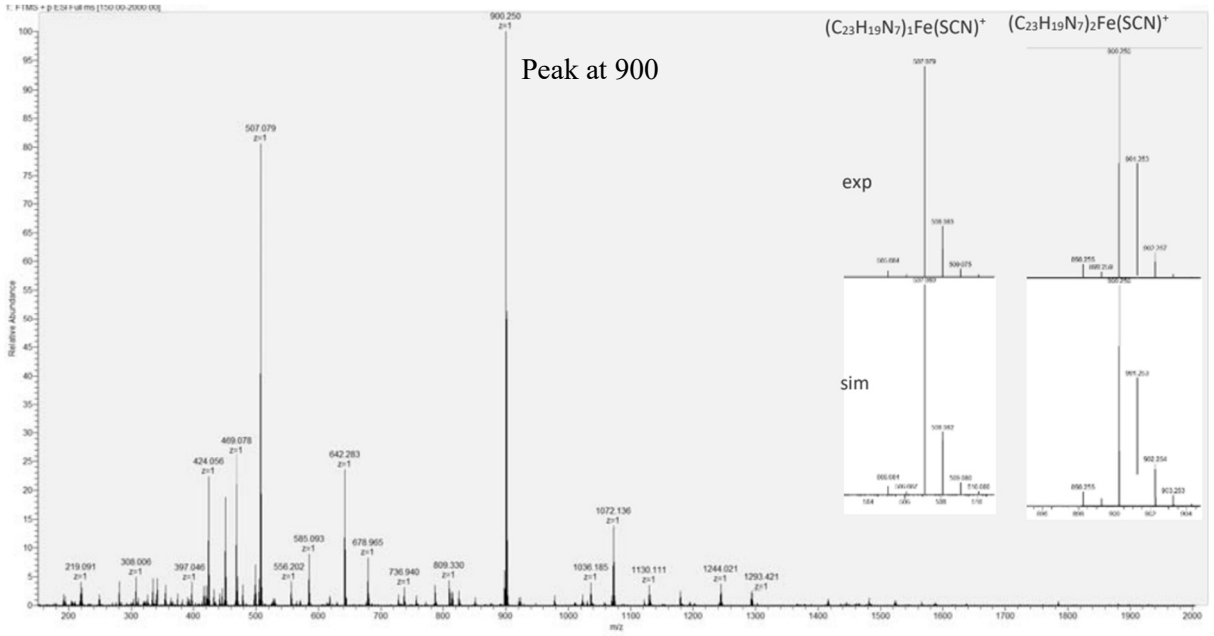

Figure 73. Nano-ESI measurement of CAT-**36** dissolved in MeCN.

3.4 PHOTOCATALYSTS DESIGNS

3.4.1 Introduction

Several systems were proposed in the literature with both the catalyst and the photosensitizer linked to form a photocatalyst (PC), either covalently, ionically, through H-bonds or π-π stacking. In some cases, the cooperativity effect could be detected with greater results obtained with the photocatalyst than with the catalyst and PS separated from each other and acting alone. This positive cooperativity effect is the sought-after effect. However, most of the photocatalysts reported employ rare and expensive metals, either in the PS part or the CAT part, or in both.[54, 134-135, 216-218]

In fact, very few systems were reported containing earth-abundant metals in the photocatalyst structure[219] and, to the best of our knowledge, none with positive cooperative effect.

This part aims at forming earth-abundant-based supramolecule to reach an efficient PC and investigate any cooperativity effects when the efficiency is enhanced compared with the individual species. New designs were proposed using precedent structures of this work and using new moieties involving phosphine ligands.

3.4.2 Evolution of the Bichelating Ligand based on Meta-xylene (PS-4)

Using the previous results from this work, and striving for the design of new earth-abundant based multi-metallic photocatalysts, a strategy involving the structure of PS-**4** was followed. Indeed, thanks to the observation of the X-ray structure of the already proven PS-**4**, a pocket could be observed, where another metal acting as a catalyst site could be inserted. To do so, the first step was to replace the non-coordinating central benzene with a coordinating pyridine to form L-**26** (Scheme 29).

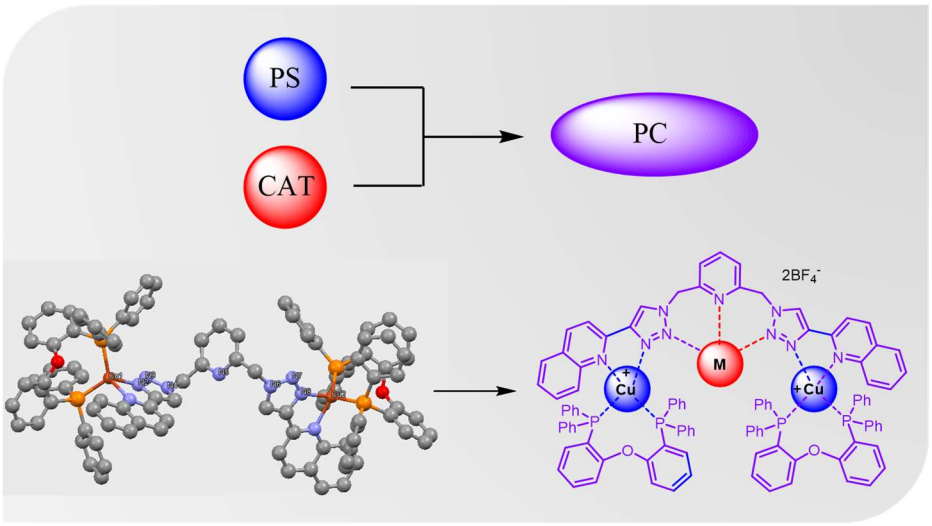

Scheme 29. Plan to design a new earth-abundant-based photocatalyst using L-**26**

3.4.2.1 Synthesis

The synthesis of L-**26** was approached identically as with the benzene ligand by using the 2,6-bis(bromomethyl)pyridine instead of the benzene reagent with a yield of 81%. The ligand L-**26** was then complexed with two equivalents of Cu(DPEPhos)$(MeCN)_2$ as previously described. The bimetallic copper complex was then dissolved in methanol with different iron precursors, and the precipitate was analyzed. When the homemade prepared $Fe(NCS)_2pyr_4$ was employed, the reaction did not lead to the desired product. Instead, the degradation of the Cu complex occurred by forming a Cu thiocyanate complex [Cu-NCS-Cu] (**38)** (Figure 74 Left). The DPEPhos-Cu moiety de-coordinated from the ligand L-**26** and formed instead a bridged SCN complex. This product was also observed changing the order of addition of the components (first adding the metal precursor with L-**26** and then addition of the Cu-DPE moiety). Furthermore, the analogue DPEPhos bridged with a Cl [Cu-Cl-Cu] (**39**) was also formed when using a different chloro-metallic precursor (Figure 74 Right). Similarly, with a bromide precursor, a Br-bridge complex was also observed [Cu-Br-Cu] (**40**) with Nano-ESI measurement (Figure.75).

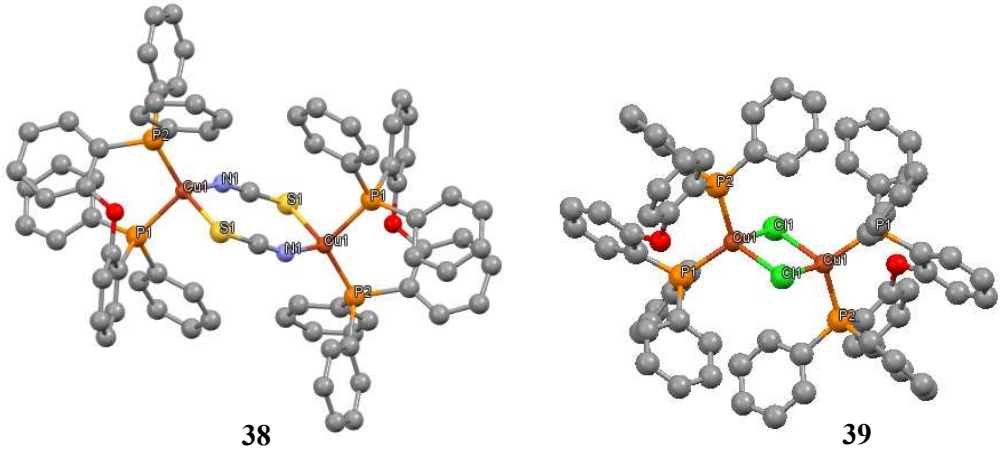

Figure 74. X-ray structures of **38** and **39** obtained as product. (Crystallography data in section **6.4**)

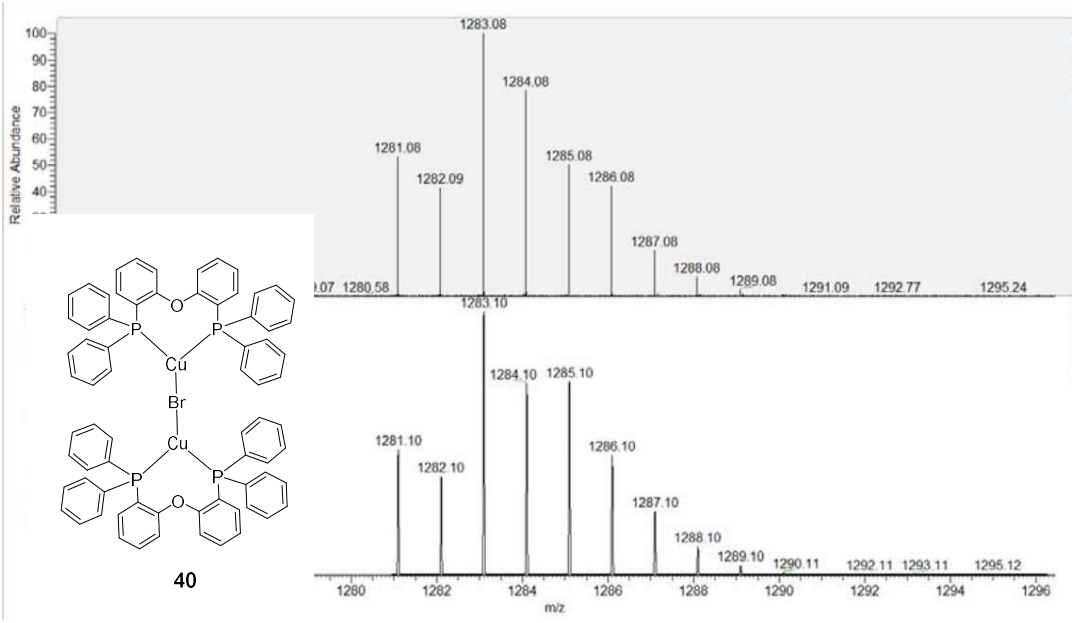

Figure 75. Nano-ESI measurement showing the presence of **40**.

Those three compounds (**38**, **39** and **40**) were reported and are known for their phosphorescence properties and long excited lifetimes of 1 µs that made them interesting for luminescent devices such as OLEDs.[220-221]

To prevent the formation of those complexes, perchlorate precursors that possess no halides or pseudohalides were tested. One equivalent of the ligand L-**26** was dissolved in acetonitrile and mixed with one equivalent of $Co(ClO_4)_2$. The more stable homoleptic complex **41a** was formed with a mass of 1148,2653 for $[M\text{-}ClO_4]^+$ seen with ESI (1148,2651 calc.) and the doubly charged $[M\text{-}2ClO_4]^{2+}$ with a mass of 524,6582 (524,6581 calc.) (Scheme 30).

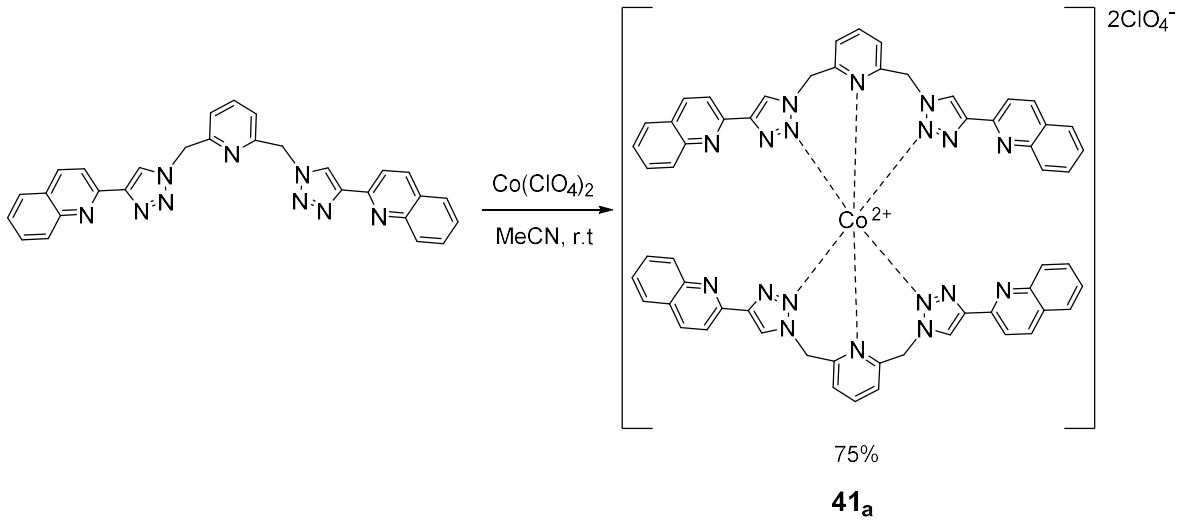

Scheme 30. Different synthetic pathway using a perchlorate precursor forming the homoleptic complex **41a**.

The complex obtained was then added to the beforehand reacted DPEPhos with $Cu(MeCN)_4BF_4$ and degradation of the first complex was observed as only the mass of the dinuclear Cu complex (**41b**) was detected in ESI $[M\text{-}BF_4]^+$ 1785,3814 (1785,3767 calc.) and doubly charged $[M\text{-}2BF_4]^+$ 849,6867 (849,6866 calc.) without any mass involving cobalt being detected (Scheme 31). (See **6.4** for X-ray data of 41_b)

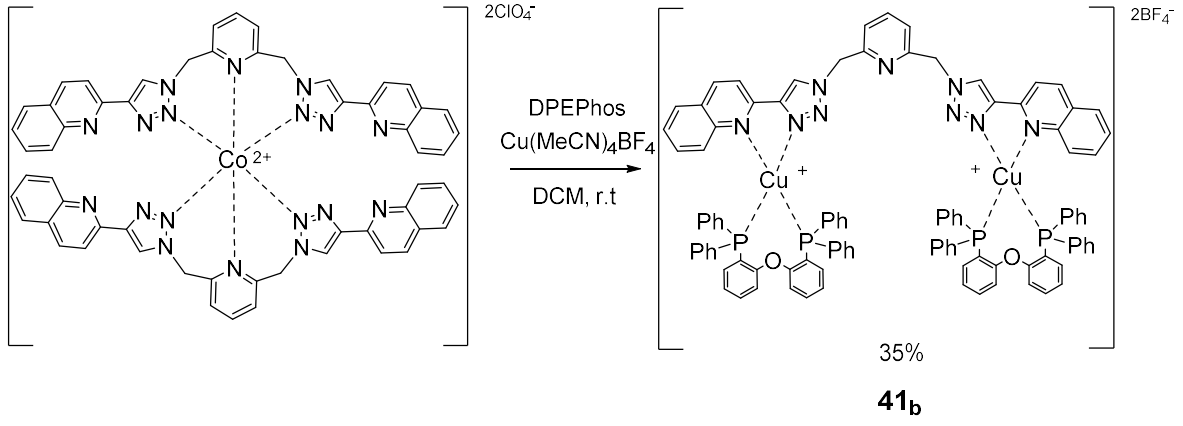

Scheme 31. Synthesis of the expected PC resulting in the degradation of the cobalt complex and forming the Cu complex **41b**.

No further investigation was conducted for this structure.

3.4.3 New Structure involving N-Xantphos and Dmp moieties

A second strategy to synthesize photocatalysts which combine PS and CAT was investigated using phenanthroline-based (phen) ligands and N-Xantphos moieties. Phen bidentate chelating ligands are well known and largely employed due to the stable complexes they form with metals and higher stability constants when complexed than with bipyridines.[222] They are poor σ donors and good π-back acceptors. Fe^{II} catalysts with phenanthroline-based ligands were proved to be very efficient for CO_2 reduction as demonstrated by the known $Fe(dmp)_2(NCS)_2$.[164] Relying on this reference, we designed a synthesis plan to form a Fe(phen) based catalyst on which another group acting as a photosensitizer would be attached. To form a stable Cu-based PS moiety, N-Xantphos was chosen for its bulkiness and its easy functionalization through its nucleophile site, with dmp as second chelating ligand due to its very strong affinity for Cu. Cu-based PS with dmp based ligands and Xantphos moieties were already proven to create stable and efficient PS.[116, 223-224]

The first step of the plan consisted of attaching the phenanthroline ligand (CAT moiety) to the N-Xantphos part (reserved for Cu based PS formation). The complexation with the different metallic precursors in different order were explored.

3.4.3.1 Synthesis

Two equivalents of NaH dissolved in dry THF allowed fast deprotonation of the nitrogen and addition of 2-Br-1,10-phenantholine resulted in the formation of the product L-**42** with a yield of 70% after purification by chromatography column (Scheme 32, top).[225] The ligand obtained was then reacted with $FeCl_2$, H_2O and NH_4NCS in water and the product CAT-**43** precipitated instantly as a red powder that was filtered off and washed with water (Scheme 32, center).[164] The Fe complex obtained was analysed by ESI mass where the fragment $[M\text{-}NCS]^+$ was observed (Figure 76, Top). The product CAT-**43** was then reacted with $Cu(MeCN)_4BF_4$ for 30 min at room temperature in dry DCM under argon and one equivalent of dmp was added (Scheme 32, bottom). After concentration and precipitation with Et_2O, the orange precipitate obtained was filtered and washed with Et_2O, which turned out not to be the expected product.

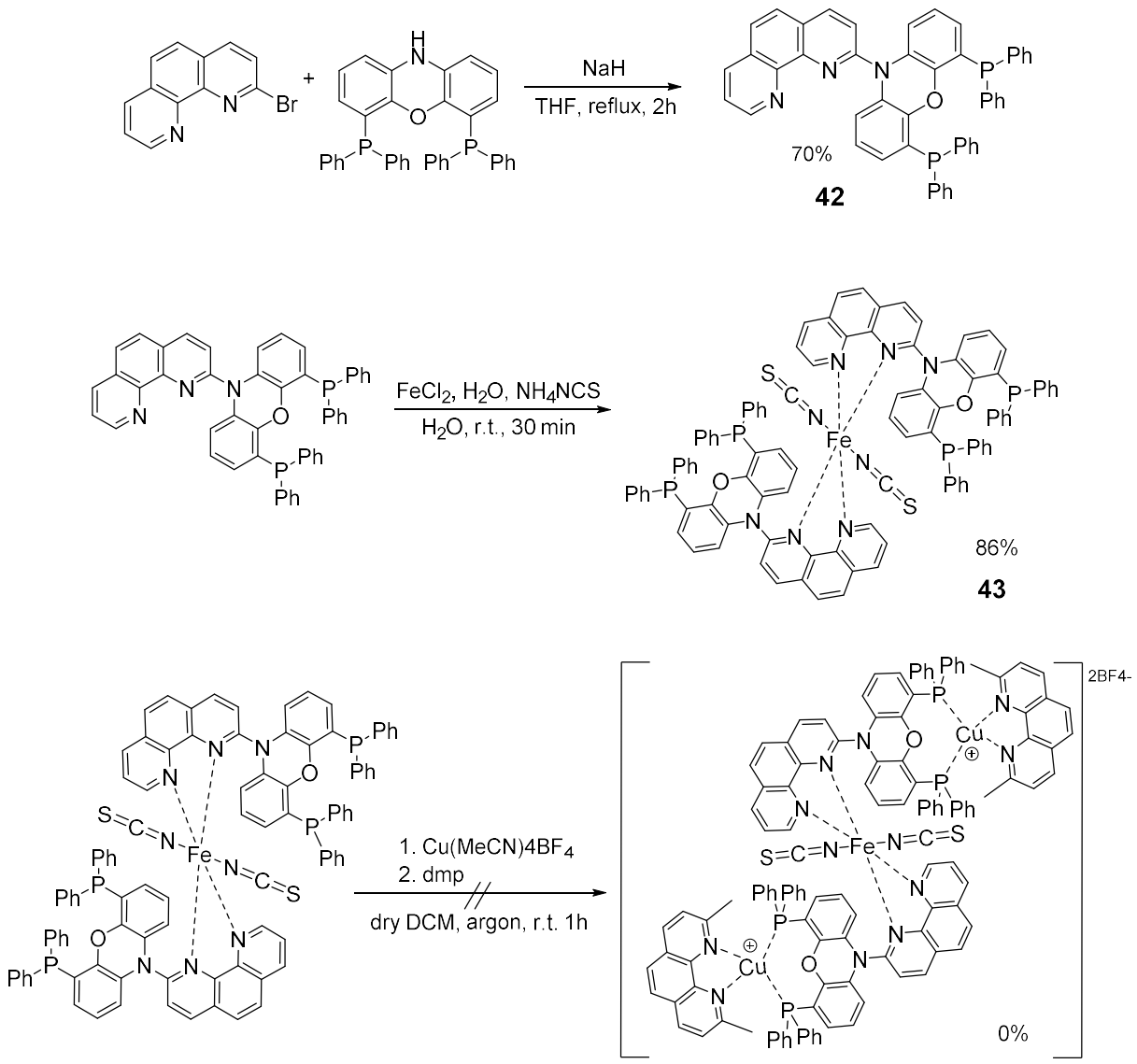

Scheme 32. Synthesis of: new ligand involving phosphines (top); new complexes targeted as catalytic moiety ready to be transformed into photocatalysts (center); no product formation with reacting with Cu-based reagent (bottom).

Instead, the product **44** was detected by Nano-ESI characterization with detection of the fragment [dmp-Cu-phen/xant] (**44**) (Figure 76, bottom), resulting from the degradation of the iron CAT-**43** complex when reacting with the Cu-based precursor and forming the more stable Cu-based complex **44** (Scheme 33).

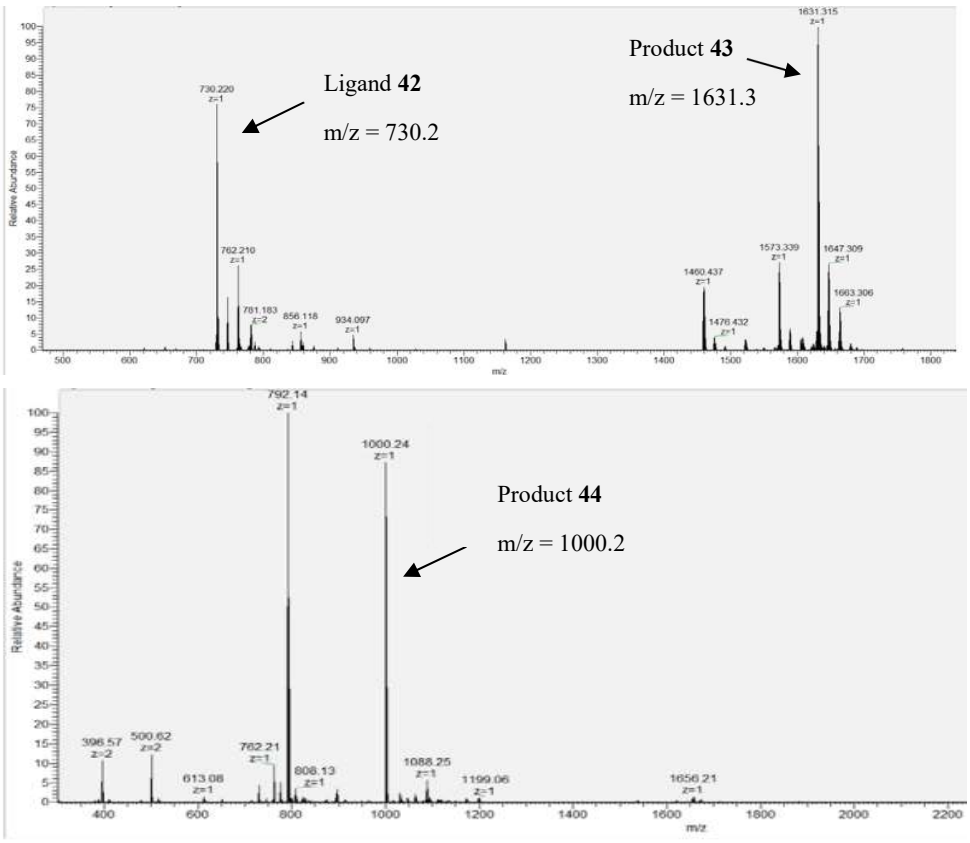

Figure 76. Nano-ESI measurement of Top**:** CAT-**43** Bottom formation of the more stable complex **44.**

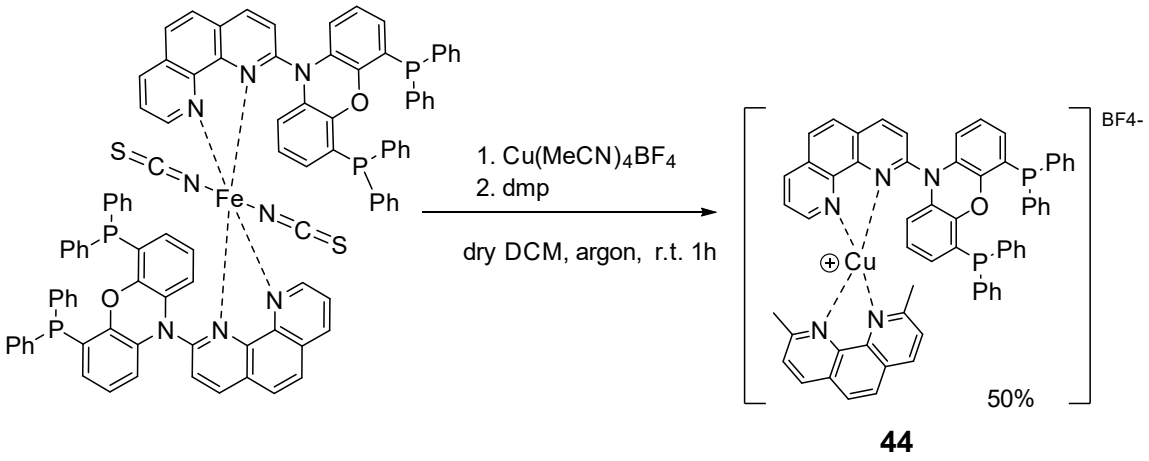

Scheme 33. Synthesis of the more stable Cu-based complex **44.**

Moreover, no fragment containing $Fe(NCS)_2$ fragments were observed which were probably washed off during the workup. The too-strong affinity of the phenanthrolines for Cu asks for a different design of the molecule. A more stable Fe complex should be formed to avoid decomplexation when adding Cu with for example porphyrins or more chelating ligands. The formation of a PC was not investigated further, but the new Fe complex formed CAT-**43**, as well as its Co, Ni and Zn (CAT-**45**, CAT-**46** and CAT-**47**) analogues were synthesized in the exact same way (Scheme 33, center), characterized and tested as catalysts for CO_2 reduction.

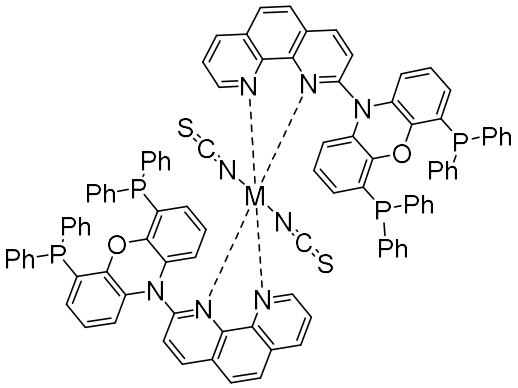

CAT-43: M = Fe, 86%
CAT-45: M = Co, 67%
CAT-46: M = Ni, 56%
CAT-47: M = Zn, 49%

Figure 77. Structure of the new complexes synthesized.

3.4.3.2 Electrochemical Characterization

The CVs of the four new complexes show many irreversible reduction processes in DMA/TEOA (Figure 78). Three reductions are visible for the Ni complex CAT-**46** (green curve) at -1.9 V, -1.79 V and -2.02 V *vs* $Me_{10}Fc^{+}/Me_{10}Fc$. The cobalt complex CAT-**45** (blue curve) shows four clear reductions at -0.86 V, -1.32 V, -1.74 V and -1.96 V *vs* $Me_{10}Fc^{+}/Me_{10}Fc$ with a potentially fifth one at -2.2 V *vs* $Me_{10}Fc^{+}/Me_{10}Fc$. Four reduction processes are visible for the iron complex CAT-**43** (red curve) at -1.33 V, -1.53 V, -1.75 V and -2.0 V *vs* $Me_{10}Fc^{+}/Me_{10}Fc$. Finally, the zinc complex CAT-**47** (orange curve) shows three reductions at -1.37 V, -1.49 V and -1.73 V *vs* $Me_{10}Fc^{+}/Me_{10}Fc$. Although the ligand alone showed four reductions in the DPV, more analysis would be needed to determine if the reductions observed are ligand or metal-based. Interestingly, the first reduction of CAT-**45** (Co) is very positively shifted compared to the others at -0.86 V *vs* $Me_{10}Fc^{+}/Me_{10}Fc$. The small reduction observed for the Fe complex CAT-**43** at -0.58 V *vs* $Me_{10}Fc^{+}/Me_{10}Fc$ was attributed to the presence of molecular oxygen.

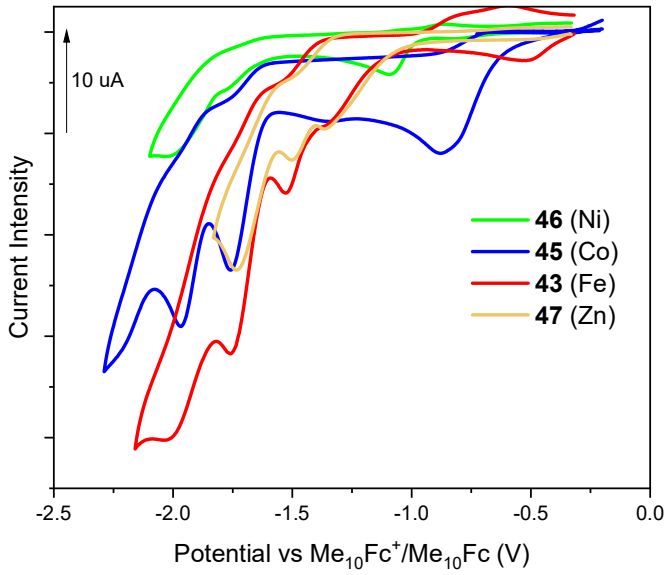

Figure 78. CVs of CAT-**43**, CAT-**45**, CAT-**46** and CAT-**47** in DMA/TEOA 5:1 v/v, 0.1 M $TBAPF_6$, reported *vs* $Me_{10}Fc+/Me_{10}Fc$.

The DPVs of the complexes (Figure 79) allow a slightly more precise visibility of the reductions with five visible reductions for the four different complexes. Under CO_2 atmosphere, the DPVs are very different depending on the complexes with for CAT-**46** (Ni) (Figure 79, A) a slightly higher current at the different reductions of the complex which could indicate an activation of CO_2 although very low. On the other hand, the Co complex CAT-**45** (Figure 79, B) shows CO_2 activation after the first reduction (-1.48 V *vs* $Me_{10}Fc^+/Me_{10}Fc$) while the CO_2-activation through the Fe and Zn complexes CAT-**43** and CAT-**47** are harder to interpret (Figure 79, C and D). Nevertheless, if the current observed under a CO_2 atmosphere is not higher than the current under Ar, shifts of the potentials are still visible, indicating that a reaction does happen. For the Fe compound CAT-**43**, the bigger shift is observed after the second reduction, as well as the Zn complex CAT-**47**. However, in the case of the zinc complex, a new peak emerges under CO_2 atm. at -0.75 V *vs* $Me_{10}Fc^+/Me_{10}Fc$, which could be due to the formation of a new species with CO_2.

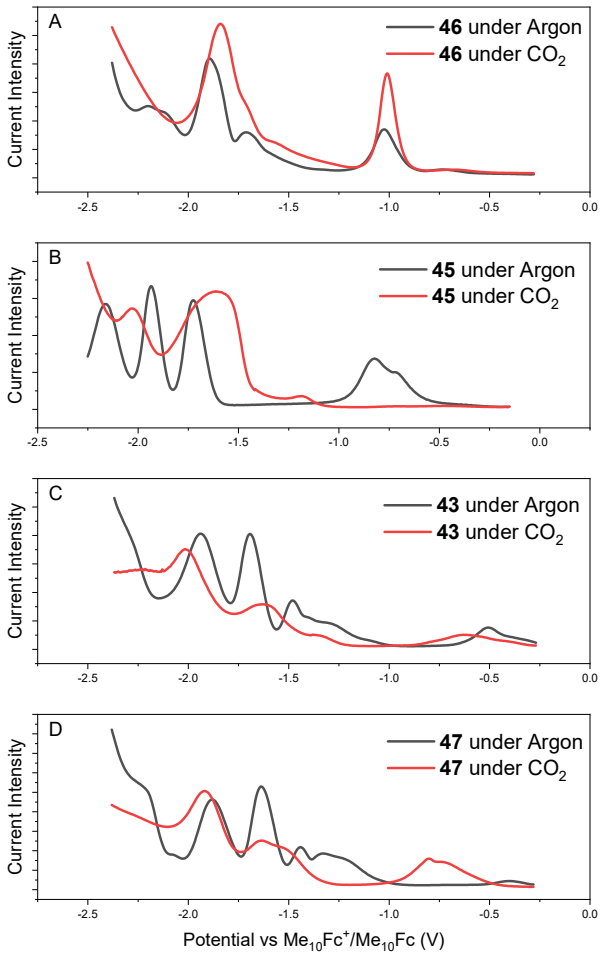

Figure 79. DPVs of CAT-**43**, CAT-**45**, CAT-**46** and CAT-**47** in DMA/TEOA 5:1 v/v, 0.1 M $TBAPF_6$, reported *vs* $Me_{10}Fc^{+}/Me_{10}Fc$.

3.4.3.3 UV-vis Characterization

Electronic absorption spectra for each complex were collected in MeCN with concentrations of ~ 10^{-3} mM (Figure 80). Intense intra-ligand transitions appear in the near UV at 225 nm and 275 nm for each complex and a lower intensity transition is observed at around 345 nm that could be attributed to a M-NCS transition.

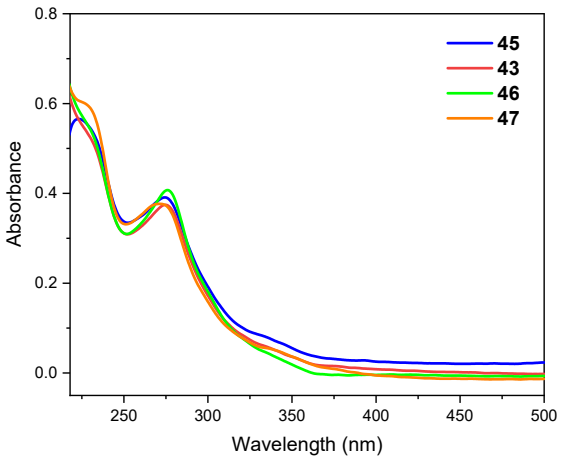

Figure 80. UV-vis absorbance of CAT-**43** (Fe), CAT-**45** (Co), CAT-**46** (Ni) and CAT-**47** (Zn) in MeCN (10^{-3} mmol/L) at 22°C.

3.4.3.4 Photocatalytic Tests

The four new complexes formed were employed in the photodriven catalytic reduction of CO_2 with PS-**24** as PS in DMA/TEOA due to their extremely low solubility in MeCN (Table 22). The iron complex CAT-**43** produced CO with a TON of 44 after 4 hours and a selectivity for CO over hydrogen of 67% (Table 22, Entry 1). Interestingly, the cobalt complex CAT-**45** that produced CO with a TON of 92 showed an excellent selectivity over hydrogen (Table 22, Entry 2). However, both Ni and Zn complexes CAT-**46** and CAT-**47** did not show any interesting activity (Table 22, Entries 3 and 4). For comparison, the known catalyst $Fe(dmp)_2(NCS)_2$ was also tested in DMA/TEOA with our system and conditions and produced CO with a TON of 71 and CO selectivity of 71% (Table 22, Entry 5). The reported results from Ishitani *et al.* with the same photosensitizer and concentrations but in MeCN/TEOA are TONco 69 and select Co over H_2 54% (Table 22, Entry 6).[164] The activity of the system was thus reproducible even in a different solvent but slightly more hydrogen was produced in their case, showing the difficulty of reproducibility or the influence of the solvent.

Table 22. Photocatalytic results with **43**, **45**, **46**, **47** and $Fe(dmp)_2(NCS)_2$ as CAT and **24** as PS in solvent/TEOA 5:1 v/v [a]

Entry	CAT	CO /µmol	H_2 /µmol	TON_{CO}	TON_{H2}	Sel.COc	solvent
1	**43**	17.5	9.46	44	21	67	DMA
2	**45**	36.6	0.27	92	0.6	99	DMA
3	**46**	-	-	0	0	-	DMA
4	**47**	0.95	-	2.4	0	100	DMA
5	$Fe(dmp)_2(NCS)_2$	28.2	10.3	71	23	75	DMA
6[b]	$Fe(dmp)_2(NCS)_2$	27.4	25.9	69	58	54	MeCN

[a] The experiment was performed with 0.1 mM CAT, 20 mM BIH and 1.0 mM PS-**24** under CO_2 atmosphere at 22 °C and the products was measured by GC after 4h irradiation at 420 nm. The products formed were analyzed from the headspace by GC. [b] reported results from the literature.[164]

3.5 Research Travel in the University of Bologna. Immobilization of Homogeneous Catalysts in Hydrogels

Preface

This research was part of collaboration with the university of Bologna (UNIBO) under the supervision of Prof. Sambri and financed by Karlsruhe House of Young Scientists (KHYS). I thank the scientists that helped me during my stay, especially Dr. Tarterini for the scanning electron microscope (SEM) measurements, Erica Locatelli for the atomic absorption (AA) and Mariangela Rea for her help with the rheology measurements. I also thank Dr. Tortorella and Chiara for their help all along my project.

3.5.1 Immobilization of Homogeneous Catalysts

Homogenous metallic catalysts are scarcely used in industry (fine chemical industry, oil refinement or polymerization processes)[226], however, their difficult separation from the media and the product constitute a major obstacle for their employment in larger scale more diverse sectors. In this project, new homogeneous earth-abundant based complexes were designed and proved to be very efficient for CO_2 reduction. In order to develop further these systems towards more sustainable ones, the strategy of immobilization was explored. Immobilization of molecular catalysts can allow their easier separation and regeneration after reaction, which is impossible with the systems developed in this work. Indeed, the presence of numerous components in high quantities like TEOA prevents easy recovery and regeneration of the complexes dissolved.

To immobilize complexes, numerous pathways are possible and were described such as the bonding (covalent, ionic or H bond) of the catalyst on supports (polymers, carbon tubes, zeolithes, MOFs and so on), or their encapsulation[227] within matrices (for example gels).[228-229]

3.5.2 Hydrogels

Hydrogels are three-dimensional networks made of crosslinked hydrophilic polymers, able to swell when absorbing water or aqueous solvents.[230] They are today widely used for many various applications such as in pharmaceutics (wound healing), food industry or cosmetics.[231-233] Their shape can adapt to the application, from flowing gels with high water content and weak mechanical strength to solid-like gels. Moreover, the wide range of chemical structure generates different physical properties (e.g.elasticity, mechanical strength) and chemical properties (e.g., polarity, hydrophilicity).

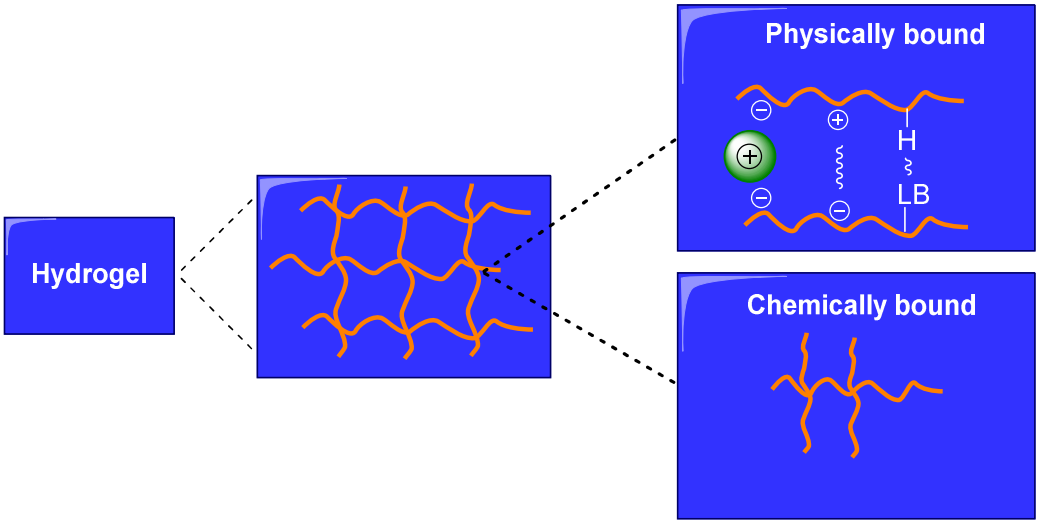

Figure 81. Different possible network allowing the formation of gels, through ionic and electrostatic interactions and through covalent bonds (cross linked).

For the molecular polymeric units to immobilize in a solid-like assembled network and form a gel, different approaches are employed that can be divided into chemically bound network or physically bound network. In the first case, the chains can covalently bond with each other using their functional groups, an example being the known formation of amides between the COO^- groups of alginate and diamines. The units can also be organized in a 3D network by other interactions such as H-bond, ionic bonds, π-stacking, and so on (Figure 81). The approach employed to build the gel will influence the properties like the swelling properties, mechanical strength and others. [234]

One very common and bio-sourced polymer employed is the polysaccharide-based alginic acid extracted from algae, which is hydrophilic but forms a gel very easily when divalent metals such as Ca are present, ionically linking the polymer chains together (Scheme 34).[235]

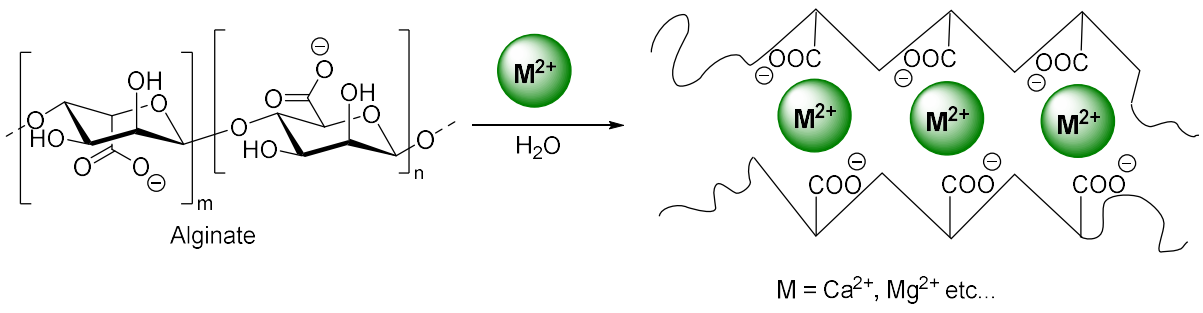

Scheme 34. Formation of gel thanks to ionic bonds between M^{2+} (e.g Ca, Mg) and the carboxylate groups of the alginate polymer.

Alginate was also extensively employed to form hydrogels by covalently bond with a varied diamines and forming new amide functions using 1-Ethyl-3-(3-dimethylaminopropyl)carbodiimide (EDC) as coupling agent for this nucleophilic addition-elimination reaction (Scheme 35).[236]

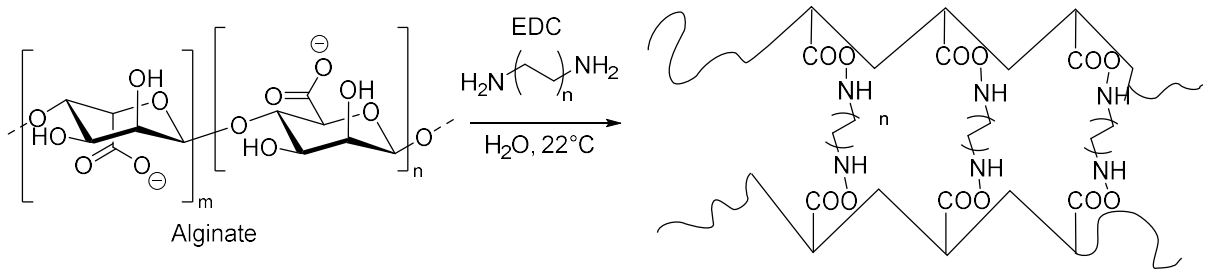

Scheme 35. Formation of a cross linked gel by chemical reaction between the carboxylic groups of the alginate polymer branches and diamines forming amides.

One particularly interesting property of hydrogels is their "Host network" ability enabling them to host and carry, within their structure, active molecules or atoms. Drugs were already incorporated inside hydrogel structures to be released inside the body allowing localized healing processes or delayed-slow release of the active drug for example.[235] Very recently, visible-light-induced photocatalysis of CO_2 were achieved in aqueous media with polycarbonate micellar rhenium catalysts where Re complexes were incorporated in polymer chains functionalized with COO^- groups able to form ionic bonds with the protonated $TEOAH^+$.[237] The newest version formed almost exclusively CO with a TON of 110 in water.[238]

3.5.3 Goal and Strategy

Hydrogels were already reported based on metal complexes which form the 3D solid-like structure by complexation[239-240] employed for their physical or photophysical properties and some materials were also employed for catalysis.[241-242] Our approach consists of immobilizing molecular metal complexes as catalyst for CO_2 photoreduction in hydrogels to widen or scale up their application. Moreover, the use of hydrogels will allow the evolution of our system towards water-based environment. Different ways will be tested using ionic bonds, covalent bonds or mechanical trap. Moreover, alginate was selected as bio-sourced hydrogel base due to its cost effectiveness and easy functionalization mainly through the carboxylic acid groups.

CAT-**11**, CAT-**12**, CAT-**17** and CAT-**18** were proved to be active catalyst for CO_2 reduction in MeCN or DMA with **6**-based ligands. To insert the complexes in hydrogels, the functionalized ligand with primary amines NH_2 and with trimethylammonium were chosen, forming the corresponding functionalized complexes CAT-**22**, CAT-**23** and CAT-**17_b** (Figure 82) that were proved to be active for CO_2 reduction in **3.2.1.4**.

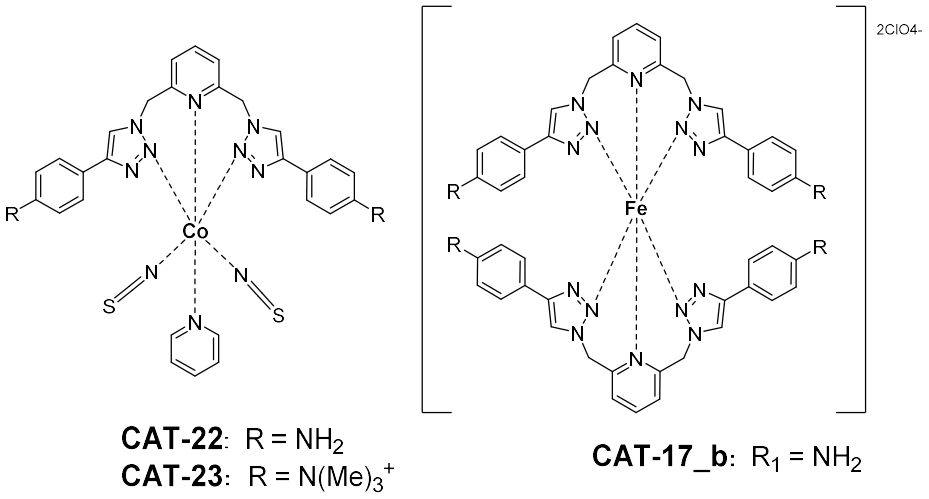

Figure 82. Structure of the functionalized complexes to be immobilized in hydrogels.

However, the functionalized group allow their incorporation into alginate-based hydrogels, by covalent bonds with NH_2 and ionic bonds with $N(Me)_3^+$. The strategies are presented in the Figure 83. The first strategy (Figure 83 Left) consists of using a calcium solution to form a gel with alginate by ionic bonds and dissolving the ionic complex CAT-**23** with the calcium salt so this one also forms ionic bonds within the network. A second strategy (Figure 83 Middle) is to use the well-known cross linking to form an alginate-based gel and to add a certain percentage of the diamine NH_2 complex so that it also acts as a linker between two alginate branches. A third option that can be tested is the simple trap of metal complexes in the alginate-based hydrogel by incorporating the complex in the alginate solution and afterwards create the gel with calcium. One can assume that the complex, insoluble in water, will be trapped inside the bead created and not likely to diffuse into the aqueous solvent around it.

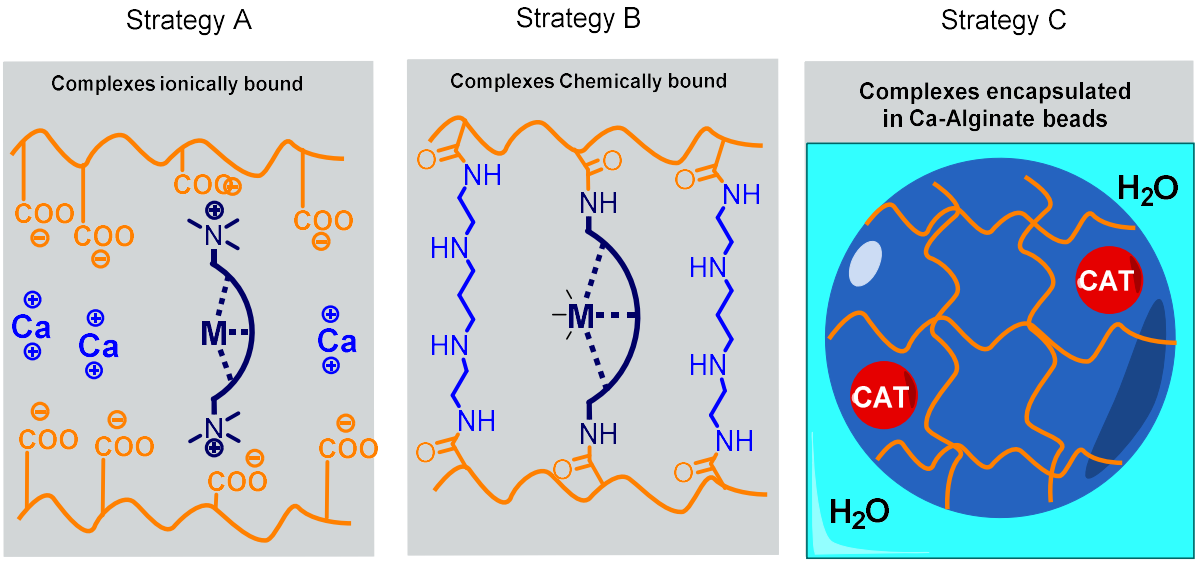

Figure 83. Different strategies to immobilize the homogeneous catalyst into hydrogels.

3.5.4 Synthesis

Strategy A: Calcium-based

To form alginate beads, alginate is dissolved in water to obtain 0.05 M solution by vigorous stirring at 50°C for 1 hour. With a Pasteur pipette of 1.000 mL, this solution is added dropwise to a 0.5 M solution of $CaCl_2$ dissolved in water, instantly beads are produced.[234] To insert the metallic complexes, the complexes were dissolved in a minimum volume of a mixture MeCN/H_2O for the $N(Me)_3^+$ complexes and THF for the NH_2-based ones due to their insolubility in water. The complexes dissolved were diluted in the solution of alginate and stirred at 50 °C for 10 minutes to prepare a solution containing 0.1 mM of catalyst. This solution was then added dropwise to the calcium solution resulting in the beads formation. The concentration of catalyst in the beads was approximated to be close to 0.1 mM, although in reality this is an over-estimation due to the introduction of the calcium ions and the possible but unlikely diffusion of the complexes from the beads to the solvent (water). The beads were let in the calcium solution for 1 hour, taken gently out, rinsed with water and dried by letting them sit on absorbing paper. The size and shape of the beads depend on the pipette employed to form the drop and had an average diameter of 0.3-0.4 mL, transparent. The beads containing iron-based catalysts had a light yellow-orange color while the beads containing the cobalt complexes were colorless. The insolubility of the complexes in water caused difficulties as not all the measured quantity of catalyst was dissolved in the solvent to be mixed with the alginate solution.

A different kind of beads were also synthesized with a 50/50 ratio of Ca^{2+}/Fe^{2+} ions. To do this, $Fe(ClO_4)_2$ was dissolved in the calcium solution to reach a 50/50 molar ratio. A 1/10 ratio (Fe/Ca) was also synthesized in the same way. The beads created appeared more opaque and slightly orange. When a 100% Fe solution was used instead of calcium, the beads formed were opaque and orange, however not stable because degrading after simple touch with a spatula. The calcium is thus necessary in a minimum quantity to guarantee the stability of the beads.

The catalysts were introduced to reach 0.1 mM of concentration and beads (Figure 84 Left). Different beads were also prepared with 1.0 mM of Cu^I photosensitizer CAT-**24** which was dissolved in a minimum quantity of MeCN and diluted with the mixture alginate in water. This solution was added dropwise in an 0.5 M solution of $CaCl_2$ which gave the Cu-based beads, using strategy B/C (Figure 84 Right). With the Cu-based PS, and in a similar way, 0.1 mM of Fe complex CAT-**17_b** was added to the beads, using the ionic strategy. while the Cu^I PS was introduced with a concentration of 1.0 mM in the beads.

Figure 84. Left Alginate beads through ionic bonds with calcium and containing CAT-**23** as CAT Right: Alginate gel formed through ionic bonds with calcium and containing PS-**24** irradiated under UV light.

Strategy B: Cross link gel with spermine

To a solution containing 0.05 mM of alginate in in 1.8 mL of water, N-ethyl-N'-(3-(dimethylamino)propyl)carbodiimide (EDC) was added (40.0 mg, 0.257 mmol) and the mixture was stirred for 15 minutes at 22°C on a stirring plate.[236] A solution of spermine (Figure 85) was prepared with 40.0 mg dissolved in 2.0 mL of water reaching a concentration of 0.197 mmol/L. 200 µL of this spermine solution was added to the previous alginate mixture. It was vigorously stirred for homogenization for 1 minute. The mixture was then let without stirring 18 h to form a gel. After 18 h, the mixtures formed a not stable viscous liquid which necessitated addition a small amount of calcium in water to help finishing the process of gelification. The formation of the gel was then due to both cross linking with diamines and ionic interaction with Ca^{2+} ions. To insert the catalysts, the complexes with the NH_2 functionalized ligands with iron, were introduced in a 1/10 ratio complex/spermine in the spermine solution. The gel was formed in a small conical cuvette of 1.5 cm^3 and gave the same shape to the gel. (Figure 86)

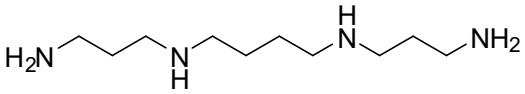

Figure 85. Structure of spermine

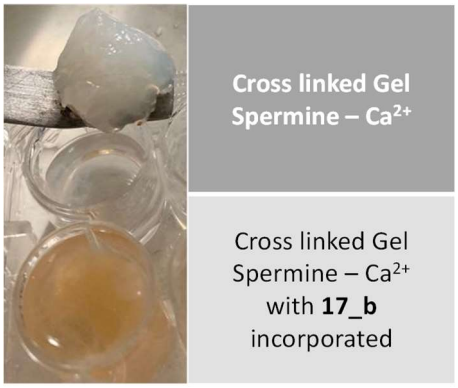

Figure 86. Cross linked gels with spermine and Ca^{2+}without catalyst incorporated (Top) and with [24] incorporated (Bottom)

3.5.5 Analysis

First, beads were prepared with the strategy A to test the stability of the alginate-based hydrogels, and immersed into different solvents: water, MeCN, DMF, MeOH, and mixtures of those three solvents with water in different ratios (3/1, 1/1 organic solvent / water). In pure solvents, the beads kept their size and color in water and DMF while the beads immersed in MeOH and MeCN became smaller, whiter and harder due to the replacement of the water molecules in the beads by the solvent molecule, shrinking the solid structure (Figure 87 Right). In mixtures of solvent 1/1 with water, the beads kept their size and color (Figure 87 Left). However, their structural stability and mechanic resistance were only observed manually without further analytical studies.

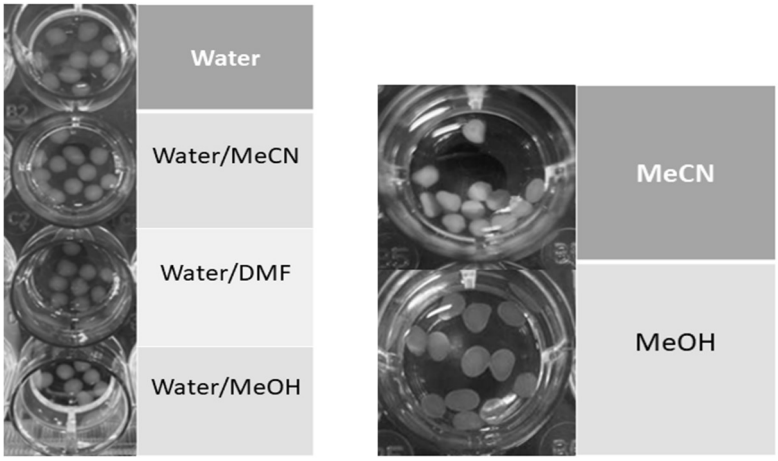

Figure 87. Stability of alginate beads formed with Ca^{2+} in different solvent mixtures.

Atomic absorption (AA) for ionically bound complexes (strategy A)

After incorporation of the complexes in the beads, preliminary visual tests were performed by adding a 1 mM solution of NaOH onto the washed beads supposed to contain the Fe complexes with a maximum concentration of 0.1 mM. After few seconds, the transparent beads turned orange and green with the formation of a precipitate characteristic of $Fe(OH)_2$ (equation 18), homogeneously dispersed inside de bead, which was not observed when NaOH was added on normal Ca-beads (Figure 88).

$$Fe^{2+} + 2OH^- \longrightarrow Fe(OH)_2(s) \qquad (18)$$

Figure 88. Green precipitate formed after addition of NaOH on a bead containing 17_b

To calculate the exact concentration of metal in the beads, atomic absorption (AA) analysis can be employed by detecting the characteristic wavelength absorbed by the atom to create electronic transition in their electron orbitals. This measure was conducted on beads containing the Fe complex CAT-**17_b** which was prepared to reach a concentration of 0.1 mM.

0.38 mg of the complex measured with a high precision scale was dissolved in 0.1 mL of MeCN to which was added 3.4 mL of water also containing 0.5 M of alginate reaching a concentration in Fe complex of 0.1 mM (MW = 1101.7 g/mol). This solution was added dropwise in a calcium solution to form the beads, which were washed with water several times and dried with absorbing paper. 1.00 g of wet beads (swollen with water) were weighed and dried over night by immersion in pure ethanol for 1 hour and 16 hours in an oven at 70°C. The same quantity of beads after evaporation of water was weighed again measuring 45 mg. It means than in 1 g of wet beads, water constitute 95.5% of the weight with the remaining mass being the alginate structure with calcium and the catalyst inserted. The 45 mg remaining were dissolved in 1.00 mL of regia solution (HCl:HNO_3 3:1) for 18 h to extract the Fe in the acidic solution. This solution was sent for AA measurement and a quantity of 15 ppm of Fe was detected.

15 ppm of Fe detected in the 45.1 mg of the dried beads dissolved in 1 mL of acid means that the quantity of iron in those 45.1 mg represents 0.675 µg that is $1.208 .10^{-8}$ mol. If we consider that each atom of iron was complexed, the number of moles of catalyst present in the solution was then also $1.208 \cdot 10^{-8}$ mol, which considering the MW of the complex (1781.7 g/mol) gives a mass of complex of 0.021 mg. This mass represents 3.4% of catalyst mass that was indeed incorporated in the beads. The low values likely due to the low solubility of the complex that did not dissolve completely when added to the alginate solution. Also, the lack of solubility also triggers difficulties for reproducibility as the control of the mass of catalyst dissolved and incorporated varies depending on the complex.

Scanning electron microscope (SEM) measurements

SEM measurement were conducted on the dried beads formed with strategy A (Table 23 and 24), on the cross linked spermine-based gels from strategy B (Table 27) and on dried beads from strategy C (Table 25 and 26) to detect the presence of the metals, their dispersion on the alginate 3D network and the shape of their surface.

Table 23. SEM of the dried beads formed with Strategy A

beads	Ca beads	Fe beads	Fe/Ca beads
shape	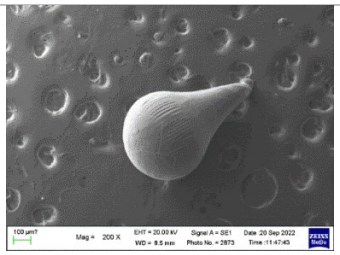 100 µm	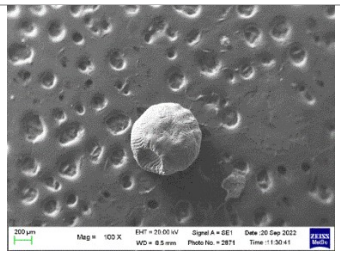 100 µm	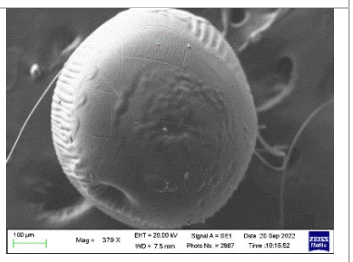 100 µm
surface	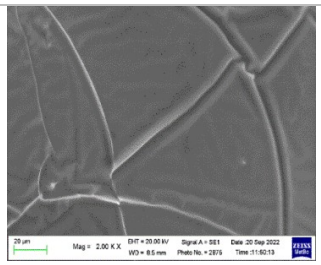	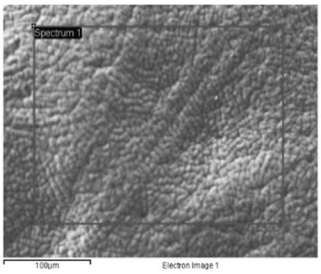	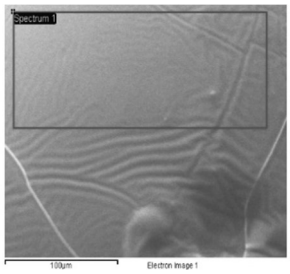
scale	20 µm	100 µm	100 µm

Table 24. SEM results with relative concentrations

Spectra of the elements analysed	Relative concentration	beads
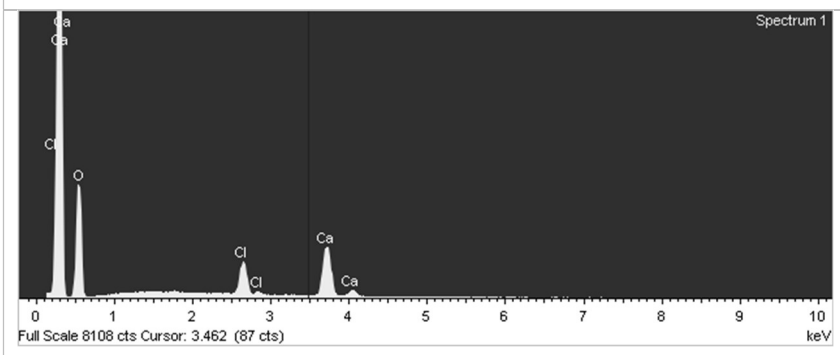	Ca: 10.7	Ca beads
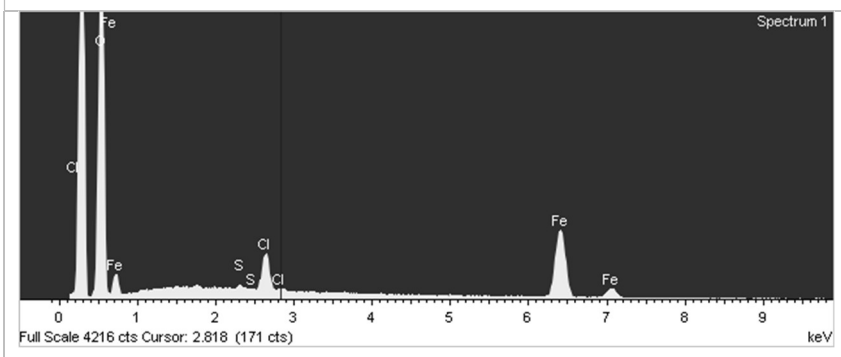	Fe: 22.2	Fe beads

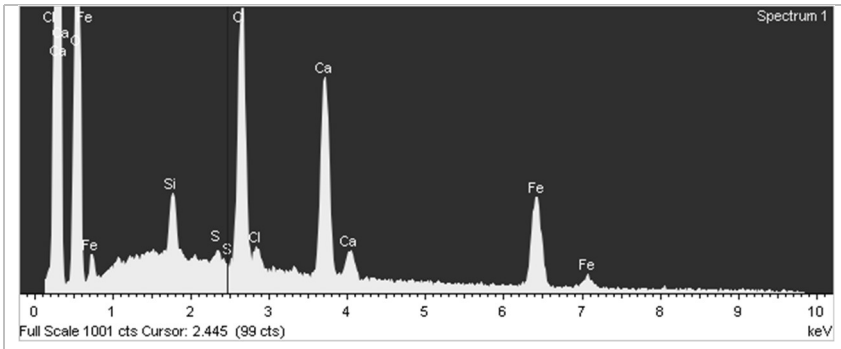	Ca: 9.37 Fe: 9.38	Fe/Ca beads

As expected, the Ca-beads presented Ca and Cl as main elements, the iron beads with $Fe(ClO_4)_2$ showed only Fe and Cl as main elements while the beads made with the a mix 50/50 Fe/Ca presented clearly the presence of both Fe and Ca in similar relative quantities. The only-Fe beads were not stable while the mix 50/50 appeared more similar to the Ca-only-beads.

Table 25. SEM of the dried beads formed with Strategy C

beads	Ca-beads with **17_b**
shape	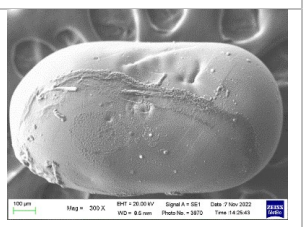
scale	100 µm
surface	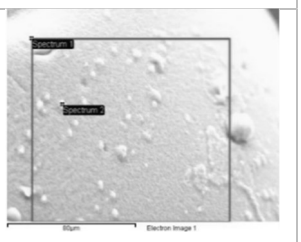
scale	80 µm

Table 26: SEM of the dried beads formed with Strategy A and C

beads	Ca beads with **23**	Ca beads with PS-**24** + (CAT-**17_b**) beads
Shape	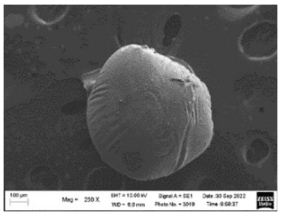	Non reported
Scale	100 µm	
surface	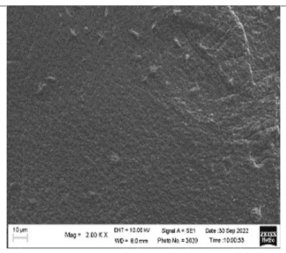	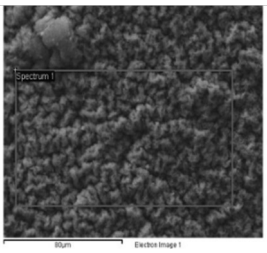
Scale	10 µm	10 µm

The shape of the beads when adding catalyst did not change in average and the metals are visible in the surface of the beads. When the metal complexes were soluble in the mixture of water and MeCN, the surface of the beads reveal homogeneous distribution of the metal. When the complexes were hardly soluble, they rather formed small aggregates could be visible on the surface of the beads. The heavier the metal atoms are, the more glimmering and less transparent they appear on the SEM image and higher energies are detected.

Table 27. SEM of the dried cross gels formed with Strategy B

Cross-gel	Cross Gel spermine	Cross Gel spermine + CAT-1**7_b**
Shape	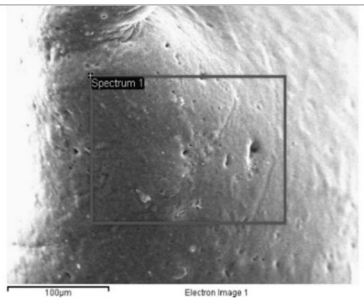	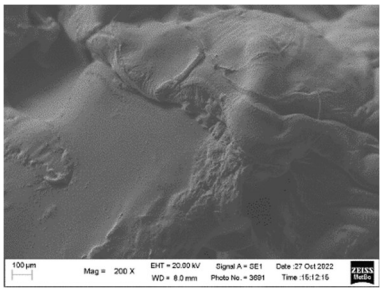
Scale	100 µm	100 µm
surface	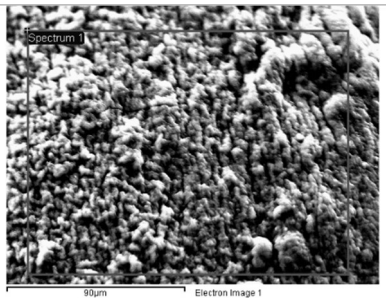	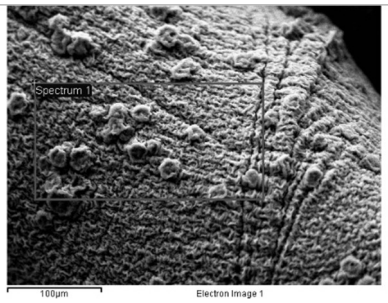
Scale	90 µm	100 µm

The SEM analysis of the cross-linked gel showed that the shape of the gels did not change when the complex was introduced with the spermine. However, the iron complex that was introduced with a concentration of 1/10 compared with the spermine seems to be visible on the surface of the gel with small round drawings, where the iron was concentrated. This means that the dispersion of the Fe complex in the gel is less homogenous than using strategy A and C with zones with higher concentrations. Calcium is also visible as its addition was necessary to form the end gel.

Table 28. Summary of the relative concentration of metal observed in the different beads and cross gels

Gels	Elements analysed and relative quantities
Ca beads with CAT-**17_b**	Fe: Very low – 0.17
Ca beads with CAT-**22**	Co: Very low – 0.12
PS-**24** + CAT-**17_b**	Cu: 0.53 Fe: traces
Cross Gel with spermine + CAT-**17_b**	Fe: 0.37

From the SEM analysis, the surface and metallic relative concentrations (Table 28) of the beads and cross-linked gels were fundamentally described. In general, and according to the results of AA, the quantities of metal in the gel are very low (below 16 ppm) and homogeneously dispersed, except when the solubility of the complex was too low (NH_2-based complexes).

Rheology experiments

Rheology experiments were recorded to describe the formed material by testing their elasticity and mechanical resistance. From basic experiments, one can determine two important factors G′ (Storage modulus) and G′′ (Loss modulus). An oscillation without normal force is applied on the sample trapped between two disks, and its response to this stimulus is analysed. The more the sample follows the oscillation the more the sample is elastic, while it is rather viscous when it lags behind the stimulus. Gel and hydrogels are typically material that behave like solids and liquid at the same time. G′ represents the resistance to deformation of the elastic ability (solid) while G′′ represents the resistance to deformation of the inelastic component of the sample (liquid).[243]

To start with, G′ and G′′ were measured with increasing shear strain, that is increasing the amplitude of the applied oscillation. On the diagram, the visco-elastic behavior of the material is evaluated according to the G' and G'' values and the complex modulus G*, which is a quantitative measure of material stiffness or resistance to deformation. If the sample is more solid like (case for gels) G′ should be higher than G′′, which are both constant until there is enough energy given to change the microstructure of the material at the transition point, where both G′ and G′′ are equal. After this cross-over point, the sample changes from being “elastically dominated” to “viscously dominated” that is more similar to a liquid. The smaller the shear strain at the transition point is, the less strong and stable the tested material is.

Concerning the normal Ca-beads prepared compared with the beads containing 1/10 Fe cations, the behaviors are very similar with for both very high G′(solid-like dominant) (18147 Pa and 10921 Pa respectively) but with fast breaking points (0.66 and 0.68% of shear strain), meaning that they are both fragile under strain (Figure 89 and Table 29). The introduction of Fe does not seem to change the basic properties of the gel except a slightly higher resistance.

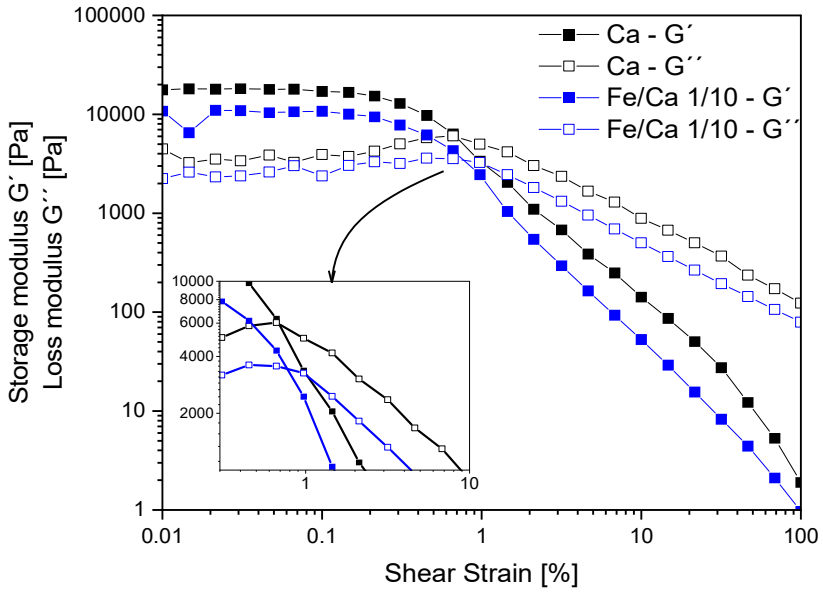

Figure 89. Rheological properties of Ca-beads (black) and Fe/Ca beads (blue) in hydrogel form. Storage modulus (G') and loss modulus (G") of each swollen condition as a function of strain amplitude.

Table 29. Results of the rheology measurements

Beads	Ca beads	Fe/Ca beads
G´ [Pa]	18147	10921
G´´ [Pa]	3869	2383
Breaking point	0.66%	0.68%

Concerning the beads that contain the metal complexes (here CAT-**17_b**), the behaviors are almost identical regarding the values G´ and G´´, which was expected to the very low presence of complex in the gel. However, the beads with the iron complex appears less resistant to shear strain as its breaking point is at 0.45% (Figure 90 and Table 30).

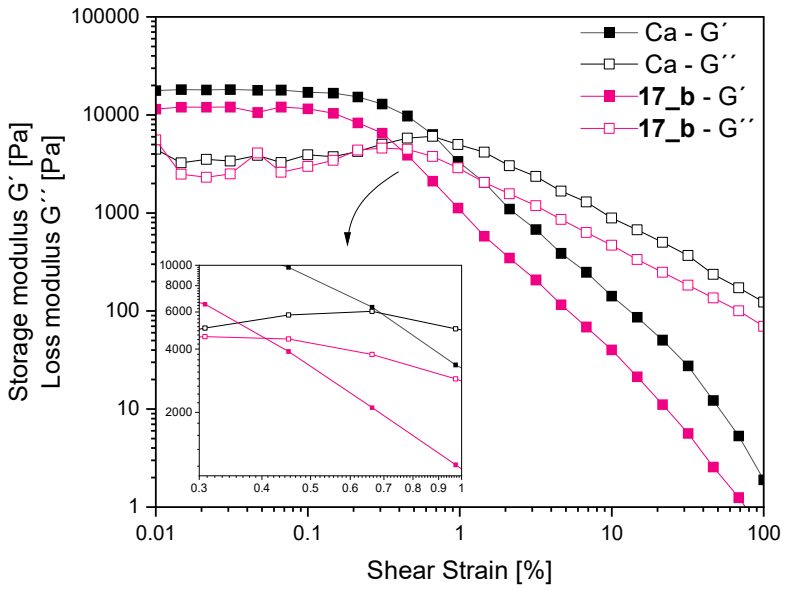

Figure 90. Rheological properties of Ca-beads (black) and Ca-beads containing **CAT-17_b** (red) in hydrogel form. Storage modulus (G') and loss modulus (G") of each swollen condition as a function of strain amplitude.

Table 30. Rheological properties of Ca-beads and Ca-beads containing **CAT-17_b**

Beads	Ca beads	Ca beads with **17_b**
G´ [Pa]	18147	11990
G´´ [Pa]	3869	3384
Breaking point	0.66%	0.45%

When introducing more complexes like 1 mM of PS **24**, the gel obtained also shows a high solid-like behavior (G´ of 10401 and G´´ of 2604), however, the introduction of a large quantity of complex (Cu PS) caused a less resistant to shear strain gel with a breaking point at 0.31% (Figure 91 and Table 31).

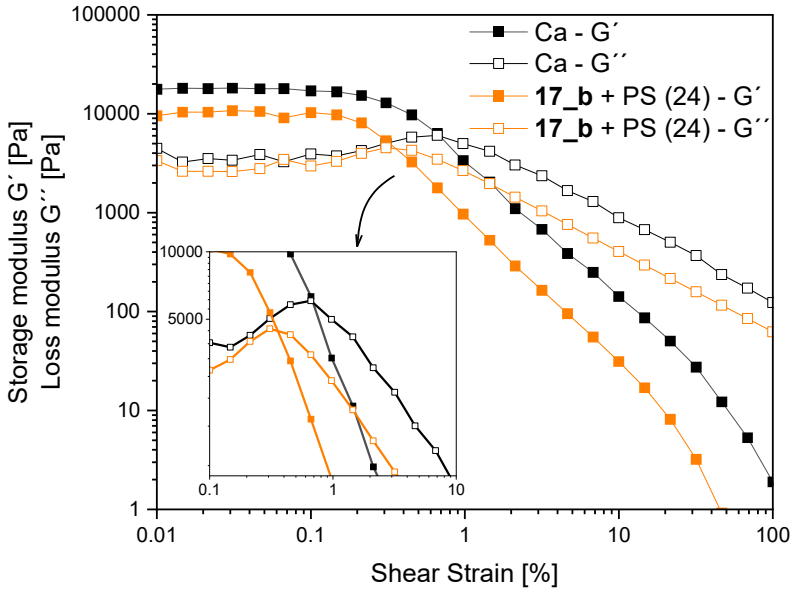

Figure 91. Rheological properties of Ca-beads (black) and Ca-beads containing CAT-**17_b** and PS-**24** (orange) in hydrogel form. Storage modulus (G') and loss modulus (G") of each swollen condition as a function of strain amplitude.

Table 31: Rheological properties of Ca-beads (black) and Ca-beads containing PS**24** and **CAT-17_b**

Beads	Ca beads	Ca-beads with PS **24** and **CAT-17_b**
G´ [Pa]	18147	10401
G´´[Pa]	3869	2604
Breaking point	0.66%	0.30%

Those results show that the introduction of ionically bound or encapsulated (strategy A and C) complexes leads to stiff and rigid gels with a small loss of mechanical resistance compared with gel without complexes. However, the differences observed are relatively low which confirm the stability of our gel under metallic complexes incorporation, even in higher quantities (1 mM).

3.5.6 Photocatalytic Tests with Beads

Photocatalytic tests were performed with the new beads formed with strategy A and C with CAT-**22**, CAT-**23**, CAT-**17_b**, and Fe^{2+}/Ca^{2+}. Using the Fe/Ca beads of strategy A, 10 beads corresponding to 180 mg were added in a vial with PS-**24** as PS (1 mM) and 20 mM of BIH dissolved in a solvent mixture MeCN/TEOA/H_2O. The test using CAT-**17_b** was conducted with 10 beads (88 mg) with the same concentration of Cu^I PS, electron donor and solvent mixture. The tests were irradiated for 4 hours at 420 nm.

As expected from the very low concentration of the complexes introduced in the beads, no CO was formed with any of the complexes inserted in the beads in the employed irradiation time. However, CO and H_2 were observed with the bead containing the mix of Fe^{2+}/Ca^{2+} (1/10).

11.7 µmol of CO were formed with 0.52 µmol of H_2 giving a selectivity for CO of 70%. Those results are not surprising as the precursor $Fe(ClO_4)_2$ also formed CO in MeCN/TEOA. However, the TON is difficult to calculate as the concentration in the bead was not yet determined. AA analysis will be conducted in the future to determine the exact quantity of catalyst introduced in a sample. In this work, the precursor $Fe(ClO_4)_2$ was already been proved to be active for CO_2 reduction in MeCN/TEOA forming 1.64 µmol of CO and 0.42 µmol of H_2 (Entry 10, Table 34, Supplementary data **5.5**). The Fe/Ca beads formed 7 times more CO than the precursor $Fe(ClO_4)_2$ which will then be interesting to investigate.

The alginate beads in every case were not very stable and degraded into agglomerate after irradiation and stirring for 4 hours. SEM analysis of those aggregates show similar surface than the beads before reaction with alginate based and small quantity of Fe incorporated (relative quantity 2.25 u.a. of Fe detected)

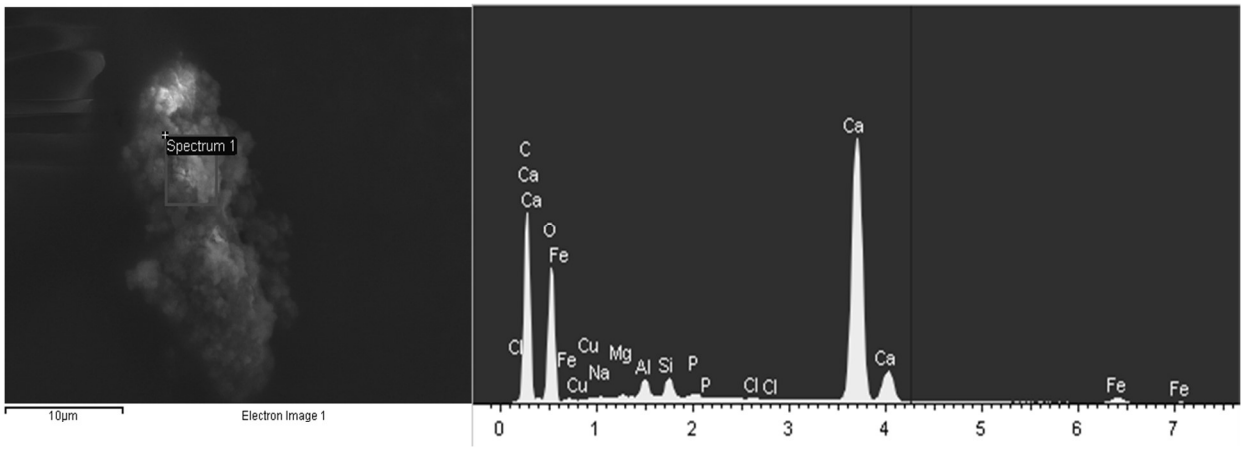

Figure 92. SEM recorded of the aggregates formed after photocatalytic reaction.

No photocatalytic test was performed with the formed cross-linked due to their lower stability under air and stirring.

3.5.7 Conclusion

The results obtained are only preliminary and represent a promising new pathway for CO_2 photoreduction. The immobilization of homogeneous complexes in hydrogel could not only allow aqueous environment but also to prevent the catalyst pollution and the Cu-PS degradation as well as help to regenerate them.

However, the results obtained are encouraging and should be repeated with more complex inserted in the beads and exact determination of concentration using AA. Moreover, a lot of factors still need to be determined such as the diffusion of CO_2 and CO into the hydrogel or the stability of the gel in the solvent employed, under irradiation, and under stirring conditions. Furthermore, the shape of the hydrogel could be shaped as a film that can be placed on the glass walls for more irradiation surface and less contact with the stirring magnetic bar.

4 CONCLUSION AND OUTLOOK

In this thesis, new systems for the photocatalytic reduction of CO_2 were developed with earth-abundant-based materials. First, new Cu^I complexes were proved active as photosensitizers, and the photocatalysis was optimized with the known Ni(cyclam)Cl_2 catalyst.

New monometallic complexes were synthesized, characterized, and tested for their activity as catalysts for CO_2 reduction. The system was optimized with one particular Fe-based catalyst and further investigated. Bimetallic and tri-metallic analogous structures were also synthesized and characterized, with CO_2 catalytic activity. Investigations into cooperativity effect are ongoing but preliminary results involving structure CAT-**34** are promising.

Attempts were made to design and synthesize earth-abundant-based photocatalysts but were not successful, however, new earth-abundant metal-based complexes, active for CO_2, were formed and characterized.

Earth-abundant photocatalytic systems introducing new Cu^I as PS and optimization with Ni(cyclam)Cl_2. Ni(cyclam)Cl_2 was one of the first reported catalyst for the reduction of CO_2 in the 80s by FISHER and EISENBERG and is still today one of the most reported investigated for this reaction.[142] However, it was to the best of our knowledge only employed along with noble metal-based PS. A highly efficient system for the photocatalytic reduction of CO_2 into CO was developed using the known Ni(cyclam)Cl_2 as CAT in combination for the first time with new Cu^I-based PS. This system produced CO almost selectively over molecular hydrogen with TONs up to 8 and quantum yield of 2.1 with PS-**4**, in line with the results reported in the literature with Ni(cyclam)Cl_2 and noble metals as PS. (Scheme 36). Those results show the potential of such eco-friendlier systems competing with noble metal-based systems.

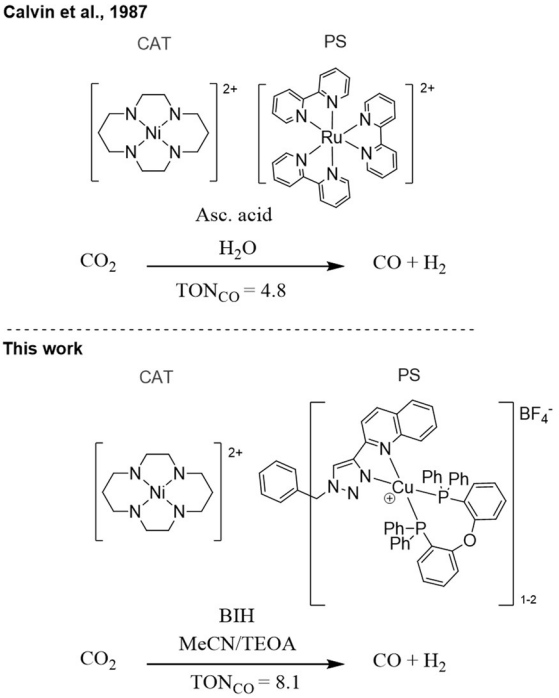

Scheme 36. Comparison with a reported system with Ni(cyclam)Cl2 as CAT and our earth-abundant system.

New earth-abundant catalysts for CO_2 reduction. New earth-abundant monometallic catalysts with 2,6-bis(1,2,3-triazol-yl-methyl)pyridine as the main ligand were synthesized and characterized by electrochemistry, photophysics and the Evans method. They were tested as catalysts for the photocatalytic reduction of CO_2 from which the Fe heteroleptic complex CAT-**11** emerged as the most efficient tested. It produced CO with a TON of 576, a selectivity over H_2 of 70% and with a total quantum yield of 7% using an irradiation at 420 nm as source of energy (Scheme 37).

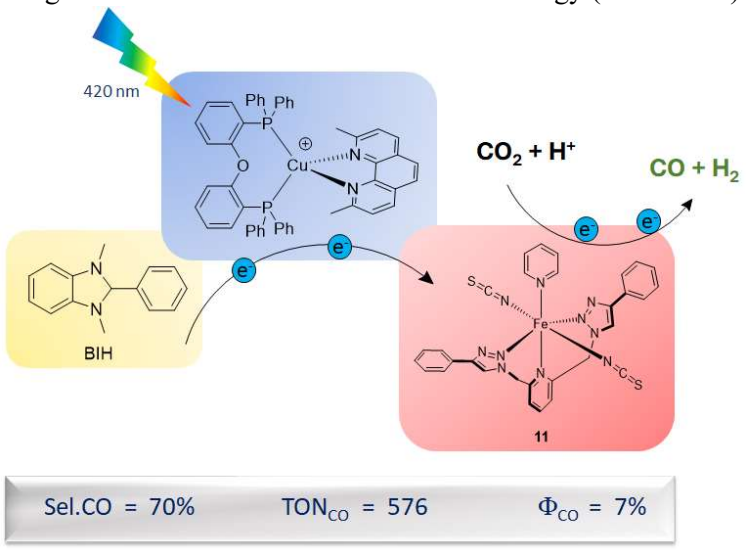

Scheme 37. New earth-abundant photocatalytic system with the Fe-based CAT-**11** producing CO and H_2.

From all the third raw TM investigated, Co and Fe were the only ones selective for CO production over molecular hydrogen with a high dependence on the employed solvent.

Using a similar ligand structure, a bimetallic Co complex CAT-**34** was synthesized and presented a three times better activity for CO_2 reduction compared with its analogue CAT-**30**, which is promising for cooperativity effect investigation (Scheme 38).

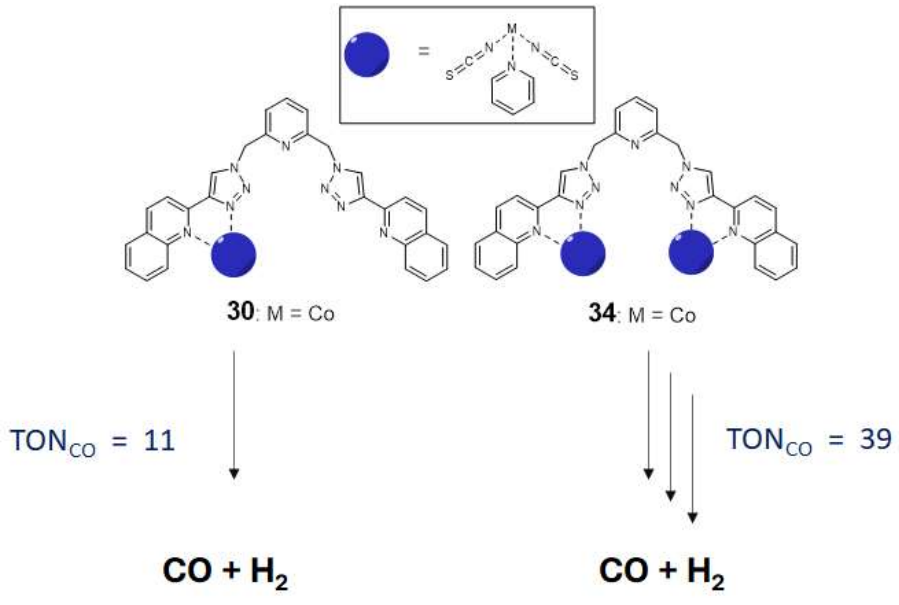

Scheme 38. Promising results obtained for cooperativity effect with the bimetallic Co complex **CAT-34**.

Trinuclear Fe complex and its magnetic properties. A trinuclear iron complex was synthesized and characterized, and revealed Fe^{II} oxidation states in HS. It was co-crystallized with a mononuclear species, independently of the ratio of the employed reagents (Figure 93).

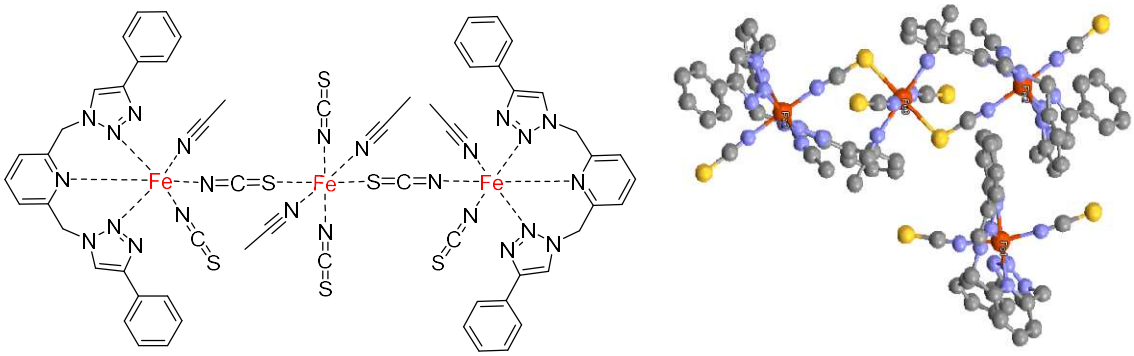

Figure 93. Left: Structure of the trinuclear Fe complex CAT-**36**, Right: Its X-ray structure, co-crystallizing with a mononuclear species. (Crystallography data in **6.4**)

Cooperativity was investigated using magnetic susceptibility measurements and its activity as CAT for CO_2 reduction compared with its mononuclear analogue, CAT-**11**. No evidence has been found yet to prove cooperativity effects between the Fe atoms. However, this trinuclear complex is currently under investigation.

Immobilization of homogeneous catalysts. The homogenous catalysts designed in this thesis have shown interesting activities for CO_2 reduction, which now have to evolve into more practical and reusable materials. Different strategies to immobilize them into bio-sourced hydrogels were explored in collaboration with Prof. Sambri from the university of Bologna (Italy).

The functionalized complexes CAT-**22**, CAT-**23** and CAT-**17_b** were employed to ionically and/or covalently bond with the carboxylic acid groups of the alginate structure (Figure 94).

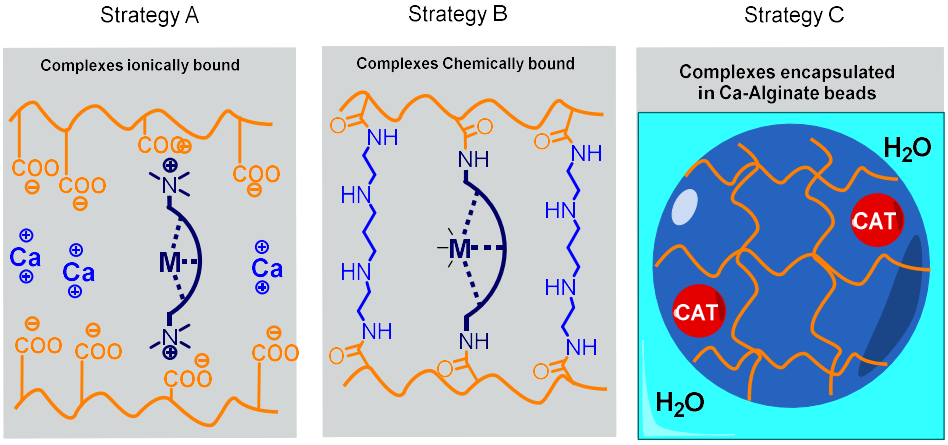

Figure 94. Different strategies approached to immobilize homogenous catalysts in alginate-based hydrogels.

The beads and cross-linked gels synthesized containing the metallic complexes were characterized using SEM and rheology (Table 32). However, atomic absorption revealed a very low quantity of metal inside the gel, likely due to the low solubility of the complexes used. This could explain their low or absent activity to transform CO_2 when employed as CAT for CO_2 photoreduction. Nevertheless, with strategy A and a mixture of Ca/Fe atoms to ionically form beads, 11 µmol of CO were detected when using those beads as CAT. Further experiments still have to be performed to incorporate more CAT into the gel and fully characterize them.

Table 32. Summary of the activity of the hydrogel formed for the photocatalytic reduction of CO_2

		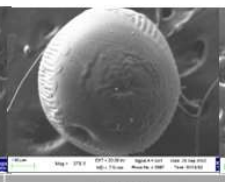	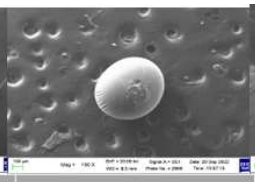	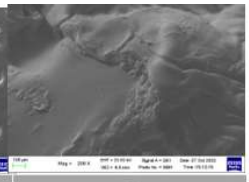
Strategy	**A**	**A / C**	**A**	**B**
Nature	Alginate – Ca	Alginate – Ca/Fe	Alginate – Ca + **23**	Alginate – Ca – **24**
Catalytic activity for CO_2 reduction	✗	✓	✗	✗
Scale	100 µm	100 µm	100 µm	100 µm

Those results are preliminary and promising for the evolution of homogeneous into immobilized systems.

Reproducibility. The reproducibility is a major drawback in artificial photosynthesis using homogeneous systems. The variety of components, various irradiation sources, analytic devices, and degree of purity of the components make those systems hard to reproduce and compare. Moreover, the strong focus on the TON of the CAT to evaluate the efficiency of the systems prevents access to a full picture of the system by neglecting other crucial information, such as the quantum yield and source of the light employed. To obtain higher TONs, lower concentrations of catalyst are employed (<1 μM), which are a source of higher error and trigger more irreproducible results.

General recommendations were reported by BELLER and coworkers to uniform the results and propose more comparable studies.[62] The recommendations mainly consist of the statement and repeat of independent experiment to average the results obtained.

During the work for this thesis, we observed that the different degree of purity of solvents and other components might affect greatly the results. Moreover, small variation in the position inside the photoreactor might change the amount of light received and therefore, influences the result. The employed glass-vials with diverse gas-tight closures, and the rotation speed of the stirring also triggered a tremendous change in the results, not only on the activity but also on the selectivity.

During this work, the recommendation stated by BELLER and coworkers were followed by using a minimum of two experiments before reporting results and by using different concentrations of catalyst to evaluate the systems when lowering the catalyst concentration. The solvent employed (included TEOA) were distilled and dehydrated over drying agents several times before use, and the solid components recrystallized at least twice. Moreover, we synthesized and characterized our catalysts that were added to the photocatalytic test rather than formed *in situ*, to minimize the risk of forming different and not controlled species. Precautions were taken by fixing a position in the photoreactor with tape, to avoid that the sample-vials could move, because of the stirring inside. Lastly, we recorded and calculated by chemical actinometry the quantum efficiencies of our systems and reported a detail description of the light system employed for easier reproducibility and comparison.

Nevertheless, even with those precaution taken; the reproducibility remained a challenge throughout this project.

5 SUPPLEMENTARY DATA

5.1 CYCLIC VOLTAMMETRY

Cyclic voltammetry and Differential Pulse voltammetry are electrochemical techniques that characterize redox behaviors of molecules. Not only the redox potentials can be determined with precision using the IUPAC[244] recommended Ferrocene as internal standard, but the activation of CO_2 can also be studied. The redox potentials are determined under argon atmosphere, avoiding the presence of O_2, whose redox potentials would pollute the cyclic voltammogram and which can also react trigger electronic transfers with the species analysed. Changing the atmosphere to CO_2, it can trigger reactions, which are revealed by shifts of the redox potentials or increase of the current, showing at which potential and thus, which redox species reacts with CO_2.

Cyclic voltammetry measures and displays potential cycles which can allow to determine the reversibility of the redox processes. Reversible or quasi reversible processes give $E_{1/2}$ as potential of equilibrium between two redox states, while irreversible processes only give an estimation of this equilibrium using the potential of the cathodic or anodic peak observed Ep. Irreversible processes can be caused mainly by two factors, slow electron transfer kinetic and a chemical reaction between the redox species generated.[245] Under CO_2 atmosphere, a reaction between a redox state of the complex studied can be shown by a shift in the potential of this same redox process, and by an increase of the current (catalytic current). The increase of the current demonstrates the formation of a new species [complex]-CO_2 adducts.

Differential Pulse voltammetry has a higher sensitivity and can allow to detect more precisely redox processes increasing the signal to noise ratio. This technique consists of applying amplitude potential pulses on a linear ramp potential. Also in this case, the reaction between the species and CO_2 is easily visible by a net increase of the current observed with a possible shift of the potential compared with the potential of the redox process under argon.

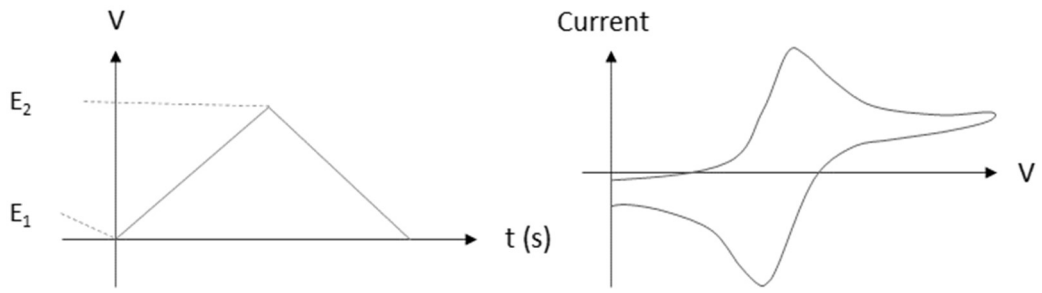

Figure 95. Cyclic voltammetry – Left: Potential in function of the time – Right: usual cyclic voltammogram (with a reversible process).

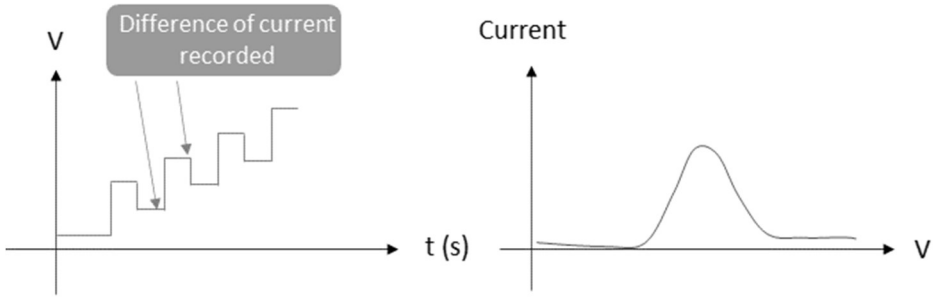

Figure 96. Differential Pulse Voltammetry – Left: Potential in function of the time and points where the current is measured (red arrows) – Right: usual voltammogram.

For both techniques, the set up employed was MeCN/TEOA (5:1 v/v) or DMA/TEOA (5:1 v/v), 0.1 M $TBAPF_6$ (recrystallized) as supporting electrolyte, a glassy carbon disk as working electrode, a Pt wire as counter electrode and a silver wire as reference. For cyclic voltammetry, the scan rates of 100 mV/s was used as standard for redox potentials values and schemes. Ferrocene or decamethylferrocene were employed as internal standards as recommended by IUPAC.[244]

The higher the reduction potential is observed, the easier they are reduced and the easier it is for them to enter the catalytic cycle for CO_2 reduction. Those techniques were thus employed for characterization and preliminary investigation for CO_2 activation.

5.2 CYCLIC VOLTAMMOGRAMS OF A BLANK, PS-24, LIGANDS L-6 AND L-26

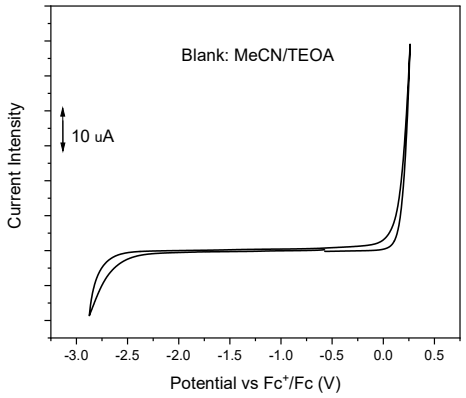

Figure 97. Cyclic voltammogram of DMA/TEOA, reported *vs* Fc+/Fc, 0.1 M $TBAPF_6$, at 100 mV/s.

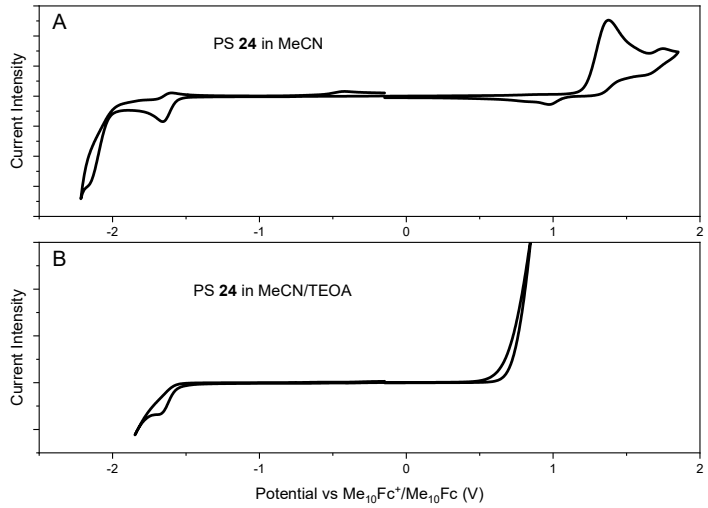

Figure 98. Cyclic voltammogram of PS-**24** in MeCN (Top) and MeCN/TEOA (Bottom), reported *vs* $Me_{10}Fc^{+}/Me_{10}Fc$, 0.1 M $TBAPF_6$, at 100 mV/s.

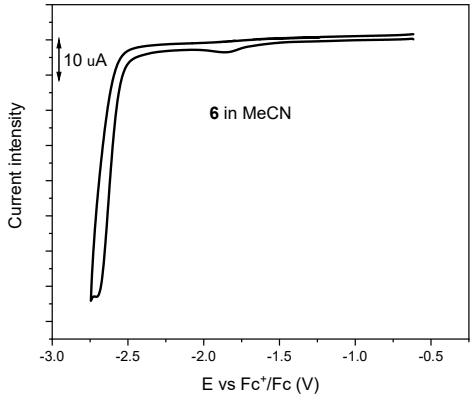

Figure 99. Cyclic voltammogram of L-**6** in MeCN, reported *vs* Fc^{+}/Fc, 0.1 M TBAPF6, at 100 mV/s.

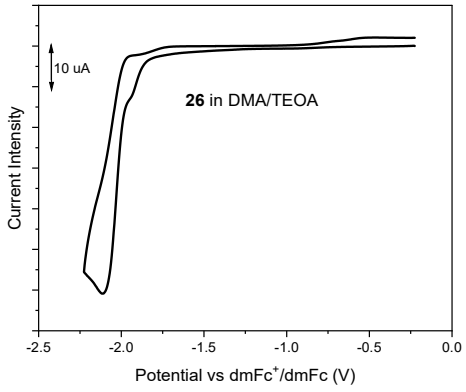

Figure 100. Cyclic voltammogram of L-**26** in DMA/TEOA, reported *vs* $Me_{10}Fc^{+}$/ $Me_{10}Fc$, 0.1 M $TBAPF_6$, at 100 mV/s

5.3 EVANS METHOD

This technique consists of determining the shift in ppm or Hz in ^{1}H NMR between a reference and the sample studied.[246] When the complex is paramagnetic, the reference signal (solvent) dissolved with it will be shifted compared to its signal without the paramagnetic substance. The shift difference in Hz allow the calculation of the number of electron unpaired in the degenerated d orbitals. The solvent used was methanol and acetonitrile.

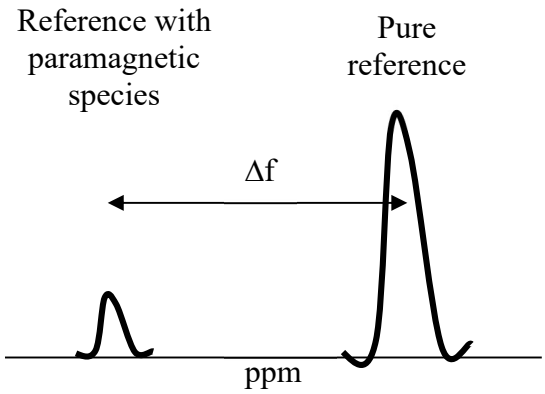

Figure 101. Difference of shift in ppm of a reference recorded alone and this reference recorded with presence of a paramagnetic species.

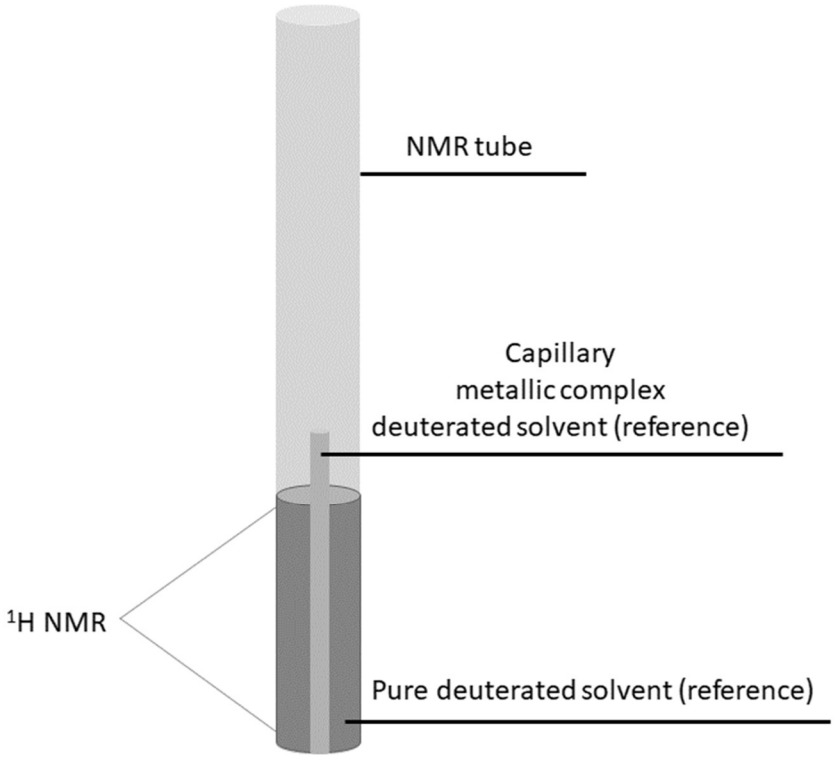

Figure 102. Preparation of the NMR sample to use the Evans method.

Table 33. Spin-only for n number of electron unpaired and equations used for calculations

Unpaired e^-	Spin-only (Bohr magnetons)
n = 1	1.7
n = 2	2.8
n = 3	3.8
n = 4	4.9
n = 5	5.9

$$\mu\mathbf{eff} = \sqrt{(n(n+2))}$$

n = sum of unpaired electrons

$$\mu\mathbf{eff} = \sqrt{(n(n+2))} = 2.84 \times \sqrt{(\chi m T)}$$

$$\chi_m = \frac{477\Delta f}{2cFspec}$$

With Δf = shift (Hz), c molar concentration mol/L

Fspec NMR frequency (Hz), χ_m molar magnetic susceptibility (cm^3/mol)

μ_{eff} calc magnetic moment measured

μ_{eff} theory magnetic moment calculated (Bohr magnetons)

Example with CAT-**11** in MeCN-d_3

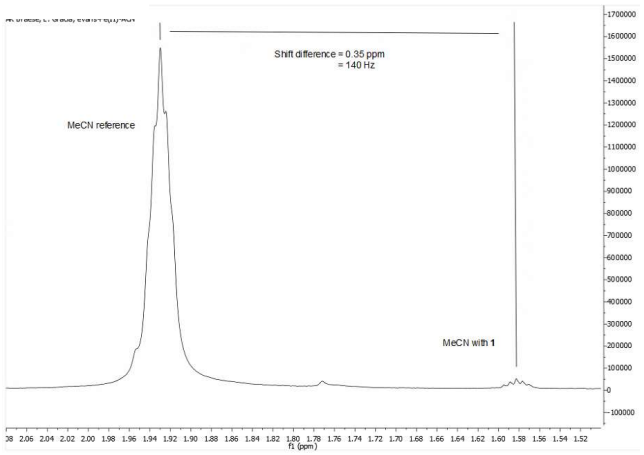

Figure 103. Example of the ^{1}H NMR spectra of the Evans test realised with the Fe CAT-**11** in MeCN d_3.

Example with CAT-**34** in THF-d_8

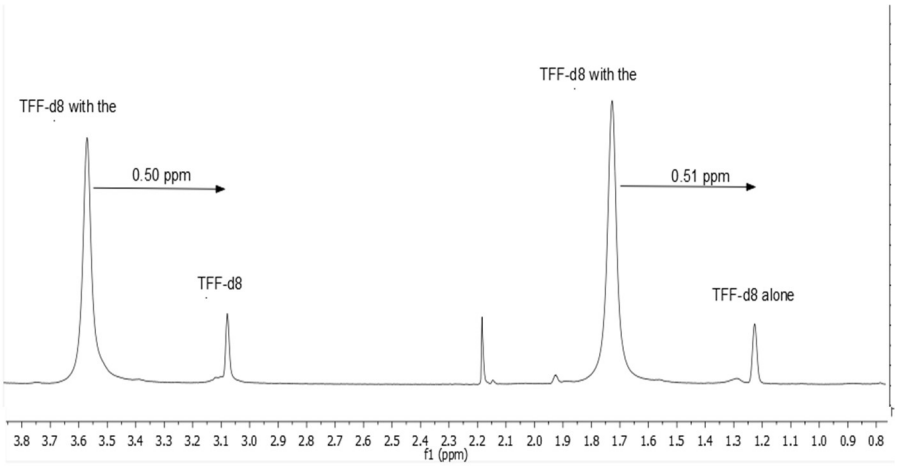

Figure 104. Example of the ^{1}H NMR spectra of the Evans test realised with the bimetallic cobalt **CAT-34** in MeCN d_3.

5.4 STERN VOLMER ANALYSIS

Reductive quenching : a) PS + hv = PS*; b) PS* + BIH → PS^- + $BI^{+\cdot}$, c) PS^- + CAT → PS + CAT^-

Oxidative quenching : a) PS + hv = PS*; b) PS* + CAT → PS^+ + CAT^-; c) PS^+ + BIH → PS + BI^+

The apparent quenching rate constants can be calculated thanks to the Stern Volmer equation 19.

$$\frac{I(0)}{I(f)} = 1 + KqTo \cdot [Q] \quad (19)$$

with **I(0)** the rate of fluorescence without quencher, **I(f)** the rate of fluorescence with quencher Q, **Kq** the quencher rate coefficient, ***To*** the lifetime of the excited state without quencher and **[Q]** the concentration of quencher. Thus, if plotting f([Q]) =I(0)/I(f) gives a linear function, it proves the feasibility of the energy transfer between PS* and the quencher with the acceleration of the slopes giving KqTo.[247]

5.5 PHOTOCATALYTIC TESTS WITH THE PRECURSORS

The metallic precursors employed bought (perchlorate based) and prepared (NCS-based) were tested as CAT in different solvents (MeCN, DMA with TEOA). Similarly to what was observed in the results with Fe-based catalysts, the Fe precursors showed a much better activity in MeCN with a higher selectivity for CO over molecular hydrogen. (Table 34, Entries 3, 4 and 10). Likewise, the cobalt precursors showed a much higher activity in DMA compared with in MeCN, however they produce more hydrogen than CO. (Table 34, Entries 1, 2, 8 and 9) The Mn precursor produced almost selectively hydrogen with a very high quantity produced (52.2 μmol, Table 34, Entry 5). Both Ni and Zn precursors did not show any relevant activities. (Table 34, Entries 6 and 7)

Table 34. Photocatalytic results with the precursors as CAT and PS-**24** in solvent/TEOA 5:1 v/v.[a]

Entry	[CAT]b	CO /μmol	H_2 /μmol	TON_{CO}	TON_{H2}	Sel.COc	Solvent/TEOA
1	$Co(NCS)_2py_4$	0.23	20.7	0,6	46	1%	ACN
2	$Co(NCS)_2py_4$	4.52	30.3	11.8	67.5	15%	DMA
3	$Fe(NCS)_2py_4$	13.1	11.3	34.3	25.1	58%	ACN
4	$Fe(NCS)_2py_4$	0.07	28.9	0.2	64.2	-	DMA
5	$Mn(NCS)_2py_4$	0.19	52.2	0.5	116	-	ACN
6	$Zn(NCS)_2py_4$	-	-	0	0	-	ACN
7	$Ni(NCS)_2py_4$	-	1.80	0	4	-	ACN
8	$Co(ClO_4)_2$, H_2O	0.11	1.71	0,3	3,8	7%	ACN
9	$Co(ClO_4)2$, H_2O	5.75	32.7	15	72.6	17%	DMA
10	$Fe(ClO_4)_2$, H_2O	1.80	0.54	4,7	1,2	80%	ACN

[a] The experiments were performed in solvent/TEOA (5:1, v/v) with 20 mM BIH and 1.0 mM PS **24** and [CAT] = 0.1 mM, under CO_2 atmosphere at 22 °C and the products were measured by GC after 4 h irradiation at 420 nm. The products formed were analyzed from the headspace by GC.

5.6 ACTINOMETRY

chemical actinometry was employed to calculate the quantum yield of our system by recording the number of photons received by the system from the source of light employed (photoreactor and solar simulator). In this technique, ferrioxalate was chosen as actinometer to be exposed to the photons sent by the light source converting the Fe^{III} ions to Fe^{II}, which have a known quantum yield. The more the actinometer (ferrioxolate) is exposed to the light (photons), the higher the conversion of Fe^{III} to Fe^{II} will be. This time-dependant conversion can be quantitatively recorded by UV-vis by complexing the formed Fe^{II} with 1,10-phenanthroline forming ferroin (lambda max 510 nm).[248]

The reactions involved are shown in Scheme 40.[249]

1.

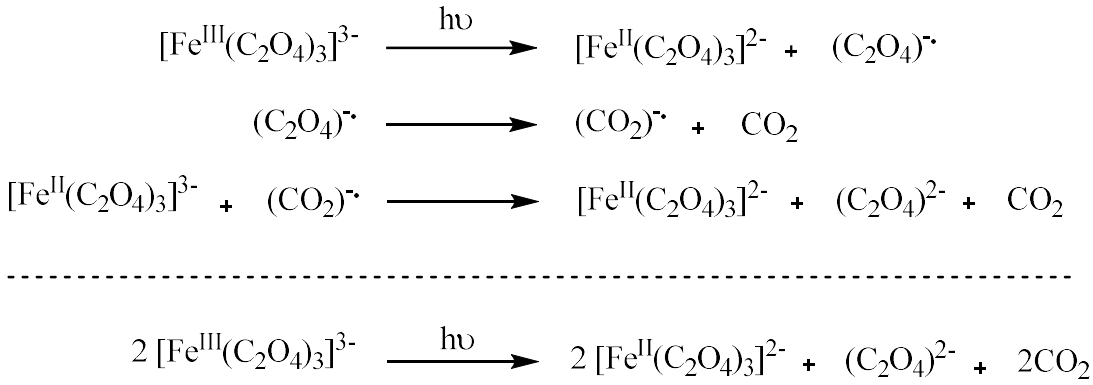

2.

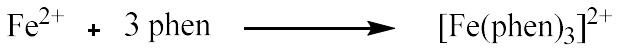

Scheme 40. Reactions involved using ferrioxolate as actinometer.

In our case, short time frames were employed (<10 seconds) and once the increasing absorption values were collected at four different times (0, 1.5, 2.5, 4 seconds), the number of photons was calculated using the following equations:

$$Np = \frac{\Delta A \,.V1\,.0.001\,.V3}{\Phi\lambda\,.\varepsilon(510).V2\,.l\,.t} \qquad (20)$$

With ε(510 nm) = 11 100 $dm^3\ mol^{-1}\ cm^{-1}$, V1 is the irradiated volume (3 mL), V2 the aliquot of the irradiated solution taken for the determination of the ferrous ions (3 mL), V3 the final volume after complexation with phenanthroline (3.5 mL) and l the optical pathlength of the irradiation cell. The calculated number of photons can then be implemented in the equation to calculate the quantum yield of the photocatalytic reaction (see introduction).

6 EXPERIMENTAL

6.1 GENERAL REMARKS

6.1.1 Material and Methods

The starting materials, solvents, and reagents were purchased from ABCR, ACROS, ALFA AESAR, APOLLO SCIENTIFIC, CHEMPUR, MERCK, SIGMA ALDRICH, TCI or THERMO FISHER SCIENTIFIC and used without further purification unless stated otherwise.

Solvents of technical quality were purified by distillation or with the solvent purification system MB SPS5 (dichloromethane, tetrahydrofuran, acetonitrile) from MBRAUN. Solvents of *p.a.* quality were purchased from ACROS, FISHER SCIENTIFIC, SIGMA ALDRICH or ROTHand were used without further purification. Other solvents were obtained from commercial suppliers: anhydrous *N,N*-dimethylformamide (SIGMA ALDRICH, <0.005% water) and *N,N*-dimethylacetamide (SIGMA ALDRICH, <0.005% water).

Oxygen-free solvents were obtained by degassing with argon for 20 minutes.

Liquids were added with a stainless-steel cannula, and solids were added in a powdered shape.

Air- and moisture-sensitive reactions were carried out under an argon atmosphere in oven-dried glassware using standard SCHLENK techniques. For reaction set-ups in the glovebox, a MBRAUN LABmaster with argon atmosphere was used. All materials used were dried for at least 24 hours at 100 °C before bringing them into the glovebox.

For the photocatalytic tests, 20 mL LABSOLUTE® glass vials from TH.Geyer were employed with 18 mm Ultra Clean caps.

Reactions at low temperatures were cooled using Dewars produced by ISOTHERM with water/ice or acetone/anhydrous ice mixtures.

Solvents were evaporated under reduced pressure at 45 °C using a rotary evaporator.

For solvent mixtures, each solvent was measured volumetrically.

Flash column chromatography was performed using MERCK silica 60 (0.040 x 0.063 mm, 230-400 mesh ASTM) and quartz sand (glowed and purified with hydrochloric acid). Additionally, a PureC-815 Flash devise by Buchi was used in combination with the columns: Büchi FlashPure EcoFlex (4g, Silica 50µm irregular), or Interchim Puriflash® (12g, Silica HP, 50µm)

All reactions were monitored by thin-layer chromatography (TLC) using silica-coated aluminum plates (MERCK, silica 60, F254). UV active compounds were detected with a UV lamp at 254 nm and 365 nm excitation. Basic potassium permanganate or Seebach solution was used as a TLC stain when required.

Mercury poisoning tests. A large excess of molecular mercury (1000 equiv.) was added in a typical catalytic test (4 mL) with 1 (0.1 mM) as catalyst under CO2 atmosphere, and vigorously stirred all along the 4 hours irradiation at 420 nm. Mercury poisoning test consists of removing possible heterogeneous metal nanoparticles if and when formed after decomposition of 1 and PS. It is an indication and not a proof to determine the presence or lack of heterogeneous materials in our photolysis solutions.

Carbon-13 labelling experiments. The solutions (4 mL) containing or not CAT-**11** (0.1 mM), PS (1 mM), BIH (20 mM) was purged with Ar for 10 min, followed by $^{13}CO2$ previously formed by adding H_2SO4 conc. on $NaH^{13}CO3$ (purchased from Sigma Aldrich). The ^{13}CO generated during the photoirradiation was detected by ^{13}C NMR.

Quantum chemical calculations. The calculations of the CO_2 binding energies were performed with the program package Turbomole using density functional theory (DFT) with the B3LYP functional and a def2-TZVP basis set. For the determination of reaction mechanisms the r2SCAN-3c method, which includes D4-dispersion as well as the geometrical Counterpoise Correction (gCP) and a modified version of the def2-TZVP basis set is used. The r2SCAN calculations were performed with ORCA 5.0.2.

6.1.2 Devices

Nuclear Magnetic Resonance Spectroscopy (NMR)

NMR spectra were recorded on a BRUKER AVANCE 400 NMR instrument at 400 MHz for ^1H NMR, 100 MHz for ^{13}C NMR, and 128 MHz for ^{11}B NMR. The NMR spectra were recorded at 22 °C in deuterated solvents acquired from EURISOTOP or DEUTERO. The chemical shift δ is displayed as parts per million [ppm] and the references used were the ^1H and ^{13}C peaks of the solvents: chloroform (^1H: δ = 7.27 ppm; ^{13}C: δ = 77.0 ppm), acetonitrile (^1H: δ = 1.94 ppm; ^{13}C: δ = 1.32 ppm and δ = 118 ppm), tetrahydrofuran (^1H: δ = 3.58 ppm; ^{13}C: δ = 67.6 ppm) and methanol (^1H: δ = 3.31 ppm; ^{13}C: δ = 49.0 ppm). The recorded spectra were evaluated by 1st order. For the characterization of centrosymmetric signals, the median point was chosen, for multiplets in the signal range. The following abbreviations were used to describe the proton splitting pattern: s = singlet, d = doublet, t = triplet, m = multiplet, dd = doublet of a doublet, ddd = doublet of doublet of a doublet, dt = doublet of triplet, td = triplet of a doublet. Absolute values of the coupling constants *J* are given in Hertz [Hz]in absolute value and decreasing order. The assignment of the signals *via* ^1H NMR spectra was based on the multiplicity and the chemical shift. The assignment of the signals *via* ^{13}C NMR spectra was based on the chemical shift. Common solvent and solvent impurity signals as follows were not explicitly listed: chloroform: ^1H NMR 1.55 (H_2O), 1.25 (H grease), 0.84-0.87 (H grease), 0.07 (silicon grease) ppm; ^{13}C NMR 29.7 (H grease), 1.2 (silicon grease) ppm; dichloromethane: ^1H NMR 1.52 (H_2O), 1.29 (H grease), 0.84-0.90 (H grease), 0.09 (silicon grease) ppm; ^{13}C NMR 30.1 (H grease), 1.2 (silicon grease)

ppm; tetrahydrofuran: ^{1}H NMR 10.84 (THF-d_8 impurity), 2.49 (H_2O), 1.73 (THF-d_8), 1.29 (H grease), 0.84-0.91 (H grease), 0.11 (silicon grease) ppm; ^{13}C NMR 29.9 (H grease), 1.2 (silicon grease) ppm.

Infrared Spectroscopy (IR)

The infrared spectra were recorded with a BRUKER ALPHA P instrument. All samples were measured by attenuated total reflection (ATR). The positions of the absorption bands are given in wavenumbers $\tilde{\nu}$ in cm^{-1} and were measured in the range from 3600 cm^{-1} to 500 cm^{-1}.

Mass Spectrometry (MS)

Electron ionization (EI) and fast atom bombardment (FAB) experiments were conducted using a FINNIGAN MAT 90 (70 eV) instrument, with 3-nitrobenzyl alcohol (3-NBA) as matrix and reference for high resolution. For the interpretation of the spectra, molecular peaks $[M]^+$, peaks of protonated molecules $[M+H]^+$, and characteristic fragment peaks are indicated with their mass-to-charge ratio (*m/z*) and their intensity in percent, relative to the base peak (100%), is given. In the case of high-resolution measurements, the maximum tolerated error is ±5 ppm.

Electron spray ionization (ESI) experiments were recorded on a THERMO FISHER SCIENTIFIC Q-EXACTIVE (ORBITRAP) mass spectrometer equipped with a HESI II probe to record high resolution or a THERMO FISHER SCIENTIFIC LTQ ORBITRAP XL. The tolerated error is ±5 ppm of the molecular mass. The spectra were interpreted by molecular peaks $[M]^+$, peaks of protonated molecules $[M+H]^+$, and characteristic fragment peaks and indicated with their mass-to-charge ratio (*m/z*).

Absorption Spectroscopy

UV-vis spectra were recorded in MeCN with ALS SEC 2020 Wide wavelength range spectrometer (200–1025 nm). Emission spectra were recorded with a Fluoromax 4 from Horiba Jobin.

Emission Spectroscopy

Emission spectra were recorded on a HORIBA SCIENTIFIC FLUOROMAX-4 spectrofluorometer equipped with a CZERNY-TURNER-type monochromator and an R928P PMT detector.

Cyclic Voltammetry

Cyclic voltammetry and differential pulse voltammetry were recorded on a Gamry Interface 1010B using a 3 electrodes cell system. The working electrode was a glassy carbon, the auxiliary electrode a Pt wire and the quasi-reference electrode an Ag wire; thus, ferrocene was used as the internal standard. All experiments were conducted in MeCN, DMA or MeCN/TEOA (5:1, v/v) with 0.1 M $TBAPF_6$ as supporting electrolyte under argon or CO_2 atmosphere. For easier comparison, according to IUPAC recommendation, all the redox properties were reported versus ferrocene (Fc^+/Fc couple).[250]

Melting Point

Melting points were measured on an OPTIMELT MPA100 device from STANFORD RESEARCH SYSTEM.

Gas Chromatography

The number of molecules CO formed was determined by quantitative GC measurement (Shimadzu GC-2030) from the headspace of the reaction, using Shimadzu BID-2030 detectors, column 1 Shimadzu SH-Rt-U-Bond PLOT; 0.32 mm ID; 10 um df; 30 m, column 2 Shimadzu SH-Rt-Msieve 5 Å; 0.32 mm ID; 30 µm; 30 m, and Ar as carrier gas. 50 µL of gas were automatically injected (AOC-6000 plus RSI LIQUID HS) with a gas-tight syringe and a split injection of 1/20. The method description is: incubation of sample at 30 °C for 5 min, injection 50 µL, 20 split ratio, at oven temp. 40 °C, 2 min after injection begin ramping over 7 min to 180 °C, hold 180 for 2 min., col.1 flow 3.32 ml/min, col.2 flow 1.85 ml/min. Calibration curves were carried out with known standard quantities of CO and H_2.

Photoreactor

A photoreactor LZC-IC2 from Luzchem with 2 fluorescent lamps (8 W) was employed. The temperature was constant at 22 °C. Actinometry using $K_3Fe(C_2O_4)_3$ was performed to determine the total photon flux ($2.5 \times 10^{-8} s^{-1}$) and the number incident photons.

Rheology

Anton Paar MCR 102 rheometer in a plate-plate geometry with a diameter of 25 mm (PP-25 plate). We did amplitude sweep tests, keeping the frequency constant at 5 s-1 and varying the amplitude of the strain oscillation from 0,001 to 1000%. T=20°C and F= 0 N (The normal force was set equal to zero, so that the sample does not feel any compression).

6.2 SYNTHESIS OF THE LIGANDS

2,6-bis(4-phenyl-1,2,3-triazol-1-ylmethyl)pyridine (**6**) was synthesized according to a previous publication.[167]

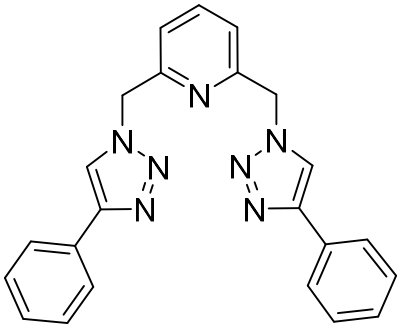

In a 100 mL flask, 2.00 equivalent (0.48 mL, 4.90 mmol) of phenylacetylene were dissolved in 10 mL of a solution of ethanol and water (7:3). 2,6-bis(bromomethyl)pyridine (662 mg, 2.40 mmol, 1.00 equiv.) was added, followed by NaN_3 (650 mg, 9.8 mmol, 4.00 equiv), sodium ascorbate (495 mg, 2.32 mmol, 1.00 equiv), $CuSO_4(\cdot 5H_2O)$ (624 mg, 3.40 mmol, 1.4 equiv) and sodium carbonate (249 mg, 2.76 mmol, 1.20 equiv). The reaction mixture was stirred for 18 h at 20 °C. The reaction was stopped by addition of a solution of NH_4OH (10%). The precipitate was filtered off, dissolved in dichloromethane and washed with NH_4OH (10 wt% solution) three times. The organic phases were washed with brine, dried over $MgSO_4$.The solvent was removed under vacuum and the crude product was purified by flash column chromatography on silica gel (*DCM*/MeOH, 99:1 to 95:5) to afford the title compound **6** as a white powder (754 mg, 1.92 mmol, 80%).

***R*f** (*DCM*/MeOH, 20:1) = 0.54. – **^{1}H NMR** (400 MHz, $CDCl_3$): δ = 8.16 (s, 2H, N*H*), 7.86 – 7.79 (m, 4H), 7.43 (t, *J* = 7.4 Hz, 4H), 7.38 – 7.34 (m, 3H), 7.32 (s, 4H, CH_2) ppm. – **^{13}C NMR** (126 MHz, $CDCl_3$): δ = 154.9 ($C_{triaz.}$), 148.5 ($C_{pyr.}$), 138.7 (C_{pyr}), 130.5 ($C_{benz.}$), 128.9 ($C_{benz.}$), 128.3 ($C_{benz.}$), 125.7 ($C_{benz.}$), 121.9 ppm, 120.2 ($C_{benz.}$), 55.2 (CH_2) – **IR** (ATR, $\tilde{\nu}$) = 3126, 3084, 3058, 3029, 3002, 2972, 2945, 1592, 1574, 1480, 1459, 1436, 1419, 1368, 1358, 1346, 1332, 1307, 1293, 1278, 1248, 1217, 1200, 1184, 1167, 1157, 1126, 1098, 1074, 1043, 1028, 996, 984, 975, 928, 909, 850, 837, 817, 802, 758, 724, 703, 687, 662, 645, 626, 591, 530, 507, 465, 435, 411 cm^{-1} - **MS** (ESI, 20 °C): *m/z* (%) =394.2 (100) $[M+H]^+$, 395.2 (12), 80.1 (28), 396.2 (3.0). **m.p**.:142°C

Trimethyl(2-quinolin-2-ylethynyl)silane was synthesized according to a previous publication.[56]

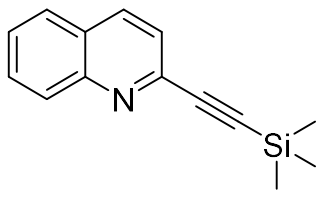

Under argon atmosphere, 2-bromoquinoline (1.25 g, 6.00 mmol, 1.00 eq) was dissolved in 20 mL of dry DIPA, dichloropalladiumtriphenylphosphine (45 mg, 0.06 mmol, 0,01 eq) was added with copper iodide (38 mg, 0.012 mmol, 0.02 eq) and trimethylsilyacetylene (4.25 mL, 30.0 mmol, 5.00 eq). The solution was stirred at room temperature for 14 hours.

The mixture was quenched with 10 mL of water, and extracted with dichloromethane and dried over sodium carbonate. The solvent was removed under reduced pressure. The crude product was purified by

flash column chromatography on silica gel (*c*Hex/DCM, 1:1) to afford the desired product as a brown oil, (1.00 g, 5.52 mmol, 92%).

***R*f** (*c*Hex/DCM, 1:1) = 0.6. **^{1}H NMR** (400 MHz, $CDCl_3$): δ = 7.92 (t, *J* = 7.6 Hz, 2H, H_{benz}), 7.59 – 7.55 (m, 1H), 7.54 – 7.49 (m, 1H), 7.36 – 7.31 (m, 2H), 0.12 (s, 9H, C*H*$_3$) ppm – **MS** (ESI, 20 °C): *m/z* (%) = 225 (100) $[M+H]^+$, 224 (18.5), 226 (21).

2-ethynylquinoline [56]

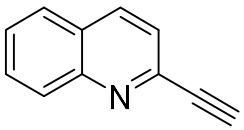

Trimethyl(2-quinolin-2-ylethynyl)silane (969 mg, 4.30 mmol, 1.00 eq) was dissolved in 15 mL of methanol, potassium carbonate (1.19 g, 8.60 mmol, 2.00 eq) was added and the solution was stirred at room temperature for 2 hours. To stop the reaction, 15 mL of water was added and the solution was extracted with dichloromethane to obtain 658 mg (4.30 mmol) of a brown oil, 86%

^{1}H NMR (400 MHz, $CDCl_3$): δ = 7.93 (t, *J* = 8.3 Hz, 2H, H_{benz}), 7.60 (dd, *J* = 8.1, 1.4 Hz, 4H, $H_{quin.}$), 7.53 (ddd, *J* = 8.4, 6.9, 1.5 Hz, 1H, $H_{quin.}$), 7.41 – 7.31 (m, 2H, $H_{benz.}$), 3.05 (s, 1H, H_{alkyne}) ppm. – **MS** (ESI): *m/z* (%) = 175 (100) $[M+Na]^+$.

1,3-bis((4-(quinol-2′yl)-1,2,3-triazol-1-yl)methyl)benzene [56]

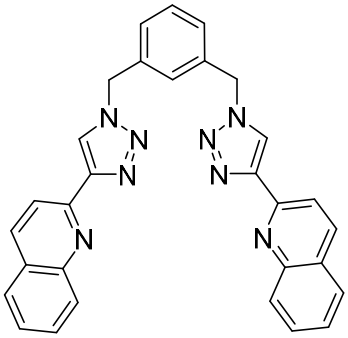

1,3-bis(bromomethyl)benzene (263 mg, 0.915mmol, 1.00 equiv.), 2-ethynylquinoline (280 mg, 1.83 mmol, 2.00 equiv.), sodium ascorbate (91 mg, 0.457 mmol, 0.50 equiv.), $CuSO_4$, $5H_2O$ (29 mg, 0.183 mmol, 0.2 equiv.) and Na_2CO_3 (58 mg, 0.549 mmol, 0.6 equiv.) were dissolved in 50 mL ethanol/water (7 : 3, v/v) and the mixture was stirred at room temperature for 24 hours. The mixture was quenched with NH_3OH (10%) 40mL and filtrated. The solid was washed with water, dissolved in DCM, dried over $MgSO_4$ and evacuated under reduced pressure and purified through recrystallization (*c*Hex/DCM). The product was filtered and dried to afford the desired product as a light-yellow solid (398 mg, 0.80 mmol, 88%).

***R*f** (*DCM*/MeOH, 20:1) = 0.47. – **^{1}H NMR** (400 MHz, $CDCl_3$): δ = 8.26 (s, 2H, $H_{triaz.}$), 8.04 (qd, *J* = 8.6, 1.8 Hz, 4H, $H_{quin.}$), 7.78 (d, *J* = 8.6 Hz, 2H, $H_{benz.}$), 7.59 (d, *J* = 8.5 Hz, 2H, $H_{quin.}$), 7.48 (t, *J* = 6.8 Hz, 2H, $H_{quin.}$). 7.29 (t, *J* = 6.8 Hz, 2H, H_{quin}), 7.24 – 7.1 (m, 4H), 5.44 (s, 4H, C*H*$_2$) ppm. – **^{13}C NMR** (126 MHz, $CDCl_3$): δ = 150.19, 149.25, 147.99, 136.93, 135.67, 130.16, 129.77, 128.99, 128.66, 127.87, 127.84, 127.79, 126.42, 122.86, 118.68, 54.04, 53.46 ppm. –**MS** (FAB, 3-NBA): *m/z* (%) = 495.2 (100) $[M+H]^+$. – **HRMS** ($C_{38}H_{31}O_4N_4$): calc.: 495.1967, found: 495.2038.

1,2-bis((4-(quinol-2′yl)-1,2,3-triazol-1-yl)methyl)benzene[56]

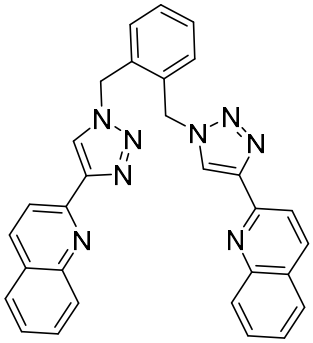

1,2-bis(bromomethyl)benzene (1.00 equiv, 0,915mmol, 263 mg), 2-ethynylquinoline (280 mg, 1.83 mmol, 2.00 equiv.), sodium ascorbate (91 mg, 0.457 mmol, 0.50 equiv.), $CuSO_4$, $5H_2O$ (29 mg, 0.183 mmol, 0.2 equiv.) and Na_2CO_3 (58 mg, 0.549 mmol, 0.6 equiv.) were dissolved in 50 mL ethanol/water (7 : 3, v/v) and the mixture was stirred at room temperature for 24 hours. The mixture was quenched with NH_3OH (10%) 40mL and filtrated. The solid was washed with water, dissolved in DCM, dried over $MgSO_4$ and evacuated under reduced pressure and purified through recrystallization (*c*Hex/DCM). The product was filtered and dried to afford the desired product as a light-yellow solid (254 mg, 0.51 mmol, 46%).

$\boldsymbol{R_f}$ (*DCM*/MeOH, 20:1) = 0.5. – **^{1}H NMR** (400 MHz, $CDCl_3$): δ = 8.78 (s, 2H), 8.42 (d, *J* = 7.2 Hz, 2H), 8.18 (d, *J* = 8.1 Hz, 2H), 7.98 (d, *J* = 7.8 Hz, 2H), 7.93 (d, *J* = 8.7 Hz, 2H), 7.72 (dd, *J* = 8.1, 7.2 Hz, 2H), 7.56 (dd, *J* = 7.8, 7.2 Hz, 2H), 7.41 (m, 2H), 7.38 (m, 2H), 6.00 (s, 4H) ppm. – **^{13}C NMR** (101 MHz, $CDCl_3$): δ = 150.29, 149.25, 147.99, 136.93, 135.67, 130.16, 129.77, 128.99, 128.66, 127.87, 127.8, 127.79, 126.42, 122.86, 118.68, 54.04, 53.46 ppm. – **MS** (FAB, 3-NBA): *m/z* (%) = 495.2 (100) $[M+H]^+$

1,4-bis((4-(quinol-2′yl)-1,2,3-triazol-1-yl)methyl)benzene[56]

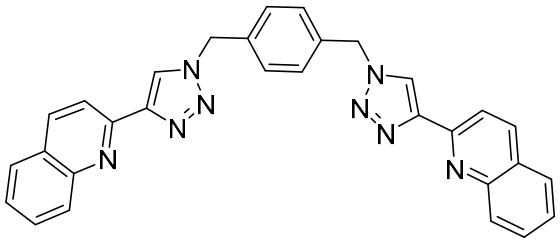

1,4-bis(bromomethyl)benzene (263 mg, 0,915mmol, 1.00 equiv,), 2-ethynylquinoline (280 mg, 1.83 mmol, 2.00 equiv.), sodium ascorbate (91 mg, 0.457 mmol, 0.50 equiv.), $CuSO_4$, $5H_2O$ (29 mg, 0.183 mmol, 0.2 equiv.) and Na_2CO_3 (58 mg, 0.549 mmol, 0.6 equiv.) were dissolved in 50 mL ethanol/water (7 : 3, v/v) and the mixture was stirred at room temperature for 24 hours. The mixture was quenched with NH_3OH (10%) 40mL and filtrated. The solid was washed with water, dissolved in DCM, dried over $MgSO_4$ and evacuated under reduced pressure and purified through recrystallization (*c*Hex/DCM). The product was filtered and dried to afford the desired product as a light-yellow solid (317 mg, 0.64 mmol, 70%). $\boldsymbol{R_f}$ (CH_2Cl_2/*c*Hex, 1:1) = 0.46. – **^{1}H NMR** (400 MHz, $CDCl_3$): δ = 8.36 (s, 2H), 8.33 (d, *J* = n.d., 2H), 8.27 (d, *J* = 8.7 Hz, 2H), 8.05 (d, *J* = 8.4 Hz, 2H), 7.83 (d, *J* = 8.1 Hz, 2H), 7.69 (dd, *J* = 9.0, 9.0 Hz, 2H), 7.52 (dd, *J* = 8.1, 6.9 Hz, 2H), 7.40 (s, 4H), 5.54 (s, 4H, CH_2) ppm. – **^{13}C NMR** (126 MHz, $CDCl_3$): δ = 150.31, 149.24, 148.01, 136.89, 135.30, 134.55, 129.74, 129.04, 128.99, 128.93, 128.74, 127.79, 126.40, 122.77, 118.64, 53.93 ppm. – **MS** (FAB, 3-NBA): *m/z* (%) = 495.2 (100) $[M+H]^+$

1-benzyl-4-(quinol-2-yl)-1,2,3-triazole [56]

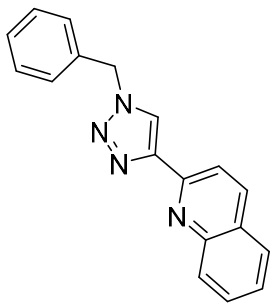

(azidomethyl)benzene (0.228 mL, 1.83 mmol, 1.00 equiv,), 2-ethynylquinoline (280 mg, 1.83 mmol, 1.00 equiv.), sodium ascorbate (90 mg, 0.457 mmol, 0.50 equiv.), $CuSO_4$, $5H_2O$ (29 mg, 0.366 mmol, 0.2 equiv.) and Na_2CO_3 (58 mg, 0.098 mmol, 0.60 equiv.,) were dissolved in 50 mL ethanol/water (7 : 3, v/v) and the mixture was stirred at room temperature for 24 hours. The mixture was quenched with NH_3OH (10%) 40mL and filtrated. The solid was washed with water, dissolved in DCM, dried over $MgSO_4$ and evacuated under reduced pressure and purified through recrystallization (*c*Hex/DCM). The product was filtered and dried to afford the desired product as a light-yellow solid (478 mg, 1.67 mmol, 91%).

***R*f** (*DCM*/MeOH, 20:1) = 0.42. – **^{1}H NMR** (400 MHz, $CDCl_3$): δ = 8.26 (d, *J* = 8.6 Hz 1H), 8.19 (s, 1H), 8.15 (d, *J* = 8.6 Hz, 1H), 7.93 (d, *J* = 8.5 Hz, 1H), 7.73 (dd, *J* = 8.1, 1.4 Hz, 1H), 7.60 (ddd, *J* = 8.4, 6.9, 1.5 Hz, 1H). 7.42 (ddd, *J* = 8.0, 6.8, 1.0 Hz, 1H), 7.38 – 7.25 (m, 5H), 5.54 (s, 2H, C*H*$_2$) ppm. – **^{13}C NMR** (126 MHz, $CDCl_3$): δ = 150.44, 149.08, 148.01, 136.89, CH), 134.38, 129.74, 129.21, 128.97, 128.89, 128.32, 127.81, 127.78, 126.37, 122.71, 118.70, 54.48 ppm. – **MS** (ESI): *m/z* (%) = 287.1 (93) $[M+H]^+$

1,3-bis((4-(quinol-2′yl)-1,2,3-triazol-1-yl)methyl)pyridine (**26**)

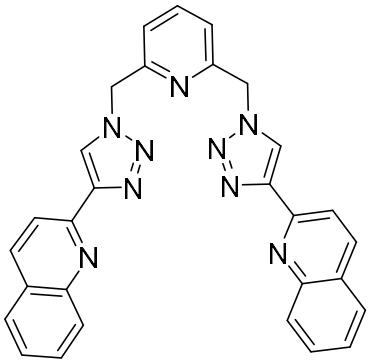

1,3-bis(bromomethyl)pyridine (265 mg, 1.00 mmol, 1.00 equiv.), 2-ethynylquinoline (306 mg, 2.00 mmol, 2.00 equiv.), sodium ascorbate (99 mg, 0.50 mmol, 0.50 equiv.), $CuSO_4$, $5H_2O$ (31.9 mg, 0.20 mmol, 0.2 equiv.) and Na_2CO_3 (63.6 mg, 0.6 mmol, 0.6 equiv.) were dissolved in 50 mL ethanol/water (7 : 3, v/v) and the mixture was stirred at room temperature for 24 hours. The mixture was quenched with NH_3OH (10%) 40mL and filtrated. The solid was washed with water, dissolved in DCM, dried over $MgSO_4$ and evacuated under reduced pressure and purified through recrystallization (*c*Hex/DCM). The product was filtered and dried to afford the title compound **26** as a light-yellow solid (400 mg, 0.81 mmol, 81%).

***R*f** (*DCM*/MeOH, 20:1) = 0.41. – **^{1}H NMR** (400 MHz, $CDCl_3$): δ = 8.48 (s, 2H), 8.30 (d, *J* = 8.5, 1H), 7.80 (dd, *J* = 8.1, 1.5 Hz, 1H), 7.74 – 7.63 (m, 2H), 7.51 (ddd, *J* = 8.0, 6.8, 1.2 Hz, 1H). 7.28 – 7.19 (m, 2H), 5.77 (s, 4H, C*H*$_2$) ppm. – **^{13}C NMR** (126 MHz, $CDCl_3$): δ = 154.81, 150.43, 149.39, 148.19, 138.90, 136.98, 129.86, 129.23, 127.89, 126.53, 123.60, 122.20, 118.80, 55.72 ppm. –**MS** (ESI): *m/z* (%) = 496 (100), 497 (36), 498 (8) $[M+H]^+$. – **HRMS-ESI** ($C_{38}H_{31}O_4N_4$): calc.: 496.1998, found: 496.1992.

4,6-bis(diphenylphosphaneyl)-10-(1,10-phenanthrolin-2-yl)-phenoxazine (**42**)

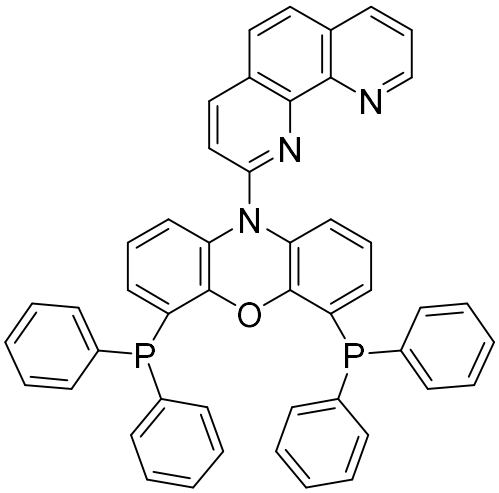

Under argon, N-Xantphos (212 mg, 0.386 mmol, 1.00 equiv.) was dissolved in dry THF (20 mL) with NaH (18.0 mg, 0.772 mmol, 2.00 equiv.) and stirred at room temperature for 1 hour. 2-bromo-1,10-phenanthroline (100 mg, 0.386 mmol, 1.00 equiv.) was then added to the mixture and it was stirred under reflux for 24 hours. The reaction was quenched with 15 mL water. The product was extracted with DCM, washed with water and brine and dried over $MgSO_4$. The solvent was removed under reduced pressure and the crude product was purified by flash column chromatography on silica gel (*DCM*/MeOH, 99:1) to afford the title compound **42** (251 mg, 0.343 mmol, 89%) a yellow solid.

***R*f** (*DCM*/) = 0.50. – **^{1}H NMR** (400 MHz, $CDCl_3$): δ = 9.25 (dd, *J* = 4.3, 1.8 Hz, 1H, $H_{phenanthroline}$), 8.34 (d, *J* = 8.5 Hz, 1H, $H_{phenanthroline}$), 8.29 (dd, *J* = 8.1, 1.8 Hz, 1H, $H_{phenanthroline}$), 7.84 (s, 2H), 7.70 (d, *J* = 8.5 Hz, 1H, $H_{phenanthroline}$), 7.67 (dd, *J* = 8.1, 4.3 Hz, 1H, $H_{phenanthroline}$), 7.27 – 7.23 (m, 20H, $H_{aromatic}$), 7.05 (dd, *J* = 8.1, 1.5 Hz, 2H, $H_{xantphos}$), 6.68 (t, *J* = 7.9 Hz, 2H, $H_{xantphos}$), 6.20 (dt, *J* = 7.9, 1.5 Hz, 2H, $H_{xantphos}$) ppm. – **^{13}C NMR** (101 MHz, $CDCl_3$): δ = 153 ($C_{phenanthroline}$), 150 ($C_{phenanthroline}$), 148 ($C_{phenanthroline}$), 146 (C_{Xant}-O), 139 ($C_{phenanthroline}$), 136, 135, 134, 133 ($C_{Ph-Xant}$), 132, 132, 129, 128 ($C_{Ph-Xant}$), 128, 127, 126, 126, 125, 123, 123, 121.1, 117 ($C_{phenanthroline}$) ppm. – ^{31}P NMR (400 MHz, $CDCl_3$): δ = -18.7 ppm – **MS** (ESI): *m/z* (%) = 730.2 (100) $[M+H]^+$, 731.2 (50), 732.2 (7), 729.2 (4) – **HRMS** (C48H33N3OP2): calc.: 730.2099, found: 730.1979. **Elemental analysis** ($C_{48}H_{33}N_3OP_2$ + NaBr (3/1)): C=75.46, H=4.35, N=5.50 (calc.); C=75.16, H=4.47, N=5.51 (found). **m.p.**:187°C

2,9-bis(4,6-bis(diphenylphosphaneyl)-phenoxazin-10-yl)-1,10-phenanthroline

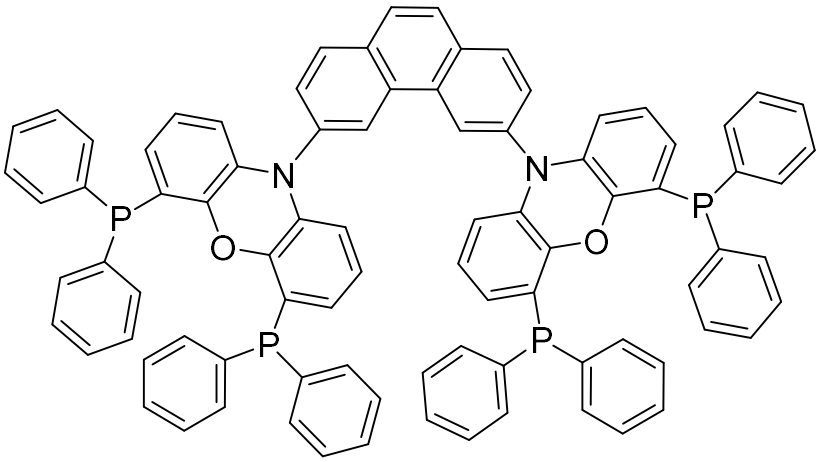

Under argon, N-Xantphos (326 mg, 0.592 mmol, 2.00 equiv.) was dissolved in dry THF (20 mL) with NaH (18.5 mg, 0.773 mmol, 2.00 equiv.) and stirred at room temperature for 1 hour. 2,9-dibromo-1,10-phenanthroline (100 mg, 0.296 mmol, 1.00 equiv.) was then added to the mixture and it was stirred under reflux for 24 hours. The reaction was quenched with 15 mL water. The product was extracted with DCM, washed with water and brine and dried over $MgSO_4$. The solvent was removed under reduced pressure and the crude product was purified by flash column chromatography on silica gel (*DCM*/MeOH, 99:1) to afford the desired product (272 mg, 0.213 mmol, 72%) a yellow solid.

$\boldsymbol{R_f}$ (*DCM*) = 0.42. – **^{1}H NMR** (400 MHz, $CDCl_3$): δ = 8.29 – 8.16 (m, 1H, $H_{phenanthroline}$), 8.13 – 8.00 (m, 2H, $H_{phenanthroline}$), 7.99 – 7.59 (m, 8H), 7.58 – 7.48 (m, 6H), 7.47 – 7.40 (m, 5H), 7.35 (dq, *J* = 7.7, 4.3 Hz, 5H), 7.25 – 7.20 (m, 24H, $H_{aromatic}$), 7.07 – 6.89 (m, 1H, $H_{xantphos}$), 7.07 – 6.89 (m, 1H, $H_{xantphos}$), 6.74 – 6.62 (m, 2H, $H_{xantphos}$), 6.60 – 6.46 (m, 2H, $H_{xantphos}$), 6.43 – 6.32 (m, 1H, $H_{xantphos}$), 6.32 – 6.25 (m, 1H, $H_{xantphos}$), 6.13 – 5.96 (m, 1H, $H_{xantphos}$) ppm. – **MS** (ESI): *m/z* (%) = 1278.8 (100) $[M+H]^+$, 1279.8 (77), 1277.8 (60), 1280.8 (36) – **Elemental analysis** ($C_{48}H_{33}N_3OP_2$ + NaBr (3/1)): C=76.75, H=4.52, N=4.26 (calc.); C=75.83, H=4.67, N=4.15 (found).

2,6-bis((4-(4-bromophenyl)-1,2,3-triazol-1-yl)methyl)pyridine (**7**)

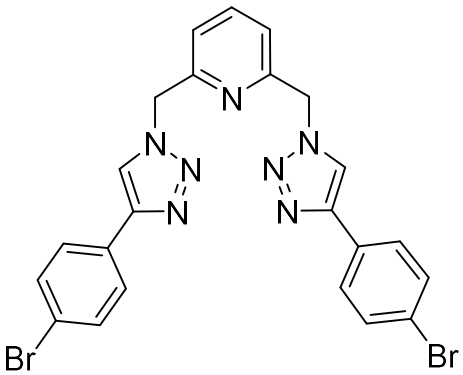

In a 100 mL flask, 2.00 equivalent (1.09 g, 6.00 mmol) of 1-bromo-4-ethynylbenzene was dissolved in 20 mL of a solution of ethanol and water (7:3). 2,6-bis(bromomethyl)pyridine (662 mg, 3.0 mmol, 1.00 equiv.) was added, followed by NaN_3 (650 mg, 9.8 mmol, 4.00 equiv), sodium ascorbate (495 mg, 2.32 mmol, 1.00 equiv), $CuSO_4(\cdot 5H_2O)$ (624 mg, 3.40 mmol, 1.4 equiv) and sodium carbonate (249 mg, 2.76 mmol, 1.20 equiv). The reaction mixture was stirred overnight at 20°C. The reaction was stopped by addition of a solution of NH_4OH (10%). The precipitate was filtered off, dissolved in dichloromethane and washed with NH_4OH (10 %solution) three times. The organic phases were washed with brine, dried over $MgSO_4$.The solvent

was removed under vacuum and the crude product was purified by recrystallization (*DCM*/MeOH) to afford the title compound **7** as a white powder (1.239 g, 2.25 mmol, 75%).

***R*f** (*DCM*/MeOH, 15:5) = 0.39. – **^{1}H NMR** (400 MHz, $CDCl_3$): δ = 7.82 (s, 2H, $H_{triaz.}$), 7.74 (t, *J* = 7.8 Hz, 1H), 7.63 (d, *J* = 8.6 Hz, 4H), 7.49 (d, *J* = 8.6 Hz, 4H), 7.23 (d, *J* = 8.6 Hz, 2H), 5.67 (s, 4H, CH_2) ppm. – **^{13}C NMR** (126 MHz, THF-d_8): δ = 155.4 ($C_{triaz.}$), 146.3 ($C_{pyr.}$), 138.6 (C_{pyr}), 131.7 ($C_{benz.}$), 130.2 ($C_{benz.}$), 127.0 ($C_{benz.}$), 121.5 ($C_{benz.}$), 121.9 ppm, 120.9 ($C_{benz.}$), 54.6 (CH_2) – **MS** (ESI, 20 °C): *m/z* (%) =551.9 (100) $[M+H]^+$, 549.99 (58), 553.99 (42). – **HRMS** ($C_{23}H_{18}N_7Br_2$): calc.: 551.9990, found: 551.9961. **m.p**.:150°C

2,6-bis((4-(4-aminophenyl)-1H-1,2,3-triazol-1-yl)methyl)pyridine (**8**)

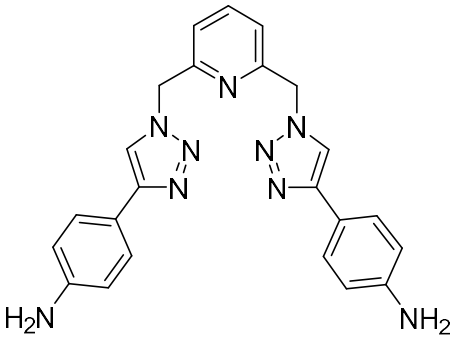

In a 100 mL flask, 2.00 equivalent (87.1 mg, 0.750 mmol) of 1-amino-4-ethynylbenzene was dissolved in 20 mL of a solution of ethanol and water (7:3). 2,6-bis(bromomethyl)pyridine (100 mg, 0.375 mmol, 1.00 equiv.) was added, followed by NaN_3 (97.5 mg, 1.50 mmol, 4.00 equiv), sodium ascorbate (74.2 mg, 0.375 mmol, 1.00 equiv), $CuSO_4 \cdot 5H_2O$ (131 mg, 0.53 mmol, 1.40 equiv) and sodium carbonate (47.6 mg, 0.45 mmol, 1.20 equiv). The reaction mixture was stirred overnight at 20°C. The reaction was stopped by addition of a solution of NH_4OH (10%). The precipitate was filtered off, dissolved in dichloromethane and washed with NH_4OH (10 % solution) three times. The organic phases were washed with brine, dried over $MgSO_4$.The solvent was removed under vacuum and the crude product was purified by column chromatography (*DCM*/MeOH 88:12) to afford the title compound **8** as a yellow powder (51.0 mg, 0.120 mmol, 32%).

***R*f** (*DCM*/MeOH, 10:1) = 0.18. – **^{1}H NMR** (400 MHz, $CDCl_3$): δ = 7.95 (s, 2H, $H_{triaz.}$), 7.72 (t, *J* = 8.0 Hz, 1H), 7. 71 (d, *J* = 8.0 Hz, 4H), 7.54 (d, *J* = 8.0 Hz, 4H), 7.46 (d, *J* = 7.8 Hz, 2H), 7.18 (d, *J* = 7.8 Hz, 2H) , 5.69 (s, 4H, CH_2) ppm. – **^{13}C NMR** (126 MHz, $CDCl_3$): δ = 171.06 ($C_{triaz.}$), 153.98 ($C_{pyr.}$), 138.32 (C_{pyr}), 131.91 ($C_{benz.}$), 127.44 ($C_{benz.}$), 122.6 ($C_{benz.}$), 122.1 ($C_{benz.}$), 121.76 ppm, 120.2 ($C_{benz.}$), 55.4 (CH_2 – **MS** (ESI, 20 °C): *m/z* (%) =223.12 (100), 221.12 (20), 224.12 (17) $[M+H+Na]^{2+}$.– **HRMS** ($C_{23}H_{22}N_9$): calc.: 424.1998, found: 424.1985.

2,6-bis((4-(4-dimethylaminophenyl)-1,2,3-triazol-1-yl)methyl)pyridine (**9**)

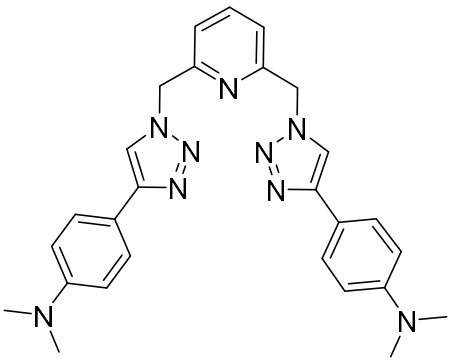

In a 100 mL flask, 2.00 equivalent (871 mg, 6.00 mmol) of 1-dimethylamino-4-ethynylbenzene was dissolved in 30 mL of a solution of ethanol and water (7:3). 2,6-bis(bromomethyl)pyridine (800 mg, 3.00 mmol, 1.00 equiv.) was added, followed by NaN_3 (780 mg, 12.0 mmol, 4.00 equiv), sodium ascorbate (594 mg, 3.00 mmol, 1.00 equiv), $CuSO_4 \cdot 5H_2O$ (1.05 g, 4.20 mmol, 1.40 equiv) and sodium carbonate (381 mg, 3.60 mmol, 1.20 equiv). The reaction mixture was stirred overnight at 20°C. The reaction was stopped by addition of a solution of NH_4OH (10%). The precipitate was filtered off, dissolved in dichloromethane and washed with NH_4OH (10 % solution) three times. The organic phases were washed with brine, dried over $MgSO_4$.The solvent was removed under vacuum and the crude product was purified by column chromatography (*DCM*/MeOH 98:2) to afford the title compound **9** as an orange powder (790 mg, 1.64 mmol, 55%).

^{1}H NMR (400 MHz, $CDCl_3$): δ = 7.74 (s, 2H, $H_{triaz.}$), 7.70 – 7.65 (m, 5H), 7.15 (d, J = 7.8 Hz, 2H, $H_{pyridine}$), 6.73 (d, J = 8.9 Hz, 4H, $H_{aromatic}$), 5.67 (s, 4H, CH_2), 2.98 (s, 12H, CH_3) ppm. – **^{13}C NMR** (126 MHz, $CDCl_3$): δ = 155.1 (C_{ar}), 150.41 (C_{ar}), 148.7 (C_{ar}), 138.92 (CH), 126.8 (CH), 122.1 (C_{ar}), 118.7 (C_{ar}), 112.6 (C_{ar}), 55.2 (CH_2), 40.3 (CH_3) ppm. – **MS** (ESI): *m/z* (%) = 480.26 (100), 479.26 (60), 481.26 (21) $[M+H]^+$. – **HRMS** ($C_{27}H_{30}N_9$): calc.: 480.2624, found: 480.2609.

2,6-bis((4-(4-trimethylammoniumphenyl)-1,2,3-triazol-1-yl)methyl)pyridine (**10**)

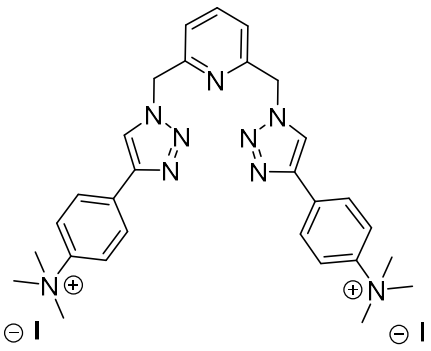

1.00 equivalent (220 mg, 0.40 mmol) of 4,4'-((pyridine-2,6 diylbis(methylene))bis(1,2,3-triazole-1,4-diyl))bis(N,N-dimethylaniline) number was dissolved in 4 mL of dichloroethane. 10.0 equiv. (0.240 mL, 4.00 mmol) of iodomethane were added and the mixture was stirred under reflux for 1 hour. The product was extracted with DCM and washed with water. The solvent was removed under reduced pressure to afford the title compound **10** as a beige powder (85.0 mg, 0.160 mmol, 36%).

^{1}H NMR (400 MHz, $CDCl_3$): δ = 8.55 (s, 2H, $H_{triaz.}$), 8.09 (d, J = 8.9 Hz, 4H, H_{ar}), 8.01 (d, J = 8.9 Hz, 4H, H_{ar}), 7.89 (td, J = 7.7, 3.0 Hz 2H, H_{pyr}), 5.79 (s, 4H, CH_2), 3.72 (s, 18H, CH_3) ppm. – **^{13}C NMR** (126 MHz, $CDCl_3$): δ = 156 (C_{ar}), 147 (C_{ar}), 146 (C_{ar}), 134 , 127, 124 (C_{ar}), 122 (C_{ar}), 57.6 (CH_2), 55.2 (CH_3) ppm. – **MS** (ESI): *m/z* (%) = 254.6 (100), 255.1 (30), 255.6 (9) $[M - 2I^-]^{2+}$. – **HRMS** ($C_{27}H_{31}N_9$): calc.: 254.6502, found: 254.6500.

6.3 SYNTHESIS OF THE COMPLEXES

[Cu(NN)(DPEPhos)]BF_4 (**2**)[56]

1-benzyl-4-(quinol-2′ yl)-1,2,3-triazole (NN) (183 mg, 0.640 mmol, 1.00 equiv.) was dissolved in dry DCM (10 mL) with DPEPhos (344 mg, 0.640 mmol, 1.00 equiv.) and $Cu(CH_3CN)_4BF_4$ (200 mg, 0.640 mmol, 1.00 equiv.) under argon atmosphere and the mixture was stirred at room temperature 1 hour.

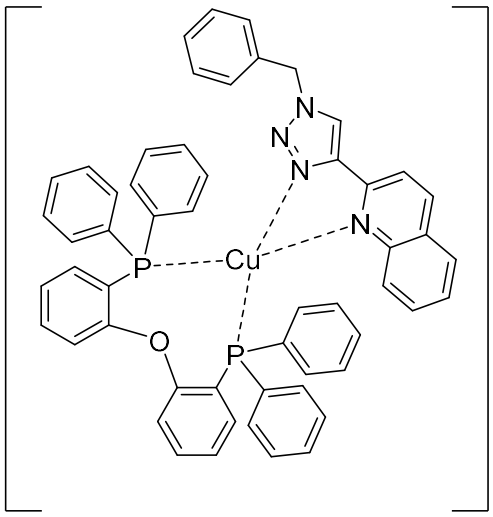

The mixture was concentrated under reduced pressure and Et_2O was added to precipitate the product. The product was filtered, thoroughly washed with Et_2O (5 × 50 mL) and dried under reduced pressure to yield the title compound **2** as a yellow solid (449 mg, 0.460 mmol, 72%).

R_f (CH_2Cl_2/*MeOH*, 15:1) = 0.64. – **^{1}H NMR** (400 MHz, $CDCl_3$): δ = 7.92 (s, 1H), 7.86 (d, J = 8.4 Hz, 1H), 8.71 – 7.19 (m, 3H), 6.76 – 6.42 (m, 25H), 6.34 – 6.25 (m, 6H), 6.03 – 5.95 (m, 4H), 4.99 (s, 2H) ppm. – **^{13}C NMR** (126 MHz, $CDCl_3$): δ = 158.55, 147.76, 145.97, 146.60, 139.00, 134.51, 134.56, 131.89, 131.57, 130.93, 130.66, 130.26, 129.62, 129.47, 128.88, 128.68, 128.53, 128.29, 127.72, 127.11, 125.80, 124.88, 120.08, 119.86, 54.97 ppm. – **^{31}P NMR** (162 MHz, $CDCl_3$): δ = -12.73 ppm. IR (ATR): ṽ = 3055, 1602, 1588, 1565, 1462, 1434, 1259, 1214, 1183, 1162, 1094, 1055, 1035, 1027, 1006, 949, 874, 857, 834, 802, 745, 720, 693, 635, 620, 544, 510, 486, 476, 467, 448, 435, 425, 414, 407, 401, 384 cm–1. – **HRMS** ($C_{54}H_{42}CuN_4OP_2$): calc.: 887.21, found:887.21. Elemental analysis ($C_{54}H_{42}CuN_4OP_2BF_4$): C=65.51, H=4.43, N=5.74 (calc.); C=65.53, H=4.357, N=5.54 (found).

[Cu(NN)(DPEPhos)]BF_4 (**4**)[56]

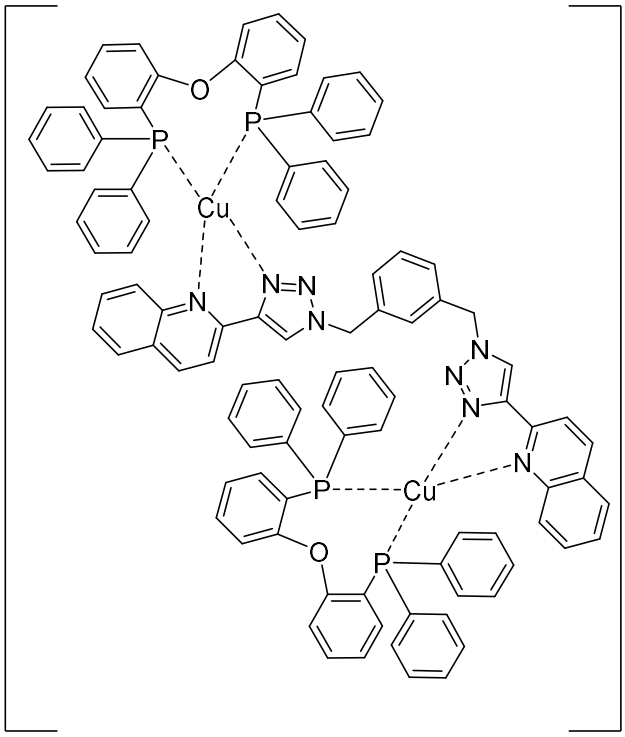

1,3-bis((4-(quinol-2′yl)-1,2,3-triazol-1-yl)methyl)benzene (NN) (227 mg, 0.46 mmol, 1.00 equiv.) was dissolved in dry DCM (10 mL) with DPEPhos (495 mg, 0.920 mmol, 2.00 equiv.) and $Cu(CH_3CN)_4BF_4$ (288 mg, 0.920 mmol, 2.00 equiv.) under argon atmosphere and the mixture was stirred at room temperature 1 hour. The mixture was concentrated under reduced pressure and Et_2O was added to precipitate the product. The product was filtered, thoroughly washed with Et_2O (5 × 50 mL) and dried under reduced pressure to yield the title compound **4** as a yellow solid (534 mg, 0.280 mmol, 62%)

***R*f** (CH_2Cl_2/*MeOH*, 15:1) = 0.49. – **^{1}H NMR** (400 MHz, $CDCl_3$): δ = 8.50 (s, 2H), 8.46 (m, 2H), 7.94 – 7.90 (m, 4H), 7.80 – 7.76 (m, 2H), 7.46 – 6.60 (m, 64H), 5.58 (s, 4H) ppm. – **^{13}C NMR** (126 MHz, $CDCl_3$): δ = 158.78, 149.87, 149.06, 147.54, 146.125, 135.89, 134.50, 132.52, 131.72, 130.43, 130.26, 129.00, 128.92, 128.76, 128.39, 127.86, 125.29, 124.75, 124.05, 123.93, 123.81, 120.77, 119.15, 55.76 ppm. – **^{31}P NMR** (162 MHz, $CDCl_3$): δ = -13.19 ppm. IR (ATR): $\tilde{\nu}$ = 3060, 1602, 1564, 1504, 1479, 1462, 1435, 1259, 1218, 1094, 1058, 1020, 1004, 999, 950, 914, 877, 837, 803, 749, 735, 694, 647, 633, 619, 545, 523, 510, 492, 477, 469, 441, 422, 412, 390, 381 cm–1. – **HRMS** ($C_{102}H_{78}Cu_2P_4N_8O_2BF_4$): calc.: 1785.38, found: 1785.39. **Elemental analysis** ($C_{102}H_{78}Cu_2N_8O_2P_4B_2F_8$): C=65.43, H=4.20, N=5.98 (calc.); C=65.29, H=4.242, N=5.93 (found).

[Cu(NN)(DPEPhos)]BF_4 (**3**)[56]

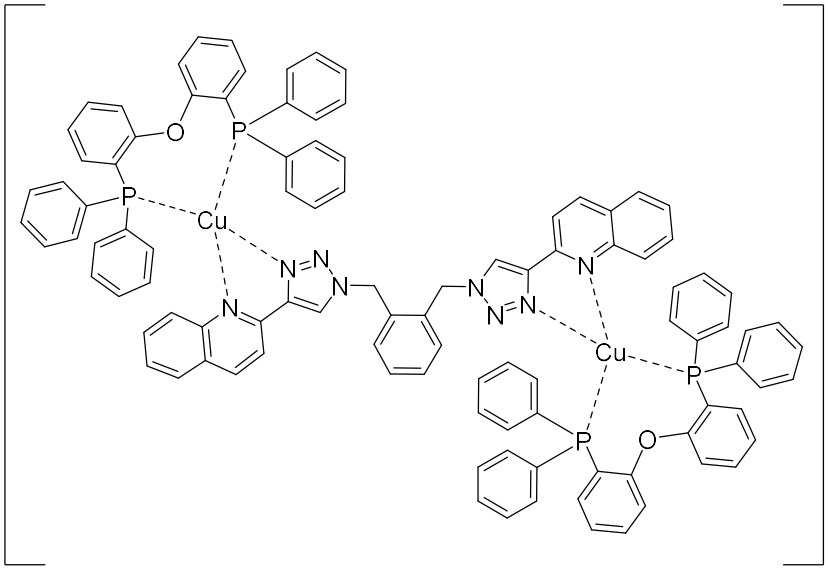

1,2-bis((4-(quinol-2′yl)-1,2,3-triazol-1-yl)methyl)benzene (NN) (138 mg, 0.28 mmol, 1.00 equiv.) was dissolved in dry DCM (10 mL) with DPEPhos (301 mg, 0.560 mmol, 2.00 equiv.) and $Cu(CH_3CN)_4BF_4$ (176 mg, 0.920 mmol, 2.00 equiv.) under argon atmosphere and the mixture was stirred at room temperature 1 hour. The mixture was concentrated under reduced pressure and Et_2O was added to precipitate the product. The product was filtered, thoroughly washed with Et_2O (5 × 50 mL) and dried under reduced pressure to yield the title compound **3** as a yellow solid (477 mg, 0.250 mmol, 91%).

***R*f** (CH_2Cl_2/*MeOH*, 15:1) = 0.50. – **^{1}H NMR** (400 MHz, $CDCl_3$): δ = 9.07 (s, 2H), 8.39 (d, *J* = 5.1 Hz, 2H), 8.11 (d, *J* = 5.1 Hz, 2H), 7.94 (d, *J* = 5.1 Hz, 2H), 7.81 (d, *J* = 5.1 Hz, 2H), 7.48 (m, 8H), 7.35 (dd, *J* = 4.5, 4.5 Hz, 2H), 7.28 - 7.24 (m, 12H), 7.22 – 7.19 (m, 8H), 7.10 (m, 4H), 7.04 (m, 4H), 6.93 (m, 6H), 6.84 (m, 8H), 6.72 – 6.69 (m, 4H), 6.60 – 6.57 (m, 8H), 5.85 (s, 4H) ppm. – **^{13}C NMR** (126 MHz, $CDCl_3$): δ = 158.62, 147.47, 146.16, 145.67, 139.04, 134.53, 134.09, 132.97, 131.97, 131.73, 131.03, 130.64, 130.35, 129.89, 129.49, 128.34, 128.32, 127.73, 127.35, 125.69, 124.69, 124.23, 120.13, 119.72, 51.52 ppm. – **^{31}P NMR** (162 MHz, $CDCl_3$): δ = -12.60 ppm. IR (ATR): $\tilde{\nu}$ = 3054, 2919, 2854, 1602, 1588, 1565, 1509, 1460, 1434, 1259, 1214, 1183, 1162, 1119, 1092, 1052, 1004, 997, 950, 874, 858, 833, 802, 744, 693, 633, 619, 544, 510, 486, 476, 446, 435, 422, 416, 408, 375 cm^{-1} – **HRMS** ($C_{102}H_{78}Cu_2P_4N_8O_2BF_4$): calc.: 1785.38, found: 1785.40. **Elemental analysis** ($C_{102}H_{78}Cu_2N_8O_2P_4B_2F_8$): C=65.43, H=4.20, N=5.98 (calc.); C=65.10, H=4.32, N=5.91 (found).

[Cu(NN)(DPEPhos)]BF_4 (**5**)[56]

1,4-bis((4-(quinol-2´yl)-1,2,3-triazol-1-yl)methyl)benzene (**NN**) (163 mg, 0.330 mmol, 1.00 equiv.) was dissolved in dry DCM (10 mL) with DPEPhos (355 mg, 0.660 mmol, 2.00 equiv.) and $Cu(CH_3CN)_4BF_4$ (207 mg, 0.660 mmol, 2.00 equiv.) under argon atmosphere and the mixture was stirred at room temperature 1 hour. The mixture was concentrated under reduced pressure and Et_2O was added to precipitate the product. The product was filtered, thoroughly washed with Et_2O (5 × 50 mL) and dried under reduced pressure to yield the title compound **5** as a yellow solid (580 mg, 0.310 mmol, 94%)

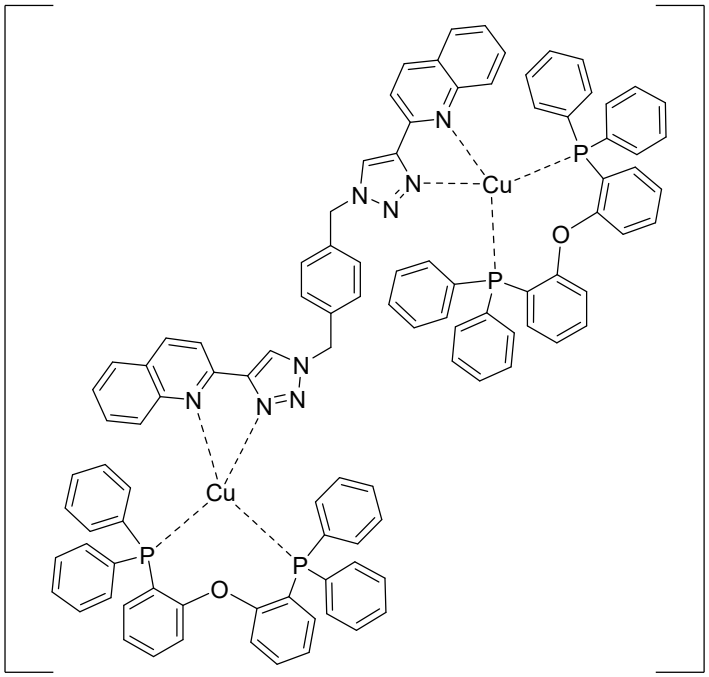

***R*f** (CH_2Cl_2/*MeOH*, 15:1) = 0.52. – **^{1}H NMR** (400 MHz, $CDCl_3$): δ = 8.48 (m, 4H), 7.92 (m, 4H), 7.78 (s, 2H), 7.43 – 6.58 (m, 64H), 5.66 (s, 4H) ppm. – **^{13}C NMR** (126 MHz, $CDCl_3$): δ = 158.73, 147.49, 146.53, 146.3, 139.59, 135.63, 134.42, 132.47, 131.28, 130.41, 129.10, 128.83, 128.36, 127.88, 125.20, 124.80, 123,98, 123.87, 123.75, 120.69, 119.08, 100.26, 55.27 ppm. – **^{31}P NMR** (162 MHz, $CDCl_3$): δ = -13.30 ppm. IR (ATR): $\tilde{\nu}$ = 3055, 3013, 1606, 1568, 1462, 1435, 1258, 1221, 1119, 1095, 1060, 1035, 1026, 1018, 1004, 999, 950, 914, 877, 839, 826, 803, 762, 751, 735, 697, 545, 521, 509, 490, 483, 446, 422, 411 cm–1. – **HRMS** ($C_{102}H_{78}Cu_2P_4N_8O_2BF_4$): calc.: 1785.38, found: 1785.39. Elemental analysis ($C_{102}H_{78}Cu_2N_8O_2P_4B_2F_8$): C=65.43, H=4.20, N=5.98 (calc.); C=65.28, H=3.96, N=6.19 (found).

M(SCN)$_2$Py$_4$[209]

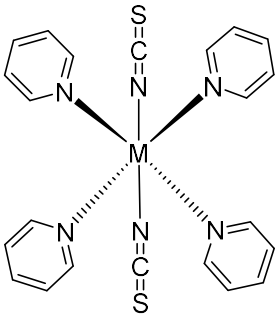

$M(ClO_4)_2$ (1.00 equiv.) was dissolved in water and a solution of NH_4SCN (2.00 equiv.) with 5.00 equivalents of pyridine in water was added dropwise to the mixture. In the case of iron, 0.10 equivalent of ascorbic acid were added to the mixture. The reaction was stirred at room temperature for 30 minutes, the precipitate was filtered and washed with a solution EtOH/Py 9:1 v/v. The solid was then dried under reduced pressure except in the case of iron where the solid was let wet with the solution EtOH/Py. The resulting crude product was used with no further purification to afford the desired products Co, Ni, Zn, Mn, Cu, Fe as pink, blue, white, yellow, light green and green solids. (69%, 87%, 92%, 74%, 85%, n.r.) respectively.

(Co) – ^{1}H NMR (400 MHz, CD_3CN): δ = 6.23 – 4.8 (m, 5H, $H_{pyridine}$) ppm, (Fe) – ^{1}H NMR (400 MHz, CD_3CN): δ = 9.90 – 9.30 (m, 5H, $H_{pyridine}$) ppm, (Ni) – ^{1}H NMR (400 MHz, CD_3CN): δ = 14.30 – 12.90 (m, 5H, $H_{pyridine}$) ppm. –

IR (ATR):

(Co): $\tilde{\nu}$ = 3068, 2867, 2065, 1628, 1598, 1571, 1485, 1441, 1213, 1068, 1038, 1006, 800, 765, 755, 711, 698, 652, 625, 480, 431, 421 cm^{-1},

m.p.:195°C

(Mn): $\tilde{\nu}$ = 3060, 2846, 2053, 1949, 1628, 1596, 1571, 1485, 1439, 1388, 1358, 1214, 1147, 1068, 1037, 1004, 965, 948, 798, 764, 754, 710, 698, 652, 622, 480, 421, 412 cm^{-1}

(Cu): $\tilde{\nu}$ = 3060, 2846, 2053, 1949, 1632, 1596, 1571, 1485, 1439, 1388, 1358, 1214, 1147, 1068, 1037, 1004, 965, 948, 798, 764, 754, 710, 698, 652, 622, 480, 421, 412 cm^{-1}

(Ni): $\tilde{\nu}$ = 3068, 2876, 2079, 2037, 1640, 1599, 1572, 1486, 1441, 1358, 1213, 1149, 1068, 1038, 1007, 884, 800, 768, 756, 711, 700, 653, 626, 482, 436, 429 cm^{-1}

m.p.:217°C

(Zn): $\tilde{\nu}$ = 3111, 3089, 3064, 2936, 2919, 2393, 2342, 2098, 2067, 1853, 1662, 1608, 1487, 1445, 1398, 1214, 1152, 1068, 1045, 1017, 959, 846, 752, 700, 690, 642, 479, 425, 412 cm^{-1}

m.p.:192°C

Ni(cyclam)Cl_2[66] (**1**)

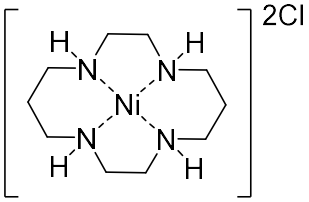

$NiCl_2$, 6(H_2O) (20.0 mg, 0.154 mmol, 1.00 equiv.) was dissolved in EtOH (5 mL) with 1,4,8,11-Tetraazacyclotetradecane (31.4 mg, 0.157 mmol, 1.02 equiv.). The mixture was stirred at room temperature for 30 minutes and the product was precipitated with addition of Et_2O (20 mL). The crude product was purified by recrystallization from water/acetone to afford the title compound **1** (30.4 mg, 0.0924 mmol, 60%) a purple solid.

IR (ATR, ṽ) = 3265, 3224, 2951, 2922, 2895, 2859, 1470, 1452, 1436, 1425, 1344, 1334, 1307, 1289, 1264, 1237, 1112, 1098, 1081, 1061, 992, 935, 871, 800, 513, 418, 405 cm^{-1}– **MS** (ESI): *m/z* (%) = 293.1 (100), 295.1 (81), 297.1 (12) $[M\text{-}Cl]^+$ – **HRMS** ($C_{10}H_{24}ClN_4Ni$): calc.: 293.1048, found: 293.1033.

[Fe(2,6-bis((4-phenyl-1,2,3-triazol-1-yl)methyl)pyridine)$(NCS)_2$py] (**11**)

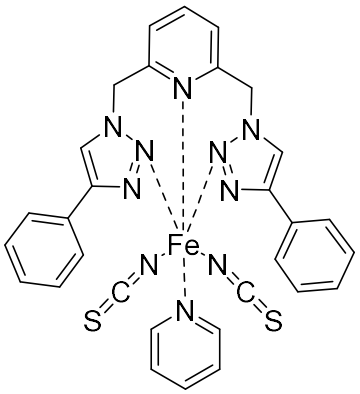

Under argon atmosphere, a solution of 2,6-bis((4-phenyl-1,2,3-triazol-1-yl)methyl)pyridine L-**6** (22.0 mg, 0.060 mmol, 1.00 equiv.) was dissolved in MeOH (5 mL) was added to a solution of $Fe(NCS)_2Py_4$ (26.6 mg, 0.060 mmol, 1.00 equiv.) in 2 mL MeOH. The mixture was stirred at room temperature for 1 hour. The solvent was removed under reduced pressure and the crude product was washed with cold MeOH and Et_2O. The resulting crude product was purified by recrystallization (*MeCN*/Et_2O) to afford the title compound **11** (24.0 mg, 0.036 mmol, 60%) as light-yellow crystals.

IR (ATR): $\tilde{\nu}$ = 3112, 3084, 3061, 3043, 3031, 2992, 2946, 2922, 2853, 2034, 2028, 1598, 1575, 1480, 1459, 1434, 1370, 1356, 1339, 1329, 1315, 1272, 1248, 1222, 1201, 1179, 1162, 1139, 1099, 1079, 1047, 1024, 994, 977, 967, 909, 839, 817, 775, 759, 727, 707, 690, 660, 628, 618, 603, 588, 547, 524, 513, 487, 483, 467, 460, 441, 429, 411, 401, 392 cm^{-1}. – **MS** (Nano-ESI): *m/z* (%) = 507.080 $[M\text{-}NCS\text{-}Py]^+$, 585.094 $[M\text{-}NCS]^+$. – Elemental analysis (Fe(**6**) + Et_2O + Py): C=58.72, H=4.29, N=19.31, S=8.74 (calc.); C=58.11, H=4.42, N=18.7, S=8.74 (found). **HRMS** ($C_{24}H_{19}FeN_8S$): calc.: 507.0803, found: 507.1263. **m.p**.:148°C

[Co(2,6-bis((4-phenyl-1,2,3-triazol-1-yl)methyl)pyridine)(NCS)$_2$py] (**12**)

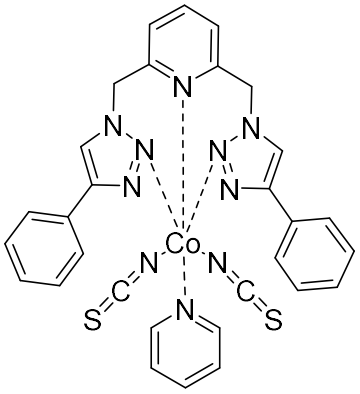

A solution of 2,6-bis((4-phenyl-1,2,3-triazol-1-yl)methyl)pyridine L-**6** (22.0 mg, 0.060 mmol, 1.00 equiv.) was dissolved in MeOH (5 mL) was added to a solution of $Co(NCS)_2Py_4$ (26.8 mg, 0.060 mmol, 1.00 equiv.) in 2 mL MeOH. The mixture was stirred at room temperature for 1 hour. The solvent was removed under reduced pressure and the crude product was washed with cold MeOH and Et_2O. The resulting crude product was purified by recrystallization (*MeCN*/Et_2O) to afford the title compound **12** (31.0 mg, 0.047 mmol, 79%) as a blue solid.

IR (ATR): $\tilde{\nu}$ = 3125, 3084, 3060, 3029, 3003, 2945, 2096, 1592, 1572, 1483, 1459, 1439, 1419, 1346, 1330, 1215, 1198, 1184, 1167, 1150, 1125, 1071, 1041, 1028, 1010, 997, 984, 975, 926, 909, 850, 837, 817, 800, 756, 722, 687, 645, 626, 591, 530, 506, 465, 435, 425, 409 cm^{-1}. – **MS** (ESI): *m/z* (%) = 510.2 [M-NCS-Py]$^+$, 589.6 [M-NCS]$^+$. – **Elemental analysis** ($C_{30}H_{24}CoN_{10}S_2$): C=55.64, H=3.74, N=21.63, S=9.90 (calc.); C=55.8, H=3.75, N=19.8, S=9.15 (found). **HRMS** ($C_{24}H_{19}CoN_8S$): calc.: 510.0785, found: 510.0777. **m.p**.:151°C

[Ni (2,6-bis((4-phenyl-1,2,3-triazol-1-yl)methyl)pyridine)(NCS)$_2$py] (**13**)

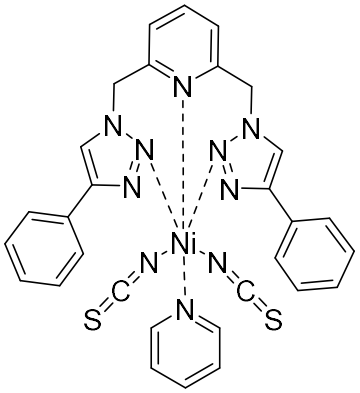

A solution of 2,6-bis((4-phenyl-1,2,3-triazol-1-yl)methyl)pyridine L-**6** (22.0 mg, 0.060 mmol, 1.00 equiv.) was dissolved in MeOH (5 mL) was added to a solution of $Ni(NCS)_2Py_4$ (29.4 mg, 0.060 mmol, 1.00 equiv.) in 2 mL MeOH. The mixture was stirred at room temperature for 1 hour. The solvent was removed under reduced pressure and the crude product was washed with cold MeOH and Et_2O. The resulting crude product was purified by recrystallization (*MeCN*/Et_2O) to afford the title compound **13** (35.0 mg, 0.051 mmol, 85%) as a light blue solid.

IR (ATR): $\tilde{\nu}$ = 3612, 3323, 3296, 3123, 3092, 2996, 2948, 2085, 1605, 1575, 1465, 1443, 1429, 1356, 1330, 1319, 1249, 1197, 1160, 1084, 1072, 1014, 990, 975, 935, 919, 823, 796, 764, 730, 694, 680, 653, 622, 599, 574, 561, 545, 520, 507, 473, 452, 443, 431, 412, 399, 391, 381 cm^{-1}. – **MS** (ESI): *m/z* (%) = 509.1 [M-NCS-Py]$^+$, 588.1 [M-NCS]$^+$. – **Elemental analysis** ($C_{30}H_{24}NiN_{10}S_2$): C=55.66, H=3.74, N=21.64, S=9.90 (calc.); C=55.79, H=3.83, N=19.72, S=9.30 (found). **HRMS** ($C_{24}H_{19}N_8NiS$): calc.: 509.0807, found: 509.0800. **m.p**.:155°C

[Mn(2,6-bis((4-phenyl-1,2,3-triazol-1-yl)methyl)pyridine)(NCS)$_2$py] (**15**)

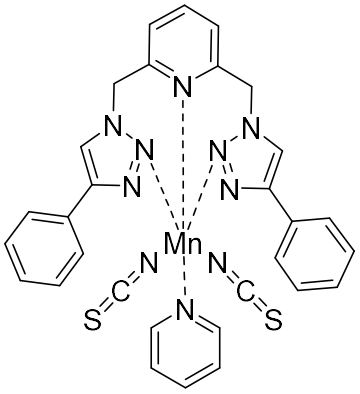

A solution of 2,6-bis((4-phenyl-1,2,3-triazol-1-yl)methyl)pyridine L-**6** (22.0 mg, 0.060 mmol, 1.00 equiv.) was dissolved in MeOH (5 mL) was added to a solution of $Mn(NCS)_2Py_4$ (29.3 mg, 0.060 mmol, 1.00 equiv.) in 2 mL MeOH. The mixture was stirred at room temperature for 1 hour. The solvent was removed under reduced pressure and the crude product was washed with cold MeOH and Et_2O. The resulting crude product was purified by recrystallization (*MeCN*/Et_2O) to afford the title compound **15** (39.0 mg, 0.056 mmol, 94%) as a blue solid.

IR (ATR): $\tilde{\nu}$ = 3123, 3084, 3058, 3029, 2084, 1595, 1572, 1485, 1459, 1439, 1419, 1346, 1215, 1200, 1184, 1149, 1125, 1069, 1037, 1006, 984, 975, 909, 850, 837, 817, 754, 724, 688, 646, 625, 591, 507, 473, 466, 416 cm^{-1}. – **MS** (ESI): *m/z* (%) = 506.1 [M-NCS-Py]$^+$. – **Elemental analysis** ($C_{30}H_{24}MnN_{10}S_2$ + Py): C=58.16, H=4.04, N=21.32, S=8.87 (calc.); C=57.71, H=3.99, N=20.74, S=8.62 (found). **HRMS** ($C_{24}H_{19}CuN_8S$): calc.: 506.0834, found: 506.0830.

[Cu(2,6-bis((4-phenyl-1,2,3-triazol-1-yl)methyl)pyridine)(NCS)$_2$py] (**14**)

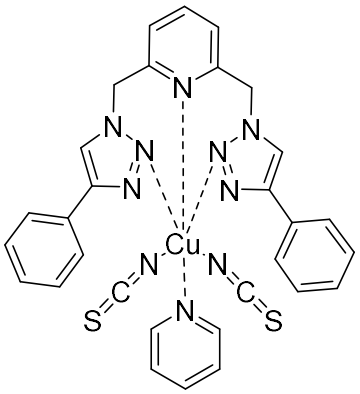

A solution of 2,6-bis((4-phenyl-1,2,3-triazol-1-yl)methyl)pyridine L-**6** (39.3 mg, 0.10 mmol, 1.00 equiv.) was dissolved in MeOH (5 mL) was added to a solution of $Cu(NCS)_2Py_4$ (49.6 mg, 0.10 mmol, 1.00 equiv.) in 2 mL MeOH. The mixture was stirred at room temperature for 1 hour. The solvent was removed under reduced pressure and the crude product was washed with cold MeOH and Et_2O. The resulting crude product was purified by recrystallization (*MeCN*/Et_2O) to afford the title compound **14** (42.0 mg, 0.065 mmol, 65%) as a green solid.

IR (ATR): $\tilde{\nu}$ = 3121, 3084, 3065, 3058, 2087, 1592, 1574, 1458, 1443, 1436, 1419, 1215, 1200, 1184, 1167, 1126, 1072, 1043, 1028, 997, 984, 975, 928, 908, 849, 837, 817, 802, 758, 724, 703, 687, 645, 626, 591, 530, 507, 465, 435, 411 cm^{-1}. – **MS** (ESI): *m/z* (%) = 513.2 [M-NCS-Py]$^+$. – **Elemental analysis** ($C_{30}H_{24}CuN_{10}S_2$ - Py): C=52.39, H=3.34, N=21.99, S=11.19 (calc.); C=50.06, H=3.24, N=18.94, S=12.80 (found). **HRMS** ($C_{24}H_{19}CuN_8S$): calc.: 514.0749, found: 514.0743. **m.p**.:148°C

[Zn(2,6-bis((4-phenyl-1,2,3-triazol-1-yl)methyl)pyridine)(NCS)$_2$py] (**16**)

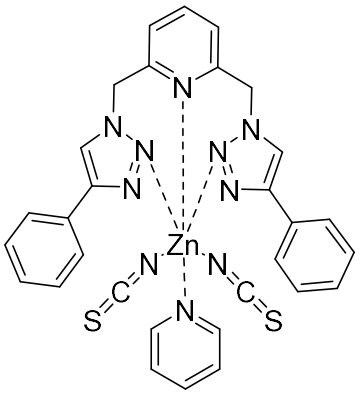

A solution of 2,6-bis((4-phenyl-1,2,3-triazol-1-yl)methyl)pyridine L-**6** (39.4 mg, 0.10 mmol, 1.00 equiv.) was dissolved in MeOH (5 mL) was added to a solution of $Zn(NCS)_2Py_4$ (49.8 mg, 0.10 mmol, 1.00 equiv.) in 2 mL MeOH. The mixture was stirred at room temperature for 1 hour. The solvent was removed under reduced pressure and the crude product was washed with cold MeOH and Et_2O. The resulting crude product was purified by recrystallization (*MeCN*/Et_2O) to afford the title compound **16** (60.0 mg, 0.092 mmol, 91%) as a white solid.

IR (ATR): $\tilde{\nu}$ = 3126, 3085, 3067, 3031, 2065, 1608, 1592, 1574, 1485, 1459, 1445, 1419, 1347, 1215, 1150, 1068, 1044, 1017, 977, 908, 837, 817, 758, 724, 688, 642, 626, 591, 507, 411 cm^{-1}. – **MS** (ESI): *m/z* (%) = 515.1 [M-NCS-Py]$^+$. – **Elemental analysis** ($C_{30}H_{24}ZnN_{10}S_2$ - Py): C=52.22, H=3.33, N=21.92, S=11.15 (calc.); C=52.06, H=3.57, N=18.96, S=11.65 (found). **HRMS** ($C_{24}H_{19}N_8SZn$): calc.: 515.0745, found: 515.0738. **m.p**.:169°C

[Fe(2,6-bis((4-phenyl-1,2,3-triazol-1-yl)methyl)pyridine)$_2$]ClO_4 (**17**)[167]

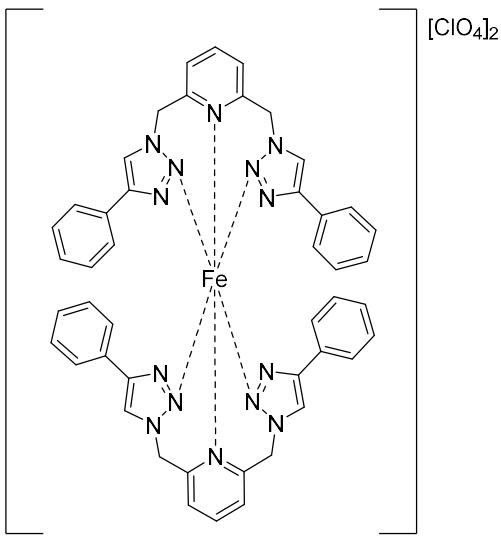

A solution of 2,6-bis((4-phenyl-1,2,3-triazol-1-yl)methyl)pyridine L-**6** (39.4 mg, 0.10 mmol, 2.00 equiv.) was dissolved in MeOH (5 mL) was added to a solution of $Fe(ClO_4)_2$ (24.9 mg, 0.050 mmol, 1.00 equiv.) in 2 mL MeOH. The mixture was stirred at room temperature for 1 hour. The solvent was removed under reduced pressure and the crude product was washed with cold MeOH and Et_2O. The resulting crude product was purified by recrystallization (*MeCN*/Et_2O) to afford the title compound **17** (49.8 mg, 0.0475 mmol, 95%) as a red solid.

^{1}H NMR (400 MHz, CD_3CN): δ = 9.46 (s, 2H), 8.89 (s, 4H), 8.32 (m, 2H), 7.86 (m, 5H), 7.29 (m, 21H), 5.72 (m, 4H) ppm. –**IR** (ATR): $\tilde{\nu}$ = 3135, 3021, 1612, 1574, 1555, 1468, 1438, 1095, 1078, 1001, 987, 975, 933, 822, 762, 738, 694, 662, 620, 565, 533, 520, 506, 484, 470, 448, 433, 425, 414, 391, 377 cm^{-1}. – **MS** (ESI): *m/z* (%) = 941.3 [M-ClO_4]$^+$, 421.1 [M-2ClO_4]$^{2+}$ – Elemental analysis ($C_{46}H_{38}Cl_2FeN_{14}O_8$ – ClO_4): C=58.64, H=4.07, N=20.81 (calc.); C=59.88, H=4.40, N=21.17 (found). **HRMS** (C46H38FeN14 + ClO4): calc.: 941.2243, found: 941.2223. **m.p**.:154°C

[Co(**6**)$_2$]ClO$_4$ (**18**)[167]

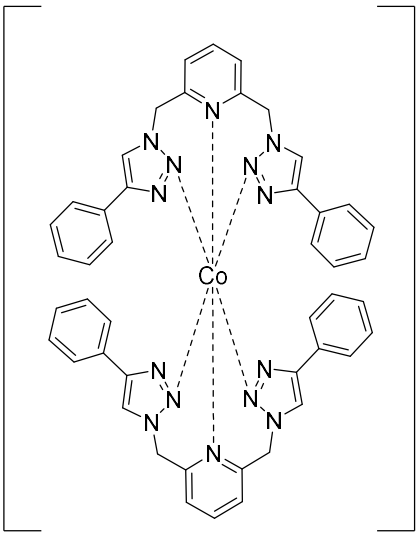

A solution of **6** (39.6 mg, 0.10 mmol, 2.00 equiv.) was dissolved in MeOH (5 mL) was added to a solution of $Co(ClO_4)_2$ (24.7 mg, 0.050 mmol, 1.00 equiv.) in 2 mL MeOH. The mixture was stirred at room temperature for 1 hour. The solvent was removed under reduced pressure and the crude product was washed with cold MeOH and Et_2O. The resulting crude product was purified by recrystallization (*MeCN*/Et_2O) to afford the title compound **18** (46.4 mg, 0.0445 mmol, 89%) as a pink solid.

IR (ATR): $\tilde{\nu}$ = 3133, 1605, 1575, 1473, 1463, 1443, 1429, 1358, 1247, 1232, 1204, 1156, 1095, 1074, 1011, 973, 952, 929, 837, 764, 731, 694, 619, 602, 524, 509, 479, 409, 388cm^{-1}. – **MS** (ESI): *m/z* (%) = 944.2 [M-ClO$_4$]$^+$ – **Elemental analysis** ($C_{46}H_{38}Cl2CoN_{14}O_8$ – ClO_4): C=52.88, H=3.67, N=18.67 (calc.); C=53.6, H=3.53, N=18.9 (found). **HRMS** ($C_{46}H_{38}CoN_{14}$ + ClO_4): calc.: 944.2226, found: 944.2210. **m.p**.:159°C

[Ni(2,6-bis((4-phenyl-1,2,3-triazol-1-yl)methyl)pyridine)$_2$]ClO$_4$ (**19**)

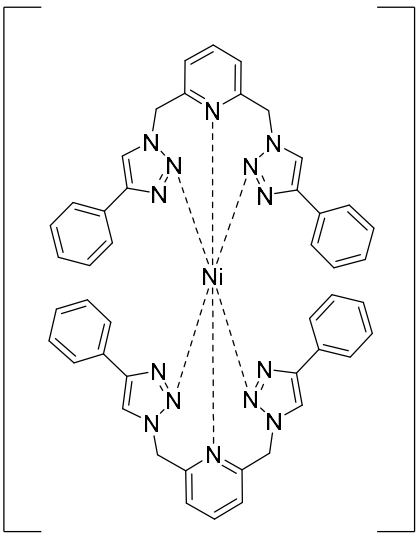

A solution of 2,6-bis((4-phenyl-1,2,3-triazol-1-yl)methyl)pyridine L-**6** (39.5 mg, 0.10 mmol, 2.00 equiv.) was dissolved in MeOH (5 mL) was added to a solution of $Ni(ClO_4)_2$ (25.2 mg, 0.050 mmol, 1.00 equiv.) in 2 mL MeOH. The mixture was stirred at room temperature for 1 hour. The solvent was removed under reduced pressure and the crude product was washed with cold MeOH and Et_2O. The resulting crude product was purified by recrystallization (*MeCN*/Et_2O) to afford the title compound **19** (45.4 mg, 0.0435 mmol, 87%) as a light blue solid.

IR (ATR, $\tilde{\nu}$) = 3132, 3088, 3063, 3029, 1606, 1594, 1575, 1475, 1462, 1443, 1432, 1358, 1333, 1252, 1203, 1163, 1095, 1074, 1030, 1014, 1001, 984, 975, 955, 931, 911, 836, 819, 764, 732, 724, 691, 622, 602, 592, 526, 509, 412 cm^{-1}.– **MS** (ESI): *m/z* (%) = 422.1 (100), 423.1 (85), 424.1 (50) [M-2ClO$_4$]$^{2+}$ – **Elemental analysis** ($C_{46}H_{38}N_{14}Ni$): C=65.34, H=4.53, N=23.19 (calc.); C=65.45, H=4.43, N=23.01 (found). **m.p**.:145°C

[Cu(2,6-bis((4-phenyl-1,2,3-triazol-1-yl)methyl)pyridine)$_2$]ClO_4 (**20**)[167]

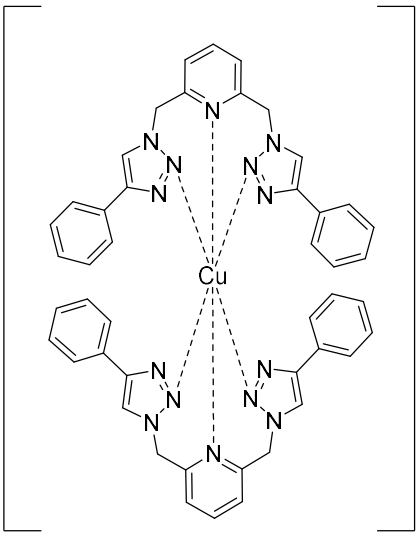

A solution of 2,6-bis((4-phenyl-1,2,3-triazol-1-yl)methyl)pyridine L-**6** (39.4 mg, 0.10 mmol, 2.00 equiv.) was dissolved in MeOH (5 mL) was added to a solution of $Fe(ClO_4)_2$ (24.9 mg, 0.050 mmol, 1.00 equiv.) in 2 mL MeOH. The mixture was stirred at room temperature for 1 hour. The solvent was removed under reduced pressure and the crude product was washed with cold MeOH and Et_2O. The resulting crude product was purified by recrystallization (*MeCN*/Et_2O) to afford the title compound **20** (49.8 mg, 0.0475 mmol, 95%) as a green solid.

– IR (ATR, ṽ) = 3125, 3092, 3070, 3017, 2955, 1604, 1575, 1466, 1442, 1428, 1358, 1201, 1098, 1067, 989, 973, 929, 846, 819, 775, 768, 758, 731, 698, 684, 657, 622, 598, 517, 503 cm^{-1} – **MS** (ESI): *m/z* (%) = 849.26 $[M\text{-}2ClO_4]^{2+}$, 941.3 $[M\text{-}ClO_4]^+$, 421.1 $[M\text{-}2ClO_4]^{2+}$ – Elemental analysis ($C_{46}H_{38}Cl_2CuN_{14}O_8$): C=52.65, H=3.65, N=18.69 (calc.); C=52.19, H=3.71, N=18.37 (found). **HRMS** ($C_{46}H_{38}CuN_{14} – 2ClO_4$): calc.: 849.2700, found: 849.2683.

[Zn(2,6-bis((4-phenyl-1,2,3-triazol-1-yl)methyl)pyridine)$_2$]ClO_4 (**21**)

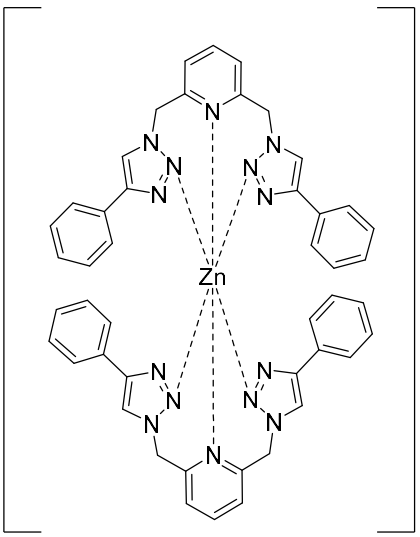

A solution of 2,6-bis((4-phenyl-1,2,3-triazol-1-yl)methyl)pyridine L-**6** (40.0 mg, 0.102 mmol, 2.00 equiv.) was dissolved in MeOH (5 mL) was added to a solution of $Zn(ClO_4)_2$ (19.0 mg, 0.050 mmol, 1.00 equiv.) in 2 mL MeOH. The mixture was stirred at room temperature for 1 hour. The solvent was removed under reduced pressure and the crude product was washed with cold MeOH and Et_2O. The resulting crude product was purified by recrystallization (*MeCN*/Et_2O) to afford the title compound **21** (49.9 mg, 0.0475 mmol, 95%) as a white solid.

IR (ATR, ṽ) = 3125, 3092, 3070, 3017, 2955, 1604, 1575, 1466, 1442, 1428, 1358, 1201, 1098, 1067, 989, 973, 929, 846, 819, 775, 768, 758, 731, 698, 684, 657, 622, 598, 517, 503 cm^{-1}.. – **MS** (ESI): *m/z* (%) = 949.2 (95), 951.2 (100), 953.2 (80) $[M\text{-}ClO_4]^+$, 426.3 $[M\text{-}2ClO_4]^{2+}$ – **Elemental analysis** ($C_{46}H_{38}ZnN_{14}$ – $Zn(ClO_4)_2$: C=49.48, H=3.43, N=17.56 (calc.); C=50.44, H=3.77, N=17.72 (found). **HRMS** ($C_{46}H_{38}N_{14}Zn$): calc.: 949.2185, found: 949.2159.

[Fe_3(2,6-bis((4-phenyl-1,2,3-triazol-1-yl)methyl)pyridine)$_2$(NCS)$_6$(MeCN)$_4$] (**36**)

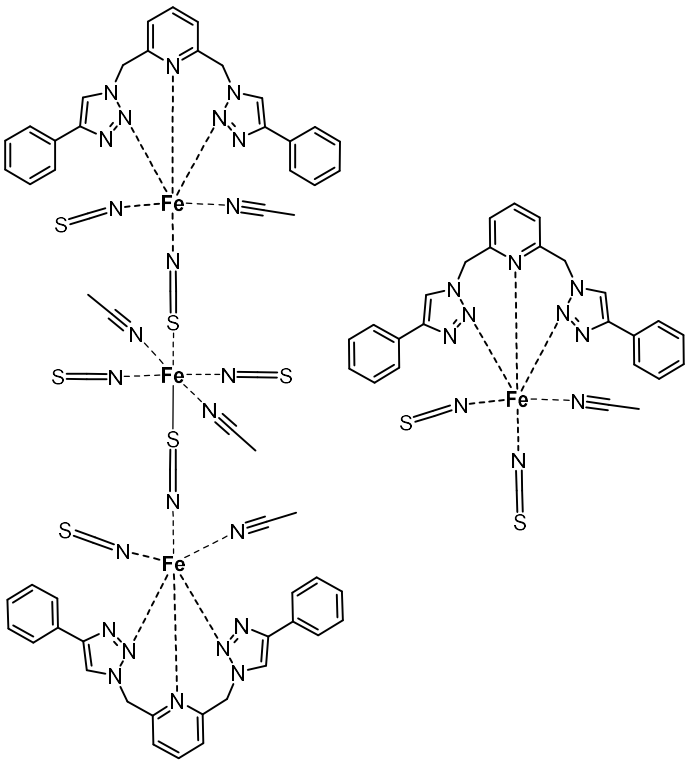

In an argon atmosphere glovebox, 69.5 mg of $Fe(SO_4).7H_2O$ (0.25 mmol, 1.00 equiv.) was dissolved in 3.0 mL of dried MeOH. 63.4 mg of $Ba(NCS)_2$ was added to this solution which was stirred for 30 min at 22°C. The precipitate formed was filtered off and the yellow solution obtained was considered $Fe(NCS)_2$ with a yield of 100%. 0.915 mL of this solution diluted in 1.085 mL of MeOH (0.0762 mmol, 1.00 equiv.) was introduced in a vial, to which a solution of 30 mg of 2,6-bis((4-phenyl-1,2,3-triazol-1-yl)methyl)pyridine L-**6** (0.0762 mmol, 1.00 equiv.) in 2.0 mL of MeOH was added. The mixture was stirred at 22°C for 2 hours and was then evaporated under Schlenk line to obtain a yellow powder that was washed with Et_2O and recrystallized in MeCN/Et_2O over several days. A maximum yield of 42% obtained was with the different ratios of reagents employed).

Nano-ESI MS: *m/z* (%) = 507.1 [Monometallic complex – NCS - py]$^+$, 900.2 [$(C_{23}H_{19}N_7)_2Fe(NCS)]^+$ – **Elemental analysis** ($C_{60}H_{50}Fe_3N_{24}S_6$ + $C_{27}H_{22}FeN_{10}S_2$): C=50.39, H=3.50, N=22.97, S=12.37 (calc.); C=45.06, H=3.40, N=18.20, S=11.15 (found).

Co(2,6-bis((4-(4-aminophenyl)-1,2,3-triazol-1-yl)methyl)pyridine)(NCS)$_2$py (**23**)

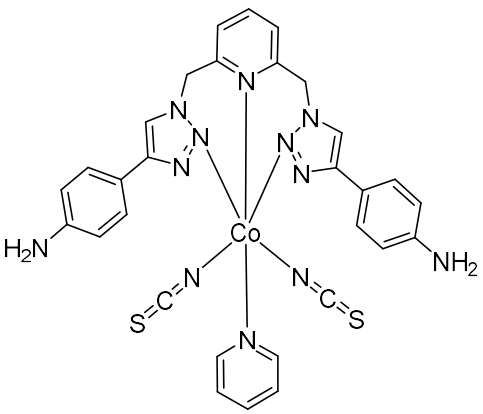

A solution of 2,6-bis((4-(4-aminophenyl)-1,2,3-triazol-1-yl)methyl)pyridine L-**8** (30.0 mg, 0.07 mmol, 1.00 equiv.) was dissolved in MeOH (5 mL) and added to a solution of $Co(NCS)_2py_4$ (34.8.0 mg, 0.07 mmol, 1.00 equiv.) in 4 mL MeOH. The mixture was stirred at room temperature for 1 hour. The solvent was removed under reduced pressure and the crude product was washed with cold MeOH and Et_2O. The resulting crude product was purified by recrystallization (*MeCN*/Et_2O) to afford the title compound **23** (42.0 mg, 0.06 mmol, 87%) as a blue powder.

MS (ESI): *m/z* (%) = 540.1 $[M\text{-}NCS\text{-}py]^+$– **HRMS** ($C_{24}H_{21}CoN_{10}S$): calc.: 540.1003, found: 540.1000.

Co(2,6-bis((4-(4-trimethylammoniumphenyl)-1,2,3-triazol-1-yl)methyl)pyridine)$(NCS)_2$py (**23**)

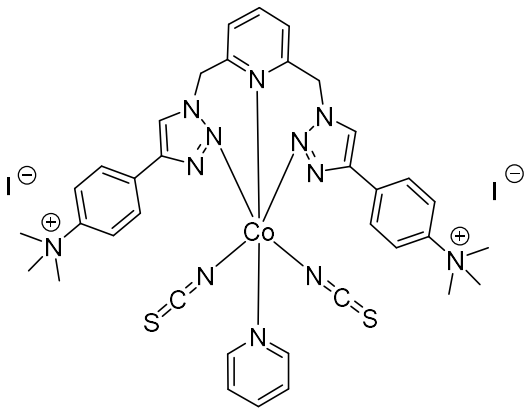

A solution of 2,6-bis((4-(4-trimethylammoniumphenyl)-1,2,3-triazol-1-yl)methyl)pyridine L-**10** (29.7 mg, 0.068 mmol, 1.00 equiv.) was dissolved in MeOH (5 mL) and added to a solution of $Co(NCS)_2py_4$ (28.5 mg, 0.068 mmol, 1.00 equiv.) in 4 mL MeOH. The mixture was stirred at room temperature for 1 hour. The solvent was removed under reduced pressure and the crude product was washed with cold MeOH and Et_2O. The resulting crude product was purified by recrystallization (*MeCN*/Et_2O) to afford the title compound **23** (34.0 mg, 0.04 mmol, 75%) as a blue powder.

MS (ESI): *m/z* (%) = 811.1 $[M\text{-}py\text{-}I]^+$– **HRMS** ($C_{31}H_{35}CoIN_{11}S2$): calc.: 811.0890, found: 811.0886.

[Fe(2,6-bis((4-(4-aminophenyl)-1,2,3-triazol-1-yl)methyl)pyridine)$_2$]ClO_4 (**17_b**)

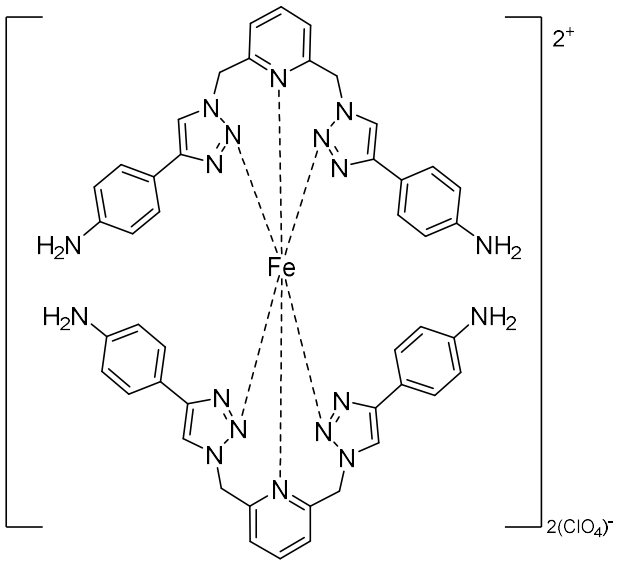

A solution of 2,6-bis((4-(4-aminophenyl)-1,2,3-triazol-1-yl)methyl)pyridine L-**8** (14.0 mg, 0.03 mmol, 2.00 equiv.) was dissolved in MeOH (5 mL) and added to a solution of $Fe(ClO_4)_2$, $5H_2O$ (4.00 mg, 0.015 mmol, 1.00 equiv.) in 2 mL MeOH. The mixture was stirred at room temperature for 1 hour. The solvent was removed under reduced pressure and the crude product was washed with cold MeOH and Et_2O. The resulting crude product was purified by recrystallization (*MeCN*/Et_2O) to afford the title compound **17_b** (10.4.0 mg, 0.01 mmol, 72%) as a beige powder.

MS (ESI): *m/z* (%) = 1001.2 $[M\text{-}ClO_4]^+$ – **HRMS** (C47H43FeN17ClO4): calc.: 1001.2716, found: 1001.2670.

[Co(**2**-(1-(phen-2-ylmethyl)-1,2,3-triazol-4-yl)quinoline)$_2$(NCS)$_2$] (**27**)

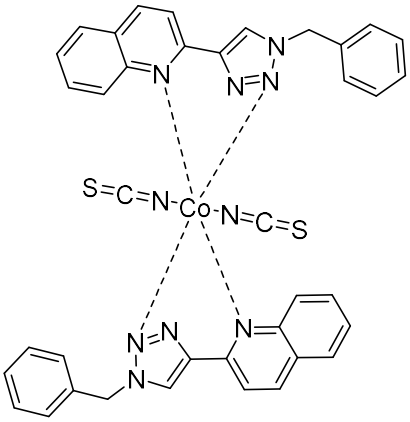

A solution of 2-(1-(phen-2-ylmethyl)-1,2,3-triazol-4-yl)quinoline **25** (23.6 mg, 0.10 mmol, 2.00 equiv.) was dissolved in MeOH (5 mL) was added to a solution of $Co(NCS)_2Py_4$ (11.8 mg, 0.05 mmol, 1.00 equiv.) in 2 mL MeOH. The mixture was stirred at room temperature for 1 hour. The solvent was removed under reduced pressure and the crude product was washed with cold MeOH and Et_2O. The resulting crude product was purified by recrystallization (*MeCN*/Et_2O) to afford the title compound **27** (26.8 mg, 0.0415 mmol, 83%) as a blue solid.

IR (ATR): $\tilde{\nu}$ = 3109, 3027, 2065, 1606, 1574, 1507, 1496, 1469, 1453, 1438, 1431, 1375, 1358, 1350, 1332, 1313, 1251, 1210, 1162, 1145, 1130, 1101, 1061, 1027, 1011, 952, 832, 817, 803, 783, 764, 732, 717, 694, 679, 654, 636, 599, 572, 531, 516, 482, 459, 399, 384cm^{-1}. – **MS** (ESI): *m/z* (%) = 689.2 (100), 690.2 (38.9), 691.2 (7.1) [M-NCS]$^+$.– **HRMS** ($C_{35}H_{28}CoN_9S$): calc.: 689.1420, found: 689.1510. **Elemental analysis** ($C_{38}H_{28}CoN_{10}S_2$): C=61.04, H=3.77, N=18.73, S=8.57 (calc.); C=59.81, H=3.69, N=18.37, S=8.21 (found). **m.p**.:129°C

[Ni(**2**-(1-(pyridin-2-ylmethyl)-1,2,3-triazol-4-yl)quinoline)$_2$(NCS)$_2$] (**29**)

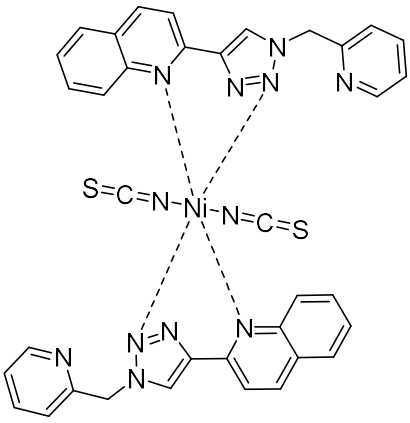

A solution of 2-(1-(pyridin-2-ylmethyl)-1,2,3-triazol-4-yl)quinoline **25** (15.0 mg, 0.05 mmol, 1.00 equiv.) was dissolved in EtOH (5 mL) was added to a solution of $Ni(NCS)_2Py_4$ (25.1 mg, 0.05 mmol, 1.00 equiv.) in 2 mL MeOH. The mixture was stirred at room temperature for 1 hour. The solvent was removed under reduced pressure and the crude product was washed with cold MeOH and Et_2O. The resulting crude product was purified by recrystallization (*MeCN*/Et_2O) to afford the title compound **29** (25.0 mg, 0.033 mmol, 67%) as a green solid.

IR (ATR): $\tilde{\nu}$ = 3111, 3055, 3026, 2094, 2078, 1608, 1577, 1509, 1497, 1469, 1453, 1439, 1432, 1377, 1358, 1350, 1333, 1315, 1254, 1211, 1160, 1146, 1130, 1103, 1062, 1028, 1014, 952, 832, 819, 803, 783, 765, 758, 734, 718, 696, 680, 656, 636, 601, 534, 518, 490, 480, 459, 402 cm^{-1}. – **MS** (ESI): *m/z* (%) = 689.2 (100), 690.2 (38.9), 691.2 (7.1) [M-NCS]$^+$. – **HRMS** ($C_{35}H_{26}N_{11}NiS$): calc.: 688.1542,

found: 688.1531. **Elemental analysis** ($C_{38}H_{28}NiN_{10}S_2$ – $NiCl_2$): C=52.04, H=3.22, N=15.97, S=7.31 (calc.); C=52.61, H=3.30, N=15.86, S=7.06 (found).

[Fe(2-(1-(pyridin-2-ylmethyl)-1,2,3-triazol-4-yl)quinoline)$_2$(NCS)$_2$] (**28**)

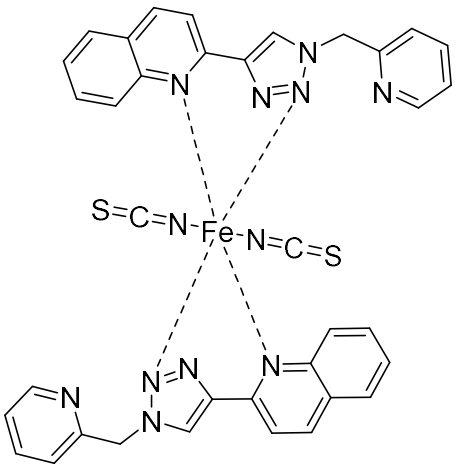

A solution of 2-(1-(pyridin-2-ylmethyl)-1,2,3-triazol-4-yl)quinoline **25** (15.0 mg, 0.05 mmol, 1.00 equiv.) was dissolved in EtOH (5 mL) was added to a solution of $Fe(NCS)_2Py_4$ (24.1 mg, 0.05 mmol, 1.00 equiv.) in 2 mL MeOH. The mixture was stirred at room temperature for 1 hour. The solvent was removed under reduced pressure and the crude product was washed with cold MeOH and Et_2O. The resulting crude product was purified by recrystallization (*MeCN*/Et_2O) to afford the title compound **28** (15.6 mg, 0.021 mmol, 42%) as a red solid.

– **IR** (ATR): $\tilde{\nu}$ = 3101, 3024, 2922, 2853, 2006, 1635, 1604, 1572, 1506, 1496, 1483, 1468, 1453, 1438, 1375, 1349, 1332, 1312, 1247, 1208, 1145, 1130, 1099, 1061, 1026, 1011, 950, 830, 820, 783, 764, 759, 717, 694, 671, 656, 635, 620, 596, 572, 531, 514, 479, 459, 429, 419, 401, 381 cm^{-1}. – **MS** (ESI): *m/z* (%) = 686.1 (100), 687.1 (33.9), 688.1 (10.5), 684.1 (6.4) $[M\text{-}NCS]^+$. – **HRMS** ($C_{35}H_{26}N_{11}FeS$): calc.: 688.1438, found: 688.1529. **Elemental analysis** ($C_{38}H_{28}FeN_{10}$ – Fe(NCS) –C_2H_6O): C=52.40, H=3.556, N=17.46, S=13.32 (calc.); C=51.63, H=3.34, N=17.31, S=13.01 (found).

[Fe(4,6-bis(diphenylphosphane-yl)-10-(1,10-phenanthrolin-2-yl)-phenoxazine)$_2$(NCS)$_2$] (**43**)

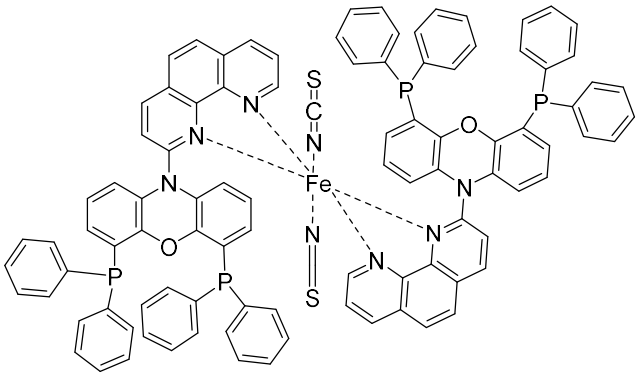

4,6-bis(diphenylphosphane-yl)-10-(1,10-phenanthrolin-2-yl)-phenoxazine **42** (81.5 mg, 0.112 mmol, 2.00 equiv.) was dissolved with $FeCl_2$, H_2O (11.1 mg, 0.056 mmol, 1.00 equiv.) in a mixture of MeCN/water 2:1 v/v (5 mL) and a solution of NH_4NCS (42.4 mg, 0.56 mmol, 10.0 equiv.) in 2 mL of water was added. The mixture was stirred at room temperature for 1 hour. The precipitate was filtered and washed with water. The resulting crude product was purified by recrystallization (*MeCN*/Et_2O) to afford the title compound **43** (48.8 mg, 0.029 mmol, 52%) as a red solid.

^{1}H NMR (400 MHz, $CDCl_3$): δ = 10.59 (s, 4H), 10.36 (s, 1H), 9.86 (s, 1H), 9.19 (s, 1H), 9.00 (s, 3H), 8.74 (s, 3H), 8.51 (m, 2H), 8.02 (m, 4H), 7.86 (m, 6H), 7.59 (m, 8H), 7.38 – 7.14 (m, 30H, $H_{phosphine}$), 6.66 – 6.55 (m, 2H), 6.12 (t, J = 7.7 Hz, 2H) ppm. – **IR** (ATR): $\tilde{\nu}$ = 3067, 3046, 3006, 2079, 2060, 1572, 1558, 1509, 1496, 1477, 1455, 1434, 1417, 1322, 1307, 1278, 1217, 1197, 1180, 1143, 1111, 1092, 1068, 1051, 1027, 999, 987, 955, 890, 868, 858, 830, 820, 793, 771, 738, 728, 690, 664, 653, 647, 619, 585, 575, 561, 538, 514, 496, 443, 428, 418, 408, 395, 384, 377cm^{-1}. – **MS** (ESI): *m/z* (%) = 1631.3 (100), 1630.3 (92), 1632.3 (60) $[M]^+$, 1573.3 $[M\text{-}NCS]^+$. – **HRMS** ($C_{97}H_{66}N_7FeO_2P_4S$): calc.: 693.1654, found: 1573.3325. Elemental analysis ($C_{102}H_{72}FeN_{10}O_2P_4S_2$ M + 2MeCN): C=71.49, H=4.24, N=8.16, S=3.74 (calc.); C=72.03, H=3.59, N=9.34, S=3.57 (found).

[Co(4,6-bis(diphenylphosphane-yl)-10-(1,10-phenanthrolin-2-yl)-phenoxazine)$_2$(NCS)$_2$] (**45**)

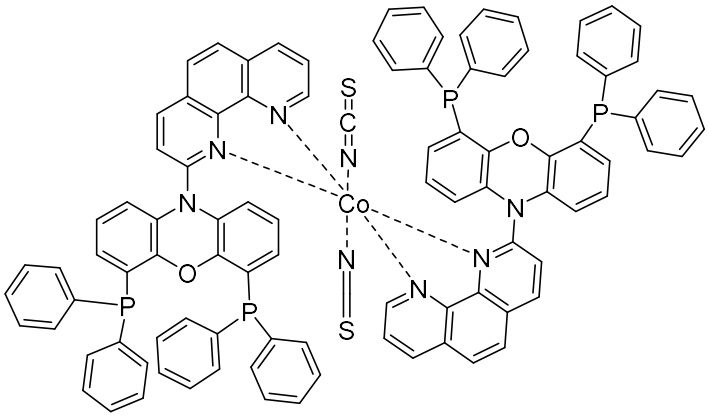

4,6-bis(diphenylphosphane-yl)-10-(1,10-phenanthrolin-2-yl)-phenoxazine **42** (81.5 mg, 0.112 mmol, 2.00 equiv.) was dissolved with $CoCl_2$, H_2O (7.25 mg, 0.053 mmol, 1.00 equiv.) in a mixture of MeCN/water 2:1 v/v (5 mL) and a solution of NH_4NCS (42.4 mg, 0.56 mmol, 10.0 equiv.) in 2 mL of water was added. The mixture was stirred at room temperature for 1 hour. The precipitate was filtered and washed with water. The resulting crude product was purified by recrystallization (*MeCN*/Et_2O) to afford the title compound **45** (58.8 mg, 0.035 mmol, 67%) as an orange solid.

^{1}H NMR (400 MHz, $CDCl_3$): *paramagnetic* IR (ATR, ṽ) = 3063, 3047, 3014, 3003, 2079, 2061, 2050, 1582, 1572, 1560, 1509, 1496, 1477, 1453, 1434, 1417, 1322, 1306, 1276, 1217, 1197, 1180, 1143, 1091, 858, 771, 738, 728, 690, 664, 653, 647, 540, 514, 494, 443, 428, 407, 397 cm^{-1}.. – **MS** (ESI): *m/z* (%) = 1576.0 (100), 1575.0 (92), 1576.9 (56) $[M\text{-}NCS]^+$. – **HRMS** ($C_{97}H_{66}CoN_7O_2P_4S$): calc.: 1576.3315, found: 1576.3324. Elemental analysis ($C_{98}H_{66}CoN_8O_2P_4S_2$): C=72.01, H=4.07, N=6.86, S=3.92 (calc.); C=70.75, H=3.92, N=10.04, S=4.63 (found). **m.p**.:293°C

[Zn(4,6-bis(diphenylphosphane-yl)-10-(1,10-phenanthrolin-2-yl)-phenoxazine)$_2$(NCS)$_2$] (**47**)

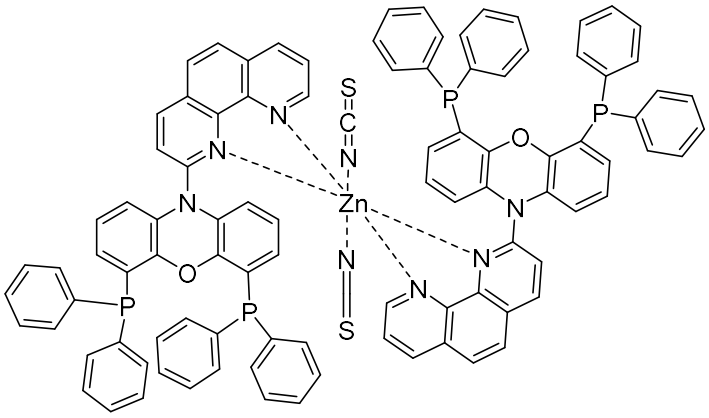

4,6-bis(diphenylphosphane-yl)-10-(1,10-phenanthrolin-2-yl)-phenoxazine **42** (40.5 mg, 0.055 mmol, 2.00 equiv.) was dissolved with $ZnCl_2$, H_2O (3.70 mg, 0.027 mmol, 1.00 equiv.) in a mixture of MeCN/water 2:1 v/v (2 mL) and a solution of NH_4NCS (20.8 mg, 0.27 mmol, 10.0 equiv.) in 1 mL of water was added. The mixture was stirred at room temperature for 1 hour. The precipitate was filtered and washed with water. The resulting crude product was purified by recrystallization (*MeCN*/Et_2O) to afford the title compound **47** (21.8 mg, 0.013 mmol, 49%) as a white solid.

^{1}H NMR (400 MHz, $CDCl_3$): δ = 9.04 (dd, *J* = 4.9, 1.6 Hz, 2H), 8.25 (d, *J* = 8.3 Hz, 2H), 8.01 (dd, *J* = 8.3, 1.6 Hz, 2H), 7.68 (d, *J* = 8.9 Hz, 2H), 7.59 - 7.48 (m, 11H), 7.45 - 7.34 (m, 15H), 7.10 - 7.01 (m, 16H), 6.98 - 6.92 (m, 6H), 6.76 (t, *J* = 7.9 Hz, 2H), 6.24 (ddd, *J* = 7.9, 3.3, 1.4 Hz, 2H), 5.79 (d, *J* = 7.9 Hz, 2H), 5.68 (m, 2H), 5.42 (t, *J* = 7.9 Hz, 2H) ppm .– **IR** (ATR): $\tilde{\nu}$ = 3065, 3050, 3024, 2055, 1572, 1509, 1496, 1477, 1453, 1434, 1415, 1322, 1303, 1276, 1217, 1197, 1180, 1159, 1143, 1112, 1091, 1068, 1026, 997, 955, 888, 858, 830, 820, 803, 792, 771, 738, 727, 690, 653, 646, 619, 584, 562, 538, 513, 492, 443, 426, 418, 407, 397, 381cm^{-1}. – **MS** (ESI): *m/z* (%) = 1582.2 (100), 1581.1 (96), 1583.2 (84), 1580.2 (76), 1584.2 (72) [M-NCS]$^+$ – **HRMS** ($C_{97}H_{66}N_7O_2P_4SZn$): calc.: 1581.3274, found: 1581.3268. Elemental analysis ($C_{98}H_{66}Cl_2N_8O_2P_4S_2Zn_2$ M+$ZnCl_2$): C=66.23, H=3.74, N=6.30, S=3.61 (calc.); C=64.70, H=3.76, N=6.22, S=3.36 (found). **m.p**.:261°C

[Ni(4,6-bis(diphenylphosphane-yl)-10-(1,10-phenanthrolin-2-yl)-phenoxazine)$_2$(NCS)$_2$] (**46**)

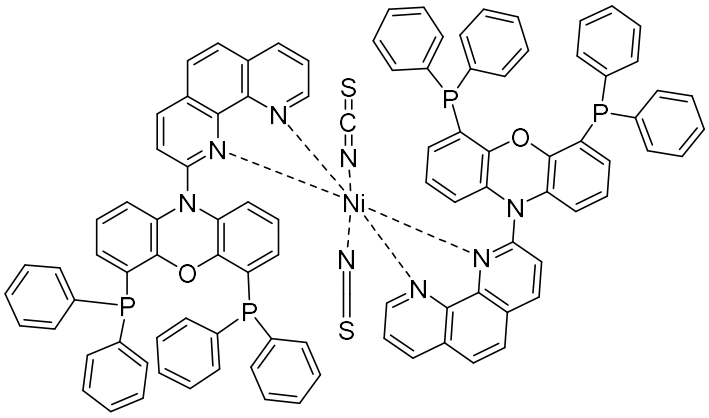

4,6-bis(diphenylphosphane-yl)-10-(1,10-phenanthrolin-2-yl)-phenoxazine **42** (40.7 mg, 0.056 mmol, 2.00 equiv.) was dissolved with $NiCl_2$, H_2O (3.5 mg, 0.027 mmol, 1.00 equiv.) in a mixture of MeCN/water 2:1 v/v (2 mL) and a solution of NH_4NCS (20.8 mg, 0.27 mmol, 10.0 equiv.) in 1 mL of water was added. The mixture was stirred at room temperature for 1 hour. The precipitate was filtered and washed with water. The resulting crude product was purified by recrystallization (*MeCN*/Et_2O) to afford the title compound **46** (24.7 mg, 0.015 mmol, 56.0%) as a dark green solid.

^{1}H NMR (400 MHz, $CDCl_3$): δ = 8.20 – 8.08 (m, 10H), 7.95 – 7.67 (m, 17H), 7.69 – 7.55 (m, 26H), 6.66 – 6.49 (m, 7H, $H_{xantphos\text{-}aromatic}$), 5.79 – 5.69 (m, 5H, $H_{xantphos\text{-}aromatic}$) ppm .– **IR** (ATR): $\tilde{\nu}$ = 3065, 3047, 2094, 2070, 1582, 1574, 1558, 1509, 1497, 1477, 1455, 1432, 1417, 1395, 1322, 1306, 1278, 1218, 1196, 1180, 1150, 1143, 1113, 1091, 1068, 1026, 955, 891, 870, 858, 830, 820, 793, 771, 761, 738, 728, 690, 664, 649, 585, 560, 540, 514, 493, 458, 445, 428, 395 cm^{-1}. – **MS** (ESI): *m/z* (%) = 1575.1 (100), 1576.1 (90), 1574.2 (78), 1577.2 (50) $[M\text{-}NCS]^+$, 1517.2 $[M\text{-}2NCS+H]^+$.– **HRMS** ($C_{97}H_{66}N_7NiO_2P_4S$): calc.: 1575.3336, found: 1575.3323. Elemental analysis ($C_{98}H_{66}Cl_2N_8O_2P_4S_2Zn_2$ M+$NiCl_2$): C=66.73, H=3.77, N=6.35, S=3.63 (calc.); C=67.77, H=3.77, N=6.76, S=3.57 (found). **m.p**.:307°C

[Zn(1,3-bis((4-(quinol-2´yl)-1,2,3-triazol-1-yl)methyl)pyridine)(NCS)$_2$py] (**33**)

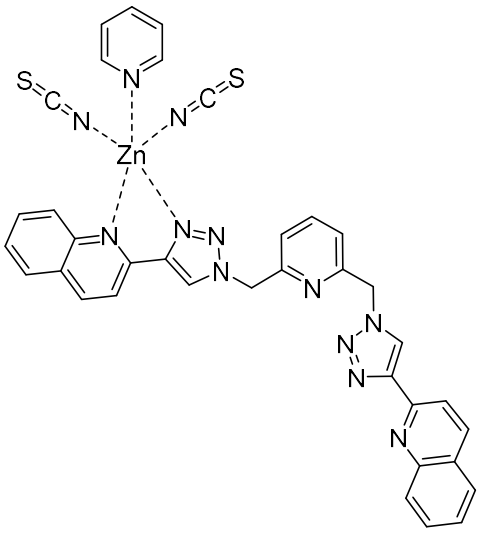

1,3-bis((4-(quinol-2´yl)-1,2,3-triazol-1-yl)methyl)pyridine (54.4 mg, 0.11 mmol, 1.00 equiv.) was dissolved in 5 mL MeOH and added dropwise to a solution of $Zn(NCS)_2Py_4$ (54.6 mg, 0.11 mmol, 1.00 equiv.) in MeOH (5 mL). The mixture was stirred at room temperature for 1 hour. The precipitate was filtered and washed with MeOH. The resulting crude product was purified by recrystallization (*MeCN*/Et_2O) to afford the title compound **33** (55.6 mg, 0.074 mmol, 67.0%) as a white solid.

^{1}H NMR (400 MHz, DMSO-d_6): δ = 8.83 (s, 2H), 8.37 (d, J = 8.6 Hz, 4H), 8.15 (d, J = 8.6 Hz, 4H), 7.95 (m, 5H), 7.90 (t, J = 7.8 Hz, 1H), 7.74 (t, J = 7.8 Hz, 2H), 7.58 (t, J = 7.3 Hz, 2H), 7.31 (d, J = 7.8 Hz, 2H), 5.84 (s, 4H, CH_2) ppm. IR (ATR, $\tilde{\nu}$) = 2973, 2908, 2866, 2473, 2065, 1751, 1602, 1490, 1468, 1448, 1366, 1272, 1248, 1157, 1092, 1074, 1051, 1027, 962, 914, 891, 858, 747, 611, 589, 544, 479, 436 cm^{-1}. – **MS** (ESI): *m/z* (%) = 307.1 (100), 308.1 (20), 309.1 (4), [M-NCS-Py]$^{2+}$, 617.1 [M-NCS-Py]$^+$. – **HRMS** ($C_{30}H_{21}N_{10SZn}$): calc.: 617.0963, found: 617.0964.

[Co(1,3-bis((4-(quinol-2´yl)-1,2,3-triazol-1-yl)methyl)pyridine)(NCS)$_2$py] (**30**)

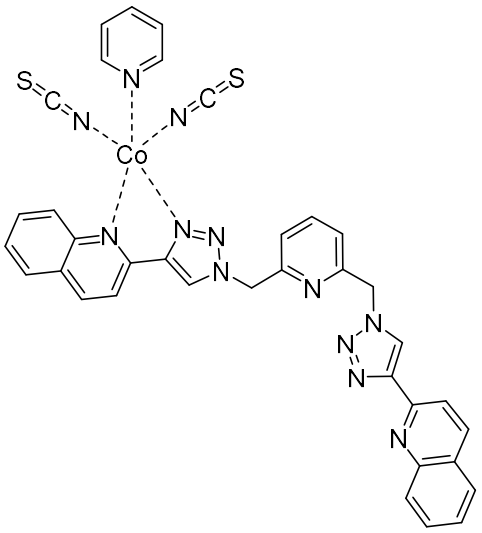

1,3-bis((4-(quinol-2´yl)-1,2,3-triazol-1-yl)methyl)pyridine **26** (54.7 mg, 0.11 mmol, 1.00 equiv.) was dissolved in 5 mL MeOH and added dropwise to a solution of $Co(NCS)_2Py_4$ (54.4 mg, 0.11 mmol, 1.00 equiv.) in MeOH (5 mL). The mixture was stirred at room temperature for 1 hour. The precipitate was filtered and washed with MeOH. The resulting crude product was purified by recrystallization (*MeCN*/Et_2O) to afford the title compound **30** (44.5 mg, 0.059 mmol, 54.0%) as a blue solid.

IR (ATR, $\tilde{\nu}$) = 3077, 2079, 2023, 1599, 1572, 1507, 1439, 1211, 1065, 1006, 833, 766, 755, 711, 698, 681, 625, 513, 480, 421 cm^{-1}.. – **MS** (ESI): *m/z* (%) = 336.1 (100), 337.1 (9), 338.1 (2), [M-Py]$^{2+}$, 612.1 [M-NCS-Py]$^+$. – **HRMS** ($C_{30}H_{21}CoN_{10}S$): calc.: 612.1003, found: 612.0994. Elemental analysis ($C_{36}H_{26}N_{12}CoS_2$ + $3H_2O$): C=53.79, H=4.01, N=20.91, S=7.98 (calc.); C=53.06, H=3.36, N=20.93, S=8.33 (found).

[Fe(1,3-bis((4-(quinol-2´yl)-1,2,3-triazol-1-yl)methyl)pyridine)(NCS)$_2$py] (**31**)

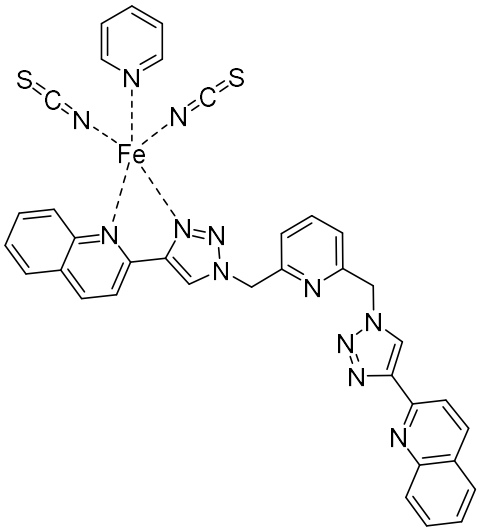

1,3-bis((4-(quinol-2´yl)-1,2,3-triazol-1-yl)methyl)pyridine **26** (87.1 mg, 0.18 mmol, 1.00 equiv.) was dissolved in 5 mL MeOH and added dropwise to a solution of Fe(NCS)$_2$Py$_4$ (86.7 mg, 0.18 mmol, 1.00 equiv.) in MeOH (5 mL). The mixture was stirred at room temperature for 1 hour. The precipitate was filtered and washed with MeOH. The resulting crude product was purified by recrystallization (*MeCN*/Et$_2$O) to afford the title compound **31** (70.5 mg, 0.094 mmol, 52%) as a red solid.

IR (ATR): $\tilde{\nu}$ = 3136, 3082, 2071, 1602, 1572, 1558, 1507, 1448, 1432, 1422, 1375, 1363, 1312, 1258, 1210, 1147, 1133, 1089, 1062, 1011, 994, 946, 833, 816, 786, 758, 721, 683, 632, 510, 489, 475, 401, 392, 375 cm^{-1} – **MS** (ESI): *m/z* (%) = 333.1 (100), 334.1 (9), 335.1 (5), 331.1 (4) [M-Py]$^{2+}$, 609.1 [M-NCS-Py]$^+$. – **HRMS** ($C_{30}H_{21}FeN_{10}S$): calc.: 609.1021, found: 609.1011. Elemental analysis ($C_{36}H_{26}N_{12}S_2Fe$ M+2CH_3OH): C=56.30, H=3.95, N=20.73, S=7.91 (calc.); C=54.26, H=3.07, N=21.85, S=7.69 (found). **m.p**.:195°C

[Ni(1,3-bis((4-(quinol-2´yl)-1,2,3-triazol-1-yl)methyl)pyridine)(NCS)$_2$py] (**32**)

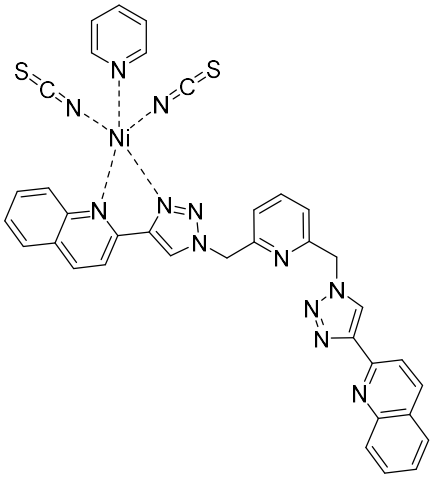

1,3-bis((4-(quinol-2´yl)-1,2,3-triazol-1-yl)methyl)pyridine **26** (87.3 mg, 0.18 mmol, 1.00 equiv.) was dissolved in 5 mL MeOH and added dropwise to a solution of Ni(NCS)$_2$Py$_4$ (86.7 mg, 0.18 mmol, 1.00 equiv.) in MeOH (5 mL). The mixture was stirred at room temperature for 1 hour. The precipitate was filtered and washed with MeOH. The resulting crude product was purified by recrystallization (*MeCN*/Et$_2$O) to afford the title compound **32** (125 mg, 0.175 mmol, 95 %) as a light blue solid.

IR (ATR): $\tilde{\nu}$ = 3133, 3068, 2079, 1601, 1574, 1557, 1509, 1459, 1441, 1421, 1373, 1261, 1214, 1200, 1145, 1133, 1062, 1041, 1013, 994, 949, 830, 816, 786, 755, 720, 696, 630, 516, 475, 432, 401 cm^{-1}. – **MS** (ESI): *m/z* (%) = 611.1 [M-NCS-Py]$^+$. – **HRMS** ($C_{30}H_{21}N_{10}NiS$): calc.: 611.1025, found: 611.1019. Elemental analysis ($C_{36}H_{26}N_{12}NiS_2$+2CH_3OH): C=56.10, H=4.21, N=20.66, S=7.88 (calc.); C=55.37, H=3.46, N=21.25, S=7.89 (found). **m.p**.:244°C

[Co(1,3-bis((4-(quinol-2′yl)-1,2,3-triazol-1-yl)methyl)pyridine)$_2$] (**35**)

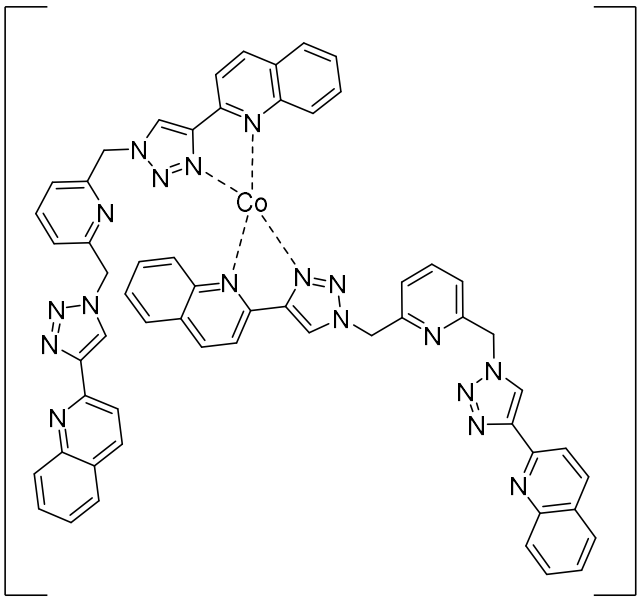

1,3-bis((4-(quinol-2′yl)-1,2,3-triazol-1-yl)methyl)pyridine **26** (30.0 mg, 0.06 mmol, 1.00 equiv.) was dissolved in 5 mL MeOH and added dropwise to a solution of $Co(ClO_4)_2$ (22.2 mg, 0.06 mmol, 1.00 equiv.) in MeOH (5 mL). The mixture was stirred at room temperature for 1 hour. The precipitate was filtered and washed with MeOH. The resulting crude product was purified by recrystallization (*MeCN*/Et_2O) to afford the title compound **35** (56 mg, 0.045 mmol, 75 %) as a pink solid.

MS (ESI): *m/z* (%) = 611.1 [M-NCS-Py]$^+$. – **HRMS** ($C_{58}H_{42}ClCoN_{18}O_4$): calc.: 1148.2662, found: 1148.2658

[(1,3-bis((4-(quinol-2′yl)-1,2,3-triazol-1-yl)methyl)pyridine)$Co_2(NCS)_4py_2$] (CAT-**34**)

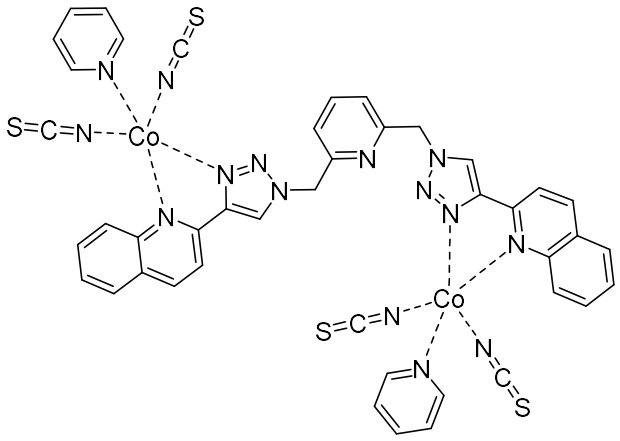

1,3-bis((4-(quinol-2′yl)-1,2,3-triazol-1-yl)methyl)pyridine **26** (16.8 mg, 0.034 mmol, 1.00 equiv.) was dissolved in 5 mL MeOH and added dropwise to a solution of $Co(SCN_2)Py_4$ (50.2 mg, 0.10 mmol, 3.00 equiv.) in MeOH (5 mL). The mixture was stirred at room temperature for 1 hour. The precipitate was filtered and washed with MeOH. The resulting crude product was purified by recrystallization (*MeCN*/Et_2O) to afford the title compound **34** (20.8 mg, 0.020 mmol, 61 %) as a purple solid.

IR (ATR): $\tilde{\nu}$ = 3403, 3316, 3149, 3060, 2945, 2051, 1646, 1602, 1572, 1555, 1507, 1502, 1460, 1436, 1419, 1374, 1366, 1305, 1235, 1211, 1193, 1146, 1130, 1062, 1044, 1026, 1014, 994, 949, 832, 786, 755, 715, 680, 656, 629, 613, 603, 584, 562, 554, 537, 514, 487, 476, 395, 387, 375 cm^{-1}. – **MS** (ESI): *m/z* (%) = 263.0 [M-NCS-2Py+2H]$^{3+}$, 787.6 [M-NCS-2Py]$^+$. – **HRMS** ($C_{33}H_{24}Co_2N_{11}S_3$): calc.: 262.6675, found: 263.0129**. FAB-MS** (m/z, 3-NBA): 787.1 [M-NCS-2Py]$^+$ **Elemental analysis**

($C_{43}H_{31}Co_2N_{15}S_4$ + Co(NCS)): C=47.15, H=2.79, N=19.99 S=14.30 (calc.); C=50.30, H=3.79, N=16.55, S=14.03 (found).

6.4 CRYSTALLOGRAPHY DATA RESOLVED BY DR. OLAF. FUHR

Entry	Name in this thesis	Name from Olaf Fuhr
1	L-**6**	LLG-97-liq
2	Ni(cyclam)Cl_2 (**1**)	Ni_Cyclam_Cl2
3	PS-**4**	LLG52-meta
4	PS-4_b	LLG-162
5	$Fe(NCS)_2py_4$ oxidized	LLG192
6	$Co(NCS)_2py_2$	LLG-182
7	$Co(NCS)_2py_4$	LLG230
8	$Ni(NCS)_2py_4$	LLG191
9	CAT-**11**	LLG-FeL-GP2
10	CAT-**12**	LLG-122
11	CAT-**17**	LLG-115
12	CAT-**18**	LLG-38
13	CAT-**19**	LLG55
14	CAT-**20**	KRS-36
15	CAT-**36**	LLG-187
16	CAT-**37**	LLG-136
17	CAT-**27**	LLG-129
18	CAT-**34**	LLG-171
19	[Cu-Cl-Cu]	LLG-196
20	[Cu-NCS-Cu]	LLG-148-farblos

2,6-bis(1,2,3-triazol-yl-methyl)pyridine (L-**6**)

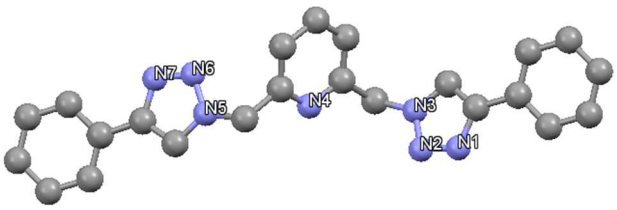

Identification code	LLG-97-liq
Empirical formula	$C_{23}H_{19}N_7$
Formula weight	393.45
Temperature/K	150.0
Crystal system	triclinic
Space group	P-1
a/Å	6.2850(5)
b/Å	7.5728(8)
c/Å	20.3690(15)
α/°	94.454(7)
β/°	90.129(6)
γ/°	103.679(7)
Volume/Å^3	938.91(14)
Z	2
ρ_{calc}g/cm^3	1.392
μ/mm^{-1}	0.449
F(000)	412.0
Crystal size/mm^3	0.12 × 0.11 × 0.1
Radiation	GaKα (λ = 1.34143)
2Θ range for data collection/°	3.786 to 124.766
Index ranges	-8 ≤ h ≤ 8, -10 ≤ k ≤ 5, -26 ≤ l ≤ 26
Reflections collected	10785
Independent reflections	4376 [R_{int} = 0.0195, R_{sigma} = 0.0171]
Data/restraints/parameters	4376/0/347
Goodness-of-fit on F^2	1.104
Final R indexes [I>=2σ (I)]	R_1 = 0.0405, wR_2 = 0.1156
Final R indexes [all data]	R_1 = 0.0476, wR_2 = 0.1206
Largest diff. peak/hole / e Å^{-3}	0.25/-0.24

[Ni(1,4,8,11-tetraazacyclotetradecane)Cl_2] (Ni(cyclam)Cl_2 CAT-**1**)

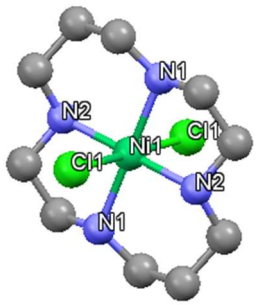

Identification code	Ni_Cyclam_Cl2
Empirical formula	$C_{10}H_{24}Cl_2N_4Ni$
Formula weight	329.94
Temperature/K	150
Crystal system	monoclinic
Space group	$P2_1/n$
a/Å	6.5634(3)
b/Å	8.3377(5)
c/Å	13.4872(6)
α/°	90
β/°	103.758(3)
γ/°	90
Volume/Å^3	716.89(6)
Z	2
ρ_{calc}g/cm^3	1.528
μ/mm^{-1}	9.718
F(000)	348.0
Crystal size/mm^3	0.16 × 0.14 × 0.1
Radiation	GaKα (λ = 1.34143)
2Θ range for data collection/°	10.944 to 124.934
Index ranges	$-2 \le h \le 8$, $-10 \le k \le 11$, $-17 \le l \le 17$
Reflections collected	4575
Independent reflections	1695 [R_{int} = 0.0160, R_{sigma} = 0.0126]
Data/restraints/parameters	1695/0/127
Goodness-of-fit on F^2	1.090
Final R indexes [I>=2σ (I)]	R_1 = 0.0239, wR_2 = 0.0635
Final R indexes [all data]	R_1 = 0.0249, wR_2 = 0.0644
Largest diff. peak/hole / e Å^{-3}	0.35/-0.53

[(1,3-bis((4-(quinol-2´yl)-1,2,3-triazol-1-yl)methyl)benzene)Cu_2(DPEPhos)$_2$] (PS-**4**)

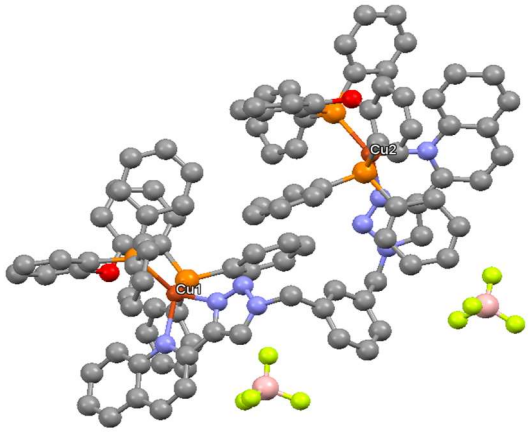

Identification code	LLG52-meta
Empirical formula	$C_{106}H_{80}B_2Cu_2F_8N_8O_4P_4$
Formula weight	1954.36
Temperature/K	150.0
Crystal system	triclinic
Space group	P-1
a/Å	14.7119(9)
b/Å	17.1432(6)
c/Å	23.5508(12)
α/°	106.731(3)
β/°	96.377(4)
γ/°	96.990(4)
Volume/Å^3	5578.9(5)
Z	2
ρ_{calc}g/cm^3	1.163
μ/mm^{-1}	2.745
F(000)	2008.0
Crystal size/mm^3	0.12 × 0.04 × 0.03
Radiation	GaKα (λ = 1.34143)
2Θ range for data collection/°	4.746 to 99.998
Index ranges	-16 ≤ h ≤ 16, -19 ≤ k ≤ 19, -26 ≤ l ≤ 16
Reflections collected	43829
Independent reflections	16651 [R_{int} = 0.1139, R_{sigma} = 0.0855]
Data/restraints/parameters	16651/0/1207
Goodness-of-fit on F^2	1.259
Final R indexes [I>=2σ (I)]	R_1 = 0.1163, wR_2 = 0.3040
Final R indexes [all data]	R_1 = 0.1650, wR_2 = 0.3438
Largest diff. peak/hole / e Å^{-3}	0.87/-1.34

[(1,3-bis((4-(quinol-2′yl)-1,2,3-triazol-1-yl)methyl)pyridine)Cu_2(DPEPhos)$_2$] (**41$_b$**)

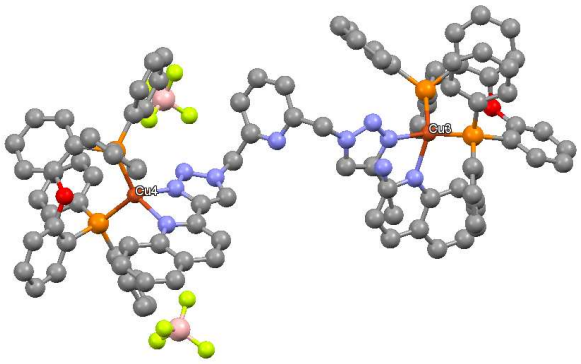

Identification code	LLG-162
Empirical formula	$C_{106}H_{84.5}BClCu_2F_4N_{11.5}O_6P_4$
Formula weight	1988.57
Temperature/K	150
Crystal system	triclinic
Space group	P-1
a/Å	9.7278(2)
b/Å	29.0886(5)
c/Å	34.4828(7)
α/°	87.437(2)
β/°	82.179(2)
γ/°	80.9650(10)
Volume/Å^3	9544.1(3)
Z	4
ρ_{calc}g/cm^3	1.384
μ/mm^{-1}	3.361
F(000)	4100.0
Crystal size/mm^3	0.14 × 0.03 × 0.02
Radiation	GaKα (λ = 1.34143)
2Θ range for data collection/°	5.184 to 114.998
Index ranges	-12 ≤ h ≤ 4, -36 ≤ k ≤ 36, -43 ≤ l ≤ 43
Reflections collected	100916
Independent reflections	38371 [R_{int} = 0.0657, R_{sigma} = 0.1076]
Data/restraints/parameters	38371/0/2345
Goodness-of-fit on F^2	0.975
Final R indexes [I>=2σ (I)]	R_1 = 0.0683, wR_2 = 0.1735
Final R indexes [all data]	R_1 = 0.1351, wR_2 = 0.2017
Largest diff. peak/hole / e Å^{-3}	2.00/-1.35

[$Fe_2py_4(NCS)_4(MeOH)_2$]

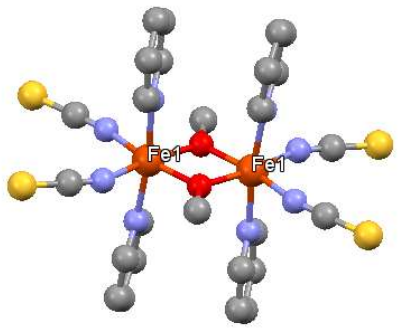

Identification code	LLG192
Empirical formula	$C_{26}H_{26}Fe_2N_8O_2S_4$
Formula weight	722.49
Temperature/K	180
Crystal system	monoclinic
Space group	$P2_1/n$
a/Å	9.8390(6)
b/Å	13.1414(6)
c/Å	12.7725(8)
α/°	90
β/°	101.975(5)
γ/°	90
Volume/Å^3	1615.52(16)
Z	2
ρ_{calc}g/cm^3	1.485
μ/mm^{-1}	6.625
F(000)	740.0
Crystal size/mm^3	0.18 × 0.16 × 0.14
Radiation	GaKα (λ = 1.34143)
2Θ range for data collection/°	8.496 to 125.044
Index ranges	$-12 \leq h \leq 12$, $-8 \leq k \leq 17$, $-16 \leq l \leq 16$
Reflections collected	11562
Independent reflections	3850 [R_{int} = 0.0237, R_{sigma} = 0.0259]
Data/restraints/parameters	3850/0/191
Goodness-of-fit on F^2	1.068
Final R indexes [I>=2σ (I)]	R_1 = 0.0442, wR_2 = 0.1253
Final R indexes [all data]	R_1 = 0.0574, wR_2 = 0.1317
Largest diff. peak/hole / e Å^{-3}	0.74/-0.60

[$Copy_2(NCS)_2$]

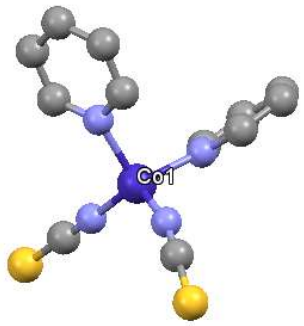

Identification code	LLG-182
Empirical formula	$C_{12}H_{10}CoN_4S_2$
Formula weight	333.29
Temperature/K	150.0
Crystal system	monoclinic
Space group	$P2_1/m$
a/Å	5.5123(5)
b/Å	10.8118(10)
c/Å	12.0416(12)
α/°	90
β/°	97.257(8)
γ/°	90
Volume/$Å^3$	711.91(12)
Z	2
$\rho_{calc}g/cm^3$	1.555
μ/mm^{-1}	8.250
F(000)	338.0
Crystal size/mm^3	0.14 × 0.03 × 0.02
Radiation	GaKα (λ = 1.34143)
2Θ range for data collection/°	6.438 to 125.21
Index ranges	$-7 \leq h \leq 2$, $-14 \leq k \leq 14$, $-15 \leq l \leq 15$
Reflections collected	4731
Independent reflections	1766 [R_{int} = 0.0171, R_{sigma} = 0.0146]
Data/restraints/parameters	1766/0/117
Goodness-of-fit on F^2	1.129
Final R indexes [I>=2σ (I)]	R_1 = 0.0313, wR_2 = 0.0756
Final R indexes [all data]	R_1 = 0.0386, wR_2 = 0.0845
Largest diff. peak/hole / e $Å^{-3}$	0.26/-0.40

[$Copy_4(NCS)_2$]

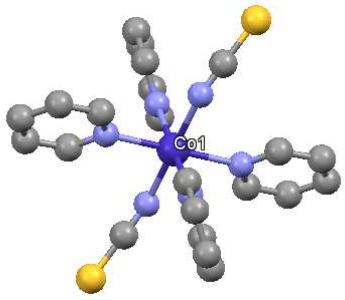

Identification code	LLG230
Empirical formula	$C_{22}H_{20}CoN_6S_2$
Formula weight	491.49
Temperature/K	180
Crystal system	monoclinic
Space group	C2/c
a/Å	12.3288(4)
b/Å	12.9782(3)
c/Å	14.9943(5)
α/°	90
β/°	107.385(2)
γ/°	90
Volume/$Å^3$	2289.57(12)
Z	4
$\rho_{calc}g/cm^3$	1.426
μ/mm^{-1}	5.271
F(000)	1012.0
Crystal size/mm^3	0.16 × 0.14 × 0.12
Radiation	GaKα (λ = 1.34143)
2Θ range for data collection/°	8.826 to 124.974
Index ranges	$-15 \leq h \leq 16$, $-16 \leq k \leq 6$, $-19 \leq l \leq 19$
Reflections collected	8840
Independent reflections	2699 [R_{int} = 0.0142, R_{sigma} = 0.0096]
Data/restraints/parameters	2699/0/182
Goodness-of-fit on F^2	1.063
Final R indexes [I>=2σ (I)]	R_1 = 0.0248, wR_2 = 0.0646
Final R indexes [all data]	R_1 = 0.0267, wR_2 = 0.0660
Largest diff. peak/hole / e $Å^{-3}$	0.20/-0.45

[Nipy$_4$(NCS)$_2$]

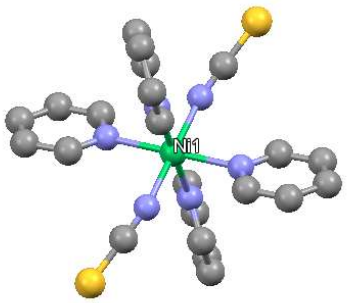

Identification code	LLG191
Empirical formula	$C_{22}H_{20}N_6NiS_2$
Formula weight	491.27
Temperature/K	180.0
Crystal system	monoclinic
Space group	C2/c
a/Å	12.3182(3)
b/Å	12.9116(3)
c/Å	14.9394(4)
α/°	90
β/°	107.420(2)
γ/°	90
Volume/Å^3	2267.10(10)
Z	4
ρ_{calc}g/cm^3	1.439
μ/mm^{-1}	6.009
F(000)	1016.0
Crystal size/mm^3	0.16 × 0.12 × 0.02
Radiation	GaKα (λ = 1.34143)
2Θ range for data collection/°	8.852 to 124.952
Index ranges	-13 ≤ h ≤ 16, -17 ≤ k ≤ 16, -19 ≤ l ≤ 9
Reflections collected	13482
Independent reflections	2720 [R_{int} = 0.0154, R_{sigma} = 0.0100]
Data/restraints/parameters	2720/0/182
Goodness-of-fit on F^2	1.020
Final R indexes [I>=2σ (I)]	R_1 = 0.0247, wR_2 = 0.0643
Final R indexes [all data]	R_1 = 0.0271, wR_2 = 0.0660
Largest diff. peak/hole / e Å^{-3}	0.20/-0.36

[(2,6-bis(1,2,3-triazol-yl-methyl)pyridine)Fe(NCS)$_2$py] (CAT-**11**)

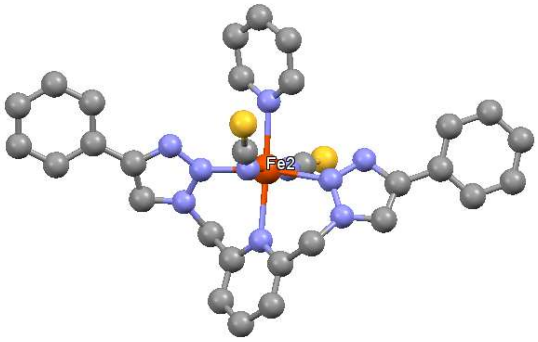

Identification code	LLG-FeL-GP2
Empirical formula	$C_{33}H_{30.5}FeN_{10.5}O_{0.5}S_2$
Formula weight	702.15
Temperature/K	180
Crystal system	monoclinic
Space group	$P2_1/n$
a/Å	15.3903(2)
b/Å	24.3563(3)
c/Å	18.3465(3)
α/°	90
β/°	96.2740(10)
γ/°	90
Volume/Å^3	6836.01(17)
Z	8
ρ_{calc}g/cm^3	1.364
μ/mm^{-1}	3.353
F(000)	2912.0
Crystal size/mm^3	0.14 × 0.12 × 0.1
Radiation	GaKα (λ = 1.34143)
2Θ range for data collection/°	5.266 to 125
Index ranges	$-20 \leq h \leq 16$, $-32 \leq k \leq 31$, $-24 \leq l \leq 18$
Reflections collected	77902
Independent reflections	16374 [R_{int} = 0.0248, R_{sigma} = 0.0220]
Data/restraints/parameters	16374/0/850
Goodness-of-fit on F^2	1.027
Final R indexes [I>=2σ (I)]	R_1 = 0.0457, wR_2 = 0.1205
Final R indexes [all data]	R_1 = 0.0639, wR_2 = 0.1312
Largest diff. peak/hole / e Å^{-3}	0.96/-0.95

[(2,6-bis(1,2,3-triazol-yl-methyl)pyridine)Co(NCS)$_2$py] (CAT-**12**)

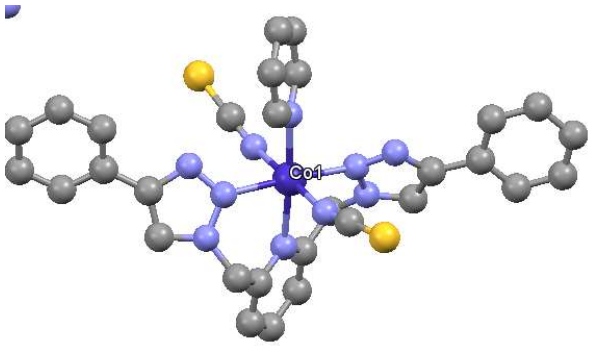

Identification code	LLG-122-liq
Empirical formula	$C_{32}H_{27}CoN_{11}S_2$
Formula weight	688.69
Temperature/K	150.0
Crystal system	monoclinic
Space group	$P2_1/n$
a/Å	10.9027(4)
b/Å	12.6920(5)
c/Å	24.0308(7)
α/°	90
β/°	93.933(3)
γ/°	90
Volume/Å^3	3317.5(2)
Z	4
ρ_{calc}g/cm^3	1.379
μ/mm^{-1}	3.775
F(000)	1420.0
Crystal size/mm^3	0.12 × 0.1 × 0.02
Radiation	GaKα (λ = 1.34143)
2Θ range for data collection/°	6.416 to 125.052
Index ranges	$-4 \leq h \leq 14$, $-16 \leq k \leq 14$, $-31 \leq l \leq 31$
Reflections collected	22581
Independent reflections	7838 [R_{int} = 0.0201, R_{sigma} = 0.0224]
Data/restraints/parameters	7838/0/414
Goodness-of-fit on F^2	1.250
Final R indexes [I>=2σ (I)]	R_1 = 0.0750, wR_2 = 0.1584
Final R indexes [all data]	R_1 = 0.0820, wR_2 = 0.1608
Largest diff. peak/hole / e Å^{-3}	0.43/-0.59

[(2,6-bis(1,2,3-triazol-yl-methyl)pyridine)$_2$Fe](ClO$_4$)$_2$ (CAT-**17**)

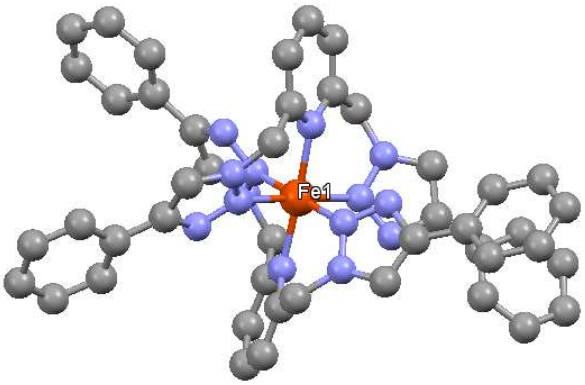

Identification code	LLG-115
Empirical formula	$C_{52}H_{51}Cl_2FeN_{15}O_9$
Formula weight	1156.82
Temperature/K	150.0
Crystal system	triclinic
Space group	P-1
a/Å	12.4102(4)
b/Å	14.6386(4)
c/Å	16.9688(6)
α/°	114.112(2)
β/°	101.373(3)
γ/°	95.961(2)
Volume/Å^3	2699.25(16)
Z	2
ρ_{calc}g/cm^3	1.423
μ/mm^{-1}	2.492
F(000)	1200.0
Crystal size/mm^3	0.15 × 0.12 × 0.02
Radiation	GaKα (λ = 1.34143)
2Θ range for data collection/°	5.868 to 125.024
Index ranges	-12 ≤ h ≤ 16, -16 ≤ k ≤ 19, -22 ≤ l ≤ 20
Reflections collected	34883
Independent reflections	12717 [R_{int} = 0.0150, R_{sigma} = 0.0153]
Data/restraints/parameters	12717/2/690
Goodness-of-fit on F^2	1.067
Final R indexes [I>=2σ (I)]	R_1 = 0.0519, wR_2 = 0.1517
Final R indexes [all data]	R_1 = 0.0580, wR_2 = 0.1573
Largest diff. peak/hole / e Å^{-3}	1.23/-1.04

[(2,6-bis(1,2,3-triazol-yl-methyl)pyridine)$_2$Co] (ClO$_4$)$_2$ (CAT-**18**)

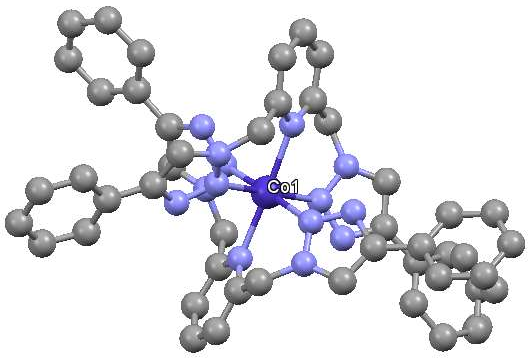

Identification code	LLG-38
Empirical formula	$C_{52}H_{50}Cl_2CoN_{15}O_9$
Formula weight	1158.90
Temperature/K	150
Crystal system	triclinic
Space group	P-1
a/Å	12.2852(4)
b/Å	14.6208(5)
c/Å	17.3378(8)
α/°	114.652(2)
β/°	102.124(4)
γ/°	94.299(3)
Volume/Å^3	2720.53(19)
Z	2
ρ_{calc}g/cm^3	1.415
μ/mm^{-1}	2.672
F(000)	1200.0
Crystal size/mm^3	0.18 × 0.04 × 0.03
Radiation	GaKα (λ = 1.34143)
2Θ range for data collection/°	5.062 to 125.066
Index ranges	-16 ≤ h ≤ 12, -19 ≤ k ≤ 16, -21 ≤ l ≤ 22
Reflections collected	35566
Independent reflections	12833 [R_{int} = 0.0198, R_{sigma} = 0.0230]
Data/restraints/parameters	12833/0/710
Goodness-of-fit on F^2	1.077
Final R indexes [I>=2σ (I)]	R_1 = 0.0473, wR_2 = 0.1254
Final R indexes [all data]	R_1 = 0.0595, wR_2 = 0.1329
Largest diff. peak/hole / e Å^{-3}	0.82/-0.57

[(2,6-bis(1,2,3-triazol-yl-methyl)pyridine)$_2$Ni] (ClO_4)$_2$ (CAT-**19**)

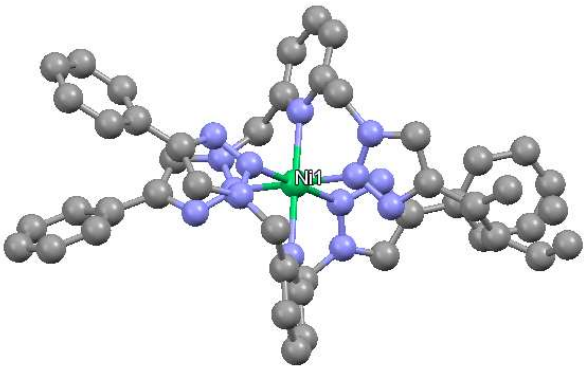

Identification code	LLG55
Empirical formula	$C_{55}H_{51.5}Cl_4N_{18.5}Ni_2$
Formula weight	1230.86
Temperature/K	150
Crystal system	monoclinic
Space group	$P2_1/n$
a/Å	13.6682(4)
b/Å	24.4825(8)
c/Å	17.5704(5)
α/°	90
β/°	93.109(3)
γ/°	90
Volume/Å^3	5871.0(3)
Z	4
ρ_{calc}g/cm^3	1.393
μ/mm^{-1}	4.963
F(000)	2540.0
Crystal size/mm^3	0.16 × 0.14 × 0.12
Radiation	GaKα (λ = 1.34143)
2Θ range for data collection/°	5.392 to 125.352
Index ranges	$-18 \leq h \leq 11$, $-27 \leq k \leq 32$, $-23 \leq l \leq 22$
Reflections collected	36766
Independent reflections	13774 [R_{int} = 0.0465, R_{sigma} = 0.0643]
Data/restraints/parameters	13774/0/698
Goodness-of-fit on F^2	1.187
Final R indexes [I>=2σ (I)]	R_1 = 0.1064, wR_2 = 0.2175
Final R indexes [all data]	R_1 = 0.1444, wR_2 = 0.2299
Largest diff. peak/hole / e Å^{-3}	0.83/-0.60

[(2,6-bis(1,2,3-triazol-yl-methyl)pyridine)$_2$Cu] (ClO_4)$_2$ (CAT-**20**)

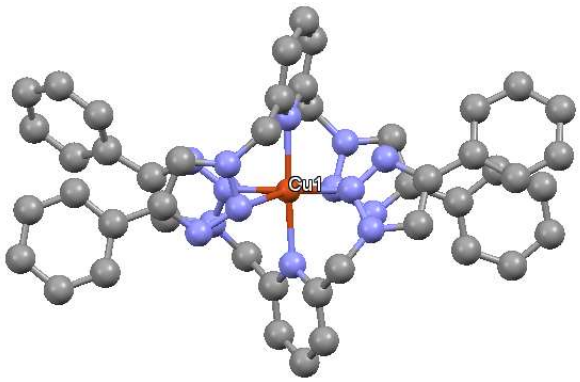

Identification code	KRS-36
Empirical formula	$C_{48}H_{41}Cl_2CuN_{15}O_8$
Formula weight	1090.40
Temperature/K	150
Crystal system	triclinic
Space group	P-1
a/Å	11.6609(5)
b/Å	12.5514(5)
c/Å	17.7093(8)
α/°	69.981(4)
β/°	78.574(4)
γ/°	79.792(3)
Volume/Å^3	2370.17(19)
Z	2
ρ_{calc}g/cm^3	1.528
μ/mm^{-1}	3.560
F(000)	1122.0
Crystal size/mm^3	0.16 × 0.13 × 0.02
Radiation	GaKα (λ = 1.34143)
2Θ range for data collection/°	4.672 to 125.1
Index ranges	-15 ≤ h ≤ 14, -16 ≤ k ≤ 16, -16 ≤ l ≤ 23
Reflections collected	29722
Independent reflections	11170 [R_{int} = 0.0325, R_{sigma} = 0.0499]
Data/restraints/parameters	11170/0/668
Goodness-of-fit on F^2	1.038
Final R indexes [I>=2σ (I)]	R_1 = 0.0478, wR_2 = 0.1212
Final R indexes [all data]	R_1 = 0.0756, wR_2 = 0.1319
Largest diff. peak/hole / e Å^{-3}	0.80/-1.00

[[(2,6-bis(1,2,3-triazol-yl-methyl)pyridine)$_3$Fe$_4$(NCS)$_8$(MeCN)$_6$] (ClO_4)$_2$ (CAT-**36**)

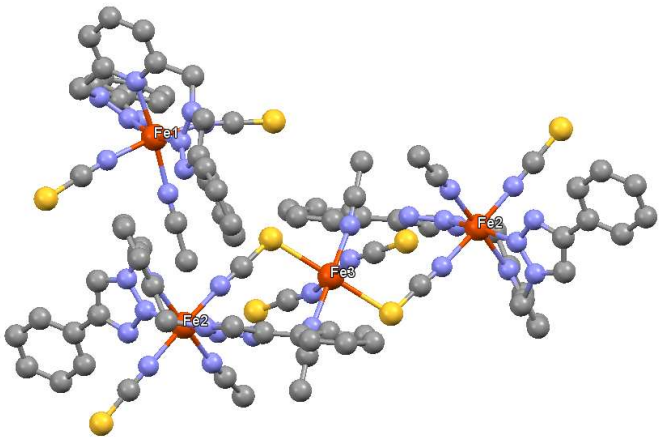

Identification code	LLG-187
Empirical formula	$C_{126}H_{120}Fe_5N_{46}O_2S_{10}$
Formula weight	2910.52
Temperature/K	180.0
Crystal system	monoclinic
Space group	$P2_1/n$
a/Å	14.7247(2)
b/Å	25.9200(5)
c/Å	18.5084(3)
α/°	90
β/°	92.4520(10)
γ/°	90
Volume/Å^3	7057.5(2)
Z	2
ρ_{calc}g/cm^3	1.370
μ/mm^{-1}	4.038
F(000)	3008.0
Crystal size/mm^3	0.14 × 0.12 × 0.1
Radiation	GaKα (λ = 1.34143)
2Θ range for data collection/°	7.246 to 124.996
Index ranges	-19 ≤ h ≤ 16, -32 ≤ k ≤ 34, -24 ≤ l ≤ 17
Reflections collected	44855
Independent reflections	16457 [R_{int} = 0.0317, R_{sigma} = 0.0473]
Data/restraints/parameters	16457/0/860
Goodness-of-fit on F^2	1.050
Final R indexes [I>=2σ (I)]	R_1 = 0.0619, wR_2 = 0.1769
Final R indexes [all data]	R_1 = 0.0965, wR_2 = 0.1970
Largest diff. peak/hole / e Å^{-3}	1.85/-1.36

[(2,6-bis(1,2,3-triazol-yl-methyl)pyridine)Ni(NCS)$_2$(MeOH)] (CAT-**37**)

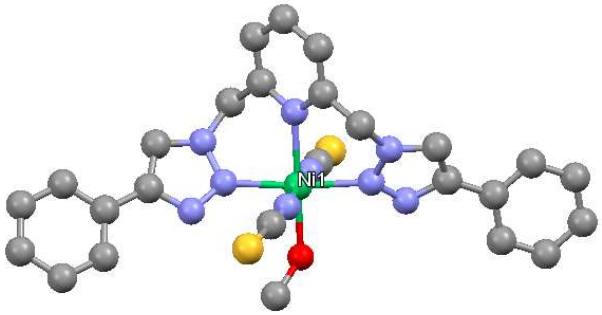

Identification code	LLG-136
Empirical formula	$C_{29}H_{29.5}N_{9.5}NiO_{1.5}S_2$
Formula weight	657.95
Temperature/K	150.0
Crystal system	monoclinic
Space group	$P2_1/n$
a/Å	14.9211(3)
b/Å	22.8349(6)
c/Å	18.0262(3)
α/°	90
β/°	96.716(2)
γ/°	90
Volume/Å^3	6099.8(2)
Z	8
ρ_{calc}g/cm^3	1.433
μ/mm^{-1}	4.609
F(000)	2736.0
Crystal size/mm^3	0.14 × 0.12 × 0.1
Radiation	GaKα (λ = 1.34143)
2Θ range for data collection/°	7.114 to 114.992
Index ranges	-13 ≤ h ≤ 18, -28 ≤ k ≤ 28, -18 ≤ l ≤ 22
Reflections collected	32396
Independent reflections	12297 [R_{int} = 0.0211, R_{sigma} = 0.0268]
Data/restraints/parameters	12297/7/771
Goodness-of-fit on F^2	1.094
Final R indexes [I>=2σ (I)]	R_1 = 0.0612, wR_2 = 0.1351
Final R indexes [all data]	R_1 = 0.0764, wR_2 = 0.1419
Largest diff. peak/hole / e Å^{-3}	0.67/-0.94

[(2-(1-(pyridin-2-ylmethyl)-1,2,3-triazol-4-yl)quinoline)Co(NCS)$_2$] (CAT-**27**)

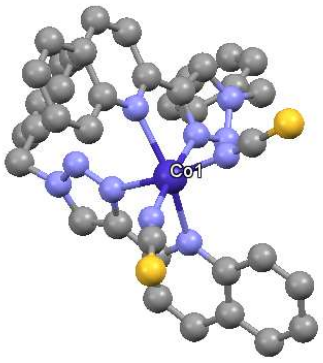

Identification code	LLG-129
Empirical formula	$C_{42}H_{34}CoN_{12}S_2$
Formula weight	829.86
Temperature/K	150.0
Crystal system	triclinic
Space group	P-1
a/Å	9.2762(4)
b/Å	14.7141(6)
c/Å	15.4774(6)
α/°	74.890(3)
β/°	85.542(3)
γ/°	86.397(3)
Volume/Å^3	2031.33(15)
Z	2
ρ_{calc}g/cm^3	1.357
μ/mm^{-1}	3.150
F(000)	858.0
Crystal size/mm^3	0.14 × 0.12 × 0.03
Radiation	GaKα (λ = 1.34143)
2Θ range for data collection/°	5.156 to 125.104
Index ranges	-11 ≤ h ≤ 12, -19 ≤ k ≤ 18, -20 ≤ l ≤ 11
Reflections collected	27488
Independent reflections	9417 [R_{int} = 0.0256, R_{sigma} = 0.0191]
Data/restraints/parameters	9417/0/516
Goodness-of-fit on F^2	1.054
Final R indexes [I>=2σ (I)]	R_1 = 0.0368, wR_2 = 0.0947
Final R indexes [all data]	R_1 = 0.0433, wR_2 = 0.0987
Largest diff. peak/hole / e Å^{-3}	0.54/-0.51

[(1,3-bis((4-(quinol-2´yl)-1,2,3-triazol-1-yl)methyl)pyridine)$Co_2(NCS)_4py_2$] (CAT-**34**)

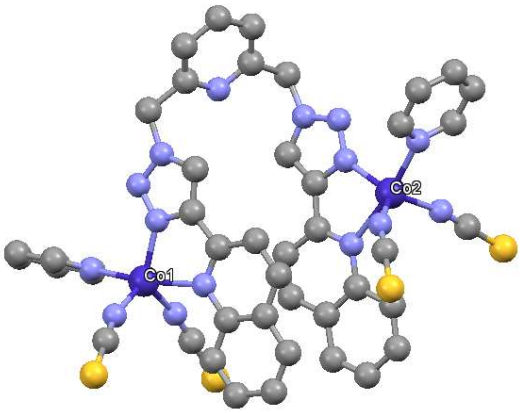

Identification code	LLG-171
Empirical formula	$C_{43}H_{31}Co_2N_{15}S_4$
Formula weight	1003.93
Temperature/K	150.0
Crystal system	triclinic
Space group	P-1
a/Å	13.8130(4)
b/Å	14.3712(4)
c/Å	14.5173(4)
α/°	95.869(2)
β/°	106.841(2)
γ/°	118.231(2)
Volume/Å^3	2330.22(12)
Z	2
ρ_{calc}g/cm^3	1.431
μ/mm^{-1}	5.202
F(000)	1024.0
Crystal size/mm^3	0.14 × 0.03 × 0.02
Radiation	GaKα (λ = 1.34143)
2Θ range for data collection/°	5.772 to 124.986
Index ranges	$-18 \leq h \leq 17$, $-18 \leq k \leq 18$, $-6 \leq l \leq 18$
Reflections collected	32672
Independent reflections	11077 [R_{int} = 0.0229, R_{sigma} = 0.0271]
Data/restraints/parameters	11077/0/577
Goodness-of-fit on F^2	1.036
Final R indexes [I>=2σ (I)]	R_1 = 0.0412, wR_2 = 0.1021
Final R indexes [all data]	R_1 = 0.0565, wR_2 = 0.1092
Largest diff. peak/hole / e Å^{-3}	0.58/-0.83

[(DPEPhos)$_2$Cu$_2$Cl$_2$] ([Cu-Cl-Cu] (**38**))

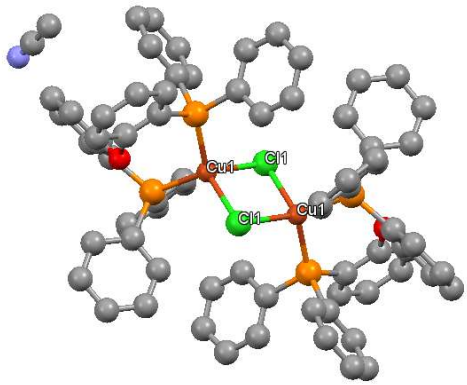

Identification code	LLG-196
Empirical formula	$C_{76}H_{62}Cl_2Cu_2N_2O_2P_4$
Formula weight	1357.13
Temperature/K	180.0
Crystal system	triclinic
Space group	P-1
a/Å	11.7709(14)
b/Å	12.3022(16)
c/Å	13.8362(18)
α/°	64.328(9)
β/°	68.835(9)
γ/°	73.117(9)
Volume/Å^3	1662.5(4)
Z	1
ρ_{calc}g/cm^3	1.356
μ/mm^{-1}	4.781
F(000)	700.0
Crystal size/mm^3	0.05 × 0.045 × 0.04
Radiation	GaKα (λ = 1.34143)
2Θ range for data collection/°	6.41 to 115.25
Index ranges	-14 ≤ h ≤ 14, -15 ≤ k ≤ 8, -17 ≤ l ≤ 13
Reflections collected	20520
Independent reflections	6889 [R_{int} = 0.0705, R_{sigma} = 0.0645]
Data/restraints/parameters	6889/0/398
Goodness-of-fit on F^2	0.973
Final R indexes [I>=2σ (I)]	R_1 = 0.0649, wR_2 = 0.1607
Final R indexes [all data]	R_1 = 0.0923, wR_2 = 0.1794
Largest diff. peak/hole / e Å^{-3}	0.96/-0.61

[(DPEPhos)$_2$Cu$_2$(NCS)$_2$] ([Cu-NCS-Cu] (**39**))

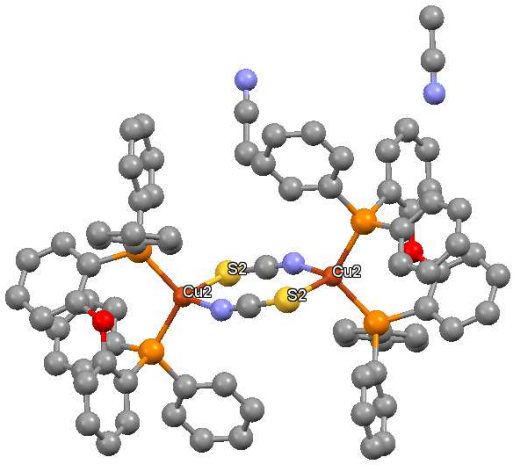

Identification code	LLG-148-farblos
Empirical formula	$C_{78}H_{62}Cu_2N_4O_2P_4S_2$
Formula weight	1402.39
Temperature/K	150
Crystal system	monoclinic
Space group	$P2_1/c$
a/Å	17.4903(3)
b/Å	23.7998(4)
c/Å	17.9228(3)
α/°	90
β/°	115.3870(10)
γ/°	90
Volume/Å^3	6740.2(2)
Z	4
ρ_{calc}g/cm^3	1.382
μ/mm^{-1}	4.637
F(000)	2896.0
Crystal size/mm^3	0.16 × 0.03 × 0.02
Radiation	GaKα (λ = 1.34143)
2Θ range for data collection/°	5.744 to 124.984
Index ranges	-22 ≤ h ≤ 23, -31 ≤ k ≤ 29, -15 ≤ l ≤ 23
Reflections collected	39851
Independent reflections	15671 [R_{int} = 0.0258, R_{sigma} = 0.0388]
Data/restraints/parameters	15671/0/831
Goodness-of-fit on F^2	1.012
Final R indexes [I>=2σ (I)]	R_1 = 0.0352, wR_2 = 0.0750
Final R indexes [all data]	R_1 = 0.0557, wR_2 = 0.0810
Largest diff. peak/hole / e Å^{-3}	0.29/-0.34

7 LIST OF ABBREVIATIONS

δ	Chemical shift (NMR)
°C	Celsius
t	Lifetime
C	Magnetic susceptibility
AA	Atomic absorption
ADP	ADENOSINE-5'-DIPHOSPHATE
Asc.	Ascorbic
Atm.	Atmosphere
ATP	Adenosine triphosphate
BIH	dimethylphenylbenzimidazoline
bpy	bipyridine
BVS	Bond valence sum
Calc.	Calculated
CAT	Catalyst
$CDCl_3$	Deuterated chloroform
CH_2Cl_2	Dichloromethane
CT	Charge Transfer
CV	Cyclic Voltammetry
cyclam	1,4,8,11-tetraazacyclotetradecane
d	Doublet (NMR)
DFT	Density Functional Theory
DLS	Dynamic light scattering
DMA	dimethylacetamide
DMF	Dimethylformamide
dmp	dimethylphenantholine
DMSO	Dimethyl sulfoxide
DPAC	9,9-Diphenyl-9,10-dihydroacridine
DPEPhos	Bis[2-(diphenylphosphino)phenyl] ether
DPV	Differential pulse voltammetry
EA	Elemental Analysis
e^-D	Electron donor
EDC	1-Ethyl-3-(3-dimethylaminopropyl)carbodiimide

equiv.	Equivalent
ESI	Electrospray Ionization
Et	Ethyl
Et_2O	Diethylether
E	Potential
et. al.	And others
FAB	Fast Atom Bombardment
Fc	Ferrocene
G´	Storage modulus
G´´	Loss modulus
GC	Gas chromatography
hu	Photon energy
HOMO	Highest Occupied Molecular Orbital
HS	High spin
IC	Internal Conversion
IR	Infrared spectroscopy
ISC	Intersystem Crossing
J	Exchange Energy Integral or Coupling Constant (NMR)
K	Kelvin
k_B	Boltzmann constant
k_F	Rate of Fluorescence
LC	Ligand centered
LS	Low spin
LUMO	Lowest Unoccupied Molecular Orbital
λ	Wavelength
λ_{max}	Emission maxima
$Me_{10}Fc$	Decamethylferrocene
MeCN	Acetonitrile
mL	Milliliter
MLCT	Metal to ligand charge transfer
mmol	Millimol
Me	Methyl
MeOH	Methanol
MOFs	Metal organic framework

Mp	Melting point
ms	Mass spectrometry
MTT	Monotriazolotriazine
MW	Molecular weight
Nano-ESI	*nano* Electrospray ionization
NADP	Nicotinamide adenine dinucleotide phosphate
NMR	Nuclear Magnetic Resonance
ns	Nanoseconds
N-Xantphos	4,6-Bis(diphenylphosphino)-10H-phenoxazine
OLED	Organic light-emitting diode
PC	Photocatalyst
ph	Phenyl
phen	phenanthroline
PLQY/Φ_{PL}	Photoluminescence Quantum Yield
ppm	Parts per million
PS	Photosensitizer
py	pyridine
q	Quartett (NMR)
qpy	quaterpyridine
rt	Room temperature
s	Singlet (NMR), Strong (IR)
Sel.	Selectivity
t	Triplet (NMR)
T	Temperature
T_1	First excited triplet state
$TBAPF_6$	Tetrabutylammonium hexafluorophosphate
TEOA	Triethanolamine
THF	Tetrahydrofuran
TLC	Thin Layer Chromatography
TOF	Turnover frequency
TON	Turnover number
tpy	terpyridine
UV	Ultraviolet
wt%	Weight percent

X-Ray	Single crystal x-ray diffraction

8 BIBLIOGRAPHY

[1] S. Arrhenius, *Lond. Edinb. Dublin Philos. Mag. J. Sci.* **1896**, *41*, 237-276.

[2] G. S. Callendar, *Q. J. R. Meteorol. Soc.* **1938**, *64*, 223-240.

[3] Y. Suzuki, Y. Takemura, K.-i. Iwamoto, T. Higashino, A. Miyashita, *Chem. Pharm. Bull.* **1998**, *46*, 199-206.

[4] How much will Earth warm if carbon dioxide doubles pre-industrial levels? https://www.climate.gov/news-features/climate-qa/how-much-will-earth-warm-if-carbon-dioxide-doubles-pre-industrial-levels,

[5] Carbon Dioxide, https://climate.nasa.gov/vital-signs/carbon-dioxide/

[6] P. L. Cheung, S. C. Kapper, T. Zeng, M. E. Thompson, C. P. Kubiak, *J. Am. Chem. Soc.* **2019**, *141*, 14961-14965.

[7] CO2 Can Directly Impact Extreme Weather, Research Suggests, https://www.scientificamerican.com/article/co2-can-directly-impact-extreme-weather-research-suggests/,

[8] Forests Absorb Twice As Much Carbon As They Emit Each Year, https://www.wri.org/insights/forests-absorb-twice-much-carbon-they-emit-each-year,

[9] L. Polimene, S. Sailley, D. Clark, A. Mitra, J. I. Allen, *J. Plankton Res.* **2017**, *39*, 180-186.

[10] E. Kabir, P. Kumar, S. Kumar, A. A. Adelodun, K.-H. Kim, *Renew. Sust. Energ. Rev.* **2018**, *82*, 894-900.

[11] Biomass, a massively available and major source of energy, an unsustainable use, https://www.encyclopedie-energie.org/en/biomass-major-source-energy-unsustainable-use/,

[12] A. G. Olabi, M. A. Abdelkareem, *Renew. Sust. Energ. Rev.* **2022**, *158*, 112111.

[13] Y.-N. Li, R. Ma, L.-N. He, Z.-F. Diao, *Catal. Sci. Technol.* **2014**, *4*, 1498-1512.

[14] M. Aresta, A. Dibenedetto, *Dalton Trans.* **2007**, 2975.

[15] T. Matsuo, H. Kawaguchi, *J. Am. Chem. Soc.* **2006**, *128*, 12362-12363.

[16] T. Sakakura, J.-C. Choi, H. Yasuda, *Chem. Rev.* **2007**, *107*, 2365-2387.

[17] S. M. Hosseini, A. Aslani, A. Kasaeian, *Energy Rep.* **2023**, *9*, 414-436.

[18] T. Hoover, *Sci. Scope* **2017**, *41*, 14-17.

[19] X. Nie, W. Li, X. Jiang, X. Guo, C. Song, in *Advances in Catalysis, Vol. 65* (Ed.: C. Song), Academic Press, **2019**, pp. 121-233.

[20] A. Nisar, S. Khan, M. Hameed, A. Nisar, H. Ahmad, S. A. Mehmood, *Microbiol. Res.* **2021**, *251*, 126813.

[21] I. S. Thakur, M. Kumar, S. J. Varjani, Y. Wu, E. Gnansounou, S. Ravindran, *Bioresour. Technol.* **2018**, *256*, 478-490.

[22] W. Zhou, K. Cheng, J. Kang, C. Zhou, V. Subramanian, Q. Zhang, Y. Wang, *Chem. Soc. Rev.* **2019**, *48*, 3193-3228.

[23] M. D. Garba, M. Usman, S. Khan, F. Shehzad, A. Galadima, M. F. Ehsan, A. S. Ghanem, M. Humayun, *J. Environ. Chem.* **2021**, *9*, 104756.

[24] L.-B. Sun, Y.-H. Kang, Y.-Q. Shi, Y. Jiang, X.-Q. Liu, *ACS Sustain. Chem. Eng.* **2015**, *3*, 3077-3085.

[25] N. Yadav, F. Seidi, D. Crespy, V. D'Elia, *ChemSusChem* **2019**, *12*, 724-754.

[26] W.-F. Tsao, G.-L. Liu, Y.-C. Su, C.-C. Lin, B.-T. Ko, *Organometallics* **2021**, *40*, 3742-3752.

[27] E. S. Sanz-Pérez, C. R. Murdock, S. A. Didas, C. W. Jones, *Chem. Rev.* **2016**, *116*, 11840-11876.

[28] X. Shi, H. Xiao, H. Azarabadi, J. Song, X. Wu, X. Chen, K. S. Lackner, *Angew. Chem. Int. Ed.* **2020**, *59*, 6984-7006.

[29] H. Yamada, *Polym. J.* **2021**, *53*, 93-102.

[30] A. Kumar, D. G. Madden, M. Lusi, K.-J. Chen, E. A. Daniels, T. Curtin, J. J. Perry Iv, M. J. Zaworotko, *Angew. Chem. Int. Ed.* **2015**, *54*, 14372-14377.

[31] A. Taheri Najafabadi, *Int. J. Energy Res.* **2013**, *37*, 485-499.

[32] E. Barbera, F. Mantoan, A. Bertucco, F. Bezzo, *Can. J. Chem. Eng.* **2020**, *98*, 1893-1906.

[33] Z. Sun, T. Ma, H. Tao, Q. Fan, B. Han, *Chem.* **2017**, *3*, 560-587.

[34] G. Guan, T. Kida, A. Yoshida, *Appl. Catal. B: Environ.* **2003**, *41*, 387-396.

[35] D. Li, C. Hao, H. Liu, R. Zhang, Y. Li, J. Guo, C. C. Vilancuo, J. Guo, in *Catalysts, Vol. 12*, **2022**.

[36] M. Subrahmanyam, S. Kaneco, N. Alonso-Vante, *Appl. Catal. B: Environ.* **1999**, *23*, 169-174.

[37] J. Wu, Y. Huang, W. Ye, Y. Li, *Adv. Sci.* **2017**, *4*, 1700194.

[38] M. J. Paul, C. H. Foyer, *J. Exp. Bot.* **2001**, *52*, 1383-1400.

[39] J. Barber, P. D. Tran, *J. R. Soc. Interface* **2013**, *10*, 20120984.

[40] A. C. Benniston, A. Harriman, *Mater. Today* **2008**, *11*, 26-34.

[41] H. Nagao, T. Mizukawa, K. Tanaka, **1994**, *33*, 3415-3420.

[42] C. D. Windle, R. N. Perutz, *Coord. Chem. Rev.* **2012**, *256*, 2562-2570.

[43] P. Kang, Z. Chen, M. Brookhart, T. J. Meyer, **2015**, *58*, 30-45.

[44] R. Francke, B. Schille, M. Roemelt, *Chem. Rev.* **2018**, *118*, 4631-4701.

[45] B. Zhang, L. Sun, *Chem. Soc. Rev.* **2019**, *48*, 2216-2264.

[46] L. Wang, I. Rörich, C. Ramanan, P. W. M. Blom, W. Huang, R. Li, K. A. I. Zhang, *Catal. Sci. Technol.* **2018**, *8*, 3539-3547.

[47] G. Magagnano, A. Gualandi, M. Marchini, L. Mengozzi, P. Ceroni, P. G. Cozzi, *Chem. Commun.* **2017**, *53*, 1591-1594.

[48] A. E. Ashley, A. L. Thompson, D. O'Hare, *Angew. Chem. Int. Ed.* **2009**, *48*, 9839-9843.

[49] D. S. Laitar, P. Müller, J. P. Sadighi, *J. Am. Chem. Soc.* **2005**, *127*, 17196-17197.

[50] Y. Wang, T. Liu, L. Chen, D. Chao, *Inorg. Chem.* **2021**, *60*, 5590-5597.

[51] A. Juris, V. Balzani, F. Barigelletti, S. Campagna, P. Belser, A. von Zelewsky, *Coord. Chem. Rev.* **1988**, *84*, 85-277.

[52] D. R. Whang, D. H. Apaydin, *ChemPhotoChem* **2018**, *2*, 148-160.

[53] A. Pannwitz, O. S. Wenger, *Chem. Commun.* **2019**, *55*, 4004-4014.

[54] R. Reithmeier, C. Bruckmeier, B. Rieger, in *Catalysts, Vol. 2*, **2012**, pp. 544-571.

[55] Y. Pellegrin, F. Odobel, *C. R. Chim.* **2017**, *20*, 283-295.

[56] L.-L. Gracia, L. Luci, C. Bruschi, L. Sambri, P. Weis, O. Fuhr, C. Bizzarri, *Chem. Eur. J.* **2020**, *26*, 9929-9937.

[57] E. Fujita, *Coord. Chem. Rev.* **1999**, *185-186*, 373-384.

[58] S. Sato, T. Arai, T. Morikawa, *Inorg. Chem.* **2015**, *54*, 5105-5113.

[59] R. N. Sampaio, D. C. Grills, D. E. Polyansky, D. J. Szalda, E. Fujita, *J. Am. Chem. Soc.* **2020**, *142*, 2413-2428.

[60] H. Koizumi, H. Chiba, A. Sugihara, M. Iwamura, K. Nozaki, O. Ishitani, *Chem. Sci.* **2019**, *10*, 3080-3088.

[61] K. Ozawa, Y. Tamaki, K. Kamogawa, K. Koike, O. Ishitani, *J. Chem. Phys.* **2020**, *153*, 154302.

[62] M. Marx, A. Mele, A. Spannenberg, C. Steinlechner, H. Junge, P. Schollhammer, M. Beller, *ChemCatChem* **2020**, *12*, 1603-1608.

[63] J.-M. Lehn, R. Ziessel, *Proc. Natl. Acad. Sci.* **1982**, *79*, 701-704.

[64] J.-M. Lehn, R. Ziessel, *J. Organomet. Chem.* **1990**, *382*, 157-173.

[65] J. Hawecker, J.-M. Lehn, R. Ziessel, *J. Chem. Soc., Chem. Commun.* **1983**, 536-538.

[66] M. Beley, J.-P. Collin, R. Ruppert, J.-P. Sauvage, *J. Chem. Soc., Chem. Commun.* **1984**, 1315-1316.

[67] M. Beley, J. P. Collin, R. Ruppert, J. P. Sauvage, *J. Am. Chem. Soc.* **1986**, *108*, 7461-7467.

[68] Y. Kuramochi, O. Ishitani, *Inorg. Chem.* **2016**, *55*, 5702-5709.

[69] M. Feller, U. Gellrich, A. Anaby, Y. Diskin-Posner, D. Milstein, *J. Am. Chem. Soc.* **2016**, *138*, 6445-6454.

[70] Y. Tamaki, O. Ishitani, *ACS Catal.* **2017**, *7*, 3394-3409.

[71] K. Kamada, J. Jung, T. Wakabayashi, K. Sekizawa, S. Sato, T. Morikawa, S. Fukuzumi, S. Saito, *J. Am. Chem. Soc.* **2020**, *142*, 10261-10266.

[72] C. Bizzarri, *Eur. J. Org. Chem.* **2022**.

[73] A. Rosas-Hernández, C. Steinlechner, H. Junge, M. Beller, *Green Chem.* **2017**, *19*, 2356-2360.

[74] P. Zhang, M. Wang, C. Li, X. Li, J. Dong, L. Sun, *Chem. Commun.* **2010**, *46*, 8806.

[75] C. Federsel, A. Boddien, R. Jackstell, R. Jennerjahn, P. J. Dyson, R. Scopelliti, G. Laurenczy, M. Beller, *Angew. Chem. Int. Ed.* **2010**, *49*, 9777-9780.

[76] S. Chakraborty, J. Zhang, J. A. Krause, H. Guan, *J. Am. Chem. Soc.* **2010**, *132*, 8872-8873.

[77] M. Albrecht, R. Bedford, B. Plietker, *Organometallics* **2014**, *33*, 5619-5621.

[78] S. Straub, P. Brünker, J. Lindner, P. Vöhringer, *Angew. Chem. Int. Ed.* **2018**, *57*, 5000-5005.

[79] A. M. Masdeu‐Bultó, M. Reguero, C. Claver, *European Journal of Inorganic Chemistry* **2022**, e202100975.

[80] M. Cokoja, C. Bruckmeier, B. Rieger, W. A. Herrmann, F. E. Kühn, *Angew. Chem. Int. Ed.* **2011**, *50*, 8510-8537.

[81] C. Steinlechner, H. Junge, *Angew. Chem. Int. Ed.* **2018**, *57*, 44-45.

[82] H. Rao, L. C. Schmidt, J. Bonin, M. Robert, *Nature* **2017**, *548*, 74-77.

[83] E. Boutin, L. Merakeb, B. Ma, B. Boudy, M. Wang, J. Bonin, E. Anxolabéhère-Mallart, M. Robert, *Chem. Soc. Rev.* **2020**, *49*, 5772-5809.

[84] S. Amanullah, P. Saha, A. Dey, *J. Am. Chem. Soc.* **2021**, *143*, 13579-13592.

[85] P. Zhang, M. Wang, C. Li, X. Li, J. Dong, L. Sun, *Chem. Commun.* **2010**, *46*, 8806-8808.

[86] M. Rakowski Dubois, D. L. Dubois, *Acc. Chem. Res.* **2009**, *42*, 1974-1982.

[87] S. Horvath, L. E. Fernandez, A. V. Soudackov, S. Hammes-Schiffer, *Proc. Natl. Acad. Sci.* **2012**, *109*, 15663-15668.

[88] R. Bonetto, R. Altieri, M. Tagliapietra, A. Barbon, M. Bonchio, M. Robert, A. Sartorel, *ChemSusChem* **2020**, *13*, 4111-4120.

[89] L. Chen, Z. Guo, X.-G. Wei, C. Gallenkamp, J. Bonin, E. Anxolabéhère-Mallart, K.-C. Lau, T.-C. Lau, M. Robert, *J. Am. Chem. Soc.* **2015**, *137*, 10918-10921.

[90] K. M. Waldie, A. L. Ostericher, M. H. Reineke, A. F. Sasayama, C. P. Kubiak, *ACS Catal.* **2018**, *8*, 1313-1324.

[91] K. E. Dalle, J. Warnan, J. J. Leung, B. Reuillard, I. S. Karmel, E. Reisner, *Chem. Rev.* **2019**, *119*, 2752-2875.

[92] H. H. Cramer, B. Chatterjee, T. Weyhermüller, C. Werlé, W. Leitner, *Angew. Chem.* **2020**, *132*, 15804-15811.

[93] E. Karamian, S. Sharifnia, *J. CO2. Util.* **2016**, *16*, 194-203.

[94] J. S. Derrick, M. Loipersberger, S. K. Nistanaki, A. V. Rothweiler, M. Head-Gordon, E. M. Nichols, C. J. Chang, *J. Am. Chem. Soc.* **2022**, *144*, 11656-11663.

[95] M. Abdinejad, A. Seifitokaldani, C. Dao, E. H. Sargent, X.-a. Zhang, H. B. Kraatz, *ACS Appl. Energy Mater.* **2019**, *2*, 1330-1335.

[96] C. Costentin, G. Passard, M. Robert, J.-M. Savéant, *Proc. Natl. Acad. Sci.* **2014**, *111*, 14990-14994.

[97] X. Chen, C. Wang, D. Qi, X. Xing, *Inorg. Chem. Front.* **2022**, *9*, 2691-2696.

[98] M. W. Drover, *Chem. Soc. Rev.* **2022**, *51*, 1861-1880.

[99] A. Kumar, P. Daw, N. A. Espinosa-Jalapa, G. Leitus, L. J. W. Shimon, Y. Ben-David, D. Milstein, *Dalton Trans.* **2019**, *48*, 14580-14584.

[100] K. S. Rawat, A. Mahata, I. Choudhuri, B. Pathak, *J. Phys. Chem. C* **2016**, *120*, 16478-16488.

[101] W. Sattler, G. Parkin, *J. Am. Chem. Soc.* **2012**, *134*, 17462-17465.

[102] J. Schneider, H. Jia, J. T. Muckerman, E. Fujita, *Chem. Soc. Rev.* **2012**, *41*, 2036-2051.

[103] A. M. Masdeu-Bultó, M. Reguero, C. Claver, *Eur. J. Inorg. Chem.* **2022**, *2022*, e202100975.

[104] C. Cometto, L. Chen, P.-K. Lo, Z. Guo, K.-C. Lau, E. Anxolabéhère-Mallart, C. Fave, T.-C. Lau, M. Robert, *ACS Catal.* **2018**, *8*, 3411-3417.

[105] M. Loipersberger, D. G. A. Cabral, D. B. K. Chu, M. Head-Gordon, *J. Am. Chem. Soc.* **2021**, *143*, 744-763.

[106] M. Stanbury, J.-D. Compain, S. Chardon-Noblat, *Coord. Chem. Rev.* **2018**, *361*, 120-137.

[107] R. Langer, Y. Diskin-Posner, G. Leitus, L. J. W. Shimon, Y. Ben-David, D. Milstein, *Angew. Chem. Int. Ed.* **2011**, *50*, 9948-9952.

[108] M. Stanbury, J.-D. Compain, M. Trejo, P. Smith, E. Gouré, S. Chardon-Noblat, *Electrochim. Acta* **2017**, *240*, 288-299.

[109] C. K. Williams, A. Lashgari, J. Chai, J. J. Jiang, *ChemSusChem* **2020**, *13*, 3412-3417.

[110] E. S. Donovan, B. M. Barry, C. A. Larsen, M. N. Wirtz, W. E. Geiger, R. A. Kemp, *Chem. Commun.* **2016**, *52*, 1685-1688.

[111] Z. Guo, F. Yu, Y. Yang, C.-F. Leung, S.-M. Ng, C.-C. Ko, C. Cometto, T.-C. Lau, M. Robert, *ChemSusChem* **2017**, *10*, 4009-4013.

[112] P. A. Forero-Cortés, M. Marx, N. G. Moustakas, F. Brunner, C. E. Housecroft, E. C. Constable, H. Junge, M. Beller, J. Strunk, *Green Chem.* **2020**, *22*, 4541-4549.

[113] D. B. Burks, S. Davis, R. W. Lamb, X. Liu, R. R. Rodrigues, N. P. Liyanage, Y. Sun, C. E. Webster, J. H. Delcamp, E. T. Papish, *Chem. Commun.* **2018**, *54*, 3819-3822.

[114] D. Hong, T. Kawanishi, Y. Tsukakoshi, H. Kotani, T. Ishizuka, T. Kojima, *J. Am. Chem. Soc.* **2019**, *141*, 20309-20317.

[115] D. Hong, Y. Tsukakoshi, H. Kotani, T. Ishizuka, T. Kojima, *J. Am. Chem. Soc.* **2017**, *139*, 6538-6541.

[116] X. Zhang, M. Cibian, A. Call, K. Yamauchi, K. Sakai, *ACS Catal.* **2019**, *9*, 11263-11273.

[117] A. Call, M. Cibian, K. Yamamoto, T. Nakazono, K. Yamauchi, K. Sakai, *ACS Catal.* **2019**, *9*, 4867-4874.

[118] J. Bonin, M. Chaussemier, M. Robert, M. Routier, *ChemCatChem* **2014**, *6*, 3200-3207.

[119] C. Kutal, M. A. Weber, G. Ferraudi, D. Geiger, *Organometallics* **1985**, *4*, 2161-2166.

[120] H. Takeda, H. Kamiyama, K. Okamoto, M. Irimajiri, T. Mizutani, K. Koike, A. Sekine, O. Ishitani, *J. Am. Chem. Soc.* **2018**, *140*, 17241-17254.

[121] D.-C. Liu, D.-C. Zhong, T.-B. Lu, *EnergyChem* **2020**, *2*, 100034.

[122] C. G. Margarit, N. G. Asimow, C. Costentin, D. G. Nocera, *ACS Energy Lett.* **2020**, *5*, 72-78.

[123] J. D. Froehlich, C. P. Kubiak, *J. Am. Chem. Soc.* **2015**, *137*, 3565-3573.

[124] H.-H. Huang, J.-H. Zhang, M. Dai, L. Liu, Z. Ye, J. Liu, D.-C. Zhong, J.-W. Wang, C. Zhao, Z. Ke, *Proc. Natl. Acad. Sci.* **2022**, *119*, e2119267119.

[125] I. Andersson, *J. Exp. Bot.* **2008**, *59*, 1555-1568.

[126] I. Bhugun, D. Lexa, J.-M. Savéant, *J. Phys. Chem.* **1996**, *100*, 19981-19985.

[127] A. Behr, *Angew. Chem. Int. Ed.* **2014**, *53*, 12674-12674.

[128] F. Huang, C. Zhang, J. Jiang, Z.-X. Wang, H. Guan, *Inorg. Chem.* **2011**, *50*, 3816-3825.

[129] E. Boutin, M. Wang, J. C. Lin, M. Mesnage, D. Mendoza, B. Lassalle-Kaiser, C. Hahn, T. F. Jaramillo, M. Robert, *Angew. Chem. Int. Ed.* **2019**, *58*, 16172-16176.

[130] Z. Bian, S. Das, M. H. Wai, P. Hongmanorom, S. Kawi, *ChemPhysChem* **2017**, *18*, 3117-3134.

[131] J. Zhang, Y. Wang, H. Wang, D. Zhong, T. Lu, *Chin. Chem. Lett.* **2022**, *33*, 2065-2068.

[132] Y. Tamaki, K. Koike, T. Morimoto, O. Ishitani, *J. Catal.* **2013**, *304*, 22-28.

[133] Y. Tamaki, K. Koike, O. Ishitani, *Chem. Sci.* **2015**, *6*, 7213-7221.

[134] H. Kumagai, Y. Tamaki, O. Ishitani, *Acc. Chem. Res.* **2022**, *55*, 978-990.

[135] D. C. Fabry, H. Koizumi, D. Ghosh, Y. Yamazaki, H. Takeda, Y. Tamaki, O. Ishitani, *Organometallics* **2020**, *39*, 1511-1518.

[136] H. Takeda, K. Koike, T. Morimoto, H. Inumaru, O. Ishitani, in *Advances in Inorganic Chemistry, Vol. 63* (Eds.: R. v. Eldik, G. Stochel), Academic Press, **2011**, pp. 137-186.

[137] K. A. Opperman, S. L. Mecklenburg, T. J. Meyer, *Inorganic Chemistry* **1994**, *33*, 5295-5301.

[138] J.-H. Jeoung, H. Dobbek, *Science* **2007**, *318*, 1461-1464.

[139] L.-M. Cao, H.-H. Huang, J.-W. Wang, D.-C. Zhong, T.-B. Lu, *Green Chem.* **2018**, *20*, 798-803.

[140] T. Ouyang, H.-H. Huang, J.-W. Wang, D.-C. Zhong, T.-B. Lu, *Angew. Chem. Int. Ed.* **2017**, *56*, 738-743.

[141] T. Ouyang, H.-J. Wang, H.-H. Huang, J.-W. Wang, S. Guo, W.-J. Liu, D.-C. Zhong, T.-B. Lu, *Angew. Chem. Int. Ed.* **2018**, *57*, 16480-16485.

[142] B. J. Fisher, R. Eisenberg, *J. Am. Chem. Soc.* **1980**, *102*, 7361-7363.

[143] E. Kimura, X. Bu, M. Shionoya, S. Wada, S. Maruyama, *Inorg. Chem.* **1992**, *31*, 4542-4546.

[144] J. Song, E. L. Klein, F. Neese, S. Ye, *Inorg. Chem.* **2014**, *53*, 7500-7507.

[145] A. J. Morris, G. J. Meyer, E. Fujita, *Acc. Chem. Res.* **2009**, *42*, 1983-1994.

[146] J. L. Grant, K. Goswami, L. O. Spreer, J. W. Otvos, M. Calvin, *J. Chem. Soc., Dalton. Trans.* **1987**, 2105-2109.

[147] C. A. Craig, L. O. Spreer, J. W. Otvos, M. Calvin, *J. Phys. Chem.* **1990**, *94*, 7957-7960.

[148] E. Kimura, S. Wada, M. Shionoya, Y. Okazaki, *Inorg. Chem.* **1994**, *33*, 770-778.

[149] K. Mochizuki, S. Manaka, I. Takeda, T. Kondo, *Inorg. Chem.* **1996**, *35*, 5132-5136.

[150] M. A. Méndez, P. Voyame, H. H. Girault, *Angew. Chem.* **2011**, *123*, 7529-7532.

[151] C. Herrero, A. Quaranta, S. El Ghachtouli, B. Vauzeilles, W. Leibl, A. Aukauloo, *Phys. Chem. Chem. Phy.* **2014**, *16*, 12067-12072.

[152] C. R. Schneider, H. S. Shafaat, *Chem. Commun.* **2016**, *52*, 9889-9892.

[153] M. F. Kuehnel, C. D. Sahm, G. Neri, J. R. Lee, K. L. Orchard, A. J. Cowan, E. Reisner, *Chem. Sci.* **2018**, *9*, 2501-2509.

[154] A. K. Feldman, B. Colasson, V. V. Fokin, *Org. Lett.* **2004**, *6*, 3897-3899.

[155] S. Jasimuddin, T. Yamada, K. Fukuju, J. Otsuki, K. Sakai, *Chemical Communications* **2010**, *46*, 8466-8468.

[156] A. Lais, M. A. Gondal, M. A. Dastageer, F. F. Al-Adel, *Int. J. Energy Res.* **2018**, *42*, 2031-2049.

[157] S. L. Behnke, A. C. Manesis, H. S. Shafaat, *Dalton Trans.* **2018**, *47*, 15206-15216.

[158] T. Kojima, *ChemPhotoChem* **2021**, *5*, 512-520.

[159] H. Ishida, K. Fujiki, T. Ohba, K. Ohkubo, K. Tanaka, T. Terada, T. Tanaka, *J. Chem. Soc., Dalton. Trans.* **1990**, 2155-2160.

[160] K. Mochizuki, S. Manaka, I. Takeda, T. Kondo, *Inorg. Chem.* **1996**, *35*, 5132-5136.

[161] W.-M. Liao, J.-H. Zhang, Y.-J. Hou, H.-P. Wang, M. Pan, *Inorg. Chem. Comm.* **2016**, *73*, 80-89.

[162] G. Neri, M. Forster, J. J. Walsh, C. Robertson, T. Whittles, P. Farràs, A. J. Cowan, *Chem. Commun.* **2016**, *52*, 14200-14203.

[163] Y. Wang, X.-W. Gao, J. Li, D. Chao, *Chem. Commun.* **2020**, *56*, 12170-12173.

[164] H. Takeda, K. Ohashi, A. Sekine, O. Ishitani, *J. Am. Chem. Soc.* **2016**, *138*, 4354-4357.

[165] W. Vreugdenhil, J. H. Van Diemen, R. A. G. De Graaff, J. G. Haasnoot, J. Reedijk, A. M. Van Der Kraan, O. Kahn, J. Zarembowitch, *Polyhedron* **1990**, *9*, 2971-2979.

[166] S. E. Lee, A. Nasirian, Y. E. Kim, P. T. Fard, Y. Kim, B. Jeong, S.-J. Kim, J.-O. Baeg, J. Kim, *J. Am. Chem. Soc.* **2020**, *142*, 19142-19149.

[167] W. S. Brotherton, P. M. Guha, H. Phan, R. J. Clark, M. Shatruk, L. Zhu, *Dalton Trans.* **2011**, *40*, 3655-3665.

[168] D. Urankar, B. Pinter, A. Pevec, F. De Proft, I. Turel, J. Košmrlj, *Inorg. Chem.* **2010**, *49*, 4820-4829.

[169] T. Otsubo, V. Boekelheide, *Tetrahedron Lett.* **1975**, *16*, 3881-3884.

[170] V. V. Rostovtsev, L. G. Green, V. V. Fokin, K. B. Sharpless, *Angew. Chem. Int. Ed.* **2002**, *41*, 2596-2599.

[171] M. Montanari, A. Bugana, A. K. Sharma, D. Pasini, *Org. Biomol. Chem.* **2011**, *9*, 5018-5020.

[172] V. Boekelheide, in *Cyclophanes I*, **1983**, pp. 87-143.

[173] W. Libus, J. Stangret, H. Inerowicz, K. Chachulska, *J. Solution Chem.* **1988**, *17*, 337-345.

[174] R. Bonetto, F. Crisanti, A. Sartorel, *ACS Omega* **2020**, *5*, 21309-21319.

[175] I. Azcarate, C. Costentin, M. Robert, J.-M. Savéant, *J. Am. Chem. Soc.* **2016**, *138*, 16639-16644.

[176] H. Triki, B. Nagy, J. Overgaard, F. Jensen, S. Kamoun, *Struct. Chem.* **2020**, *31*, 103-114.

[177] O. C. Gagné, F. C. Hawthorne, *Acta Crystallogr B Struct Sci Cryst Eng Mater* **2015**, *71*, 562-578.

[178] D. G. Cuttell, S.-M. Kuang, P. E. Fanwick, D. R. McMillin, R. A. Walton, *J. Am. Chem. Soc.* **2002**, *124*, 6-7.

[179] J. Kim, H. Y. Cho, W. S. Ahn, *Catal. Surv. Asia* **2012**, *16*, 106-119.

[180] T. Laussmann, I. Grzesiak, A. Krest, K. Stirnat, S. Meier-Giebing, U. Ruschewitz, A. Klein, *Drug Test Anal.* **2015**, *7*, 56-64.

[181] M. Izakovič, J. Šima, M. Žitňanský, *J. Coord. Chem.* **2005**, *58*, 1039-1046.

[182] M. Wriedt, C. Näther, *Z. Anorg. Allg. Chem.* **2010**, *636*, 1061-1068.

[183] Z.-C. Fu, C. Mi, Y. Sun, Z. Yang, Q.-Q. Xu, W.-F. Fu, *Molecules* **2019**, *24*.

[184] A. Barbieri, G. Accorsi, N. Armaroli, *Chem. Commun.* **2008**, *19*, 2185-2193.

[185] J. Sosoe, C. Cruché, É. Morin, S. K. Collins, *Can. J. Chem.* **2020**, *98*, 461-465.

[186] J. A. Widegren, R. G. Finke, *J. Mol. Catal. A. Chem.* **2003**, *198*, 317-341.

[187] C. G. Kalodimos, I. P. Gerothanassis, A. Troganis, B. Loock, M. Momenteau, *J. Biomol. NMR* **1998**, *11*, 423-435.

[188] H. Takeda, Y. Monma, O. Ishitani, *ACS Catal.* **2021**, *11*, 11973-11984.

[189] S. G. Balasubramani, G. P. Chen, S. Coriani, M. Diedenhofen, M. S. Frank, Y. J. Franzke, F. Furche, R. Grotjahn, M. E. Harding, C. Hattig, A. Hellweg, B. Helmich-Paris, C. Holzer, U. Huniar, M. Kaupp, A. Marefat Khah, S. Karbalaei Khani, T. Muller, F. Mack, B. D. Nguyen, S. M. Parker, E. Perlt, D. Rappoport, K. Reiter, S. Roy, M. Ruckert, G. Schmitz, M. Sierka, E. Tapavicza, D. P. Tew, C. van Wullen, V. K. Voora, F. Weigend, A. Wodynski, J. M. Yu, *J Chem Phys* **2020**, *152*, 184107.

[190] A. Becke, *Chem. Phys*, *98*, 5648.

[191] A. Schäfer, H. Horn, R. Ahlrichs, *The Journal of Chemical Physics* **1992**, *97*, 2571-2577.

[192] A. Schäfer, C. Huber, R. Ahlrichs, *The Journal of Chemical Physics* **1994**, *100*, 5829-5835.

[193] S. Grimme, A. Hansen, S. Ehlert, J. M. Mewes, *J Chem Phys* **2021**, *154*.

[194] E. Caldeweyher, S. Ehlert, A. Hansen, H. Neugebauer, S. Spicher, C. Bannwarth, S. Grimme, *The Journal of chemical physics* **2019**, *150*, 154122.

[195] H. Kruse, S. Grimme, *The Journal of chemical physics* **2012**, *136*, 04B613.

[196] F. Weigend, R. Ahlrichs, *Phys. Chem. Chem. Phys.* **2005**, *7*, 3297-3305.

[197] N. Frank, *Wiley Interdiscip Rev Comput Mol Sci* **2012**, *2*, 73-78.

[198] F. Neese, *Wiley Interdisciplinary Reviews: Computational Molecular Science* **2017**, e1606.

[199] G. Dai, J. Liu, *Journal of Materials Science* **2020**, *55*, 14301-14314.

[200] S. Straub, P. Brunker, J. Lindner, P. Vohringer, *Angew Chem Int Ed Engl* **2018**, *57*, 5000-5005.

[201] S. Straub, P. Vohringer, *Angew Chem Int Ed Engl* **2021**, *60*, 2519-2525.

[202] A. Chapovetsky, M. Welborn, J. M. Luna, R. Haiges, T. F. Miller III, S. C. Marinescu, *ACS central science* **2018**, *4*, 397-404.

[203] G. Frenking, I. Fernández, N. Holzmann, S. Pan, I. Krossing, M. Zhou, *JACS Au* **2021**, *1*, 623-645.

[204] L. Zhang, S. Li, H. Liu, Y.-S. Cheng, X.-W. Wei, X. Chai, G. Yuan, *Inorg. Chem.* **2020**, *59*, 17464-17472.

[205] C. Zhang, P. Gotico, R. Guillot, D. Dragoe, W. Leibl, Z. Halime, A. Aukauloo, *Angew. Chem. Int. Ed.* **2022**, *n/a*.

[206] C. Janiak, *J. Chem. Soc., Dalton. Trans.* **2000**, 3885-3896.

[207] N. W. Kinzel, C. Werlé, W. Leitner, *Angew. Chem. Int. Ed.* **2021**, *60*, 11628-11686.

[208] Y. Wang, L. Chen, T. Liu, D. Chao, *Dalton Trans.* **2021**, *50*, 6273-6280.

[209] C. Näther, I. Jess, C. Krebs, M. P. M. Poschmann, *Z. Anorg. Allg. Chem.* **2022**, *648*, e202200023.

[210] R. Taylor, O. Kennard, W. Versichel, *Acta Crystallographica Section B: Structural Science* **1984**, *40*, 280-288.

[211] D. Basu, T. J. Woods, T. B. Rauchfuss, *Dalton Trans.* **2018**, *47*, 7256-7262.

[212] T.-W. Chiou, W.-F. Liaw, *Inorg. Chem.* **2008**, *47*, 7908-7913.

[213] P. W. Ball, *Coord. Chem. Rev.* **1969**, *4*, 361-383.

[214] J. Olguín, S. Brooker, *Coord. Chem. Rev.* **2011**, *255*, 203-240.

[215] W. Liu, H. H. Thorp, *Inorg. Chem.* **1993**, *32*, 4102-4105.

[216] Y. Tamaki, T. Morimoto, K. Koike, O. Ishitani, *Proc. Natl. Acad. Sci.* **2012**, *109*, 15673-15678.

[217] K. Maeda, *Adv. Mater.* **2019**, *31*, 1808205.

[218] E. Kimura, S. Wada, M. Shionoya, Y. Okazaki, *Inorg. Chem.* **1994**, *33*, 770-778.

[219] B. Ma, G. Chen, C. Fave, L. Chen, R. Kuriki, K. Maeda, O. Ishitani, T.-C. Lau, J. Bonin, M. Robert, *J. Am. Chem. Soc.* **2020**, *142*, 6188-6195.

[220] G. Chakkaradhari, T. Eskelinen, C. Degbe, A. Belyaev, A. S. Melnikov, E. V. Grachova, S. P. Tunik, P. Hirva, I. O. Koshevoy, *Inorg. Chem.* **2019**, *58*, 3646-3660.

[221] M.-W. Hong, L. Song, Y. Zhao, L.-S. Qin, C.-Y. Wang, H.-S. Shi, J.-Y. Guo, X.-D. Tao, K.-Y. Shu, W.-X. Chai, *J. Clus. Sci.* **2014**, *25*, 1627-1640.

[222] S. R. Maqsood, N. Islam, S. Bashir, B. Khan, A. H. Pandith, *J. Coord. Chem.* **2013**, *66*, 2308-2315.

[223] E. Mejía, S.-P. Luo, M. Karnahl, A. Friedrich, S. Tschierlei, A.-E. Surkus, H. Junge, S. Gladiali, S. Lochbrunner, M. Beller, *Chem. Eur. J.* **2013**, *19*, 15972-15978.

[224] R. Giereth, M. Obermeier, L. Forschner, M. Karnahl, M. Schwalbe, S. Tschierlei, *ChemPhotoChem* **2021**, *5*, 644-653.

[225] K. Wu, T. Zhang, L. Zhan, C. Zhong, S. Gong, Z.-H. Lu, C. Yang, *Adv. Opt. Mater.* **2016**, *4*, 1558-1566.

[226] J. C. Mol, *J. Mol. Catal. A. Chem.* **2004**, *213*, 39-45.

[227] A. Orejón, A. M. Masdeu-Bultó, P. Salagre, S. Castillón, C. Claver, A. Padilla, B. Almena, F. L. Serrano, *Ind. Eng. Chem. Res.* **2008**, *47*, 8032-8036.

[228] M. Reguero, C. Claver, R. M. B. Carrilho, A. M. Masdeu-Bultó, *Adv. Sustain. Syst.* **2022**, *6*, 2100493.

[229] O. Piermatti, R. Abu-Reziq, L. Vaccaro, in *Catalyst Immobilization*, **2020**, pp. 1-22.

[230] Y. S. Zhang, A. Khademhosseini, *Science* **2017**, *356*, eaaf3627.

[231] S. Peers, A. Montembault, C. Ladavière, *J. Control. Release* **2020**, *326*, 150-163.

[232] F. Pinelli, L. Magagnin, F. Rossi, *Mater. Today Chem.* **2020**, *17*, 100317.

[233] F. Ahmadi, Z. Oveisi, S. M. Samani, Z. Amoozgar, *Res. Pharm. Sci.* **2015**, *10*, 1.

[234] S. Bashir, M. Hina, J. Iqbal, A. Rajpar, M. Mujtaba, N. Alghamdi, S. Wageh, K. Ramesh, S. Ramesh, *Polymers* **2020**, *12*, 2702.

[235] F. Abasalizadeh, S. V. Moghaddam, E. Alizadeh, E. akbari, E. Kashani, S. M. B. Fazljou, M. Torbati, A. Akbarzadeh, *J. Biol. Eng.* **2020**, *14*, 8.

[236] F. Vallée, C. Müller, A. Durand, S. Schimchowitsch, E. Dellacherie, C. Kelche, J. C. Cassel, M. Leonard, *Carbohydr. Res.* **2009**, *344*, 223-228.

[237] F.-Y. Ren, K. Chen, L.-Q. Qiu, J.-M. Chen, D. J. Darensbourg, L.-N. He, *Angew. Chem. Int. Ed.* **2022**, *61*, e202200751.

[238] G. A. Bhat, A. Z. Rashad, T. M. Folsom, D. J. Darensbourg, *Organometallics* **2020**, *39*, 1612-1618.

[239] Z. Li, Z. Wei, F. Xu, Y. H. Li, T. J. Lu, Y. M. Chen, G. J. Zhou, *Macromol. Rapid Commun.* **2012**, *33*, 1191-1196.

[240] Z. Li, Z. Hou, H. Fan, H. Li, *Adv. Funct. Mater.* **2017**, *27*, 1604379.

[241] L. Bahsis, E.-H. Ablouh, H. Anane, M. Taourirte, M. Julve, S.-E. Stiriba, *RCS Adv.* **2020**, *10*, 32821-32832.

[242] C. K. Karan, M. Bhattacharjee, *Eur. J. Inorg. Chem.* **2019**, *2019*, 3605-3611.

[243] F. A. Morrison, *Understanding rheology, Vol. 1*, Oxford university press New York, **2001**.

[244] G. Gritzner, J. Kuta, **1984**, *56*, 461-466.

[245] N. Elgrishi, K. J. Rountree, B. D. McCarthy, E. S. Rountree, T. T. Eisenhart, J. L. Dempsey, *J. Chem. Educ.* **2018**, *95*, 197-206.

[246] E. M. Schubert, *J. Chem. Educ.* **1992**, *69*, 62.

[247] M. H. Gehlen, *J. Photochem. Photobiol. C: Photochem. Rev.* **2020**, *42*, 100338.

[248] J. Lee, H. Seliger, *J. Chem. Phys.* **1964**, *40*, 519-523.

[249] J. Demas, W. Bowman, E. Zalewski, R. Velapoldi, *J. Phys. Chem.* **1981**, *85*, 2766-2771.

[250] G. Gritzner, J. Kuta, *Pure Appl. Chem.* **1984**, *56*, 461-466.

9 APPENDIX

9.1 ACKNOWLEDGMENTS

First and foremost, I would like to thank my supervisor Dr. Claudia Bizzarri, for her encouragement and guidance during the last three years. Her impressive scientific rigor and organization skills pushed me to grow as a scientist and a critical thinker. I also would like to thank her for all the hours she spent teaching me about electrochemistry, GC and all the other techniques we used. Not only she supported us regarding chemistry but she also always pushed us to develop our soft skills by discussing the meaning of quality, questioning our motivations or exercising monotasking during team meetings.

I also would like to thank her for her leadership style, as she always adapted to each of our different characters; with me she was kind, supportive, always available for science and personal discussion and she adapted to my very special organization skills. Her dedication to her goals will always inspire me.

I also thank Prof. Stefan Bräse for the opportunity to work on my PhD within his group and his support all along my thesis. He was welcoming and available all along my time spent in the institute and also supported me to join the MBA program with KSOP.

Prof. Frank Breher is kindly acknowledged for accepting the co-reference of this thesis.

I would like to acknowledge my collaboration partners who helped me diversify and deepen my research. Many thanks go to Prof. Annie Powell and Jonas Braun who worked on the physical properties of my complexes. I also thank them for the few hours spent with them talking about chemistry in such a nice atmosphere. I also thank Prof Karin Fink and Dr. Elham Barani for their theoretical calculations. It was always a pleasure to work with Elham and her explosive positive energy. I also thank Cecilia Bruschi for her contribution to our first joint publication. Thanks also go to Prof. Ruben and Sören Schlittenhardt for their magnetic measurements on my complexes. Many thanks go to PD. Patrick Weis for his mass measurements and his availability, and to Dr. Marco Neumaier for his expertise and mass measurements. I also thank Dr. Olaf Fuhr for his X-ray measurements and his availability.

I would like to acknowledge Dr. Andreas Rapp, Angelika Mösle, Lara Hirsch and Carolin Kohnle for their analytical expertise and availability. I also thank Richard von Budberg for his glass skills and his kindness and Lisa Wanner for measuring the melting points.

I deeply thank Janine Bolz and Christiane Lampert for their great assistance and help with bureaucracy as well as their kindness.

A great thank you goes to the students who worked with me, Philipp, David, Karsten, Wiktoria, Sven and Philip. With you I learnt a lot and could develop my management skills. I also would also like to thank the Bizzarri group with whom I shared this experience with.

I would like to acknowledge KSOP for the opportunity to take part in the Fundamental MBA program and gain insights into management and business.

I thank KHYS for the opportunity to deepen my project working at the University of Bologna for three months. I deeply thank Prof. Letizia Sambri for the chance to work in her group and her kindness. I also thank Chiara, Silvia and Mariangela for their help during this research stay. Many thanks also go to Fabrizio, Erica and Luca for their expertise and to have been immensely welcoming.

I would like to thank the people I met here in Karlsruhe and who became my friends. Thank you Hannes for your emotional support during these three years, thank you Celine for all the laughs spent with you, thank you Anna-Lena, Christoph and Steffen for all the fun bouldering with you.

Finally, I want to express my gratefulness for my parents. You have always supported me, letting me chose my own path, and even pretended listening when I was talking chemistry… Of course, thank you to my sister Léa for existing and to Gautier for bringing a new adventure to life called Meije, who I can't wait to laugh with.

9.2 LIST OF PUBLICATIONS

Peer-reviewed Publications:

Lisa-Lou Gracia, Elham Barani, Jonas Braun, Anthony B. Carter, Dr. Olaf Fuhr, Prof. Annie K. Powell, Prof. Dr. Karin Fink, Dr. Claudia Bizzarri, *ChemCatChem* **2022**, 14, e2022011.

Lisa-Lou Gracia, Luisa Luci, Cecilia Bruschi, Prof. Dr. Letizia Sambri, Dr. Patrick Weis, Dr. Olaf Fuhr, Dr. Claudia Bizzarri, *Chem. Eur. J.* **2020**, 26, 9929 –9937.

Akash Kaithal, **Lisa-Lou Gracia**, Clément Camp, Elsje Alessandra Quadrelli, and Walter Leitner, *J. Am. Chem. Soc.* **2019**, 141, 44, 17487–17492

Conference Posters:

L. Gracia, C. Bizzarri, "New Photosensitizers based on heteroleptic Cu^{I} complexes and CO_2 photocatalytic reduction with known abundant-earth catalysts" International conference on photochemistry, from 18th to 23rd July 2021